# ABSTRACT

Title of Document: PERSONAL COOLING SYSTEM WITH PHASE CHANGE MATERIAL

Yiyuan Qiao, Doctor of Philosophy, 2020

Directed By: Reinhard Radermacher, Professor
Yunho Hwang, Research Professor
Department of Mechanical Engineering

Personal cooling systems (PCS) are attracting more attention recently since they can set back building thermostat setpoints to achieve energy savings and provide high-level human comfort by focusing on micro-environment conditions around occupants rather than the entire building space. Thus, a vapor compression cycle (VCC)-based PCS with a condenser integrated with the phase change material (PCM) is proposed. The PCM heat exchanger (PCMHX) works as a condenser to store waste heat from the refrigerant in the cooling cycle, in which the PCM melting process can affect the system performance significantly. Different from most previous study, various refrigerant heat transfer characteristics along the condenser flow path can result in the uneven PCM melting, leading to the degradation of the system performance. Therefore, enhancing heat transfer in the PCM, investigating the proposed PCS performance, improving PCMHX latent heat utilization in terms of the distribution of PCM melting, and developing a general-purpose PCM model are the objectives of this dissertation.

Five PCMHX designs with different heat transfer enhancements including increasing heat-transfer area, embedding conductive structures, and using uniform refrigerant distribution among condenser branches are introduced first. Compared with

non-enhanced PCM, the graphite-matrix-enhanced PCMHX performs the best with 5.5 times higher heat transfer coefficient and 49% increased coefficient of performance (COP). To investigate the proposed system performance, a system-level experimental parametric study regarding the thermostat setting, PCM recharge rates, and cooling time was conducted. Results show that the PCS can work properly with a stable cooling capacity of 160 W for 4.5 hours. A transient PCM-coupled system model was also developed for detailed system performance, PCM melting process and heat transfer analysis. From both experiment and simulation work, the uneven PCM melting was presented, which could result in an increase of condenser temperature and a degradation of system COP with time. Results show that one significant reason for the uneven PCM melting is the variation of the refrigerant temperature and heat transfer coefficient. Therefore, through experimental analysis, several solutions were proposed to minimize the negative effect of the uneven PCM melting. In addition, to extend the PCMHX application, a multi-tube PCMHX model was developed for general-purpose design. A new multi-tube heat transfer algorithm was proposed, and variable tube shape, connection, and topology for tubes and PCM blocks were considered. The comparison with other PCMHX models in the literature shows that the proposed model exhibits much higher flexibility and feasibility for comprehensive multi-tube configurations. The PCS coupled with PCMHX could achieve energy savings for a range of 8-36% depending on the climate and building types in the U.S.

# PERSONAL COOLING SYSTEM WITH PHASE CHANGE MATERIAL

By

Yiyuan Qiao

Dissertation submitted to the Faculty of the Graduate School of the
University of Maryland, College Park, in partial fulfillment
of the requirements for the degree of
Doctor of Philosophy
2020

Advisory Committee:
Professor Reinhard Radermacher, Chair
Professor Ichiro Takeuchi, Dean's Representative
Research Professor Yunho Hwang
Professor Jelena Srebric
Professor Amir Riaz
Professor Bao Yang

# Dedication

*To my family.*

# Acknowledgements

I would like to thank my advisors, Prof. Reinhard Radermacher and Dr. Yunho Hwang, for providing me the opportunity to work and study with world-class scholars during my past four years at CEEE. Their deep insights, timely guidance, visions and innovative thoughts always benefited me. My dissertation cannot be finished without their assistance. I would also like to thank all of my professors during my graduate study, especially my committee members: Dr. Ichiro Takeuchi, Dr. Jelena Srebric, Dr. Amir Riaz and Dr. Bao Yang. Thanks to their insights and comments on my dissertation.

I would like to thank Jan Muehlbauer for his broad experience in the lab and technical help for the RoCo project. I would like to thank Dr. Vikrant Aute and Dr. Jiazhen Ling for their ideas and expertise on RoCo. Thanks to my CEEE predecessors Yilin Du, Darren Key and Dr. Rohit Dhumane for their work and effort on RoCo.

I would like to thank Dr. Feng Cao for giving me invaluable advice and encouraging me to pursue this degree. I would like to thank Lei Gao, Ransisi Huang and Zhenyuan Mei for their knowledge and emotional support during the most difficult time of my Ph.D. study. Thanks to Wenyi Wang for his advice on my future research. I want to thank Tianyue Qiu, Ellery Klein and Joseph Baker for helping and encouraging me when I worked at CEEE Lab for more than three years.

I would like to thank my husband for his patience and support all the time. Thanks to my parents and sister for their emotional support, understanding and love. I would have not been able to finish this dissertation without their support.

# Table of Contents

# List of Tables

# List of Figures

# Nomenclature

| | |
|---|---|
| $A, A'$ | heat transfer area ($m^2$) |
| $a, e$ | copper sponge parameters |
| $C$ | specific heat (kJ $kg^{-1}$ $K^{-1}$) |
| $C_v$ | flow coefficient (--) |
| $E$ | energy (kJ) |
| $h$ | enthalpy (kJ $kg^{-1}$) |
| $H$ | latent heat (kJ $kg^{-1}$) |
| $i, j$ | segment number |
| $k$ | thermal conductivity (W $m^{-1}$ $K^{-1}$) |
| $K$ | spring constant (N/m) |
| $L, l$ | length (mm) |
| $Le$ | Lewis number (--) |
| $m$ | mass (kg) |
| $\dot{m}$ | mass flow rate (g $s^{-1}$) |
| $n$ | number of the variables |
| $N$ | Compressor speed (rpm) |
| $P$ | pressure (kPa) |
| $Q$ | heat exchanger capacity (W) |
| $r, R$ | radius (mm) |
| $R_t$ | thermal resistance (K $W^{-1}$) |

| | |
|---|---|
| $t$ | time (s) |
| $T$ | temperature (°C) |
| $t^*$ | normalized time |
| $U$ | overall heat transfer coefficient (W $m^{-2}$ $K^{-1}$) |
| $V$ | volume ($m^3$) |
| VED | volumetric energy density (kJ $m^{-3}$) |
| $W$ | power consumption (W) |
| x | distance from the cell node to the edge |
| $x_i$ | independent variable |
| $y$ | deflection of spring in TXV (m) |
| $z$ | length in z direction (mm) |

**Greek symbols**

| | |
|---|---|
| $\alpha, \alpha_1, \alpha_2, \alpha_3$ | heat transfer coefficient (W $m^{-2}$ $K^{-1}$) |
| $\eta$ | efficiency |
| $\rho$ | density (kg $m^{-3}$) |
| $\lambda$ | liquid fraction (--) |
| $\delta$ | thickness of wall (mm) |
| $\omega$ | uncertainty, humidity ratio (kg $kg^{-1}$) |

**Subscripts**

| | |
|---|---|
| a, air | ambient |
| avg | average value |
| b | bulb sensor of TXV |
| B | boundary |
| c | cooling cycle |
| cross | cross-section |
| comp | compressor |
| cond | condenser |
| cyc | overall cycle |
| CENG | CENG-matrix |
| cross | cross-section |
| CS | copper sponge |
| dia | diaphragm of TXV |
| eff | effective value |
| end | end |
| evap | evaporator |
| f | given function, fluid |
| fan | fan |
| fin | fin |
| HTF | heat transfer fluid |
| i | inner, PCM sequence of control volume nodes |

| | |
|---|---|
| in | inlet |
| ini | initial |
| isen | isentropic |
| j | PCM sequence of control volume nodes |
| l | liquid phase |
| loss | heat loss |
| m | melting, motor |
| max | maximum |
| o | outer |
| out | outlet |
| p | PCM |
| r | recharge cycle, radial direction |
| ref | refrigerant |
| s | solid phase |
| sat | saturation |
| sp | spring |
| sys | overall system |
| T, t | tube |
| top | top |
| total | total |
| th | throttle of TXV |

| | |
|---|---|
| tr | transient |
| vol | volumetric |
| W | wall |
| w | tube sequences in generalized PCMHX models |
| z | axial direction, slice sequence in generalized PCMHX models |

**Abbreviations**

| | |
|---|---|
| CENG | Compressed expanded natural graphite |
| COP | Coefficient of performance |
| DSC | Differential scanning calorimeter |
| ET-CS | Eight-tube copper sponge enhanced PCMHX |
| ETSH-GM | Eight-tube, small headers and graphite matrix enhanced PCMHX |
| ET-GM | Eight-tube graphite matrix enhanced PCMHX |
| FT-CS | Eight-tube copper sponge enhanced PCMHX |
| FT-N | Four-tube non-enhanced PCMHX |
| HTF | Heat transfer fluid |
| MCHX | Micro-channel heat exchanger |
| NSD | Normalized subcooling degree as PCM performs phase change |
| PCM | Phase change material |
| PCMHX | PCM heat exchanger |
| PCS | Personal cooling system |

| | |
|---|---|
| rpm | Revolutions per minute |
| TES | Thermal energy storage |
| TXV | Thermal expansion valve |
| VCC | Vapor compression cycle |

# Chapter 1: Introduction

## *1.1 Motivations*

Regarding building air conditioning, space cooling takes up to 31% of the building energy consumption, and it could be reduced by increasing the thermostat set point. For instance, by increasing the thermostat setting temperature from 22.2°C to 25°C, the average cooling energy consumption can be reduced by 29%, while leading to the reduction of occupants' thermal comfort (Hoyt et al., 2014; Huang and Gurney, 2016). To maintain an equal level of human comfort and meanwhile achieve energy savings, a personal air-conditioning system is an attractive option. Moreover, many fields choose thermal energy storage (TES) using phase change materials (PCM) for energy management because of the advantages of PCM properties, such as the large energy density and its capability to thaw within a narrow temperature range. These features make it a good choice to apply PCM in the personal cooling system (PCS). Therefore, a PCS with a vapor compression cycle (VCC) and PCM is proposed.

In the cooling cycle, an evaporator with a fan and nozzle provides localized cooling for users. Meanwhile, the heat released from the refrigerant is dumped to the PCM instead of ambient air to avoid the addition to building cooling loads. In addition, the PCS has a PCM regeneration operation to solidify the PCM either using a thermosiphon cycle or reversed heat pump cycle. Unlike conventional cooling systems, the whole system including the PCMHX can be assembled together, equipped with a robotic base, and powered by an electric battery to achieve mobility. By using this PCS, the building

thermostat setting could be about 4 K higher, leading to a decrease in building energy consumption, while maintaining qualified human comfort.

## *1.2 Literature Review*

### 1.2.1 PCM Heat Transfer Enhancement Methods

The characteristics of PCM can affect the VCC system performance significantly, since better PCM conduction could lead to a higher heat transfer rate and lower approach temperature difference in the condenser. However, PCM conductivity is usually lower than 1.0 W $m^{-1}$ $K^{-1}$ so that the heat transfer enhancement is necessary for this system. Various technologies and methods have been proposed in the literature to enhance the PCM heat transfer, which can be divided into two categories (as shown in Table 1-1): (1) extending heat transfer area and (2) increasing effective thermal conductivity.

Ways to increase heat transfer area include using finned tubes (Al-Abidi et al., 2014; Caron-Soupart et al., 2016; Mat et al., 2013), multi-tube arrays (Al-Abidi et al., 2014; Fang et al., 2018; Joybari et al., 2017; Liu and Groulx, 2014; Tay et al., 2012), spiral-coiled tubes (Chen et al., 2016), spiral-wired tubes (Youssef et al., 2018) and encapsulation of PCM (Alam et al., 2015; Li et al., 2018; Wu et al., 2016). Ways to increase the thermal conductivity include impregnating different structures or particles, such as nanoparticle (Arasu and Mujumdar, 2012; Arıcı et al., 2017; Mahdi and Nsofor, 2017), graphite or metal powder (Dannemand et al., 2016; Merlin et al., 2016), metal foam (Mahdi and Nsofor, 2017; Martinelli et al., 2016; Tian and Zhao, 2011; Zhao et al., 2010) and compressed expanded natural graphite (CENG) matrix (Chen et al.,

2016; Mallow et al., 2018; Medrano et al., 2009). From the literature review on enhanced PCM heat exchangers (PCMHX), many researchers focused on the shell-and-tube heat exchanger (HX) with the heat transfer fluid (HTF) circulated inside the tube and the PCM filled in the annular section.

Merlin et al. (2016) experimentally studied different combinations of bare or finned tubes and graphite powder or PCM/CENG composite, as illustrated in Figure 1-1. With laminar flow inside tubes, the finned tube PCMHX caused a twofold increase in the heat transfer coefficient, while the PCM/CENG composite exchanger increased it by a factor of eight. PCM coupled with the CENG matrix can achieve the best overall heat transfer coefficient of about 3000 W $m^2$ $K^{-1}$.

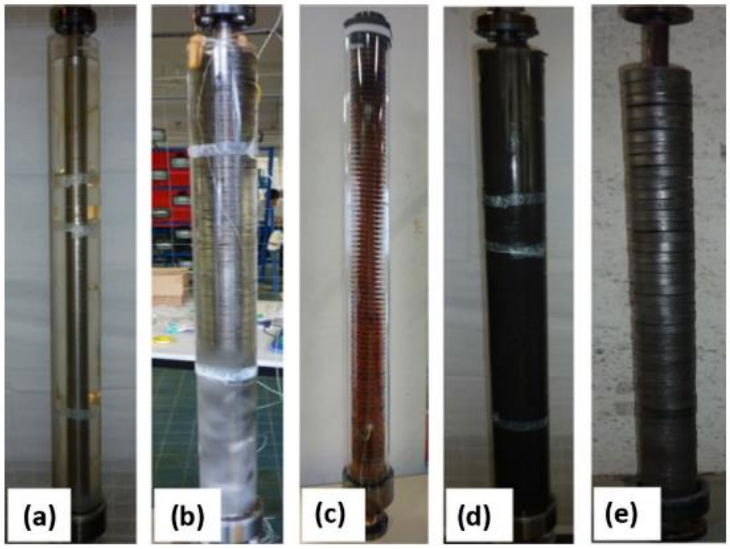


(a) Bare copper tube PCMHX. (b) Aluminium finned-tube PCMHX. (c) Copper finned-tube PCMHX. (d) Graphite powder-PCMHX. (e) CENG-PCMHX. (Merlin et al., 2016)

**Figure 1-1. Photos of the heat exchangers.**

**Table 1-1: PCMHX enhancement methods**

| Methods | References | HTF | Boundary condition | Experiment or Simulation | Highlights |
|---|---|---|---|---|---|
| Finned tubes | Al-Abidi et al., 2014 | Water, Laminar | Constant $T_{in}$ | Experiment | Different locations |
| | Caron-Soupart et al., 2016 | Water, Laminar | Constant $T_{in}$ | Experiment | 5~10 times ↑ |
| Multi-tube arrays | Fang et al., 2018 | Fluid, Laminar | Constant $T_{in}$ | CFD | Simplified to single tube |
| | Tay et al., 2012 | Water, Laminar | | Experiment | 1, 2 and 4 tubes |
| Spiral coils | Chen et al., 2016 | Water, Turbulent | Constant $T_{in}$ | CFD + Experiment | Effect of $T_{in}$ and radius |
| Spiral wires | Youssef et al., 2018 | glycol water | Constant $T_{in}$ | CFD | Effect of flow rate and $T_{in}$ |
| Encapsulation of PCM | Li et al., 2018 | Air | Constant $T_{in}$ | Modeling + Experiment | Cyclic test |
| | Wu et al., 2016 | Air | Constant $T_{in}$ | Modeling | Different Cascaded PCMs |
| Nanoparticles | Arıcı et al., 2017 | -- | Constant $T_{wall}$ | CFD | 0~3 vol%: 30% ↑ |
| | Mahdi and Nsofor, 2017 | Water, Laminar | Constant $T_{in}$ | CFD | Nanoparticles + metal foam |
| Graphite powder | Merlin et al., 2016 | Water, Laminar | Constant $T_{in}$ | CFD | 4 times ↑ |
| Metal foam | Martinelli et al., 2016 | Water, Laminar | Constant $T_{in}$ | Experiment | 10 times ↑ |
| | Zhao et al., 2010 | -- | Constant $T_{wall}$ | Experiment | 95% porosity: 3~10 times↑ |
| Graphite matrix | Merlin et al., 2016 | Water, Turbulent | Constant $T_{in}$ | Experiment | > 10 times ↑ |
| | Medrano et al., 2009 | Water, Laminar | Constant $T_{in}$ | Experiment | > 10 times ↑ |

Medrano et al. (2009) compared various configurations at the component level, including finned tube PCMHX, graphite matrix PCMHX and compact PCMHX. Results show that the PCM/CENG composite had the highest overall heat transfer coefficient in a range of 700-800 W $m^{-2}$ $K^{-1}$, which was ten times higher than the finned tube PCM. They indicated that CENG enhancement was the significant heat transfer intensification, while the finned tube was not able to enhance heat transfer for more than three times due to the limited increase of heat transfer area.

Moreover, compared with pure PCM, the copper foam could increase the overall heat transfer rate by three to ten times with the porosity of 85-95% investigated by Zhao et al. (2010) and Martinelli et al. (2016).

For the melting process in metal-foam-enhanced PCM or pure PCM, natural convection was studied in (Al-Abidi et al., 2014; Dhumane et al., 2017; Longeon et al., 2013; Lorente et al., 2014; Mallow et al., 2018; Martinelli et al., 2016; Mat et al., 2013; Murray and Groulx, 2014; Zhao et al., 2010) showing that the convective motion in PCM caused by buoyancy force had a positive effect on heat transfer enhancement. In the solidification process, however, this effect can be ignored.

It is also observed that most enhanced PCMHX were studied at the component level with the constant inlet temperature of the single-phase HTF with the experimental setup similar to Figure 1-2. Therefore, the PCM melting process and PCMHX performance cannot affect the inlet temperature.

Only a few researchers used PCM with the melting process as condensers in the VCC system, such as Bakhshipour et al. (2017), Wang et al. (2007a, 2007b) and Gu et al. (2004). However, in their systems, PCMHX was placed before or after the normal

condensers, and PCM absorbed only the sensible heat or a small proportion of condensation heat from the refrigerant. As a result, the influences of the PCMHX on the systems were not dominant.

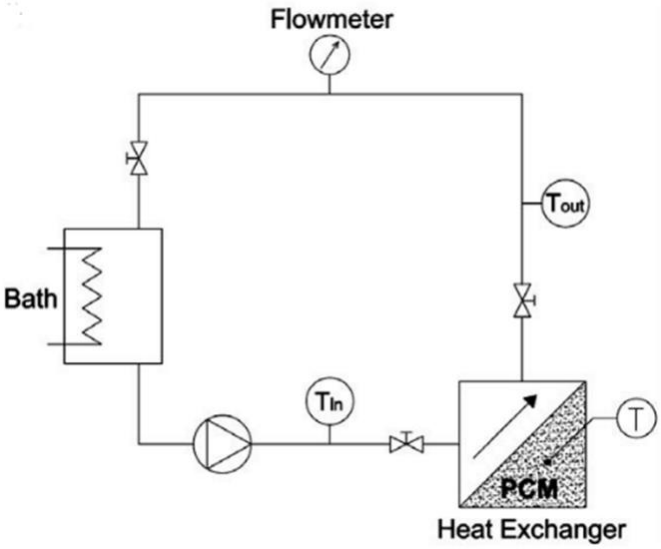


**Figure 1-2. Example of PCMHX experimental setup with constant inlet HTF temperature (Medrano et al., 2009).**

### 1.2.2 PCS Technologies

Personal cooling receives growing attention since it provides a micro-environment and saves air-conditioning energy consumption in buildings. Currently, global building air-conditioning energy consumption keeps increasing as more people demand higher-level thermal comfort (Heidarinejad et al., 2018; Zhu et al., 2017). PCS have the potential to address two following challenges effectively. They can create comfortable local environments for occupants rather than the entire space. Moreover, by using PCS, the building's thermostat set point could be set to a higher temperature, which will result in a lower air-conditioning system's energy consumption. If the building

thermostat set point increases from 22.2 °C to 25 °C, 29% energy savings could be achieved (Hoyt et al., 2014). In recent years, due to the dual advantages of PCS, many studies have been conducted to investigate personal cooling with different systematic designs as listed in Table 1-2. Technologies applied in personal cooling include:

(1) Local ventilation from fans. Zhai et al. (2013) investigated controlled air movement and comfort in different humid environments. Pasut et al., (2015) studied a novel chair coupled with fans for human comfort test, in which three fans were installed in the back and seat of a conventional mesh chair. In (Zhao et al., 2013), jackets with fans placed at the upper back, lower back, mid back, chest and stomach were experimentally studied and compared. Similarly, a portable vest with small fans placed at the lower back was investigated in (Yi et al., 2017).

(2) Radiant cooling by water-cooled panels. A novel radiant cooling desk with water-cooled panels was investigated by He et al., (2017). Cooled water from a cooling-water chiller was circulated in plastic capillary tubes inside the aluminum alloy panels, which could provide radiant cooling for occupants. The water temperature was higher than 18 °C, leading to a higher coefficient of performance (COP) of the chiller. Meanwhile, the radiant cooling desk improved thermal sensation and improved human comfort. Figure 1-3 shows the example of the radiant cooling panel used on the desk (He et al., 2017).

(3) Vacuum desiccant cooling. A garment with vacuum desiccant cooling pads was proposed and experimentally developed in (Yang et al., 2012). The garment was 3.4 kg and provided the unit cooling capacity of 373.1 W $m^{-2}$.

**Table 1-2: Summary of the technologies used for PCS**

| Technologies | References | Applications | Drawbacks | Other apparatus required |
|---|---|---|---|---|
| Local ventilation | Zhai et al. 2013 | Desk fans | Inadequate cooling | -- |
| | Pasut et al., 2015 | Chairs with fan installed | | |
| | Zhao et al., 2013<br>Yi et al., 2017 | Jackets with fan placed at different locations | | |
| Thermoelectric cooling | Choi et al., 2007 | Car seats with stationary thermoelectric unit | Low efficiency | -- |
| | Lou et al., 2018 | Used in clothing (24.6 W) | | |
| Radiant cooling | Y. He et al., 2017 | Desks with cooled water circulated inside | Not movable | Needs chillers and other connection |
| Vacuum desiccant cooling | Yang et al., 2012 | Garments with vacuum desiccant cooling pads | Not movable | Need Vacuum pumps |
| Flow localization | Makhoul et al. 2013 | Personalized ventilator nozzle and diffuser (energy savings of 36%) | Not movable | Based on conventional building AC units |
| | Antoun et al. 2016 | | Inadequate cooling | |
| PCM for thermal management | Hou et al., 2019 | Water-to-PCM HX installed in garments (2 hours cooling, 40 minutes recharge) | Unsteady cooling | Need micro-chillers |
| | Kang et al., 2018<br>Tan and Fok, 2006 | Garments or helmets with PCM pads | | -- |

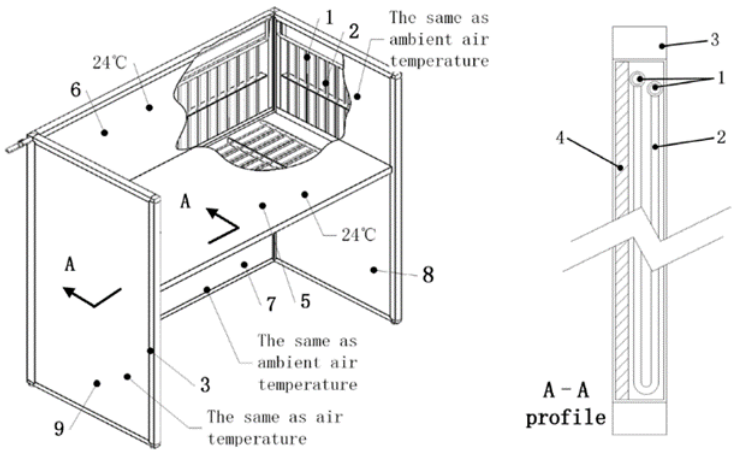


1- tubes 2- capillary tubes 3- support 4- rubber insulation layer 5, 6, 7, 8, 9- radiant panels.

**Figure 1-3. Example of the Schematic diagram of the radiant cooling workstation (He et al., 2017).**

(4) Thermoelectric cooling. A thermoelectric device was used in a car seat to provide cooling in summer and heating in winter as proposed in (Choi et al., 2007), which provided stationary personal comfort and thermal management.

Moreover, a portable thermoelectric unit was developed for personal cooling and building energy saving as in (Lou et al., 2018). In this unit, ambient air was cooled down by thermoelectric unit, and then flowed through a tree-like tube network in clothing to provide cooling. The airflow was supplied by a micro-blower. From the experimental investigation, 24.6 W of personal cooling capacity was achieved.

(5) Flow localization based on conventional air conditioning systems. In this technology, the cooled airflow and ventilation could be optimized and localized for stationary personal cooling, although the refrigerant system is the conventional air-conditioning system.

Makhoul et al. (2013) and Chakroun et al. (2011) carried out the study on a personalized ventilator nozzle and ceiling diffuser for cooling needs around occupants. The design can maintain human comfort in the microclimate with a lower temperature than that of building a macroclimate region.

Antoun et al. (2016) found that coaxial personalized ventilation could achieve energy savings of 36% compared with conventional mixing ventilation.

Al Assaad et al. (2018) proposed an intermittent personalized ventilation system with displacement ventilation as illustrated in Figure 1-4. From the validated model, the new design could achieve maximum energy savings of 54.61% compared with standalone displacement ventilation.

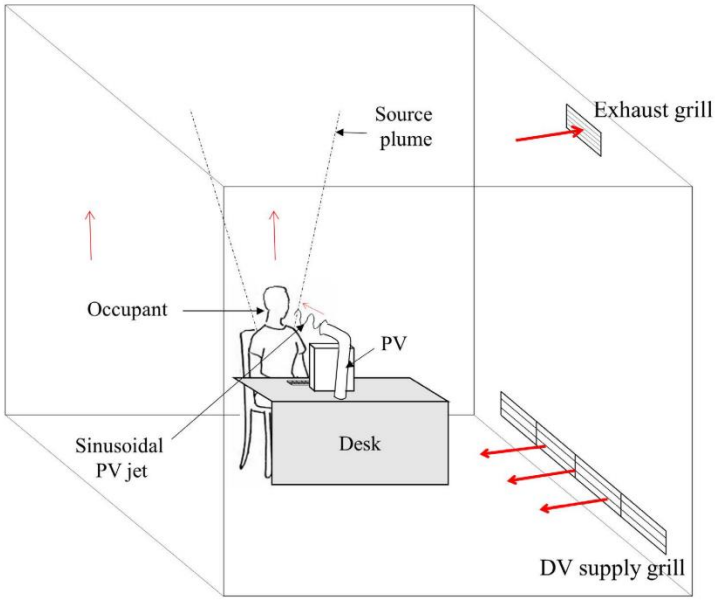


DV: displacement ventilation. PV: personalized ventilation

**Figure 1-4. Space conditioned by a displacement ventilation system and an intermittent personalized ventilation system. (Al Assaad et al., 2018)**

(6) PCM for thermal management. Textiles with applications of PCM could be used as smart temperature regulated textiles, since PCM absorbs or releases heat over a narrow temperature range in terms of latent heat (Mondal, 2008).

Hou et al. (2019) developed a novel personal cooling garment based on both experiments and simulations. The cold water from a micro-chiller system flowed in tubes that were merged inside the PCM, and meanwhile provided cooling to the PCM, which was surrounded by textiles. This PCM-liquid cooling vest had three operation modes: cooling storage, wearing mode, and the combination of cooling storage and wearing mode. Results showed that with the mass of 1.8 kg, wearing mode could operate for at least 2 hours. Cooling storage took 40 minutes in single cooling storage mode or 60 minutes in the combination mode. In addition, a hybrid personal cooling with a fan, PCM and insulation pads were also be used in the clothing (Kang et al., 2018). Based on both experiments and simulation, it shows that the insulation pads and PCM with high melting temperatures and greater latent heat can provide good personal cooling performance to human. The schematic diagram can be found in Figure 1-5.

A helmet design with PCM was developed in (Tan and Fok, 2006), which could achieve two-hour cooling without an external power supply. Moreover, a helmet with a fan and PCM was studied in (Ghani et al., 2016), in which the effect of forced convection from fans, radiation heat and wind speed were discussed.

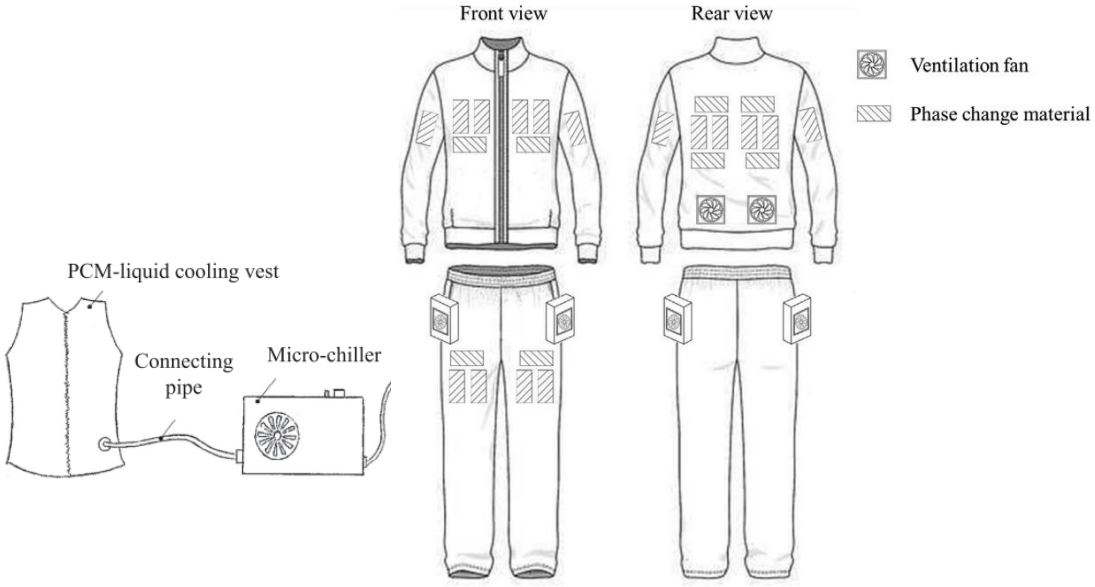


(a) PCM-liquid vest (Hou et al., 2019) (b) Hybrid garment (Kang et al., 2018)

**Figure 1-5. Examples of the PCM coupled with garment for personal cooling**

### 1.2.3 PCMHX Passive Storage

Compared with other technologies, advantages of the PCM used for thermal management are significant, as PCM can absorb or release heat within a small temperature range, and it can provide continuous cooling or heating thanks to the great latent heat. The technology of PCM used as thermal energy storage has two categories: passive storage and active storage. The driving force in passive storage is the temperature difference between PCM and the surroundings, while that of the active storage method comes from fans, pumps or compressors.

From the passive storage point of view, the application of PCM does not lead to high-quality thermal comfort, although building energy consumption could be reduced. PCM for passive storage can be integrated into building structures to regulate indoor temperature swings and save air-conditioning energy (Berardi and Soudian, 2019; de

Gracia, 2019; Stritih et al., 2018; Weinlader et al., 2016). However, indoor temperature regulation by passive storage is limited by the temperature difference between walls and building structures. Moreover, PCM for passive cooling could also be used in refrigerators for thermal storage and performance improvement during the compressor-off period, while instant system efficiency is limited by the cooling storage process (Azzouz et al., 2008; Cheng and Yuan, 2013; Oró et al., 2013).

### 1.2.4 PCMHX Active Storage

The driving force for active storage methods comes from fans, pumps or compressors. It means PCM-to-air, PCM-to-liquid and PCM-to-refrigerant exchangers can be applied to the active storage. Three categories of PCMHX applied as the active storage are as follows.

#### 1.2.4.1 PCM-to-air heat exchanger

PCM can be integrated into the air channels to storage cold during night time and release cold during the day time in order to reduce building energy consumption, and the air is used as HTF to charge and discharge PCM (Dardir et al., 2019; Lizana et al., 2019).

#### 1.2.4.2 PCM-to-water heat exchanger

Water or liquid is the most common HTF in PCMHXs literature, and the most common boundary condition is the constant HTF inlet temperature for both experimental and numerical study in the component level, which limits the application fields.

Rahimi et al. (2019) carried out an experimental study using helical shell-and-tube PCM-to-water heat exchanger and discussed the effect of different tube diameter and different inlet HTF temperatures on HX characteristics.

Seddegh et al. (2017) investigated the HTF inlet temperature and HTF flow rate effect on the thermal storage performance by experiments. Results showed that the HTF flow rate does not show a significant effect, while as HTF temperature increased from 70 °C to 80 °C, the charging time reduced by up to 68%. This is because the main challenge in this application is the PCM side heat transfer resistance, since most PCM have relatively low thermal conductivity. One way is to increase the heat transfer difference between PCM and HTF, and in addition, more literature focus on the PCM side heat transfer enhancement. PCM thermal conductivity enhancement methods include using fins (Martinelli et al., 2016), conductive particles, graphite or metal foams (Qiao et al., 2019; Yang et al., 2014), nano-particles (Mahdi and Nsofor, 2017), encapsulation PCM (Yuan et al., 2018), and combined methods. In the aforementioned PCM-to-water HX investigation, all HTF inlet temperature is constant, which did not reflect the actual applications.

However, a few literatures addressed the study with the changed HTF inlet condition, in which PCM-to-water heat exchangers were discussed in the system level. The examples can be found in Figure 1-6.

Wu et al., (2015) used PCM-to-water HX for the cold storage in a water-loop-based sub-system at the evaporator side, which was coupled in the heat pump system. They developed a dynamic model for the heat pump system and a water-loop PCM

energy storage system. They also validated the model by a detailed comparison between experimental and simulation data.

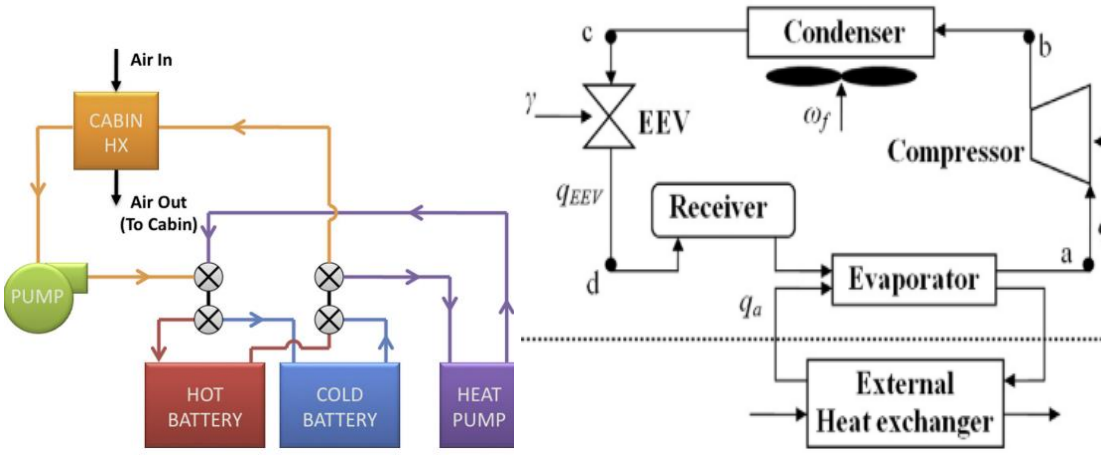


(a) Wu et al., (2015) (b) Fleming et al. (2013)

**Figure 1-6. Examples of PCM-to-water HX used in water-loop-based sub-systems**

Fleming et al. (2013) simulated a dynamic thermal energy storage system with a non-steady water inlet temperature of the shell-and-tube PCMHX applied in the vehicles. In their model, the water inlet temperature is determined by the coupled water-loop system performance of the previous time step.

1.2.4.3 PCM-to-Refrigerant HX

Here PCM-to-refrigerant is defined as HX in which the refrigerant works as HTF vaporized or condensed as flow through the PCM, and therefore, this type of PCM storage device can work as evaporators or condensers in thermal storage systems. The phase change process of both PCM and refrigerant side makes the heat transfer analysis more complicated than the other two types which utilize single-phase air or liquid. There are only a few literature studies on the PCM-to-refrigerant HX.

Gu et al. (2004) modeled an air-conditioning system with PCM condensers for waste heat storage in series with a cooling tower, as illustrated in Figure 1-7. However, the subcooling at the cooling tower outlet was set to be zero, and the condensing temperature was set to be constant, leading PCMHX isolated from the rest of the refrigeration system.

Khalifa and Koz (2016) used PCM-to-refrigerant HX in the PCS for cold storage. They conducted the numerical study of a PCM-to-refrigerant HX as the evaporator in the refrigeration system, while in the simulation, the tube wall temperature was maintained at a constant of 16 °C. Thus, in this model, the PCM phase change process did not affect refrigeration system performance, and the model is not for system-level analysis. The PCM-to-refrigerant HX is insulated from the rest of the system.

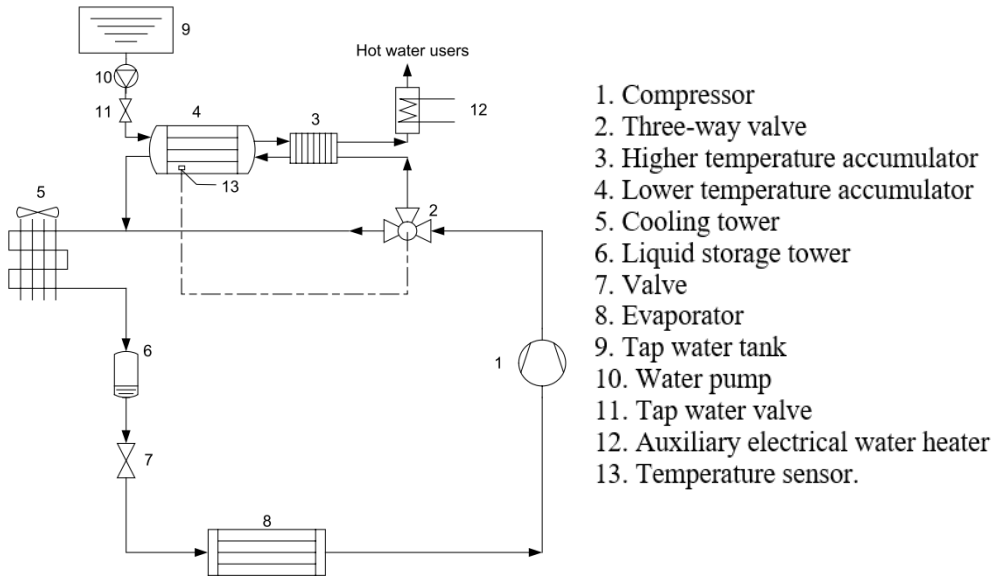


**Figure 1-7. Example of the PCM-to-refrigerant HX application: Schematics of the air conditioning system with thermal energy recovery devices (Gu et al., 2004).**

Bakhshipour et al. (2017) developed a model for a refrigeration system with a PCM-to-refrigerant HX located after the main condenser before the expansion valve shown as Figure 1-8 (a). The whole system and two-dimensional (2-D) PCMHXs were simulated associatively using MATLAB software. The parametric study concerning PCM geometry and the refrigerant property was conducted. Results also showed that utilizing PCM can increase the performance of coefficient by 9.58%. Nevertheless, refrigerant was already single-phase liquid in their PCMHX model, since the subcooled liquid came from the main air-to-refrigerant condenser. Their PCMHX should be categorized as the PCM-to-liquid HX as illustrated in Figure 1-8 (b).

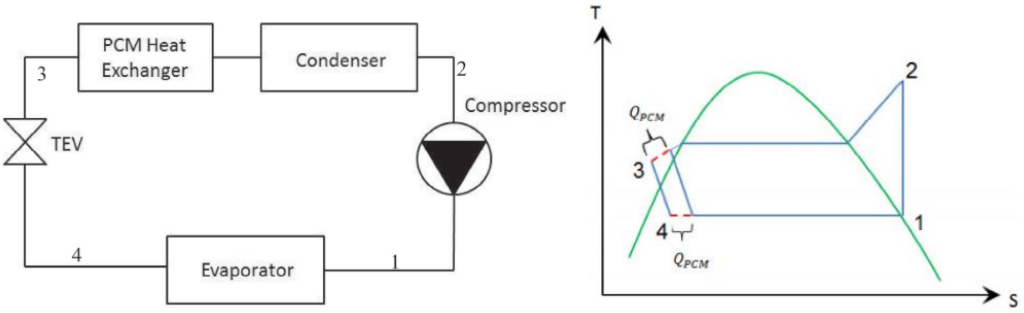


(a) System schematics (b) P-h diagram

**Figure 1-8. Example of the PCM-to-refrigerant HX application (Bakhshipour et al., 2017)**

Similarly, Wang et al. (2007a, 2007b) integrated PCM as the supplementary before or after the conventional condensers and evaporators, as illustrated in Figure 1-9. Results show that the system COP can increase up to 8% based on the experiment and simulation. In these systems, PCM-to-refrigerant HX did not work as the main condenser/ evaporator, refrigerant did not perform phase change in their HX.

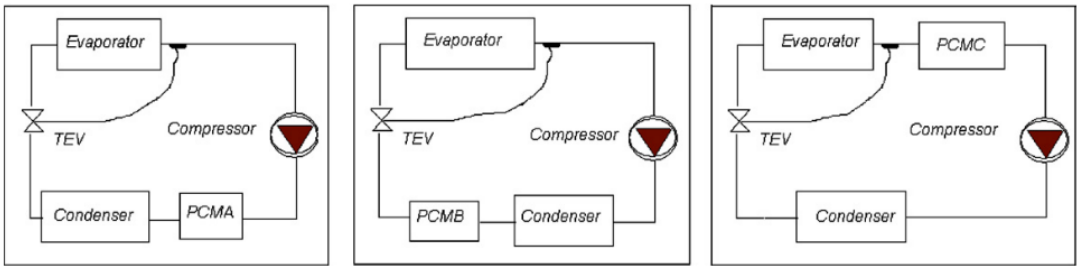


**Figure 1-9. Examples of the PCM-to-refrigerant HX applications (Wang et al., 2007a, 2007b)**

Dhumane et al. (2019) simulated the PCS with paraffin wax incorporated with the condenser for heat storage. They applied a lumped PCM model with empirical PCM side heat transfer coefficient as a function of PCM liquid fraction and did not consider the detailed PCM and refrigerant heat transfer characteristics.

The most significant difference between the PCM-to-refrigerant HX and the other two types of PCMHXs is that the refrigerant undergoes phase change leading to the heat transfer coefficient changed with refrigerant quality along the flow direction, which affect PCM melting performance. Moreover, the PCM-to-refrigerant HX is coupled in the dynamic system and the inlet refrigerant temperature changes immediately with the system response to PCM melting performance. Contrarily, for the HTF of air or water, the heat transfer coefficient variations are limited, and inlet temperatures are not a direct reflection of system performance.

### 1.2.5 PCMHX Modeling

Simulation of the phase change process is not easy due to the non-linear nature at moving melting interfaces. The two most common numerical methods can be used to

build a numerical heat transfer model for PCMHX: (1) enthalpy method, and (2) effective heat capacity method (Al-Abidi et al., 2013; Jin et al., 2018).

(1) enthalpy method: By introducing enthalpy, the phase change process can be modeled in a much simpler way. Latent heat and specific heat capacity are combined as an enthalpy term in the thermal energy equation to avoid nonlinearity in the heat conduction problem (Eyres et al., 1946; Hunter and Kuttler, 1989). The governing equation is the same for the liquid phase, mushy phase, and solid phase, as illustrated in Eq. (1-1).

$$\rho \frac{\partial H}{\partial t} = \nabla(k \nabla T) \tag{1-1}$$

For a certain PCM, the differential scanning calorimetry (DSC) measurement can determine the enthalpy function with PCM temperature $H(T)$. The melting interface conditions are automatically achieved by evaluating the PCM enthalpy (Adine and El Qarnia, 2009; Dutil et al., 2011; Jin et al., 2018; Piia Lamberg and Sirén, 2003). Most PCMs are not pure, and thus phase change happens over a temperature range rather than at a constant temperature.

(2) effective heat capacity method. The effective heat capacity method applies a general form of conduction equation, in which specific heat capacity Cp is nonlinear with PCM temperature (Bouhal et al., 2018; Jian-you, 2008), as illustrated in Eq. (1-2).

$$\rho C_p \frac{\partial T}{\partial t} = \nabla(k \nabla T) \tag{1-2}$$

The key to solving the heat transfer problem lies in the appropriate use of the nonlinear specific heat function (Chen et al., 2016). The accuracy of the effective heat capacity method depends on the melting temperature range.

Most PCMHX models were developed using commercial CFD software, and only a few self-developed numerical models were found based on the literature review (Al-Abidi et al., 2013). More details are as following.

#### 1.2.5.1 Approach through CFD Software

Via CFD software, the detailed PCM heat and mass transfer phenomenon can be modeled. Three types of governing equations including continuity, momentum and thermal energy equations can be implemented in the numerical model. The PCM numerical study using CFD software to handle different PCM geometric configurations has been widely conducted.

The copper foam/paraffin composite that can be used for PCM thermal performance improvement has been simulated in the cubic box with different heating positions (Zheng et al., 2018). Compared with the pure PCM, the copper foam/paraffin presented a 20% shorter melting time. In addition, the solid-liquid interfaces by numerical study and experiments were compared as illustrated in Figure 1-10, and results show that the CFD software approach is capable of solving this PCM melting problem.

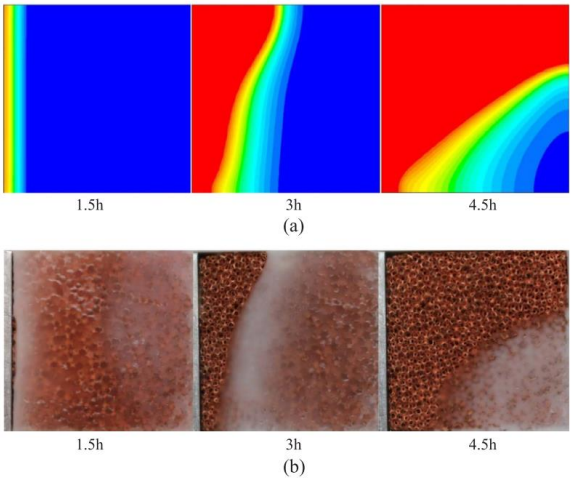


**Figure 1-10: (a) Numerical results and (b) Experimental results(Zheng et al., 2018).**

Triple-tube PCMHX using nanoparticle-metal foam combination is simulated in (Mahdi and Nsofor, 2017). The solid-liquid interfaces, temperature profiles and performance of different nano-PCM porosity were analyzed. Results show that the new combination of the nanoparticle-mental foam has excellent heat transfer enhancement and can save time up to 96%.

Finned rectangular PCM-to-air HX simulation is addressed in (Jmal and Baccar, 2018) with the configuration illustrated in Figure 1-11. The natural convection of a laminar PCM flow was investigated considering with and without fins. The study presented evolutions of the PCM liquid-solid interface and liquid fraction characterizing PCM melting phenomenon and figured out the fin parameters effects on the PCM nature convection and PCMHX thermal performance.

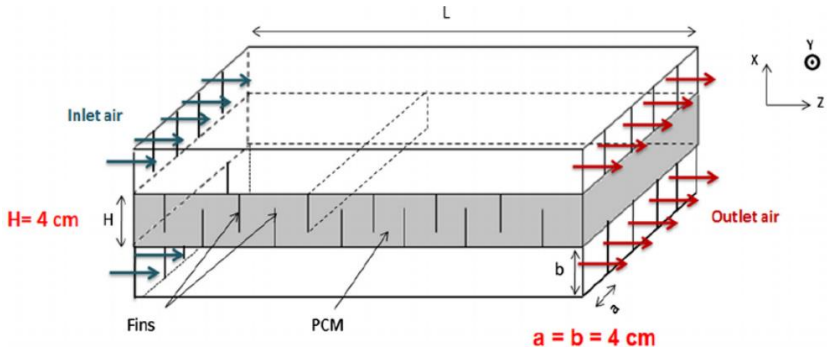


**Figure 1-11. (a) PCM-to-air HX configuration (Jmal and Baccar, 2018).**

Shell-and-tube spiral coil PCMHXs with HTF flowing inside the spiral tube were presented numerically in (Ahmadi et al., 2018). Governing equations were built for both HTF and PCM domains. The different spiral tube parameters as illustrated in Figure 1-12 were studied and compared. The effect of HTF mass flow rate and inlet temperature were also investigated.

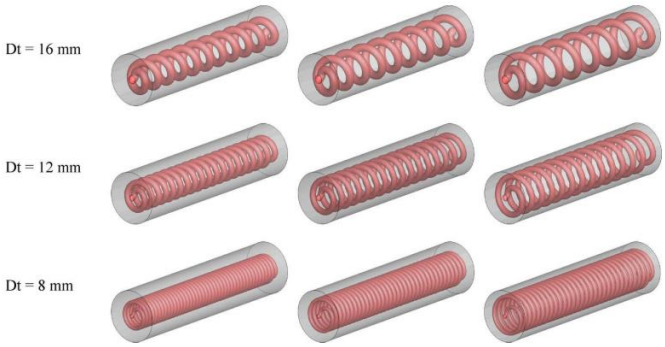


**Figure 1-12. Studied cases of shell-and-spiral tube PCMHX (Ahmadi et al., 2018).**

1.2.5.2 Approach through Self-coding

Adine and El Qarnia (2009) presented a simulation on single-shell-and-tube PCMHX with the HTF of water and two types of PCMs as illustrated in Figure 1-13. The parametric study regarding HTF inlet temperature, mass flow rate and proportion

of the two types of PCM was conducted. Since they developed the model by self-coding based on the thermal energy equations formulated by using the enthalpy method, the free convection was not taken into consideration.

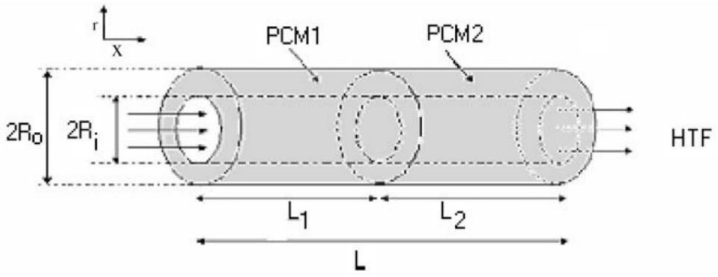


**Figure 1-13. Schematic of the shell-and-tube PCMHX with two types of PCM (Adine and El Qarnia, 2009).**

Lamberg et al., (2004) did a numerical study on cubic PCM domains by self-coding using both enthalpy method and effective specific heat method, and compared the effect of the fins to the PCM melting performance. PCMHX schematics are illustrated in Figure 1-14, in which Figure (a) shows the case without fins and (b) with two fins. The heat transferred from the wall to the PCM. Although through self-developed coding, only the thermal energy equations were implemented in the numerical model without considering the liquid PCM movement, the nature convection effect was simulated through a heat transfer enhancement coefficient ($h_c$). Therefore, adding the new coefficient, the thermal energy equation changes from Eq.(1-1) to Eq. (1-3).

$$\rho \frac{\partial H}{\partial t} + h_c \nabla T = \nabla (k \nabla T) \tag{1-3}$$

The heat transfer enhancement coefficient ($h_c$) of a rectangular PCM domain can be found in (P. Lamberg and Sirén, 2003) and (Lamberg et al., 2004). And its value depends on the PCM properties and wall temperature, rather than time and PCM locations.

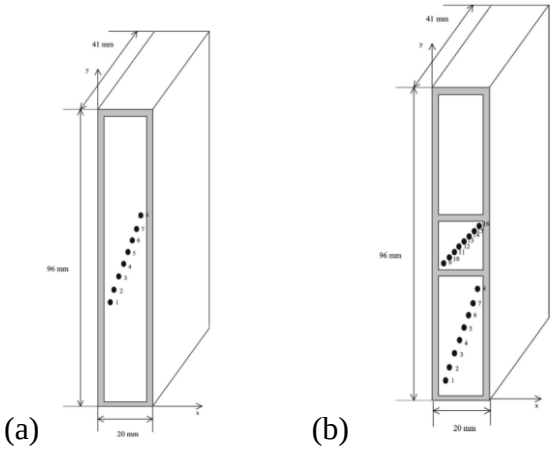


(a) (b)

**Figure 1-14. Schematic of the PCMHX with cubic PCM domains (Lamberg et al., 2004).**

The other way to consider the free convection in the thermal energy equation is to use an equivalent thermal conductivity, $k_{eq}$, as illustrated in (1-4) in which Ra is Rayleigh number, and C and m are constant values (Zukowski, 2007).

$$\frac{k_{eq}}{k} = CRa^n \left(\frac{\delta}{l}\right)^m \tag{1-4}$$

Fleming et al. (2013) used a simplified 1-D model to simulate multi-tube shell-and-tube HX. Although the original design is the multitube design, they used one tube cylinder to represent all other tubes, and ignored the heat transfer in the axial direction,

as illustrated in Figure 1-15. So that the heat transfer was considered only occurring in the radial direction.

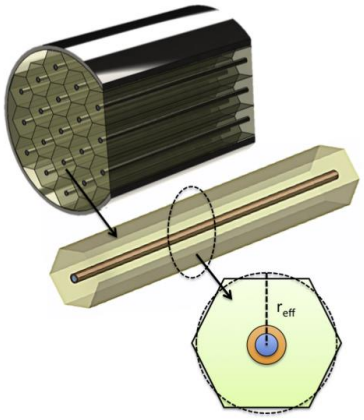


**Figure 1-15. Simplification from multi-tube PCMHX to a single tube and surrounding PCM (Fleming et al., 2013).**

There are only a few investigations concerning the PCM-to-refrigerant HX, and there is a research gap on detailed analysis of PCM-to-refrigerant HX heat transfer performance. The current PCM-to-refrigerant models are not detailed enough for PCM heat transfer analysis, since some focused on the system simulation using lumped PCM model with the average PCM temperature (Gu et al., 2004) (Dhumane et al., 2019), some neglected axial conduction in the PCM and only considered PCM latent heat (Wang et al., 2007b), and some isolated the PCM-to-refrigerant HX from the system by setting the wall temperature to be constant (Khalifa and Koz, 2016).

### 1.2.6 Effect of the Refrigerant Subcooling

The subcooling at the exit of the condenser is determined by the refrigerant charge in the vapor compression-based system. As more refrigerant charged in the system, both the condensing pressure and the refrigerant liquid fraction in the condenser

increase, leading to the increase of the condenser capacity, evaporator capacity, and compressor work (Wang et al., 2019). Thus, there is an optimal subcooling reflecting the best refrigerant charge amount to obtain the maximum coefficient of performance (COP). There have been many studies conducted on the optimal subcooling in the steady-state vapor compression systems (Azzouzi et al., 2017; Poggi et al., 2008).

Kim et al. (2014) investigated the single-stage and the cascade heat pump system experimentally and numerically. The maximum COP was observed at the subcooling of 3~7 K with different ambient temperatures. They also indicated in the cascade system, the optimal degree of subcooling is the high stage is more important to be controlled.

Pitarch et al. (2017) found that the optimal subcooling linearly depends on the temperature lift of the secondary fluid in the condenser for R290, R1234yf, and R32. Corberán et al. (2008) experimentally studied the effect of the refrigerant charge on the capacity and COP at various operating conditions. They indicated that the optimal subcooling is dependent on the approach temperature at the outlet of the condenser, which is related to the condenser size and the flow arrangement. The optimal subcooling of the counter-flow arranged condenser is 10 K. At the same time, that of parallel flow is 5 K.

Pottker and Hrnjak (2015) presented the analysis on the effect of the condenser subcooling on the different refrigerants showing that the refrigerant with less latent heat of vaporization tends to benefit more from the subcooling optimization, and the optimal subcooling is around 8 K.

However, the investigations on the effect of subcooling on refrigeration systems coupled with PCM-to-refrigerant condensers are limited. For a little research on PCM-to-refrigerant condensers used in refrigeration systems, Gu et al. (2004) applied a PCM-to-refrigerant heat exchanger at the condenser side for heat recover, while the subcooling is set to be zero. Bakhshipour et al. (2017) applied the PCM-to-refrigerant heat exchanger as a sub-cooler after the main condenser in a refrigerator system showing that the system COP can increase by 9.58%. Yet, the refrigerant entering the PCM sub-cooler is already the subcooled liquid. Dhumane et al. (2019) applied PCM at the condenser side for heat storage, while the PCM was regarded as the lumped model. Thus, the refrigerant subcooling area in the condenser tube length direction was not considered.

### 1.2.7 Literature Review Summary

From the literature review, the summary of the PCMHX enhancement, PCS technologies, PCMHX applied in air-conditioning system and PCM modeling, and research gaps are illustrated in Table 1-3.

**Table 1-3: literature review summary**

| Research areas | Learning | Gaps |
|---|---|---|
| Heat transfer enhancement methods in PCM | - The common boundary condition was the constant water inlet temperature (80+ papers)<br>↑ HTA: Multi-tube & helical tubes<br>↑k: graphite matrix & copper sponge | - No system-level investigation on PCM heat transfer enhancement methods with complicated and changed boundary conditions *(Addressed by Research Objective-1)* |
| Technologies for PCS | - PCS technologies: ventilation, thermoelectric cooling, radiant cooling, vacuum desiccant cooing, flow localization, and PCM<br>- Only a few papers are related VCC-based PCS with PCM | - Lack of investigation on VCC-based PCS with PCM-to-refrigerant HX as the main condenser/evaporator, especially the detailed parametric study *(Addressed by Research Objective-2(a))* |
| PCMHX applied in air-conditioning systems | - PCM-to-water HX and PCM-to-air HX were more widely studied than PCM-to-refrigerant HX<br>- Most PCM-to-refrigerant HX worked as the supplementary for condensers/evaporators | |
| PCMHX simulation | - CFD was widely used for complex PCM domain simulation<br>- Only about 10 papers simulated PCM-to-refrigerant HX using self-developed models, while did not consider refrigerant temperature variation | - Lack of simulation on 2-D PCM-to-refrigerant condenser considering refrigerant-side temperature variation *(Addressed by Research Objective-2(b))*<br>- No multi-tube PCMHX model for general-purpose configuration *(Addressed by Research Objective-3)* |
| Subcooling effect on VCC and PCM | - Optimal subcooling presented in VCC systems | - No study on the effect of refrigerant subcooling on PCM-coupled VCC systems *(Addressed by Research Objective-2(c))* |

## *1.3 Objectives*

To fill the research gaps regarding PCS and PCMHX, this study focuses on the investigation of VCC-based PCS integrated with PCM including experimental evaluation and model development. This thesis aims to:

1. Compare different PCM heat transfer enhancement methods as applied in the VCC system.

2. Investigate the innovative PCM-coupled PCS performance, and provide guidelines for PCM-to-refrigerant HX application considering the heat transfer characteristic variation of the refrigerant.

(a) Investigate the PCS with experimental parametric study

(b) Simulate the uneven PCM melting in PCM-to-refrigerant HX considering the refrigerant-side temperature variation

(c) Evaluate and minimize negative effects of the refrigerant subcooling on both the system performance and the PCM melting process

3. Develop a 3-D general-purpose multi-tube PCMHX model for flexible and comprehensive PCMHX configurations.

## *1.4 Dissertation Overview*

The research overview is illustrated in Figure 1-16. Chapter 2 to Chapter 7 describe main research results. Chapter 8 is the conclusion and future work. The dissertation workflow summarizes chapters as following.

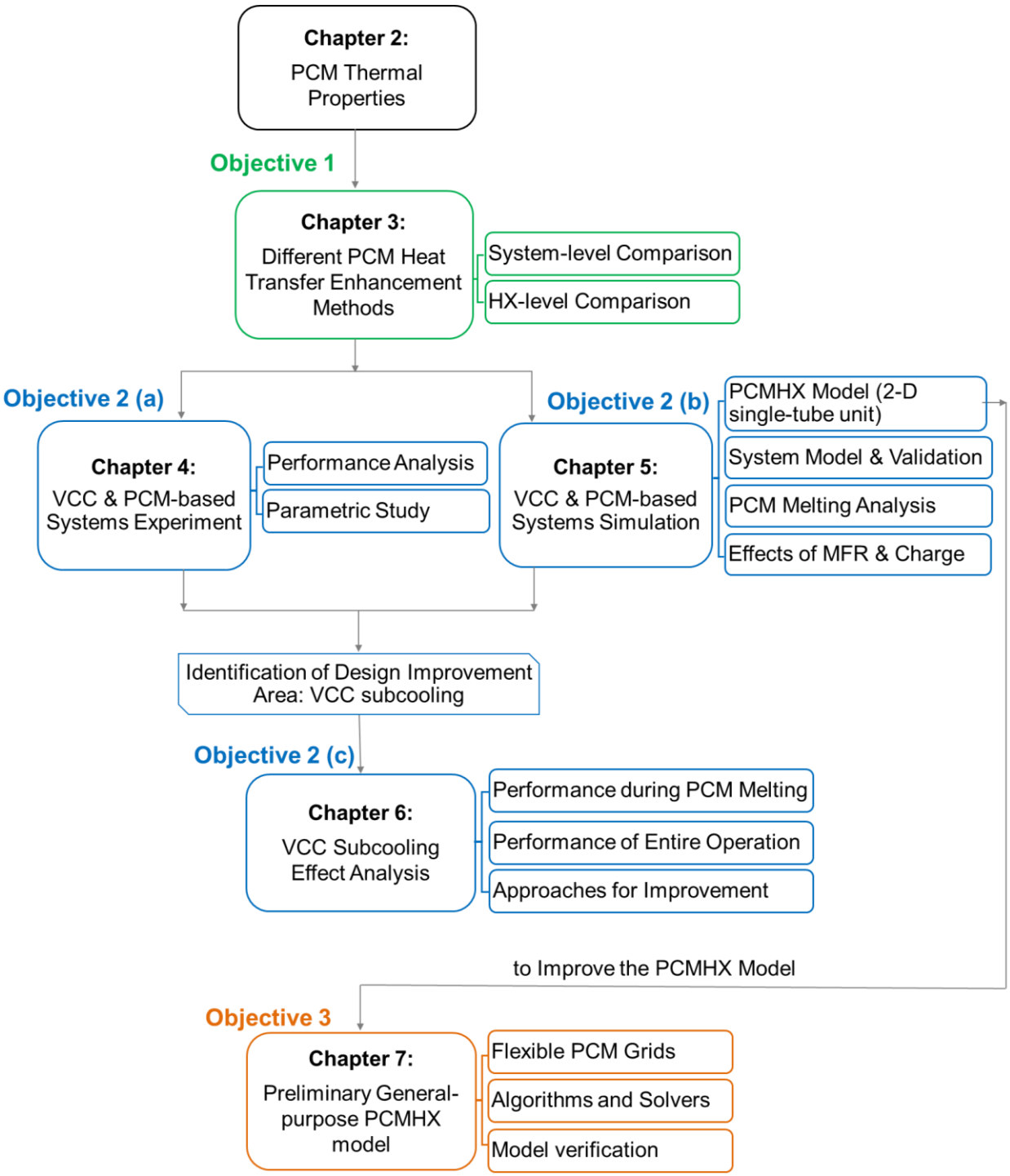


**Figure 1-16: Research Overview**

Chapter 2: PCM Thermal Properties

- Present DSC curves of PCM, thermal properties calculation and effects of the heating/cooling rate.
- Propose enthalpy function of the current PCM, PureTemp 37.

Chapter 3: Comparison of Different PCM Heat Transfer Enhancement Methods

- Present an experimental study on five PCMHXs using different enhancement methods, such as embedding a graphite matrix, adding a copper sponge, using the doubled heat transfer area and using bigger headers.
- Discuss the uneven PCM melting in horizontal and vertical directions.
- Analyze the system-level performance, such as condenser temperature, COP and capacity.
- Evaluate the component-level performance, such as overall heat transfer coefficient, PCM-side effective heat transfer coefficient and thermal resistances.

Chapter 4: Performance Analysis on PCS with PCMHX

- Present an experimental evaluation on both cooling cycle and PCM regeneration cycle, and evaluate system performance.
- Discuss effects of different thermostat setting, recharge rate and cooling time on system performance.

Chapter 5: Simulation of PCM-to-refrigerant HX in Systems

- Develop a 2-D PCMHX model using enthalpy method.

- Develop the coupled VCC system model.
- Present the experimental verification.
- Present PCM melting process includes temperature profile and liquid fraction.
- Discuss the effect of the compressor speed on PCM melting performance.
- Analyze the PCM heat transfer performance and address reasons for the uneven melting.
- Present a solution for more uniform PCM melting.

Chapter 6: Effects of Condenser Subcooling on PCM-VCC Systems

- Present a system experimental study for different subcooling effect analysis.
- Propose a definition for normalized subcooling.
- Discuss the system and PCMHX performance during PCM melting process.
- Discuss the system and PCMHX performance during the entire duration.
- Provide several approaches to improve PCM latent heat utilization and corresponding system performance for further PCM-to-refrigerant HX application.

Chapter 7: General-purpose PCMHX Model Development:

- Introduce the flexible Voronoi grid for PCM domain.
- Present a new algorithm to simulate multi-tube PCM heat transfer.
- Present the development of the slice solver and top-level solver.

- Verify the PCMHX model by a case study.

Chapter 8: Conclusions and Future work

Chapter 9: Contributions

# Chapter 2: PCM Thermal Properties

## *2.1 DSC Measurement*

During the phase change process, PCM can absorb or release heat within a narrow range of temperature change thanks to its large latent heat. To figure out the amount of the latent heat capacity, the DSC measurement is necessary. DSC is a thermo-analytical facility to measure the heat transfer rate that can increase or decrease at a certain temperature for the material sample. The heat flow is related to the specific heat (Cp) at a given temperature. For instance, Figure 2-1 shows the DSC results of a PCM named ALFOL® 14 Alcohol from TA Instruments DSC Q100 while PCM temperature is increased from -10 °C to 80 °C. The y axis denotes the heat flow of the unit mass of the PCM sample. In Figure 2-1 (a), the negative heat flow means that heat is absorbed by the material. There is a peak of the heat flow at a temperature range of 35 °C to 50 °C reflecting the phase change temperature range of the material. During this process, the PCM temperature increasing/decreasing rate equals the heating/cooling rate from DSC and maintains constant. Similarly, the positive heat flow means that the heat is released by the material so that its temperature decreases, and the peak illustrates the temperature range of the solidification process.

The PCM thermal properties include melting temperature, latent heat, melting glide can be obtained by DSC curves, while the heating/cooling rate can influence the measurement. Eqs. (2-1) and (2-2) illustrate calculations of the specific heat and the enthalpy of the PCM, respectively, in which $\dot{Q}$ is the heat transfer rate, and m is the mass of the PCM sample, so that $\dot{Q}$/m is the heat flow per unit mass flow as given in

the DSC curve. $T_0$ is the reference temperature for enthalpy calculation. $v_T$ is the heating/cooling rate. *Cp* in this equation can be regarded as the effective specific heat.

$$Cp = \frac{\dot{Q}}{m\, v_T} \tag{2-1}$$

$$h_p = \int_{T_o}^{T} \frac{\dot{Q}}{m\, v_T} dT \tag{2-2}$$

Figure 2-2 illustrates the obtained *Cp* during the melting process based on the DSC measurement. It can be seen that with different heating rates, the obtained *Cp* curves are different. For the slower heating rate, the peak presents at a lower temperature, and the phase change temperature range is smaller, which is close to the real properties. Since the faster heating rate can lead to a flat and shifted curve, a hypothetic *Cp* curve is needed to eliminate the effect of the heating/cooling rate in DSC, as shown by the dashed line in Figure 2-3 (a) (Longeon et al., 2013). The area below the *Cp* curve between the temperature of 28 °C to 46 °C is the same for these three cases, which can be regarded as the latent heat from Eq. (2-2).

The latent heat is the enthalpy change from the phase-change start temperature to the end temperature as illustrated in Figure 2-4 (Mondal, 2008). The peak of the *Cp* appears at the melting temperature.

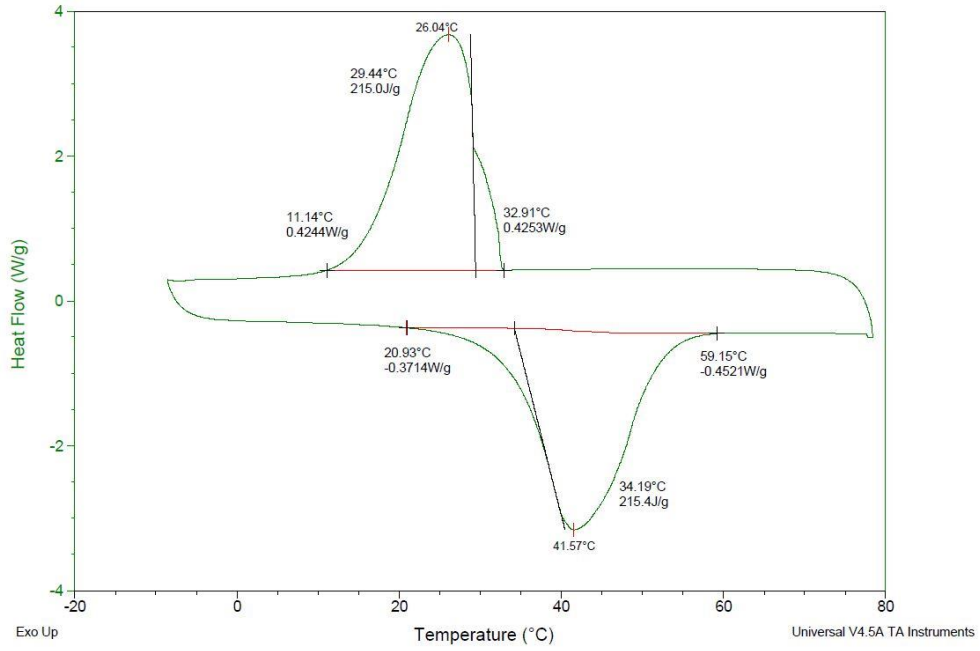


(a) Heating/cooling rate of 10 K $min^{-1}$

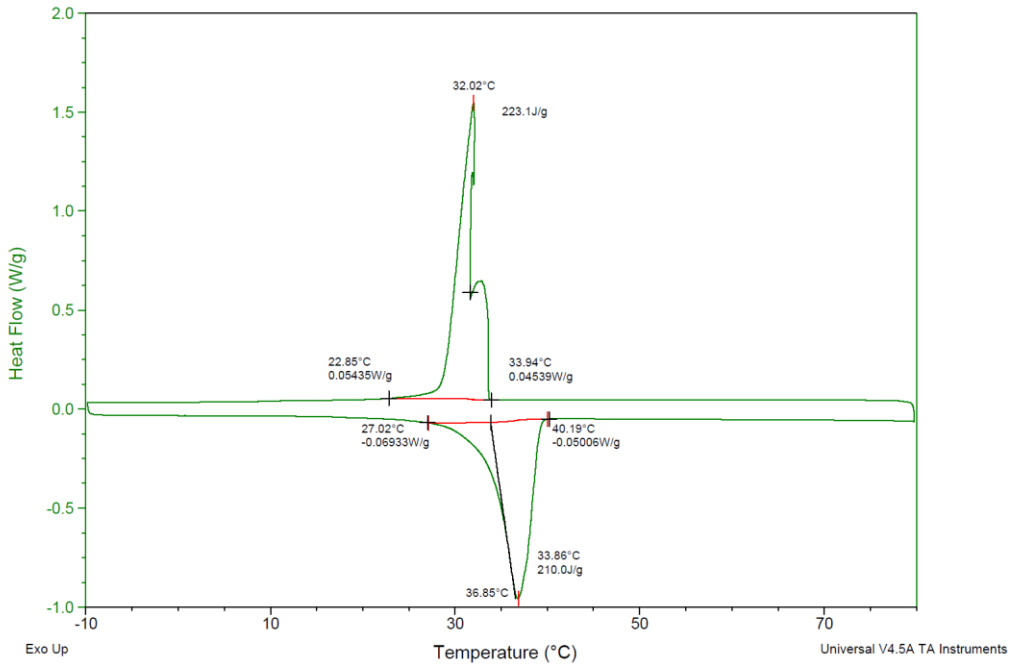


(b) Heating/cooling rate of 1 K $min^{-1}$

**Figure 2-1: DSC results of ALFOL® 14 Alcohol with different heating/cooling rate.**

In addition, the enthalpy curve can also be affected by the heating/cooling rate as in Figure 2-3 (b) (Caron-Soupart et al., 2016). For both melting and solidification process, a lower heating/cooling rate can result in a narrower temperature range for phase change. In the melting process, the lower heating rate can also lead to a lower melting temperature. Contrarily, the lower cooling rate leads to a higher solidification temperature. This result is corresponding to the discussion in Figure 2-1 (a) and (b).

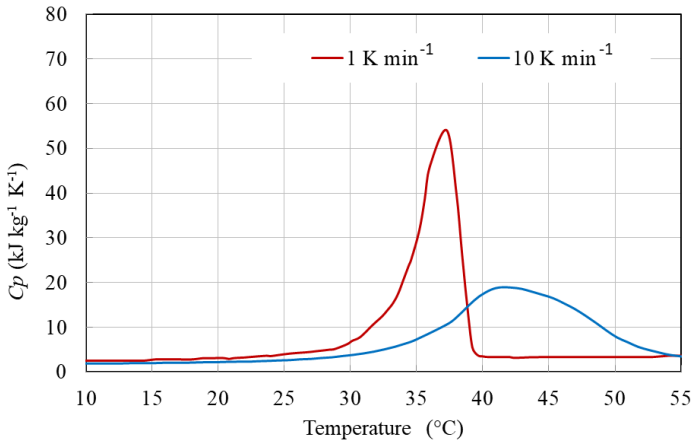


**Figure 2-2: The Specific heat based on the DSC curve as given in Figure 2-1 and calculation as given in Eq. (2-1).**

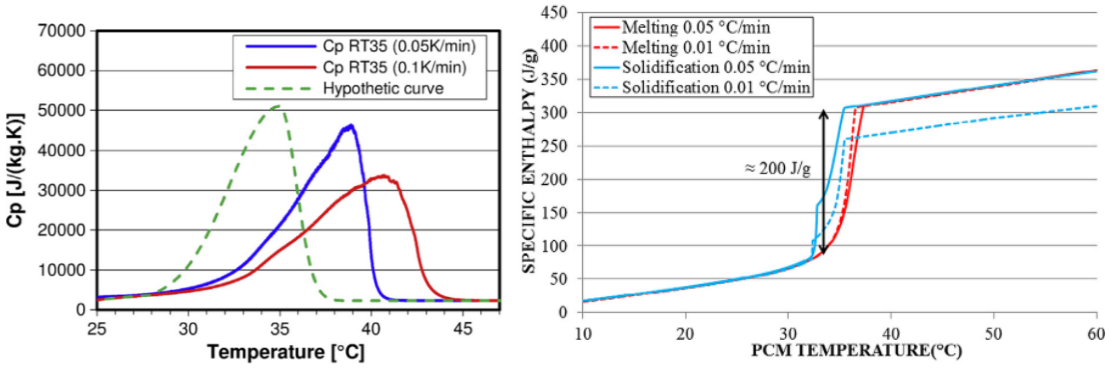


(a) Cp curve (Longeon et al., 2013) (b) Enthalpy curve (Caron-Soupart et al., 2016)

**Figure 2-3: Obtained PCM Cp curves and enthalpy curves affected by the heating/cooling rate in DSC.**

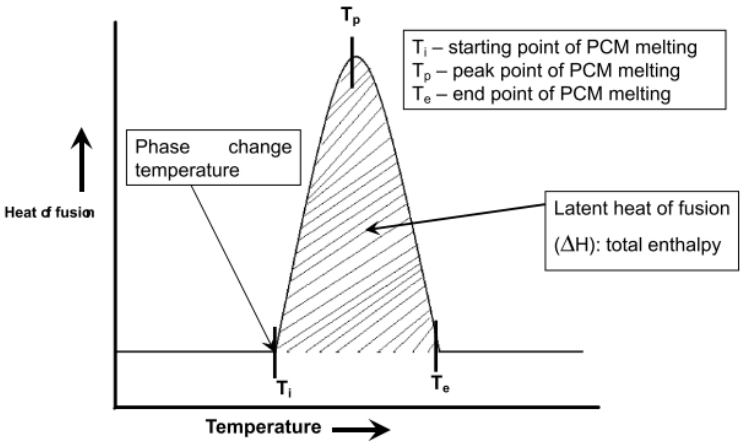


**Figure 2-4: PCM thermal properties (Mondal, 2008).**

*2.2 Properties of PCM in This Study*

The PCM used in this study was a type of organic wax named PureTemp37. The DSC curve with heating/cooling rate of 1 K $min^{-1}$ can be found in (PureTemp, n.d.), and that of 5 K $min^{-1}$ can be found in Mallow et al. (2018). Other material properties are listed in Table 2-1.

**Table 2-1: Properties of PureTemp37.**

| Properties | Unit | Value |
|---|---|---|
| Melting temperature | °C | 37 |
| Latent heat | kJ $kg^{-1}$ | 210 |
| Thermal conductivity | W $m^{-1}$ $K^{-1}$ | 0.15 (liquid), 0.25 (solid) |
| Density | kg $m^{-3}$ | 840 (liquid), 920 (solid) |
| Specific heat | kJ $kg^{-1}$ $K^{-1}$ | 2.63 (liquid), 2.21 (solid) |

PCM enthalpy curve with a function of temperature is proposed as Eq.(2-3), in which the first term presents the latent heat of PCM. $C_{p,s}$ and $C_{p,l}$ are the specific heat for solid and liquid PCM, respectively. $T_{ini}$ is the initial PCM temperature. $T_m$ is the melting point.

$$h(T_p) = L_p\left(\frac{1.3\ atan(T_p - T_m)}{\pi} + 0.5\right) + (T - T_{ini})\frac{C_{p,l} + C_{p,s}}{2} \qquad (2\text{-}3)$$

Two enthalpy curves from DSC results and one from the equation are illustrated in Figure 2-5. As the melting temperature is 37°C, the enthalpy curve from the equations are more precise. The proposed correlation is used in the numerical model of the PCM and PCMHXs.

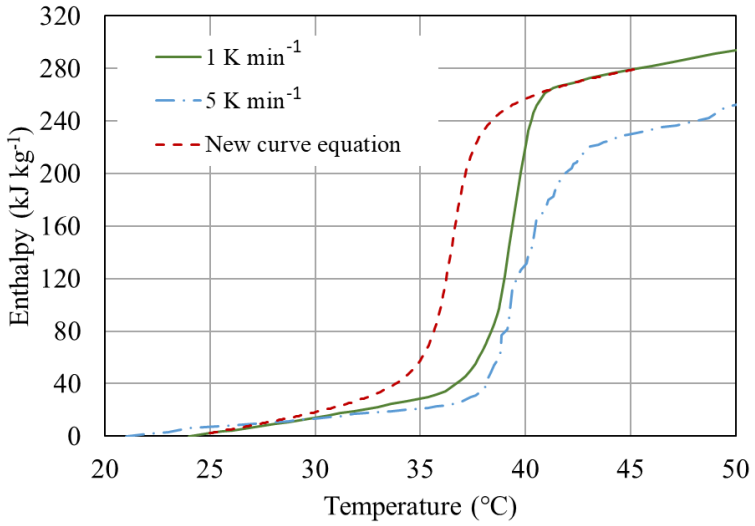


**Figure 2-5: PCM enthalpy curve.**

## *2.3 Chapter Summary*

This chapter presents the DSC result analysis to obtain PCM thermal properties, such as melting temperature, latent heat and enthalpy curve. Enthalpy is the integration

of the specific heat over the temperature change. And the latent heat is the enthalpy change over the temperature range of the phase-change process. The heating/cooling rate during the DSC measurement can affect the DSC curve so that the new hypothetic curve is necessary to eliminate this effect. Therefore, the PCM enthalpy correlation is proposed for the simulation and is compared with the DSC results.

# Chapter 3: Comparison of Different PCM Heat Transfer Enhancement Methods

As mentioned in the literature review, the low thermal conductivity of the PCM impedes its wide application, and therefore the heat transfer enhancement is necessary. This chapter focuses on the comparison of five different PCM heat transfer enhancement methods as applied in the VCC system for personal cooling.

## *3.1 Experimental Setup and Test Apparatus*

The proposed system can perform two modes: (1) cooling mode by VCC and (2) PCM regeneration mode by thermosiphon cycle. In the cooling mode, the heat released from the refrigerant in condenser tubes is stored in the PCM, and cooling is provided by an upper air-to-refrigerant exchanger shown in Figure 3-1. A receiver is installed after the PCM condenser and before the thermostatic expansion valve (TXV) to store liquid refrigerant for maintaining the normal operation of the thermosiphon cycle. After PCM stores enough heat in VCC, the regeneration mode can be enabled to charge PCM by turning off the compressor and then bypassing the compressor, expansion valve and the receiver. Then, the liquid refrigerant stored in the receiver can flow down by gravitational force, and fill into PCMHX tubes and headers. Since the selected PCM melting temperature is about 37 °C, the liquid PCM temperature is higher than the ambient. Thus, the liquid PCM at the bottom is the heat source, and the air through the upper air-to-refrigerant exchanger is the heat sink. In this case, the liquid refrigerant could vaporize in the PCMHX, then flows upward, and be condensed at the upper

exchanger by air. In other words, in the thermosiphon cycle, the PCMHX works as an evaporator, and the upper air-to-refrigerant heat exchanger works as a condenser.

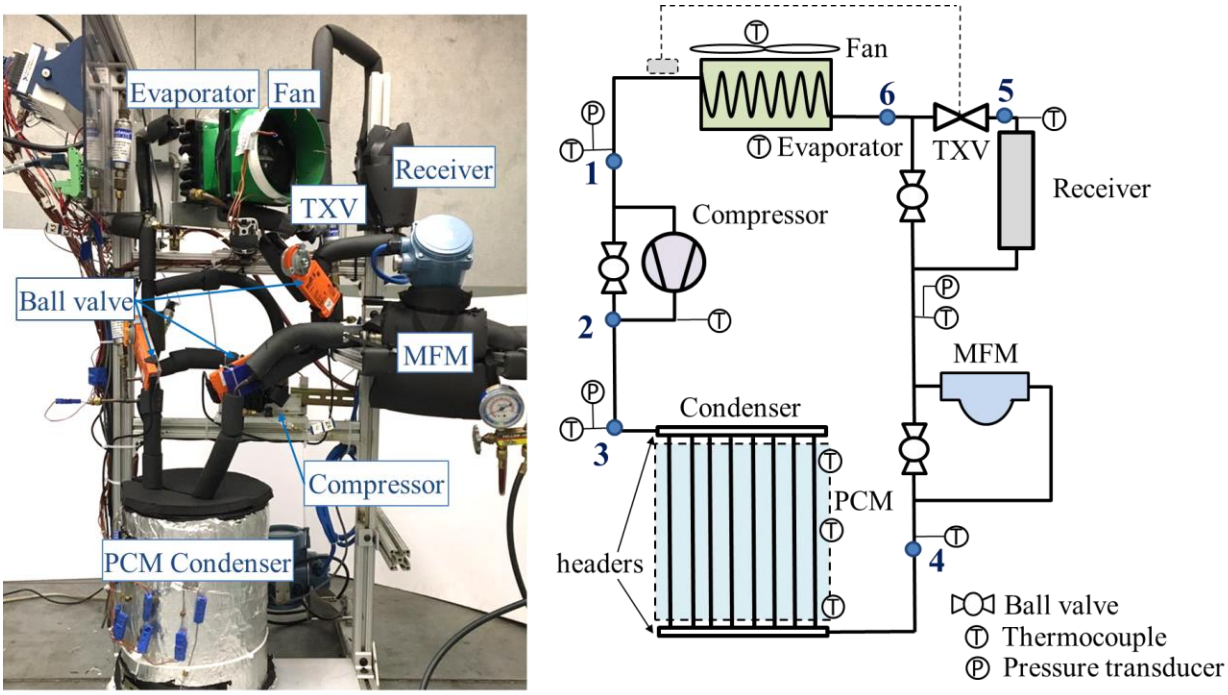


(a) Experimental setup (b) System schematic diagram

**Figure 3-1. Breadboard system with the cooling operation.**

Figure 3-1(a) is the photograph of the experimental setup, and Figure 3-1(b) is the system schematic. Ball valves and the coupled actuators were used for bypassing compressor, receiver, expansion valve and mass flow meter (MFM) for thermosiphon operation. The upper heat exchanger was two-row fin-and-tube HX from Thermatron with the model of 720TPM2A01. The model of the fan is Noctua NF-14 with the measured volume flow rate of about 0.031 $m^3 s^{-1}$. The expansion device is a commercial thermal expansion valve with the designed superheat of 5 K. The Aspen Q-serious rotary compressor was selected with the displacement of 1.4 mL, and compressor speed was set to be 2200 r $min^{-1}$ in cooling mode. Table 3-1 shows the specifications of the

measurement devices. The system mass flow rate was measured by a flow meter placed in the liquid line. Temperature sensors and pressure transducers were placed in the system as shown in Figure 3-1(b). Power consumptions of the fan and compressor were measured through DC current and voltage transducers. All measurement devices were connected to the acquisition system with LabVIEW® interface. R134a was chosen as the refrigerant in the system. The PCM PureTemp37 properties are listed in Table 2-1. PCM melts over the temperature range from $T_s$ to $T_l$, during which the variations of the specific heat are obtained by the differential scanning calorimeter (DSC) measurement with the scanning rate of 1 K $min^{-1}$. The melting temperature glide, which is the temperature change during the phase change, is about 2 K.

**Table 3-1: Specifications of the measurement devices**

| Instrument | Supplier | Uncertainty | Measurement range |
|---|---|---|---|
| Thermocouple type T | Omega | ±0.5 °C | -250 – 350 °C |
| Coriolis mass flow meter | Micro Motion | ± 0.10% | Calibrated in 0-3 g $s^{-1}$ |
| Pressure transducer | Setra AccuSense | ±1.7 kPa | 0 – 3,447 kPa absolute |
| DC current transducer | CR Magnetics | ± 1.0% | 0 – 10 ADC |
| DC voltage transducer | CR Magnetics | ± 1.0% | 0 – 50 VDC |

In order to illustrate the capabilities of this TES design with both cooling and recharge operations, Figure 3-2 shows examples of air temperatures and system pressures during cyclic operations with the copper sponge used for PCM enhancement. In Figure 3-2 (a), when VCC was used for providing cooling, the air outlet temperature

was about 4 K lower than the inlet. In the thermosiphon loop, the heat was released by the upper air-to-refrigerant exchanger so that the air outlet temperature was higher than the inlet. The temperature difference was changed slightly with time due to the dynamic PCM states and system conditions. As shown in Figure 3-2 (b), during the cooling mode, the pressure of the PCM condenser was higher than that of the air-to-refrigerant evaporator. Whereas, in the thermosiphon cycle, system pressures were almost the same everywhere, and decreased with time due to the change of PCM temperature in the solidification process.

### *3.2 PCMHX Specifications*

Photographs and design properties of the PCMHX are presented in Figure 3-3 and Table 3-2, respectively. The PCMHX investigated in this study were the shell-and-tube types with the multi-tube arrangement, in which refrigerant flows inside tubes, and PCM is filled within the annular space outside the tubes. Each comprises enhanced or non-enhanced PCM and the copper tubing structure including branches, inlet tubes, outlet tubes and two headers for refrigerant distribution at the top and collection at the bottom. The inlet tube connected with the top header was from the compressor. The outlet tube was connected to the bottom header. Both branch tubes and enhancement structures were uniformly distributed in the PCM container.

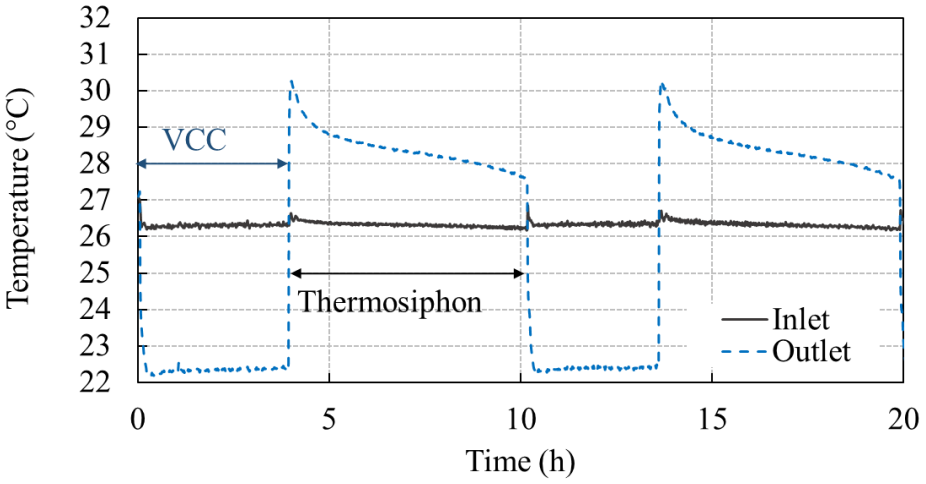


(a) Air temperatures at upper exchanger

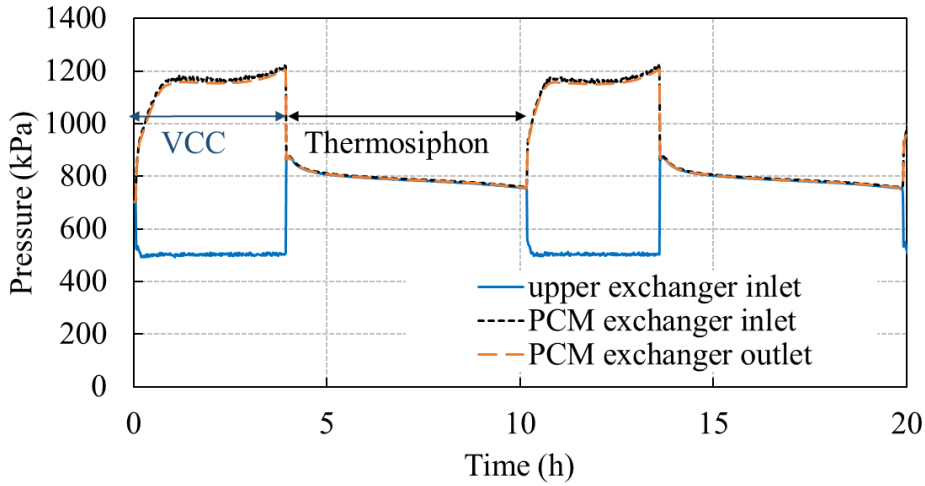


(b) System pressures

**Figure 3-2. Examples of air temperatures and system pressures of both cooling and PCM regeneration cycles of the TES system with copper-sponge-enhanced PCMHX.**

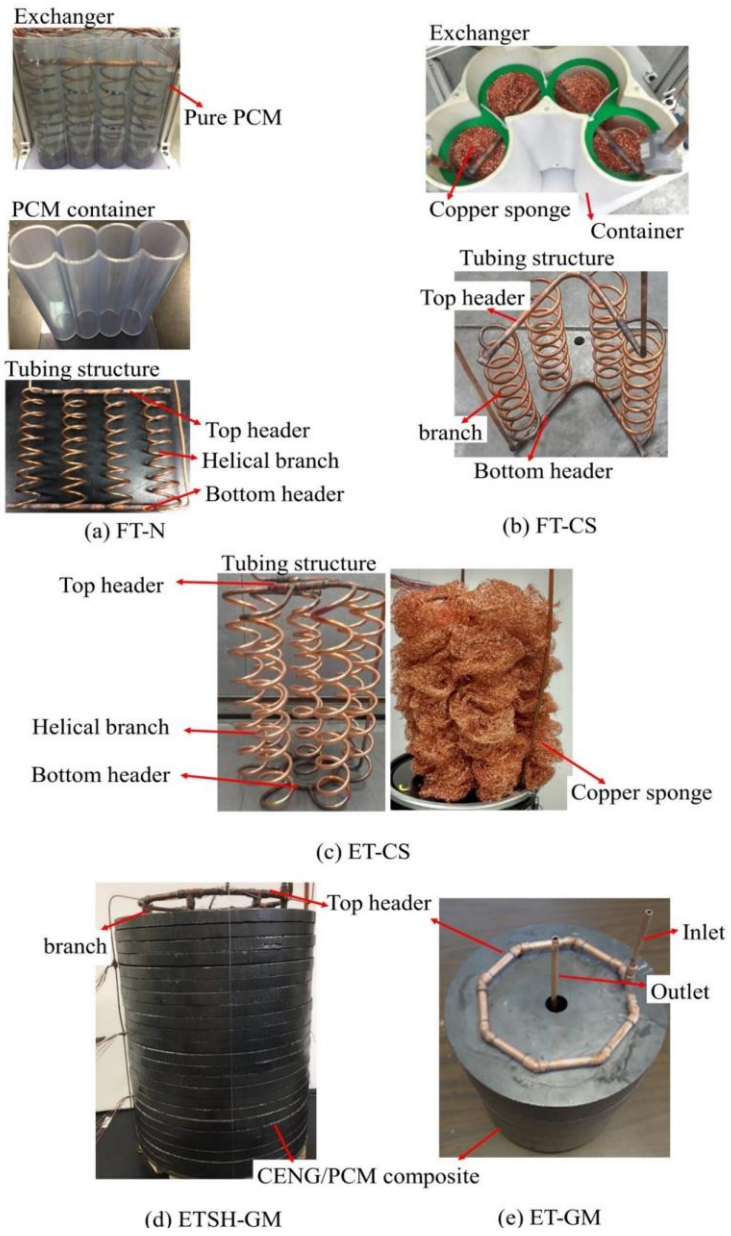


((a) FT-N: Four-tube non-enhancement PCMHX. (b) FT-CS: Four-tube copper sponge enhanced PCMHX. (c) ET-CS: Eight-tube copper sponge enhanced PCMHX. (d) ETSH-GM: Eight-tube with small header graphite matrix enhanced PCMHX. (e) ET-GM: Eight-tube graphite matrix enhanced.)

**Figure 3-3. Photographs of five PCMHX.**

To construct copper-sponge-enhanced exchangers, the copper tubing structure and copper sponge could be put into the PCM container. Then, liquid PCM was poured into the container slowly to prevent voids. To construct graphite enhanced PCMHX, straight branches could be pushed into the holes that punched on the graphite/PCM composite blocks. There were no gaps between branch tubes and the enhanced PCM. From the perspective of the heat transfer performance, the following crucial parameters were analyzed and compared: heat transfer area, conductive enhancement and distribution of the refrigerant flow within branches. All branch tubes have the same inside diameter of 4.8 mm and an outside diameter of 6.4 mm. The mass fraction is the radio of enhancement materials mass to the total mass of the enhanced PCM.

The baseline (FT-N) was designed with four helical branch tubes and the non-enhanced PCM. The helically coiled branches are used to extend the heat transfer surface area. The geometric parameters of the second PCMHX (FT-CS) are identical to the baseline but with the additional conductive structure of the copper sponge in 5.5% by mass. The third exchanger (ET-CS) consists of eight branch tubes, so that its heat transfer area was two times greater than FT-CS, while both enhancement properties and tube dimensions were the same. Different from previous researches with the foam porosities lower than 95% (Mahdi and Nsofor, 2017; Martinelli et al., 2016; Tian and Zhao, 2011; Zhao et al., 2010), the porosity of copper sponge used in this study reaches 99.5% in order to reduce the exchanger weight. The effective thermal conductivity of the copper-sponge-enhanced PCM, which is six times that of the pure PCM, is calculated by the correlation in (Yang et al., 2014), which is six times that of the pure PCM. The correlation is shown in Eq. (3-1), which is based on the analytical

unit cell model for high porosity ranges. The comparison with experimental data and other model predictions could be found in (Yao et al., 2015).

$$\frac{k_{eff}}{k_{CS}} = \frac{(1-\varepsilon)}{\left(1-e+\frac{3e}{2a}\right)[3(1-e)+\frac{3}{2}ae]} + \frac{k_p}{k_{CS}}\varepsilon \tag{3-1}$$

Additionally, the other two PCMHXs (ETSH-GM and ET-GM) were CENG matrix enhanced with eight branch tubes. Each branch was designed with the straight tube rather than the helical tube, the length of which was only 25% of the first three exchangers. This is because the effective thermal conductivity of the PCM/CENG composite is much greater leading to less required heat transfer area in ETSH-GM and ET-GM. Since ETSH-GM consists of smaller diameter headers than ET-GM, the effect of the refrigerant distribution in branches on the PCM melting process and system performance could be investigated for ETSH-GM and ET-GM. The relationship between the effective thermal conductivity of PCM/CENG composite and the bulk density have been experimentally measured and theoretically analyzed in the literature as shown in Figure 3-4, in which the thermal conductivities of pure PCMs are similar to that of PureTemp37 with a range from 0.2 to 0.3 $W \cdot m^{-1} \cdot K^{-1}$ (Bonnissel et al., 2001; Haillot et al., 2011; Mallow et al., 2018; Merlin et al., 2016; Mills et al., 2006; Py et al., 2001; Wang et al., 2013). The bulk density is equal to the mass of CENG divided by the total volume of the composite. If the bulk density is greater than 50 $kg \cdot m^{-3}$, the

CENG matrix has better conduction in the direction perpendicular to the compression force than that parallel to the compression (Bonnissel et al., 2001; Py et al., 2001).

**Table 3-2: Five different PCMHX design.**

| PCMHX | | FT-N | FT-CS | ET-CS | ETSH-GM | ET-GM |
|---|---|---|---|---|---|---|
| Enhancement | Configuration | - | Copper sponge | Copper sponge | CENG matrix | CENG matrix |
| | k ($Wm^{-1}K^{-1}$) | 0.15 | 0.9 | 0.9 | 12 ⊥<br>5.5 ‖ | 21.1⊥<br>7.5 ‖ |
| | Fraction (wt.%) | 0 | 5.2 | 5.2 | 13 | 19.1 |
| | Porosity (vol.%) | 1 | 99.5 | 99.5 | 94.7 | 91.9 |
| | Density ($kg\ m^{-1}$) | - | - | - | 119.1 | 182.6 |
| Tube | Branch shape | Helical | Helical | Helical | Straight | Straight |
| | Coil diameter (mm) | 41 | 41 | 41 | - | - |
| | Tube length (mm) | 1,200 | 1,200 | 1,200 | 300 | 300 |
| | Height (mm) | 300 | 300 | 280 | 300 | 300 |
| | Bare tube length (mm) | 0 | 0 | 0 | 20 | 20 |
| Header | Tube length (mm) | 32 | 32 | 38.1 | 51.8 | 51.8 |
| | Tube ID (mm) | 7.9 | 7.9 | 7.9 | 4.8 | 7.9 |
| | Tube OD (mm) | 9.5 | 9.5 | 9.5 | 6.4 | 9.5 |
| Additional information | Ap($m^2$) | 0.097 | 0.097 | 0.194 | 0.045 | 0.045 |
| | Vi ($mm^3$) | 111.4 | 111.4 | 211.1 | 65.98 | 92.5 |
| | Terminal time (min) | 177 | 179 | 321 | 291 | 271 |

Table 3-2 shows the effective thermal conductivities of both directions by the correlations (Bonnissel et al., 2001). For the CENG used in this study, the compression force is in the direction of condenser length, which is vertical. Therefore, horizontal conduction is better than vertical conduction.

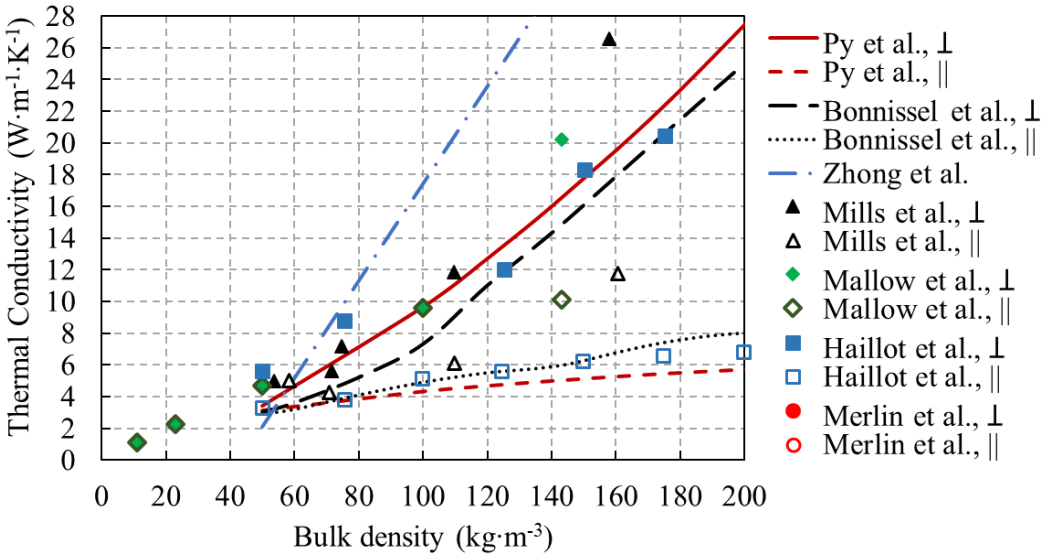


**Figure 3-4. The effective thermal conductivity of PCM/CENG composite from literature. ‖: Parallel. ⊥: Perpendicular.**

The analysis of the PCM melting process can be performed based on the TES unit composed of a PCM cylinder and a single tube at the center. In first three heat exchangers (see Figure 3-5(a)), thermocouples were placed in three locations: a top layer that is 30 mm below the top header, a middle layer that is at one-half the length of the TES unit and a bottom layer that is 30 mm above the bottom collection header. In each layer, the PCM temperatures were measured at three locations: the center of the coil, the edge of the TES unit and the tube surface.

As the small header of ETSH-GM results in the maldistribution of refrigerant in the eight branches, one TES unit cannot represent the whole PCMHX. In order to

observe the influence of the uneven flow distribution, more thermocouples were placed 5 mm close to the first branch at the top layer and the last branch at the bottom layer. All other thermocouples for PCM temperature were 5 mm away from the edge (see Figure 3-5(b)).

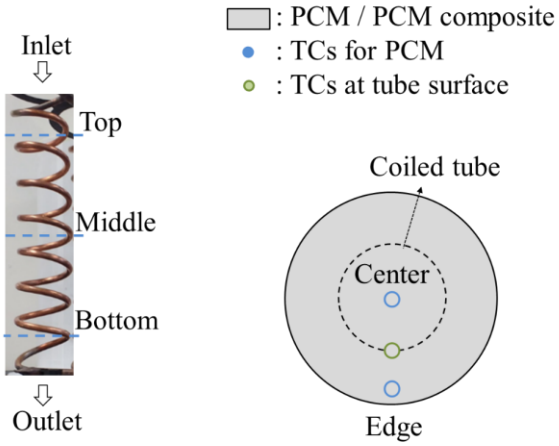


(a) TCs placed in TES unit of FT-N, FT-CS and ET-CS

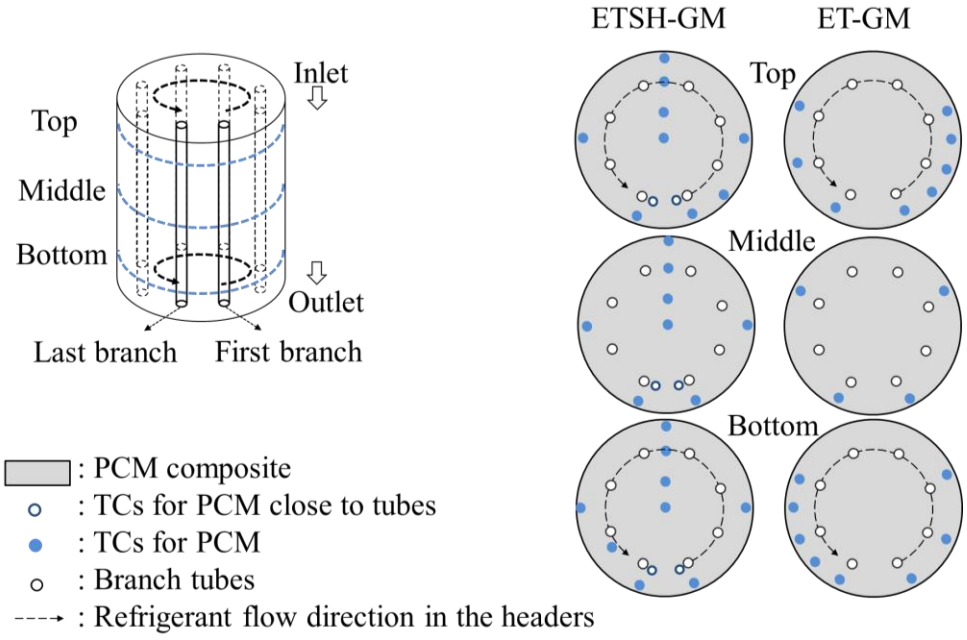


(b) TCs placed in ETSH-GM and ET-GM

**Figure 3-5. Thermocouples (TCs) placed in the TES unit and PCMHX.**

*3.3 Data Reduction and Uncertainty Analysis*

The condenser capacity, evaporator capacity, and COP are calculated in Eqs. (3-2) to (3-4), respectively. Eq. (3-5) gives the energy released from the HTF, i.e., the refrigerant, to PCM in the condenser, which is the integration of the condenser capacity with time $t$.

$$\dot{Q}_{cond}(t) = \dot{m}(t) \cdot \left(h_{cond,in}(t) - h_{cond,out}(t)\right) \tag{3-2}$$

$$\dot{Q}_{evap}(t) = \dot{m}(t) \cdot \left(h_{evap,out}(t) - h_{evap,in}(t)\right) \tag{3-3}$$

$$COP(t) = \frac{\dot{Q}_{evap}(t)}{W_{comp}(t)} \tag{3-4}$$

$$E_{HTF}(t) = \int_0^t \dot{Q}_{cond}(t')\, dt' \tag{3-5}$$

The comparison is based on system performance for a certain duration. The total thermal energy stored in PCM, $E_p(T)$, is calculated as in Eq. (3-6) with the assumption of the lumped PCM temperature. The initial PCM temperature $T_{ini}$ is 26.5°C, which is same with the ambient temperature.

$$E_p(T) = \begin{cases} m_p \int_{T_{ini}}^{T} C_s\, dT, & T < T_s\ (solid) \\ m_p \left( \int_{T_{ini}}^{T_s} C_s\, dT + \int_{T_s}^{T} C(T) dT \right), & T_s < T < T_l\ (Two-phase) \\ m_p \left( \int_{T_{ini}}^{T_s} C_s\, dT + H + \int_{T_l}^{T} C_l\, dT \right), & T > T_l\ (Liquid) \end{cases} \tag{3-6}$$

Terminal time, $t_{max}$, is defined by thermal energy rather than the temperature, which is the time when the total energy stored in PCM reached $E_p(T_{end})$. $t_{max}$ could be calculated by Eq. (3-7) through the iteration process, in which the total heat stored in PCM, $E_p(T_{end})$, should equal the sum of total heat released from the refrigerant, $E_r(t_{max})$ and heat loss from PCM container wall, $E_{loss}$. $T_{end}$ is set to be 39°C in this study, since we want to take advantage of all latent heat and prevent high condensing temperature.

$$t_{max}:\ E_{HTF}(t_{max}) = E_p(T_{end}) + E_{loss} \tag{3-7}$$

As such, system performance including COP, power consumption, and heat exchanger capacity can be described based on normalized time, $t^*$, from 0 to 1 instead of real-time. From Eq. (3-7) and Eq. (3-8), if PCM melting is uniform everywhere, the period of PCM in the solid phase is in a range of $t^*$ from 0 to 0.1, that of the molten PCM is during 0.1 to 0.99, and that of liquid is from 0.99 to 1.

$$t^* = \frac{t}{t_{max}} \tag{3-8}$$

The overall heat transfer coefficient at the HTF side, $U_{HTF}$, can be calculated from Eq. (3-9), in which $A_{HTF}$, $T_{c,sat}$ and $\overline{T}_p$ are the refrigerant-side heat transfer area, condensing temperature and the average temperature of PCM, respectively. The effective heat transfer coefficient of the PCM side, $\alpha_{p,eff}$, can be obtained by Eq. (3-10), in which $A_p$ is the heat transfer area at PCM side, refrigerant side convective heat transfer coefficient, $\alpha_{HTF}$, could be calculated from the correlation in Shah (2009).

$$U_{HTF} = \frac{\dot{Q}_{cond}}{(T_{c,sat} - \overline{T}_p)A_{HTF}} \tag{3-9}$$

$$\alpha_{p,eff} = \frac{1}{A_p(\frac{1}{U_{HTF}A_{HTF}} - \frac{1}{\alpha_{HTF}A_{HTF}} - R_{t_w})} \tag{3-10}$$

The uncertainty of calculated parameters can be determined by error propagation as in Eq. (3-11), where $\omega_f$ and $\omega_{x_i}$ are resultant uncertainty and the uncertainties of independent variables (see Table 3-1), respectively. $f$ is the given function, and $n$ is the number of the variables $x_i$. The uncertainty of temperature is 0.5℃, and that of pressure is 1.7 kPa. Based on the calculation, the uncertainties of exchangers capacities were less than 1%, and the uncertainty of COP was less than 1.9%. The uncertainty of the heat transfer coefficient of each heat exchanger was shown in Figure 3-15, which was less than 2%.

$$\omega_f = \sqrt{\sum_{i=1}^{n} (\frac{\partial f}{\partial x_i}\omega_{x_i})^2} \tag{3-11}$$

## *3.4 Results and Discussion*

### 3.4.1 Test Conditions

The time evolutions of the VCC states with FT-N and ET-GM are presented in Figure 3-6. The state points correspondingly represent the locations in the system as in Figure 3-1. The cooling mode was operated properly with constant superheat at the evaporator outlet. The evaporating pressure kept nearly constant owing to the steady

evaporating conditions. Moreover, since the condensing temperature was affected proportionally by the PCM temperature, the condensing pressure increased with the increase of the normalized time.

In Figure 3-6, the heat transfer rate in process 3 – 4 is the PCMHX capacity. To make an accurate system analysis, the heat loss of the system needs to be considered. Although the tubing between each component was insulated, the heat loss in two following system sections cannot be ignored: section 2 – 3 between compressor outlet and PCM condenser inlet, due to the high refrigerant temperature at the compressor outlet, and section 4 – 5 between PCM condenser outlet and expansion valve inlet, owing to the long connecting tube and the large surface area of the receiver. It has been found that the sum of the heat loss from these two sections was 5 – 11% of the total heat released in the process 2 – 5. As shown in Figure 3-7, the condenser capacities of the five different PCMHXs were very similar within the difference of less than 5%. Moreover, it is noted that the condenser capacity decreased at the beginning due to the rapid increase of the condensing pressure, and then kept nearly constant for the most period. At the end, it decreased slightly because of the gently increased condensing pressure. Therefore, it can be concluded that when $t^* > 0.1$, the processes of PCM absorbing heat and melting was conducted under the constant heat transfer rate. This testing condition is different from the most other experimental studies which is performed with the steady inlet temperature of HTF and the reduced heat transfer rate as in the previous research (Caron-Soupart et al., 2016; Chen et al., 2016; Fang et al., 2018; Gasia et al., 2018; Hosseini et al., 2014; Liu and Groulx, 2014; Longeon et al., 2013; Martinelli et al., 2016; Medrano et al., 2009; and Trp, 2005).

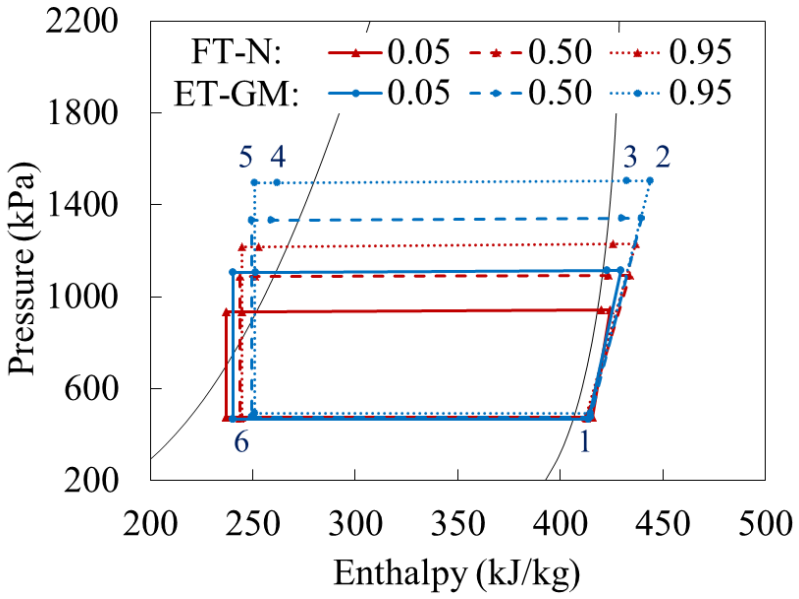


**Figure 3-6. Evolution of the pressure-enthalpy of the system with FT-N and ET-GM at t*= 0.05, 0.50 and 0.95.**

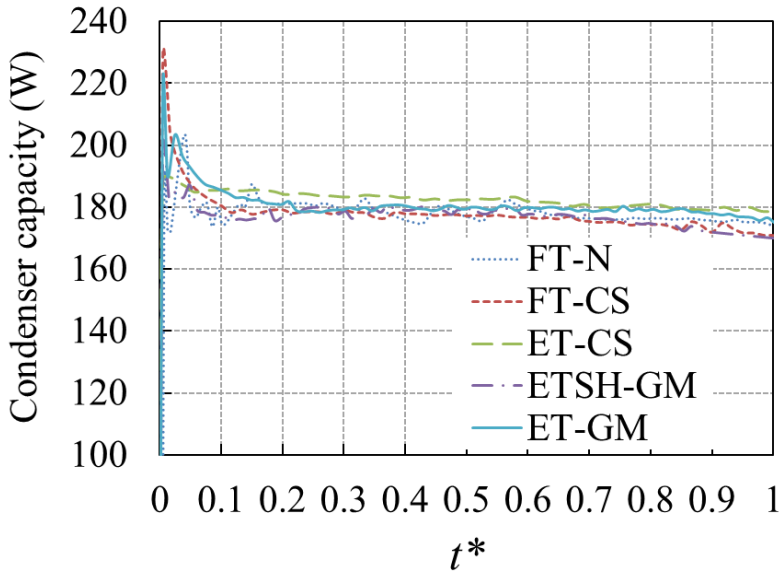


**Figure 3-7. Evolution of the condenser capacities of the system with five different enhanced PCMHX.**

In addition, in the previous study, the PCM melting process could not affect inlet temperature, while in our study, PCM melting performance could affect system condensing temperature and other system performance. Thus, this testing condition could lead to different PCM melting performance, such as melting rate and temperature profile, compared with the previous study.

### 3.4.2 PCM Melting Process

Figure 3-8 shows that PCM temperatures and tube temperatures of FT-N were time-dependent. Tube wall temperatures increased rapidly at $t^* > 0.1$, but then kept steady until $t^*$ increased to more than 0.5. This could be explained as follows. During $t^* < 0.1$, most solid PCM was heated up by conduction, and condensing temperature increased rapidly because only the small portion of the PCM was under sensible heat transfer. During $t^* > 0.1$, the mushy zone began to develop and to move from the location close to the tube wall to the PCM farther from the wall in the radial direction. Therefore, the temperature of PCM can keep relatively low until all PCM in radial direction reached the melting temperature, which occurred at $t^* = 0.55$ for the top level in this study. Longeon et al. (2013) showed a similar result despite different test conditions used.

Figure 3-8 also presents that the PCM melting rates were decreasing in the downward direction. When the temperature of the top PCM reached 50°C, the middle PCM temperature was 44°C, but the bottom PCM was still in the two-phase state. The first reason could be that the heat flux varied along the condenser tube length direction. From the inlet to outlet, the refrigerant changed from superheated vapor to two-phase

and then to subcooled liquid, leading to the different refrigerant temperatures and heat transfer coefficients in these three zones. At the top, the heat transfer coefficient of the vapor refrigerant was less than that of the middle. However, the thermal resistance was dominated by the PCM side. Thus, the heat transfer flux at the top was still higher than the other regions because of its higher inlet refrigerant temperature. For the refrigerant at the bottom, both the heat transfer coefficient and temperature were lower than the middle, leading to the smallest heat flux among the three regions. The second reason could be the influence of natural convection during the PCM melting process. It could displace heat to the upper part by an upward motion of hotter PCM, while colder PCM remained at the bottom. Thus, natural convection could speed up the melting of top-layer PCM, and slow down bottom PCM melting.

In this PCMHX design, the PCM in the middle section of the coils melted faster than the PCM outside the coils owing to the less volume of PCM in the middle. Thus, there was a temperature difference between the PCM at the center and the edge.

As shown in Figure 3-9, the PCM temperature of the center and edge at the top were very close with the difference smaller than 1 K, while at the bottom, this difference was greater than 2 K. This also illustrated the different PCM melting rates in the vertical direction because of the two reasons mentioned above.

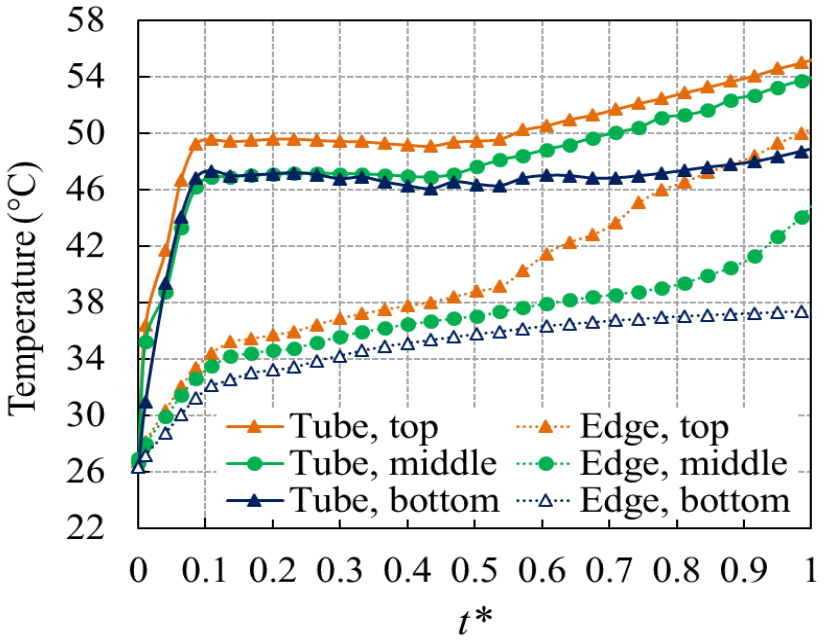


**Figure 3-8. Tube and PCM temperatures of the FT-N.**

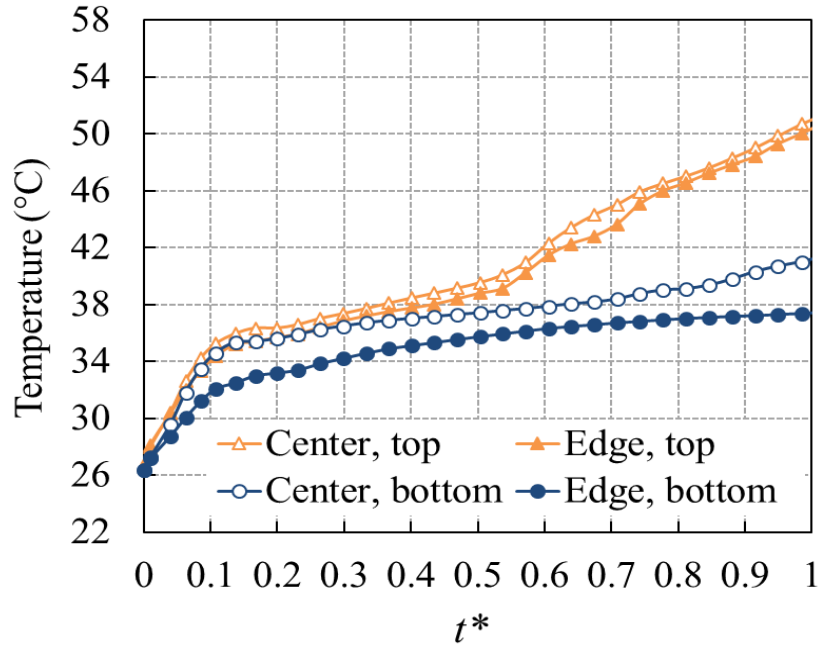


**Figure 3-9. PCM temperatures at the edges and coil centers of the FT-N.**

In other studies of literature review (Chen et al., 2016; Mallow et al., 2018), natural convection was prevented or weakened in the CENG-matrix-enhanced PCM. Figure

3-10 shows the PCM temperatures in ETSH-GM. Unlike the temperature profiles of FT-N, in ETSH-GM the top PCM temperatures were similar to its middle ones. Also, it shows that the temperatures of the PCM/CENG composite at the top, about 45°C, cannot be as high as the PCM in ET-N, owing to the lack of natural convection. On the other hand, similar to FT-N, the bottom PCM temperatures of ETSH-GM were lower than the middle layers. Some reasons are the lower refrigerant heat transfer coefficient and the lower refrigerant temperature near the outlet of the condenser, resulting in less heat flux at the bottom. The other reason is that the CENG matrix has a lower thermal conductivity in the direction parallel to compression, which is the vertical direction in this study. As a result, even though the top and middle PCM had already melted to liquid with relatively higher temperatures, its influence on the bottom PCM was limited.

By comparing Figure 3-10 (a) and (b), it was observed that PCM temperatures near the first several tubes were higher than that near the last tubes. The reason could be the maldistribution of refrigerant owing to the small header. After flowing into the top distribution header, more refrigerant flowed through the first several tubes rather than the last several tubes because of the less pressure drop. Therefore, the heat flux in the first several tubes was much greater than the last ones, leading to faster PCM melting and higher PCM temperature near the first several tubes.

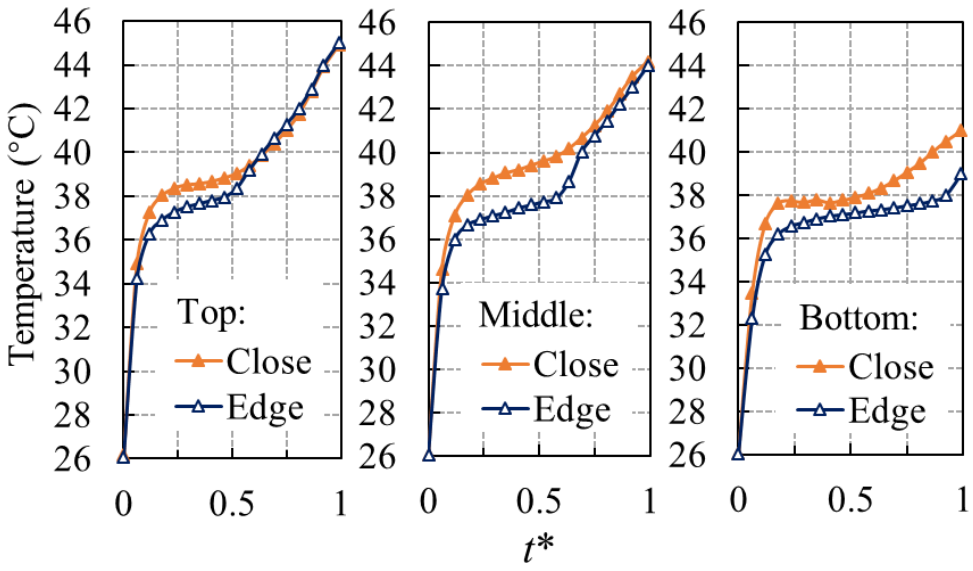


(a) PCM temperature near the first tube

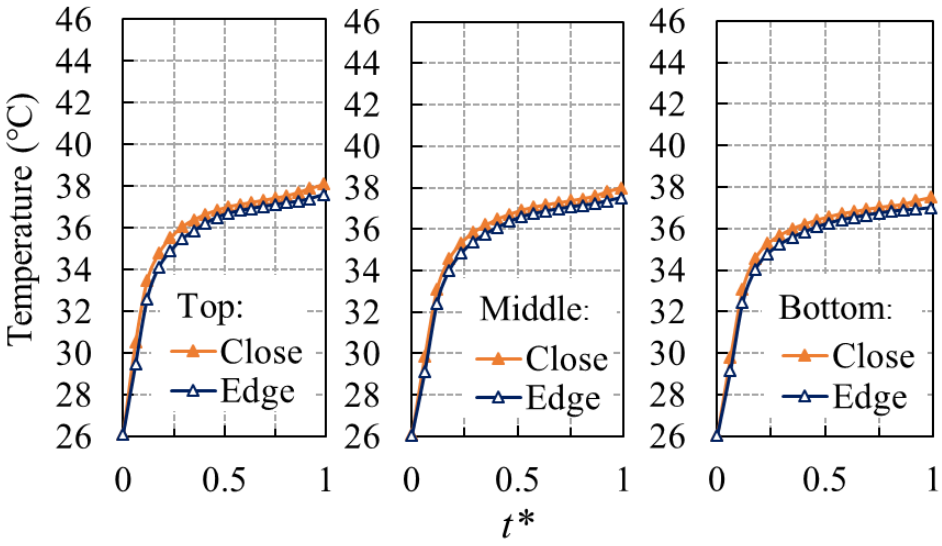


(b) PCM temperature near the last tube

**Figure 3-10. PCM temperatures in ETSH-GM at the top, middle and the bottom of the first tube and the last tube.**

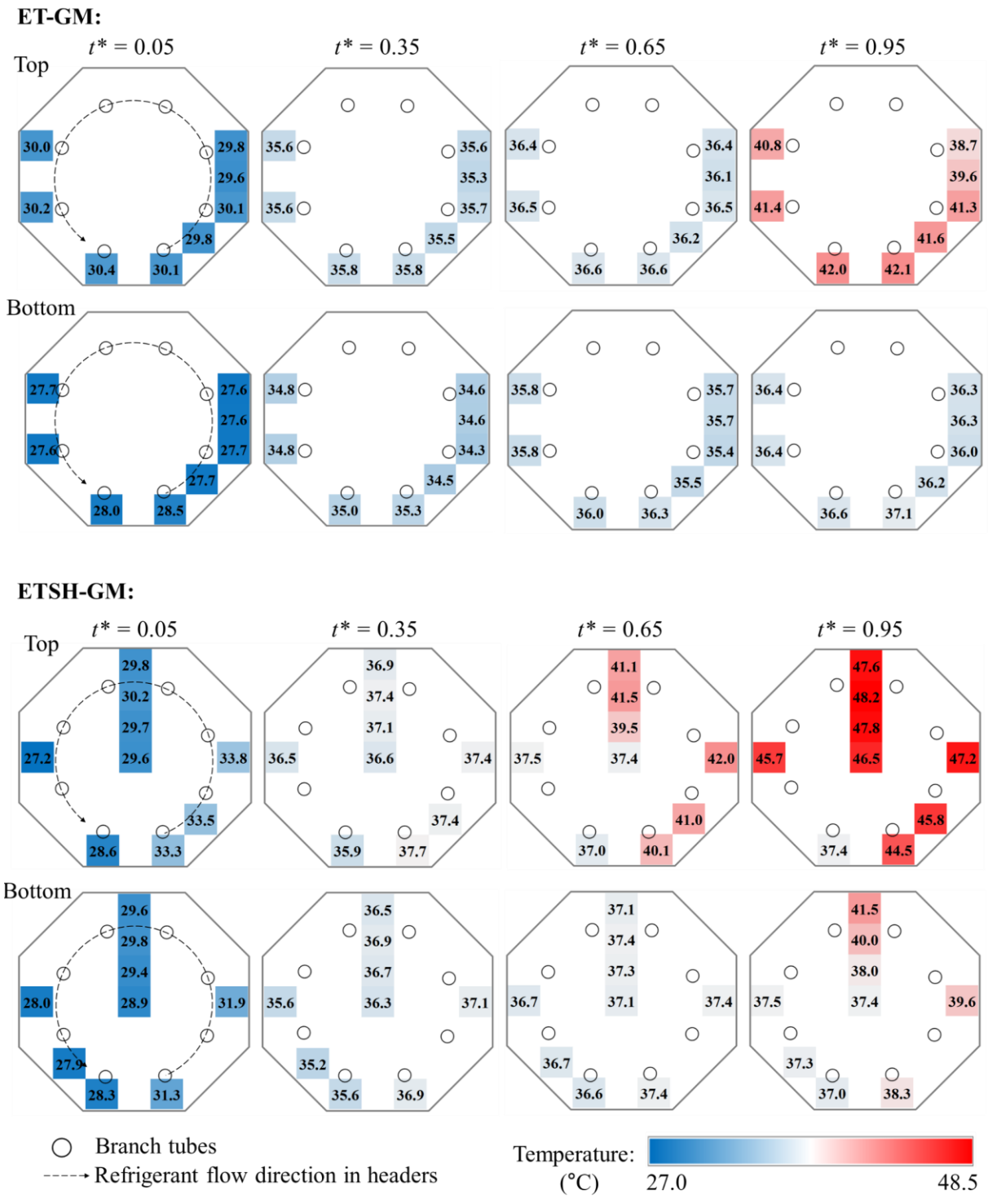


**Figure 3-11. PCM temperatures at the top and bottom layers of CENG-PCM.**

Figure 3-11 illustrates the PCM temperatures in two CENG-enhanced heat exchangers, in which the locations of temperatures were identical with the thermocouples presented in Figure 3-5 (b). It presents that the temperature distribution of ET-GM was much more uniform than that of ETSH-GM, especially when $t^* > 0.65$. In ETSH-GM, the temperature difference between different locations at edges could reach 10.2 K at $t^* = 0.95$, however, this difference is less than 3.4 K in ET-GM. This is because the bigger header of ET-GM could result in a similar pressure drop as similar mass flow rate was distributed into each branch, Thus, both the refrigerant mass flow rate and PCM melting rate could be uniformly distributed between branches.

From Figure 3-8 to Figure 3-11, it can be concluded that PCM melting rates along the vertical direction are different due to the effect of the refrigerant-side heat transfer condition and/or the PCM side natural convection. In addition, in ETSH-GM, this uneven melting also occurs in the horizontal direction. In return, this uneven PCM melting in both directions could also lead to the change of refrigerant-side condensing temperature and system performance, which is discussed in the following section.

### 3.4.3 Condensing Temperature

Figure 3-12 shows that the system condensing temperature increased with cooling time, since condensing temperature should follow the increased PCM temperature to keep the approximate steady heat transfer rate. The additional reason could be the uneven melting in the vertical direction. After the top PCM melted to a liquid, its temperature increased rapidly by the sensible heat transfer so that the temperature difference between PCM and the refrigerant at the top was reduced. In this case, the

condensing temperature had to increase to maintain enough heat transfer. Therefore, condensing temperatures began to increase obviously at the same time when top PCM melted to liquid at $t^* = 0.55$ from Figure 3-8 to Figure 3-10.

From Figure 3-12 (a), it is noted that FT-CS, which has the same heat transfer surface area but with the addition of copper sponge of 5 % by mass, could achieve about 1 K lower condensing temperature than the baseline. Whereas ET-CS with two times larger heat transfer area and 5% copper sponge by mass could get 6 K lower condensing temperature. It seems that the heat transfer area can affect the condensing temperature primarily because of the limitation of the copper sponge fraction in this design.

Moreover, as shown in Figure 3-12 (b), the condensing temperature of ETSH-GM was 3 K lower than the baseline, and that of ET-SH was 8 K lower. This is due to the significantly increased thermal conductivity of the PCM/CENG composite. In ETSH-GM, since the refrigerant flow rates in the first several tubes were greater than the last several tubes as analyzed in the previous section, the condensing temperature was higher than ET-SH to maintain total condenser capacity. This refrigerant maldistribution of ETSH-GM could lead to uneven utilization of PCM latent heat.

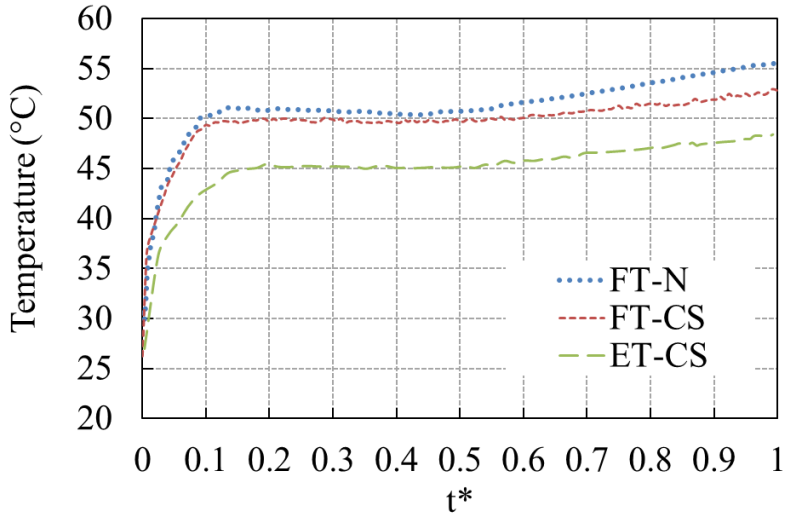


(a) FT-N, FT-CS and ET-CS

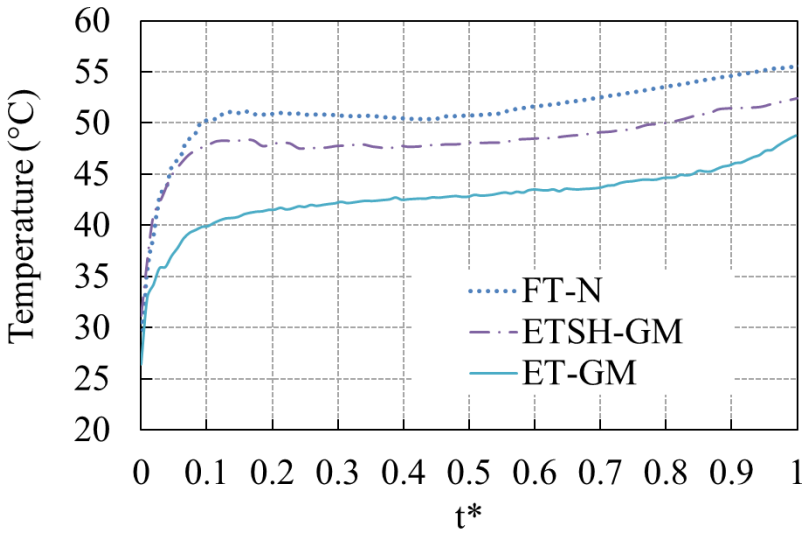


(b) FT-N, ETSH-GM and ET-GM

**Figure 3-12. Evolution of the condensing temperature with different PCMHX.**

### 3.4.4 System COP

Figure 3-13 shows that the evolution of the TES system COP with each PCMHX with the normalized time. The decreasing slope was much steeper before $t^*$ of 0.1. Since the evaporating condition was steady during the cooling time, the suction

pressure and the mass flow rate were approximately steady while the compressor power consumption increased with time corresponding to the condensing temperature curves. Thus, COP decreased rapidly with time until $t^* = 0.1$. It is also found that at $t^* = 0.1$, using FT-CS and ET-CS, enhanced by copper sponge, COP was increased by 13.3% and 50%, respectively. Using ETSH-GM and ET-GM, enhanced by CENG, system COP was increased by 23.3% and 80%, respectively. And at $t^* = 0.9$, COPs of FT-CS, ET-CS, ETSH-GM and ET-GM were increased by 15.4%, 38.5%, 19.2%, and 50.0% respectively. It can be concluded that ET-GM has good system performance in terms of its highest COP.

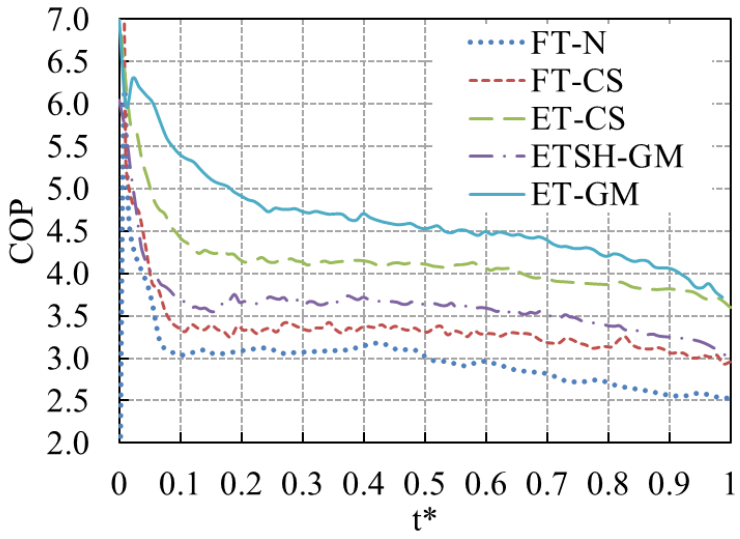


**Figure 3-13. Evolution of the system COP with each PCMHX.**

### 3.4.5 PCMHX Comparison

Based on the baseline of FT-N as the reference, the normalized thermal resistances are illustrated in Figure 3-14 (a), including the thermal resistance in both PCM side, $R_{t_p}$, and refrigerant side, $R_{t_{HTF}}$. It can be seen that the normalized $R_{t_{HTF}}$ of ET-CS

was less than a half of that in the baseline, while $R_{t_{HTF}}$ of ET-GM or ETSH-GM was increased. This is because the heat transfer area of ET-CS was increased by 89%, and the lower condensing pressure could increase the heat transfer coefficient of the refrigerant-side. However, in ET-GM or ETSH-GM, the heat transfer area was much smaller although the condensing temperature was much lower. As for $R_{t_p}$, it is decreased by 17% in ET-CS by adding copper sponge. However, from the previous studies, the copper foam could increase the heat transfer rate by 10 times (Zhao et al., 2010). This disagreement is because the copper foam used in this study has a much higher porosity of 99.95% than the literature, leading to the thermal conductivity increased by only 6 times than the pure PCM. Whereas in Zhao et al. (2010), the conductivity was increased by more than 80 times as calculated from Yang et al., (2014) with a lower foam porosity of 91%. Therefore, the heat transfer enhancement by the copper sponge in FT-CS was not as great as the past studies found in the literature review. In ET-CS, $R_{t_p}$ was about a half of that in FT-CS because of the doubled heat transfer area. Moreover, in two CENG-enhanced PCM, $R_{t_p}$was decreased by 40%–80% due to the significantly increased PCM effective thermal conductivity although the heat transfer area was only a quarter of the baseline. The $R_{t_p}$ of ETSH-GM was two times higher than that of ET-GM, because of refrigerant maldistribution and less enhancement.

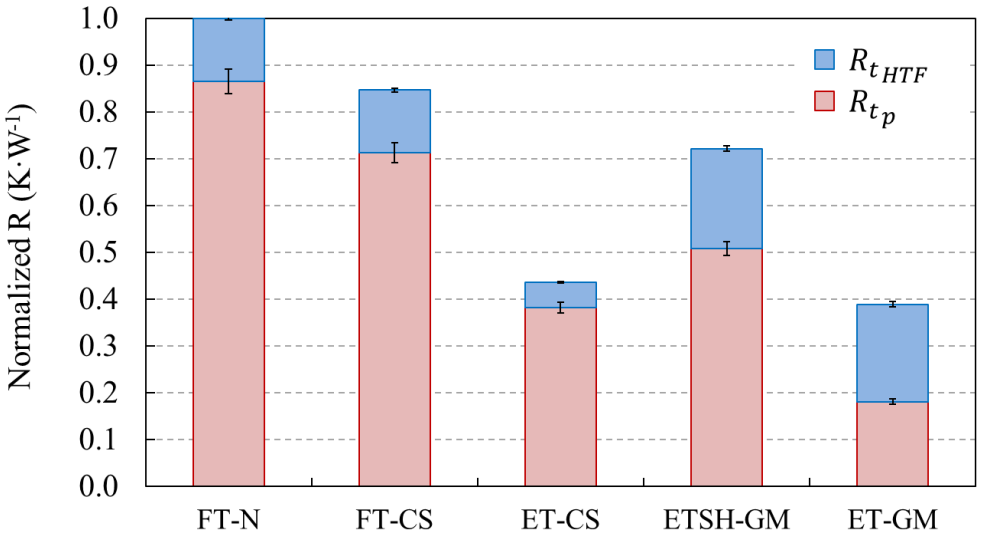


(a) Normalized thermal resistance

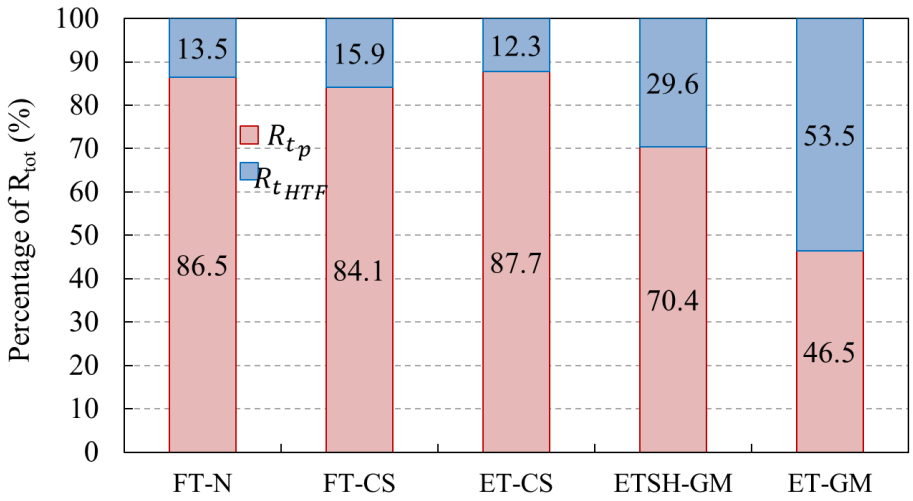


(b) Proportion of the thermal resistance

**Figure 3-14. Thermal resistance and proportions in PCMHX (Baseline: FT-N).**

The fraction of the thermal resistance on each side (see Figure 3-14(b)) indicates that the portion of $R_{t_p}$ in FT-CS, ETSH-GM and ET-GM was decreased because of the addition of the conductive structure. Due to the excellent heat transfer enhancement by CENG, the dominant thermal resistance of ET-GM was the refrigerant rather than the

PCM side. Different from the other four heat exchangers, the proportion of $R_{t_p}$ of ET-CS increased by 1.2% as compared with the baseline, which implies that the heat transfer augmentation at the refrigerant side due to the decreased pressure was greater than the PCM side enhancement in this design.

From Figure 3-15, it is found that the overall heat transfer coefficient, $U_{HTF}$, of two copper-sponge-enhanced PCMHXs were only increased by 15 –18% as limited by the PCM-side significantly. However, $U_{HTF}$ of PCM/CENG composite in ET-GM could reach more than 900 $Wm^{-2}{\cdot}K^{-1}$, which was increased by 5.5 times. And the PCM-side effective heat transfer coefficient, $\alpha_{p,eff}$, was increased by 13–21% by using copper sponge, while it was increased by a factor of 10 in ET-GM.

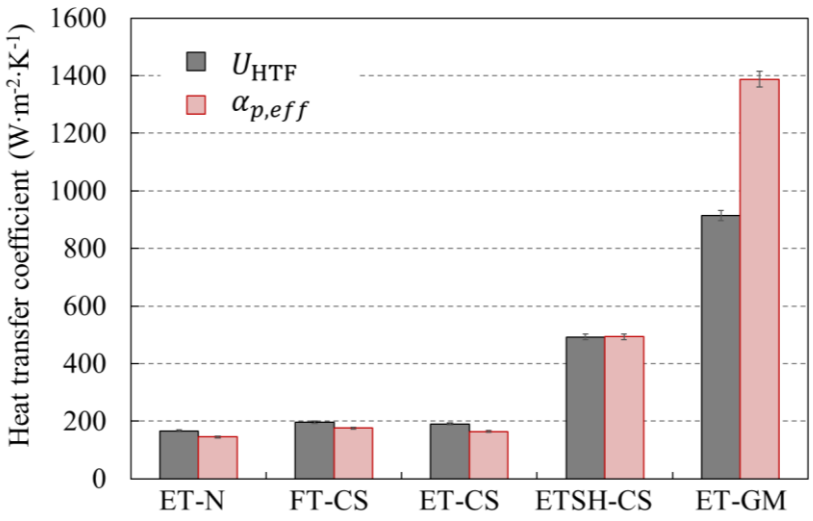


**Figure 3-15. Overall heat transfer coefficient and PCM side heat transfer coefficient.**

Based on Figure 3-14 and Figure 3-15, it can be summarized that the PCM/CENG composite used in ET-GM could result in excellent heat transfer performance compared

with the other four heat exchangers. The bigger size of the header for even refrigerant distribution and large heat transfer areas could be also helpful to reduce the thermal resistance. The copper sponge should also be added more in this study to enhance PCM side heat transfer.

### 3.4.6 System-level Comparison

To compare the TES system performance clearly with the baseline, the normalized system performance and heat exchangers characteristics are presented in Figure 3-16. The heat exchangers' characteristics include the heat exchanger inner volume, $V_i$, the overall thermal conductance at the refrigerant-side, $U_{HTF}A_{HTF}$, the heat transfer area at the PCM-side, $A_p$, and volumetric energy density (VED). VED is the heat storage capability in the unit volume, which is the ratio of the total energy stored in PCM to the total PCM composite volume. It indicates that all the enhanced PCMHX could achieve less compressor power consumption and higher COP than the baseline. ET-GM had the highest COP and lowest compressor power consumption, which are 149% and 70% of the baseline, respectively, owing to its highest $U_{HTF}A_{HTF}$ even though with less heat transfer area. Its VED is decreased by 8%, which is acceptable in the application. Besides, ET-CS was the second best with 20% less power consumption and 32% higher COP due to its higher $U_{HTF}A_{HTF}$. However, its inner volume was increased by 89%, leading to the largest receiver and the greatest system refrigerant charge. ETSH-GM and FT-CS could increase system performance as well. Nevertheless, the increase in $U_{HTF}A_{HTF}$ of ETSH-GM was limited by the

maldistribution of refrigerant flow, and that of FT-CS was impeded by the less heat transfer area.

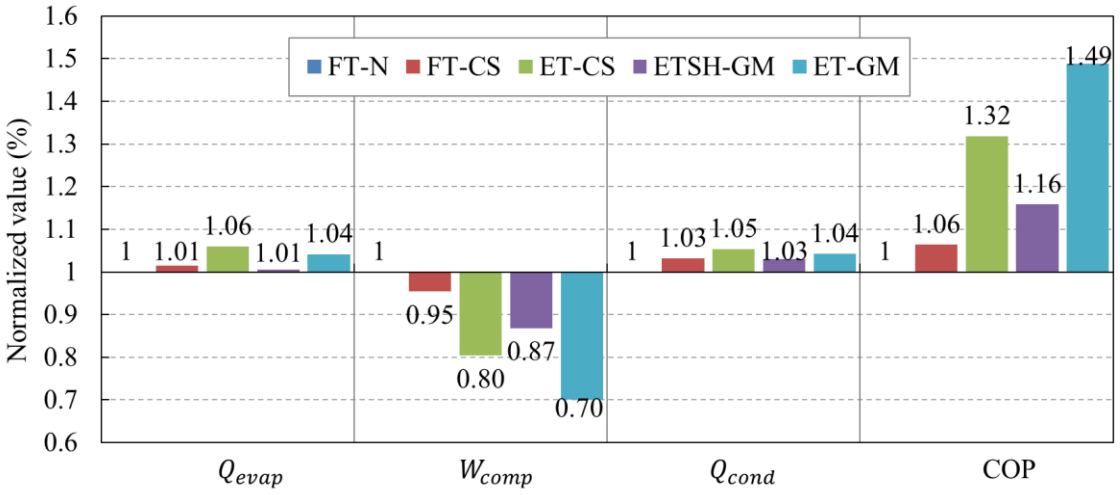


(a) Normalized system performance

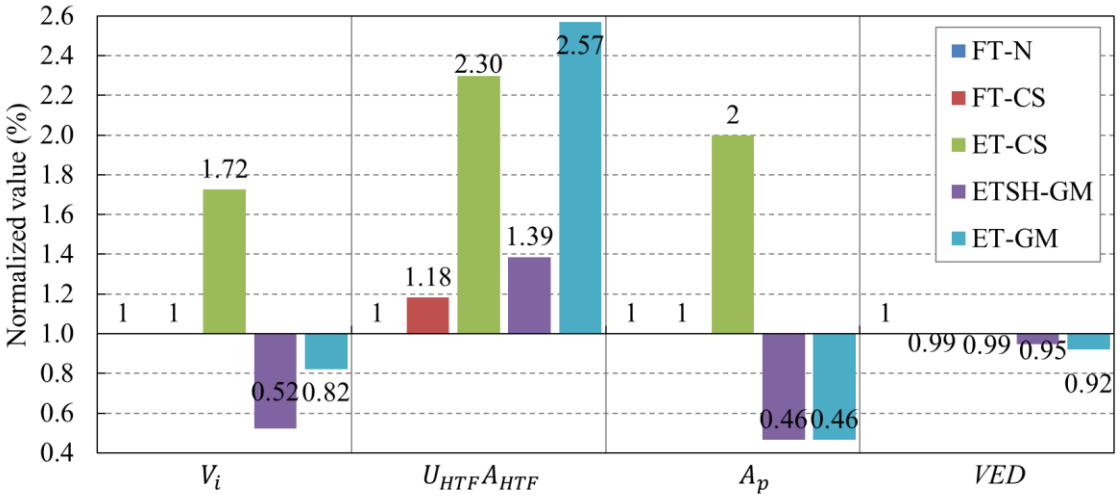


(b) Normalized PCMHX performance

**Figure 3-16. Normalized performance of the TES system and PCMHX in system-level comparison (Baseline: FT-N).**

## *3.5 Chapter Summary and Conclusions*

In this chapter, five PCMHXs were proposed and investigated for the TES system of a PCS. This TES system could work properly in cooling mode by the VCC operation and in PCM regeneration mode by the thermosiphon cycle operation. This chapter focuses on the cooling cycle, in which the PCM absorbs heat from the condenser under approximately constant heat transfer rate.

In the component level, it was found that PCM melting rates were different along the vertical direction. This is due to the contributions of PCM side natural convection and different refrigerant-side heat transfer parameters along the condenser length. The influence of the refrigerant flow distribution on uneven melting in the horizontal direction was also demonstrated. In the system-level analysis, the effects of the heat transfer enhancement, heat transfer area and flow distribution in branches on system performance were experimentally studied.

Compared with the non-enhanced PCMHX and other enhanced candidates, the PCM/CENG composite heat exchanger (ET-GM) was found to be the best with the highest COP (49% over baseline), highest *UA* (2.6 times higher than the baseline), and 18% smaller inner volume. The copper-sponge-enhanced PCMHX (ET-CS) was the second-best with 32% increased COP, 30% higher UA, and two times larger heat transfer area, although the inner volume was two times larger than the baseline. The overall heat transfer coefficient using CENG reached more than 900 $Wm^{-2} K^{-1}$, which is consistent with the literature with the same order of magnitude (Medrano et al., 2009; Merlin et al., 2016). The PCM effective heat transfer coefficient was increased by a

factor of 10 by using the PCM/CENG composite, while the PCM side resistance was not the dominant portion.

It can be concluded that ET-GM is recommended for the system. The PCM/CENG composite used in ET-GM can lead to the excellent heat transfer performance compared with other exchangers. A bigger header with uniform refrigerant flow distribution and greater heat transfer area is beneficial to decrease the thermal resistance of PCMHX. In addition, the copper sponge enhanced PCMHX is the second best. As apply this type of HX, more copper sponge added in the PCM side can be helpful for the PCM side heat transfer enhancement.

This study fills the gap of heat-transfer-enhanced PCM applied in an air-conditioning system. The experimental results and the comparisons could be helpful for the PCMHX development as well as the applications in other fields such as solar energy storage, electric system cooling, and residential thermal management.

# Chapter 4: Performance Analysis on PCS with PCMHX

In this Chapter, a VCC-based PCS with PCMHX is described first, which is different from the system illustrated in Chapter 2. This novel design having a cooling and PCM regeneration cycle can achieve both localized cooling and building energy savings. The effects of thermostat set points and surrounding temperatures were compared and discussed experimentally. The higher recharge rate and higher averaged overall COP are preferred, although these two objectives are always contracting. Thus, different PCM recharge rates caused by different compressor speeds were studied. In addition, the cooling time is determined by the occupants' needs and cooling loads of the building, and leads to different system performance. Therefore, the effect of cooling time was also investigated in this Chapter.

## *4.1 System Description*

### 4.1.1 Experimental Setup

The novel PCS with PCMHX has two operation cycles: a cooling cycle and PCM regeneration cycle. While the cooling cycle operates in the buildings for providing personal cooling to occupants, the regeneration cycle is to recharge PCM and release stored heat to the surroundings, so that the whole system should operate in the environment where no cooling is needed, such as balcony or garage. The proposed PCS prototype can be powered by electric battery and coupled with a robotic base so that it can move automatically between different places.

Figure 4-1 shows the experimental setup and two cycles. The cooling cycle is based on a VCC, in which condenser tubes are submerged in a PCM. The refrigerant condensation heat is discharged to the PCM to prevent injecting the heat into the local environment. An upper microchannel heat exchanger (MCHX) works as an evaporator with a fan and nozzle to provide a localized cooling. When PCM regeneration is needed, the refrigeration cycle is reversed so that PCMHX works as an evaporator, and MCHX works as a condenser. The PCM releases heat to refrigerant and is solidified during the recharge cycle, while the upper MCHX discharges the heat to the environment where no cooling is needed. To switch from one cycle to the other, a reversing valve, two check valves, and two TXVs were applied. Each check valve was installed before the corresponding TXV. Another recharge option is using a thermosiphon cycle as can be found from Chapter 2. However, the recharge time of the thermosiphon cycle is much longer than that of the reverse cycle.

R-134a was the selected refrigerant. The compressor used in the system was a rotary compressor with a displacement volume of 1.4 cc. The compressor speed was set to 2,100 rpm (revolutions per minute) for the cooling cycle. A Coriolis type flow meter was installed in the vapor line to measure the target mass flow rate of the system. The DC fan motor was selected to deliver the airflow rate of 0.031 $m^3s^{-1}$. In-stream T-type thermocouples were used for temperature measurement and installed between each component, as illustrated in Figure 4-1. Pressure transducers were selected to measure refrigerant pressures at the inlet and outlet of both MCHX and PCMHX. Current transducers and voltage transducers were used to measure the powers of the fan motor and compressor. All measurement data from sensors and transducers were

provided to the data acquisition system operated with data acquisition software developed in LabView®.

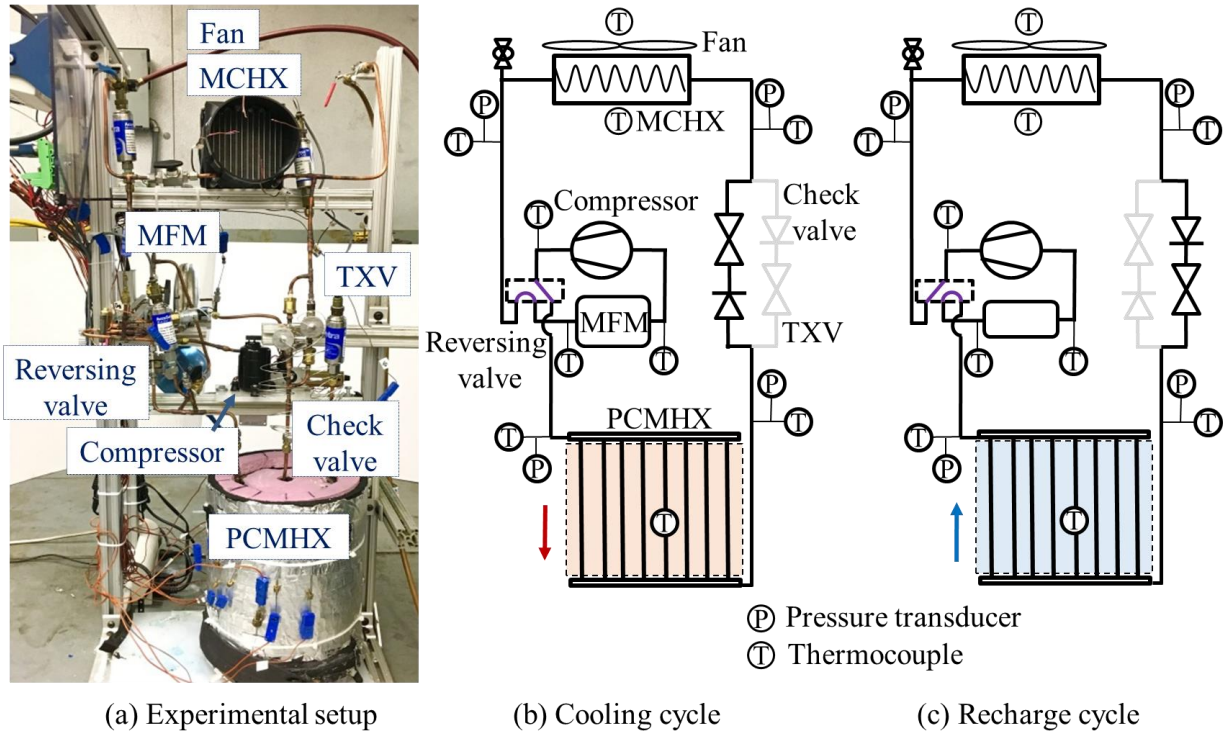


**Figure 4-1. Picture of the experimental setup and cycle schematics.**

### 4.1.2 PCM/CENG HX

The PCMHX applied for the PCS is a shell-and-tube type HX with multi-tube design as illustrated in Figure 3-3 (e). The PCMHX consists of a PCM soaked in a graphite composite block, two headers at the top and bottom, eight parallel copper tubes, and insulation foam around the PCM block. The insulation foam used was the flexible rubber foam from Armaflex® with a thickness of 0.019 m and the thermal conductivity of 0.04 $Wm^{-1}K^{-1}$. In the experiment, the heat loss from the PCM insulation foam to the surrounds is about 6% of the PCMHX capacity. The mass of the PCM

composite was 13.0 kg. There were no gaps between the PCM composite block and copper tubes. For the cooling cycle, the refrigerant discharged from the compressor flows into the top distribution header through the inlet tube. Then it passes through eight copper tubes and is condensed while releasing heat to PCM. After condensed in the PCMHX, the liquid refrigerant is collected in the bottom header and flows through the outlet tube to the TXV. For the recharge cycle, the refrigerant flow direction is reversed in PCMHX from that of the cooling cycle. Table 4-1 illustrates the specifications of PCMHX. For the selected PCM/CENG composite, the graphite volume fraction was 8% resulting in the radial effective thermal conductivity of 24 $Wm^{-1}K^{-1}$, which is increased by 100 times as compared with the pure PCM (Bonnissel et al., 2001; Py et al., 2001).

**Table 4-1. CENG/PCMHX design properties.**

| Parameters | Unit | Value |
|---|---|---|
| PCM container diameter | mm | 265 |
| PCM composite height | mm | 280 |
| Tube length | mm | 300 |
| Tube without PCM length | mm | 20 |
| Numbers of tubes | -- | 8 |
| Tube inside diameter | mm | 4.8 |
| Tube outside diameter | mm | 6.4 |
| Header length | mm | 51.8 |
| Header inside diameter | mm | 7.9 |
| Header outside diameter | mm | 9.5 |

The PCM used in the PCS is the same as in Chapter 2, which is an organic wax PureTemp37. The characteristics of PCM, such as melting temperature, can affect the VCC system performance. The selected melting temperature cannot be very high to prevent excessive condensing temperature during the cooling cycle. On the other hand, it cannot be lower than the ambient temperature to properly regenerate the PCM and to prevent losing the latent heat in the off period. Therefore, the melting temperature of 37°C was selected. The DSC measurement shows that the phase change temperature is about 37°C with a temperature glide of 4 K (Mallow et al., 2018), meaning that it begins to melt at around 35°C and completes the melting process at around 39°C. The latent heat is 210 $kJ \cdot kg^{-1}$. The properties of PureTemp37 are listed in Table 2-1.

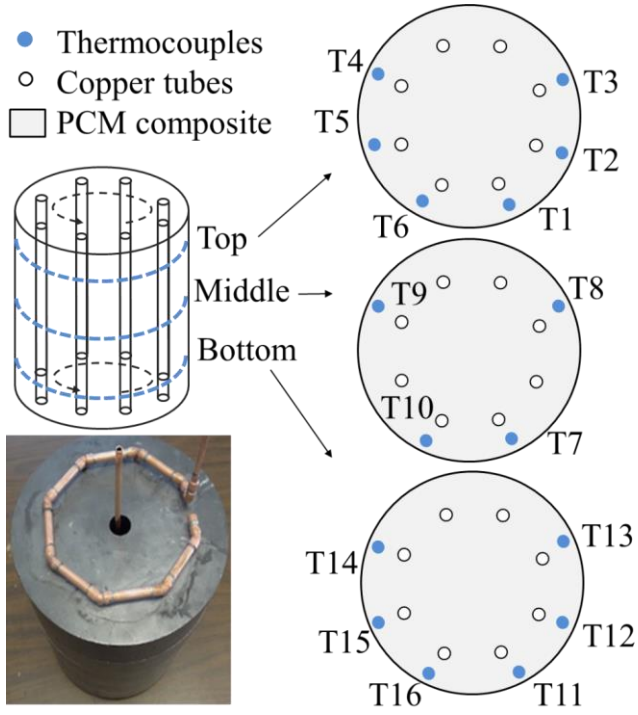


**Figure 4-2. Thermocouples placed at the top, middle and bottom of PCMHX.**

To obtain temperature information and analyze the phase change process of the PCM/CENG composite, thermocouples were installed as illustrated in Figure 4-2. T1-T6 were placed at the top layer, T7-T10 were at the middle layer, and T11-T16 were placed at the bottom layer. T1-T6 and T11-T16 were installed 65 mm from the top and bottom surfaces, respectively. T7-T10 were placed in the middle of the PCMHX in the length direction. In each layer, several thermocouples were placed 15 mm from the composite edge near the branches to obtain the averaged PCM temperature.

### *4.2 Data reduction and Uncertainty Analysis*

Refrigerant properties, such as specific enthalpy, are determined by the pressures and temperatures measured by sensors installed in each component. The measured mass flow rate was used to calculate the heat exchanger capacity. System performance, such as heat exchanger capacity, power consumption, and COP, changes over the operation time due to the dynamic PCM states. The condenser capacity and evaporator capacity are calculated according to eq. (4-1) and eq.(4-2), respectively. In the cooling cycle, the PCMHX serves as a condenser, while the MCHX serves as an evaporator. Therefore, we have $\dot{Q}_{cond} = \dot{Q}_{\mathrm{PCMHX}}$ and $\dot{Q}_{evap} = \dot{Q}_{\mathrm{MCHX}}$. $h_{cond,in}$ and $h_{cond,out}$ are the specific enthalpies at the PCMHX inlet and outlet, respectively. $h_{evap,in}$ and $h_{evap,out}$ are the specific enthalpies at the MCHX inlet and outlet, respectively. In the recharge cycle, heat exchanger functions are switched so that $h_{cond,in}$ and $h_{cond,out}$ are specific enthalpies of the MCHX, and $h_{evap,in}$ and $h_{evap,out}$ are those of the PCMHX. $\dot{m}$ is the mass flow rate measured by the mass flow meter. We also have $\dot{Q}_{evap} = \dot{Q}_{\mathrm{PCMHX}}$ and $\dot{Q}_{cond} = \dot{Q}_{\mathrm{MCHX}}$.

$$\dot{Q}_{cond}(t) = \dot{m}(t) \cdot \left(h_{cond,in}(t) - h_{cond,out}(t)\right) \quad (4\text{-}1)$$

$$\dot{Q}_{evap}(t) = \dot{m}(t) \cdot \left(h_{evap,out}(t) - h_{evap,in}(t)\right) \quad (4\text{-}2)$$

The transient system COP is calculated with eq. (4-3), in which $W_{comp}$ and $W_{fan}$ are the compressor and fan power consumption, respectively.

$$COP_{tr}(t) = \frac{\dot{Q}_{evap}(t)}{W_{comp}(t) + W_{fan}(t)} \quad (4\text{-}3)$$

Eq. (4-4) calculates the accumulated heat stored in PCM ($E_p(t)$). $t_c$ is the cooling terminal time. $Q_{loss}$ is the heat loss from PCM top, bottom, and side walls according to the difference between the average PCM temperature and surrounding temperature. In the cooling cycle (meaning $0 \le t \le t_c$), $[\dot{Q}_{cond}(t) - \dot{Q}_{loss}(t)]$ is the heat input from refrigerant minus the heat loss from the PCM container surface to the surrounding. When $t = t_c$, $\int_0^{t_c}\left[\dot{Q}_{cond}(t) - \dot{Q}_{loss}(t)\right] dt$ is the total thermal energy stored in PCM during the cooling cycle. In the recharge cycle (meaning $t_c < t \le t_r$), $\int_0^{t_c}\left[\dot{Q}_{cond}(t) - \dot{Q}_{loss}(t)\right] dt - \int_{t_c}^{t_r}\left[\dot{Q}_{evap}(t) + \dot{Q}_{loss}(t)\right] d$ is the accumulated energy remained in the PCM, which equals the total heat stored during the cooling cycle minus the heat released from PCM during the recharge cycle.

$$E_p(t) = \begin{cases} \int_0^t [\dot{Q}_{cond}(t) - \dot{Q}_{loss}(t)]\, dt, 0 \le t \le t_c\ (cooling) \\ \int_0^{t_c} \left[\dot{Q}_{cond}(t) - \dot{Q}_{loss}(t)\right] dt - \int_{t_c}^{t} \left[\dot{Q}_{evap}(t) + \dot{Q}_{loss}(t)\right] dt, t_c < t \le t_r\ (recharge) \end{cases} \quad (4\text{-}4)$$

The recharge terminal time ($t_r$), could be obtained by setting $E_p(t_r)$=0 in eq. (4-4), which means $\int_0^{t_c}\left[\dot{Q}_{cond}(t) - \dot{Q}_{loss}(t)\right] dt = \int_{t_c}^{t_r}\left[\dot{Q}_{evap}(t) + \dot{Q}_{loss}(t)\right] dt$.

Moreover, the total accumulated cooling energy used for space cooling and total accumulated cooling energy used for PCM solidification are calculated by eq. (4-5) and eq. (4-6), respectively. The total energy consumption from the fan motor and compressor of the cooling cycle and that of the recharge cycle are calculated by eq. (4-7) and eq. (4-8), respectively.

$$E_{evap,c} = \int_0^{t_c} \dot{Q}_{evap}(t)\, dt \quad (4\text{-}5)$$

$$E_{evap,r} = \int_{t_c}^{t_r} \dot{Q}_{evap}(t)\, dt \quad (4\text{-}6)$$

$$E_c = \int_0^{t_c} W_{comp}(t) + W_{fan}(t) dt \quad (4\text{-}7)$$

$$E_r = \int_{t_c}^{t_r} W_{comp}(t) + W_{fan}(t)\, dt \quad (4\text{-}8)$$

The averaged performance is used for comparisons. The averaged-cooling system COP and recharge system COP could be calculated by eq. (4-9) and eq. (4-10), respectively.

$$COP_c = \frac{E_{evap,c}}{E_c} \tag{4-9}$$

$$COP_r = \frac{E_{evap,r}}{E_r} \tag{4-10}$$

The overall system COP ($\mathrm{COP_{overall}}$), can be used for analyzing the overall system performance by considering power consumption over both the cooling cycle and regeneration cycle, which could be calculated according to eq. (4-11).

$$COP_{overall} = \frac{E_{evap,c}}{E_c + E_r} \tag{4-11}$$

The uncertainties of parameters can be obtained from Eq. (3-11). $\omega_i$ is the uncertainty of independent variable $x_i$, which can be found in Table 3-1. Based on the uncertainty calculation, the maximum uncertainties for $\dot{Q}_{cond}(t)$ and $\dot{Q}_{evap}(t)$ were both less than 2.5%. The uncertainties of the transient COP and averaged COP were less than 4%. And the uncertainty for the accumulated energy is less than 1%.

## *4.3 Results and Discussion*

### 4.3.1 System Performance with Both Cooling and Recharge Cycles

Hereafter the "dual-cycle" is defined as a combination of cooling and recharge cycles. The dual-cycle PCS system performance is discussed in this section. The surrounding temperature was controlled to be 26 °C constant. Compressor speed was set to be 2,100 rpm for both cycles.

Figure 4-3 shows the operating pressures of PCMHX and MCHX during the dual cycle. In the cooling cycle, the evaporator pressure in MCHX was constant due to the stable surrounding temperature and evaporating conditions. The condenser pressure increased gradually at the beginning, and then, the increasing slope became smaller. After 3.5 hours, the condenser pressure increased faster than that of before. It is because the PCM temperature increased faster than that before 3.5 hours as it was in single-phase while absorbing heat. It is noted that the top and middle PCM temperatures increased fast before 0.5 hours and after 3.5 hours in the cooling cycle (Figure 4-4), and therefore, resulted in the condenser pressure increased rapidly near the beginning and end of the cooling cycle. Moreover, as illustrated in Figure 4-5, cooling capacity changed less than 13% during the cooling cycle, which means the proposed PCS could provide stable cooling capacity for 4.5 hours. It is vital to notice that comparing with applying in other PCS, such as passive cooling storage in textiles (Kang et al., 2018), using PCM in VCC can provide a stable cooling capacity.

The reverse cycle-based recharge cycle began at 4.5 hours. From Figure 4-3, it shows that the pressures of both PCMHX and MCHX decreased with recharge time.

The reasons could be explained as follows. In the recharge cycle, the PCMHX worked as an evaporator, and the heat was released from the PCM to the refrigerant. During this process, the PCM is solidified while its temperature was decreased. Therefore, the evaporator pressure was decreased. This resulted in a density decrease at the compressor inlet, and a decreased mass flow rate as well (see Figure 4-5). Thus, both MCHX and PCMHX capacities reduced. As the TXV operated properly to maintain a degree of superheating, the condenser pressure in MCHX decreased as well.

From Figure 4-4, it can be seen that the bottom PCM temperature was lower than those at the top and middle sections. During the cooling cycle, the bottom PCM was still in the phase-changing progress while the top and middle PCM completely melted to the liquid phase. This is because the refrigerant flowed downwards from the top header to the bottom in the PCM condenser. After releasing heat to the PCM while flowing down, the refrigerant became a subcooled liquid in the bottom section. Since the heat transfer coefficient of single-phase refrigerant is much lower than that of the two-phase, the heat transfer at the bottom layer was much less than the middle layer, leading to a slower PCM melting rate at the bottom layer. Moreover, during the recharge cycle, the middle layer PCM solidified faster than that at the top layer. The reason could be that the heat transfer rate in the middle layer was higher than the top. Since the refrigerant flowed upwards in the PCM evaporator during the recharge cycle, the refrigerant at the top layer was in the superheated vapor phase, and therefore, the heat transfer coefficient of the middle layer was higher than that of the top layer. As for the bottom layer PCM, since it did not melt to liquid completely during the cooling cycle, its temperature was reduced much faster than the other layers.

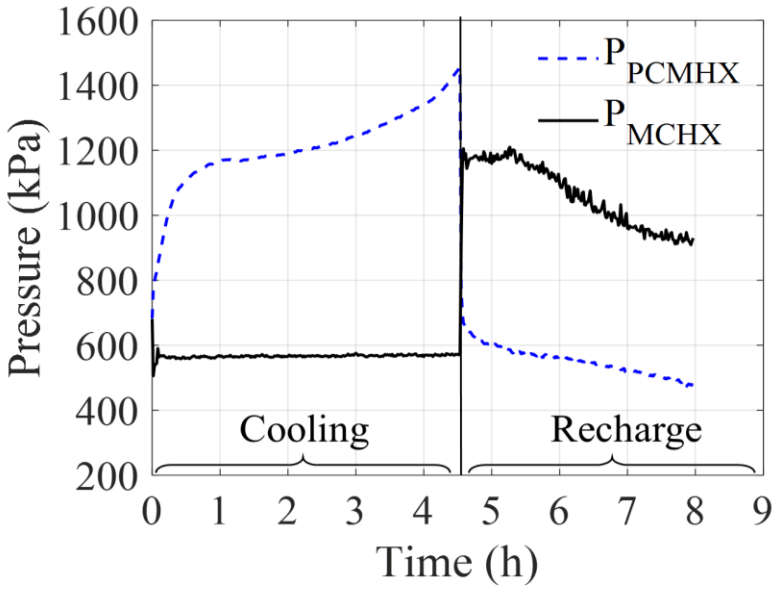


**Figure 4-3. Operating pressures of PCMHX and MCHX during dual cycles.**

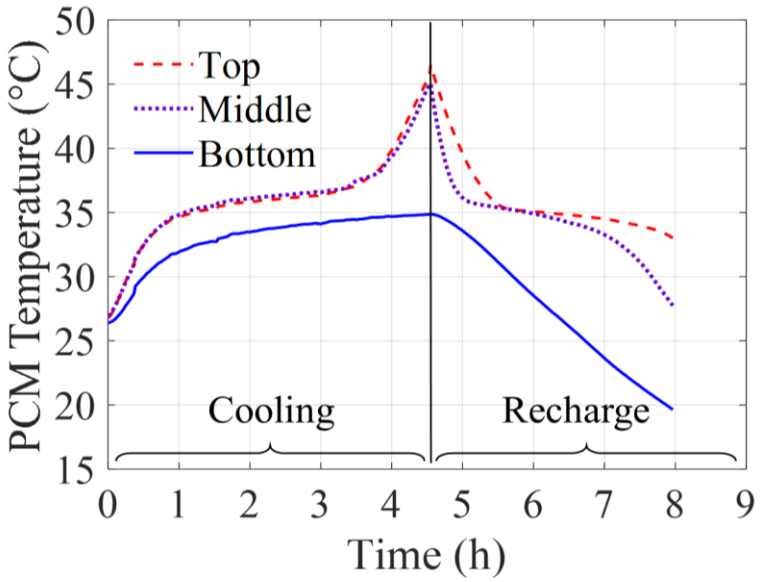


**Figure 4-4. PCM temperatures at the top, middle and bottom layers in PCMHX during dual cycles.**

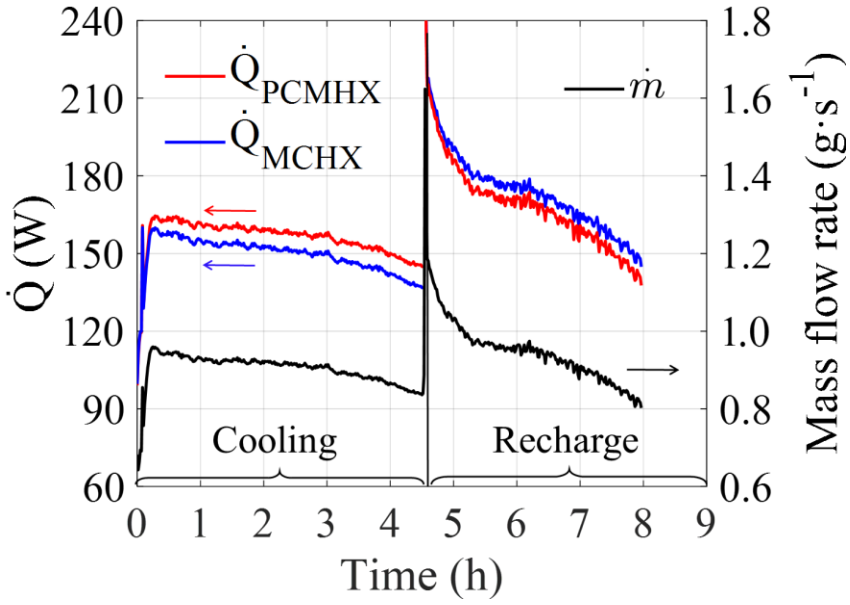


**Figure 4-5. PCMHX capacity, MCHX capacity and mass flow rate during dual cycles.**

It should be noted that this uneven PCM melting in the vertical direction implies the uneven utilization of PCM latent heat. If the bottom PCM could keep the same temperature as the top and middle, the averaged PCM temperature and PCS condenser pressure can be lower than that in the current design.

### 4.3.2 Effect of Thermostat Set Point on the Cooling Cycle

The proposed PCS can be used in an inadequately conditioned building. Therefore, I evaluated the effect of the thermostat setting, which is surrounding temperature to PCS, on the PCS performance. In this experimental study, the PCS surrounding temperature was varied at 26 °C, 28.5 °C and 31 °C. Before testing, I placed the PCMHX at surrounding for more than 48 hours so that its initial temperature was the same as the surrounding temperature. Since the heat loss from PCM container to the

surroundings is only 6% of the condenser capacity, the effect of the surrounding temperature on the system performance is mainly due to the change of the evaporating conditions and the PCM initial temperatures.

According to the authors' knowledge, there are two aspects of potential methods to achieve more uniform PCM melting. The first method is to decrease the subcooled refrigerant length in the PCMHX by decreasing the refrigerant charge and installing a heat exchanger after the PCM condenser to maintain a certain refrigerant subcooling degree before the expansion valve. Therefore, the PCM melting rate could be more uniform in the PCMHX. The second way is to optimize the PCMHX design configuration. For example, applying U-shape tube configuration could make the refrigerant outlet at the same side with the inlet, and therefore, the PCM that melts slower near the outlet could be heated by the PCM that melts faster near the inlet. More complicated PCM tube configuration can be proposed for better PCMHX design to achieve more uniform PCM melting and utilize more PCM latent heat. Although current study mainly focuses on the system performance analysis, I would like to point out that the PCMHX could be optimized further by taking advantage of all the latent heat and thus improve system performance.

Figure 4-6 shows the system pressures in each surrounding temperature tested. It shows that higher surrounding temperature leads to both higher condenser and evaporator pressures. However, at the beginning (first 0.5 hours) and the end of cooling cycles (after 3 hours from the start), condenser pressure differences among different surrounding temperatures were more significant than during the main cooling period. This is due to when the surrounding temperature becomes higher, the opening of TXV

becomes wider to maintain the superheat, which results in higher evaporating pressure. It can result in a higher refrigerant density at the compressor inlet, leading to a higher mass flow rate (see Figure 4-7) and PCMHX capacity (see Figure 4-8). The greater PCMHX capacity can cause faster PCM melt and higher PCM temperature, especially when the PCM starts to absorb heat in terms of sensible heat during the beginning of the cooling cycle and at the end of the cooling cycle. Thus, the higher surrounding temperature can result in higher condenser pressure in PCMHX obviously at the cycle beginning and end. However, during the period from the first 0.5 hours to 3 hours, the PCM starts to melt and becomes in two-phase. Although PCMHX capacities of three cases were different, PCM temperatures were similar, and thus condenser pressure differences were less than the cycle beginning and end.

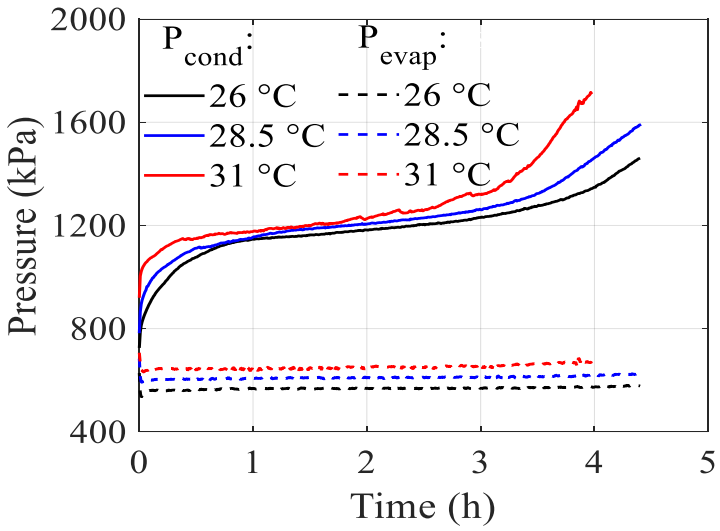


**Figure 4-6. Condenser pressures in PCMHX and evaporator pressures in MCHX during cooling cycles with different surrounding temperatures.**

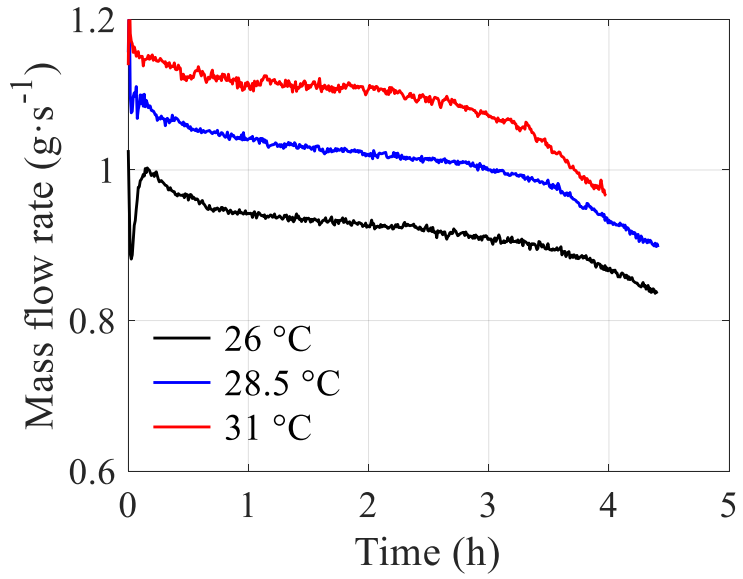


**Figure 4-7. Refrigerant mass flow rates of the system during cooling cycles with different ambient temperatures.**

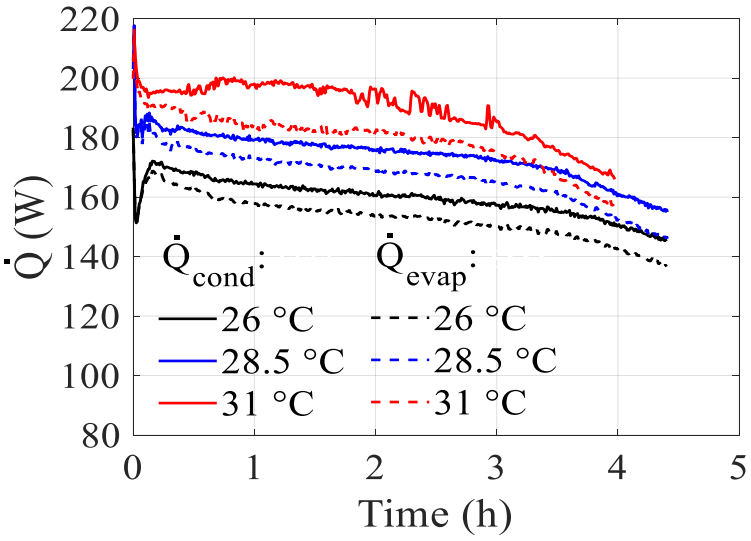


**Figure 4-8. Evaporator and condenser capacities during cooling cycles with different ambient temperatures.**

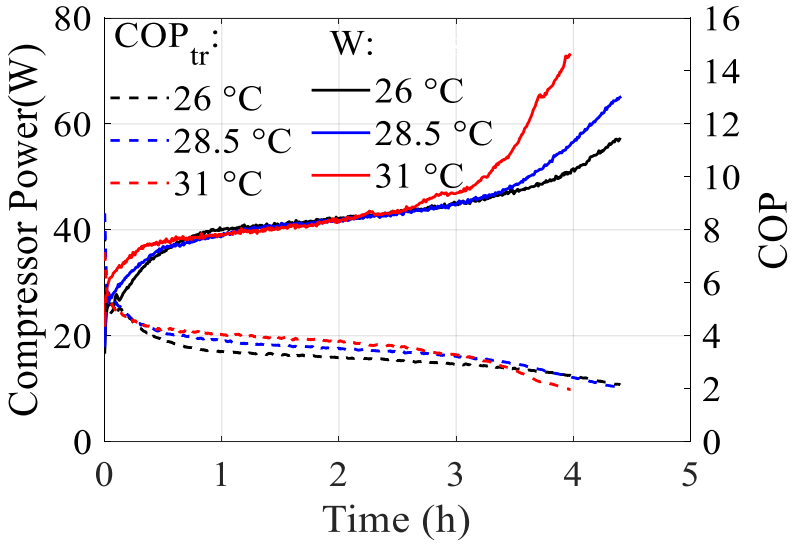


**Figure 4-9. Compressor power consumptions and system COP during cooling cycles with different surrounding temperatures.**

Figure 4-9 illustrates the compressor power under each surrounding condition. During the periods before 0.5 hours and after 2.5 hours, the compressor power increased with the surrounding temperature. This is because although both condenser and evaporator pressures increased with surrounding temperature (see Figure 4-6), the increase of the condenser pressure was greater than the evaporator pressure. Moreover, between 0.5 hours to 2.5 hours, the compressor power consumption was almost the same between different surrounding temperatures, because the increase of the evaporator pressure was similar to that of the condenser pressure. It also shows the transient cooling system COP in the figure. All of them decreased with cooling time, due to the increased compressor power consumption and slightly decreased evaporator capacity. Before 0.4 hours, COP with different surrounding temperatures was very similar. It could be explained by the fact that the increase of the surrounding

temperature can lead to an increase in both compressor power and evaporator capacity to the same degree.

After 0.4 hours until 3 hours, COP of 31 °C and 28.5 °C was up to 19% and 12% higher than that of 26 °C, respectively. This is because of the higher evaporator capacity and the similar power consumption under the higher surrounding temperature as discussed before. However, as time increased, for the system under higher surrounding temperature, the higher power consumption and the decreasing evaporator capacity can lead to a decrease of the COP. Thus, ultimately, the transient system COP of 31 °C became lower than that of 28.5 °C at 3.2 hours, and that of 26 °C was the highest after 3.8 hours.

In summary, the benefit of using this PCS in a room with a higher-thermostat-setting is evident in higher cooling capacity and system COP, where people need a greater cooling load to maintain thermal comfort.

### 4.3.3 Effect of Regeneration Rate

The PCS should have a faster recharge speed and higher overall COP. However, in most cases, these two aims are conflicting. Therefore, the experimental study to investigate the effects of the recharge rate on the overall COP was carried out. To achieve this comparison, I tried to achieve the same initial conditions for the regeneration cycle by running cooling cycles in advance with the same operating conditions and the same system performance, such as terminal condenser pressure, PCM temperatures and total accumulated heat stored in PCM. The cooling time was about 4.5 hours. The surrounding temperature was set to be 26°C always. After the

cooling cycles, recharge cycles were investigated experimentally with compressor speeds of 2,100 rpm, 2,600 rpm, and 3,100 rpm. Higher compressor speed can lead to greater mass flow rate and heat exchanger capacity, and thus a higher regeneration rate.

As illustrated in Figure 4-10 (a), system pressure curves of three tests approximately overlapped. Terminal condenser pressures were the same, and differences between the three cooling times were less than 2%. Figure 4-10 (b) shows the thermal energy stored in PCM, and it shows almost the same, within the difference of 0.6%. Thus, it is concluded that the recharge performance comparisons were based on the same initial conditions.

Figure 4-11 shows the accumulated heat remaining in PCM during the recharge process with different compressor speeds, as calculated by eq. (4-4). The recharge cycle was finished when the accumulated heat was released thoroughly. The required recharge time ($t_r - t_c$) was 3.44 hours, 2.90 hours and 2.43 hours for compressor speeds of 2,100 rpm, 2,600 rpm, and 3,100 rpm, respectively. Compared with the speed of 3,100 rpm, more than 19% and 41% recharge time was needed for 2,600 rpm and 2,100 rpm, respectively, due to the lower refrigerant mass flow rate and less PCMHX evaporator capacity.

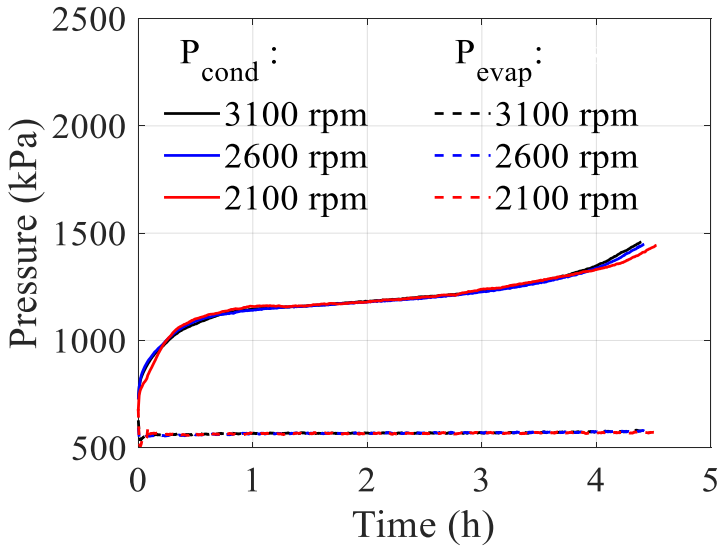


(a) Operating pressures

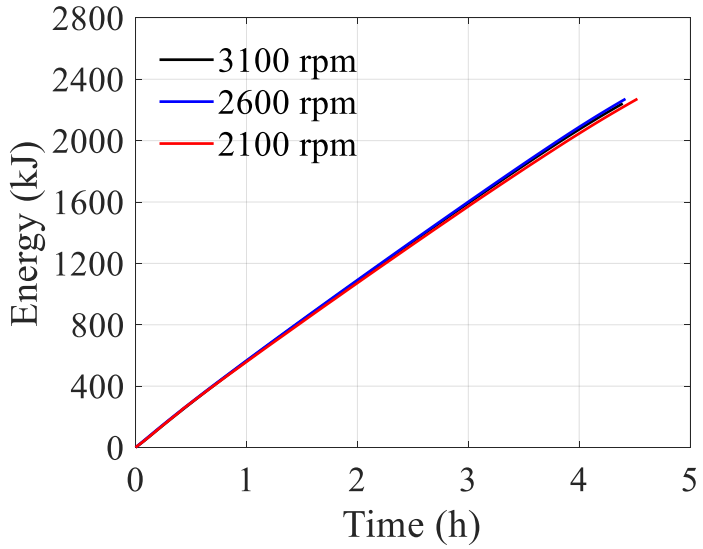


(b) Accumulated heat stored in PCM

**Figure 4-10. Operating pressures and accumulated heat stored in PCM during cooling cycles.**

Figure 4-12 shows the averaged COP of cooling, recharge, and overall dual system, represented by $COP_c$, $COP_r$, and $COP_{overall}$, respectively. $COP_c$ of different recharge-cycle compressor speeds were almost the same, within the difference of 1.1%,

based on a similar cooling cycle. It is noted that $COP_r$ increased with the decrease of the compressor speed as expected. This is because a lower refrigerant flow rate led to a less pressure difference between the compressor inlet and outlet, and thus higher $COP_r$. However, $COP_{overall}$ were close between three recharge rates. By increasing compressor speed from 2,100 rpm to 3,100 rpm, the required recharge time was decreased by 30%, while the overall dual-system COP was reduced by 8%. This is because more recharge time was required for the recharge cycle with lower compressor speed, resulting in higher energy consumption of the fan. Thus, the advantage of higher COP with lower compressor speed was offset by longer recharge time. Therefore, in this study, the optimal recharge-cycle compressor speed was 3,100 rpm, in terms of noticeably recharge-cycle time reduction yet slightly decreased COP.

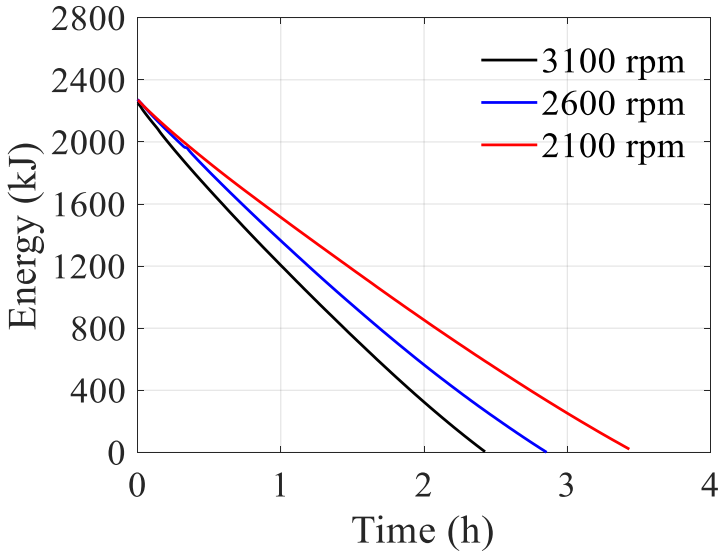


**Figure 4-11. Energy stored in PCM with different compressor speeds during recharge cycles.**

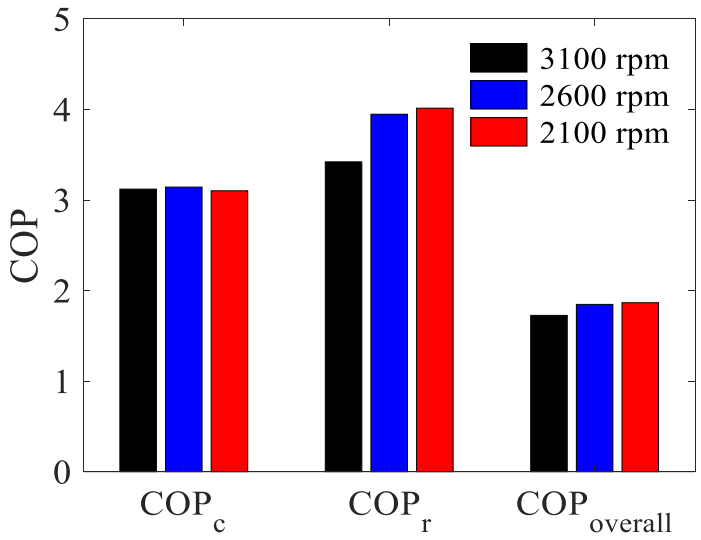


**Figure 4-12. Averaged cooling COP ($COP_c$), recharge COP ($COP_r$) and overall dual-system COP ($COP_{overall}$) with different recharge-cycle compressor speeds.**

4.3.4 Effect of Cooling Time

In this section, four cycles with different cooling times were performed and compared to discuss the effect of the cooling time on the average system performance, and the PCM initial states and system operating conditions, such as surrounding temperature, were the same. Also, the respective recharge cycle was accompanied after each cooling cycle. The normalized values were applied in this comparison to emphasize the difference. The cooling time of 6.5 hours was used as the baseline to obtain the normalized values.

Transient COP at the end of the cooling cycle ($COP_{tr}$) is illustrated in Figure 4-13. As the discussion of Figure 4-9, it decreased obviously with the cooling time because of the increase of PCM temperature. Besides, the averaged COP of the cooling system ($COP_c$) and that of the recharge system ($COP_r$) are presented. $COP_c$ decreased with the increased cooling time, since longer cooling time can lead to higher PCM terminal

temperatures and lower transient COP, and as a result, decrease the averaged cooling cycle COP. However, it is noted that $COP_r$ increased with cooling time and then decreased.

The reason could be explained as follows. When the cooling time was too short, PCM was still solid with a relatively lower terminal temperature. At the recharge cycle beginning, this lower PCM temperature can result in a lower evaporator temperature in PCMHX. Thus, less cooling time can result in a lower averaged recharge cycle COP. When the cooling time was in an appropriate range, after switching to the recharge system, evaporator temperature could be higher leading to better system performance. If the cooling time was too long, the recharge cycle could have higher evaporator temperature and higher COP at the beginning, however, the PCM temperature distribution was more non-uniform, as illustrated in Figure 4-4. The top PCM temperature was higher than the bottom. As the recharge process is progressed, this uneven PCM temperature could reduce the evaporator temperature, especially at the end of the recharge cycle. In other words, for too long recharge time, the faster COP degradation near the cycle end could offset the higher COP at the recharge cycle beginning, therefore leading to the decreased averaged recharge cycle COP.

Figure 4-14 illustrates the overall system COP ($COP_{overall}$), which decreased with the increase of cooling time. When the normalized cooling time was in a range of 0.4 to 0.7, COP did not change obviously. From this study, to achieve appropriate cooling time and energy savings, the normalized cooling time is suggested less than 0.7.

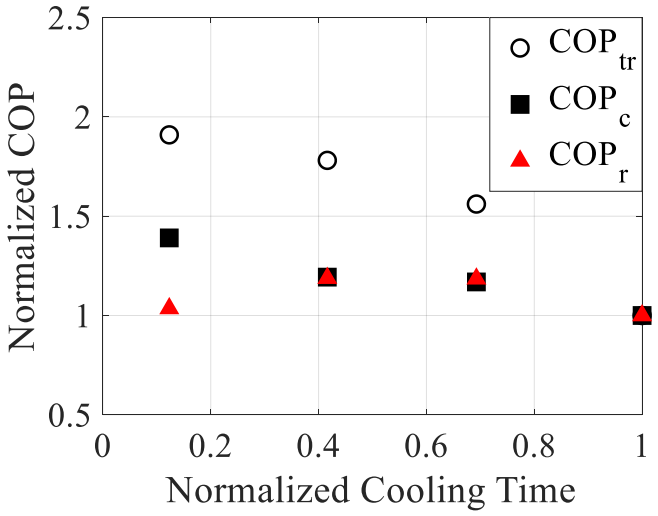


**Figure 4-13: Normalized transient COP at the end of the cooling operation ($COP_{tr}$), averaged cooling COP ($COP_c$) and recharge COP ($COP_r$) with different cooling time.**

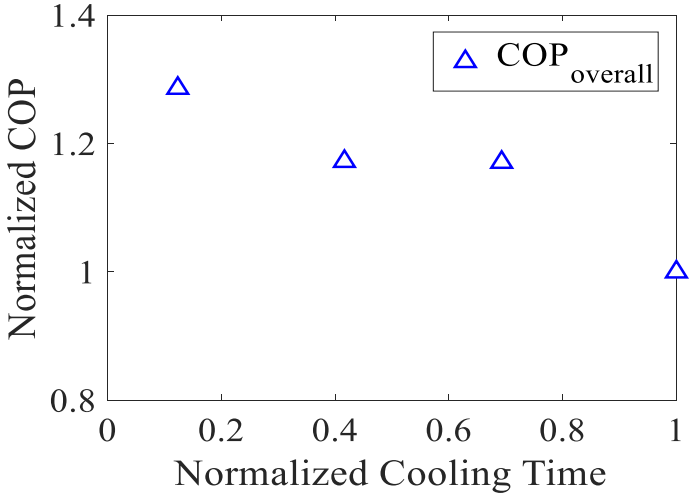


**Figure 4-14: Normalized overall dual-system COP ($COP_{overall}$) with different cooling time.**

Considering the PCS application, the cooling time could be different depending on the required cooling load and occupants' needs. Therefore, the PCM could be partially discharged or even not undergo a phase change in the cooling cycle. Regarding the

impact of cooling operation time, this experiment drew a direct link between required cooling time and average system performance, although this relationship was also determined by PCMHX design. Moreover, further detailed control strategy could be added in the present PCS to obtain better system performance, for instance, using PCM temperature as the criteria to switch between the cooling and recharge cycle.

### *4.4 Chapter Summary and Conclusions*

This Chapter proposes the PCS integrated with the graphite enhanced PCM for active thermal storage. PCMHX works as a condenser in the cooling cycle, while as an evaporator in the recharge cycle. The system performance, such as COP, compressor power consumption, evaporator capacity, condenser capacity, and PCM temperature profiles, were measured for both cooling and recharge cycles. Moreover, the effects of the thermostat setting, recharge rate and cooling time were experimentally investigated.

In the cooling cycle, the evaporator capacity was decreased by less than 13%, showing that the proposed PCS could provide a stable cooling to occupants. Results indicate that the PCS can provide a cooling capacity of 160 W for 4.5 hours. The PCM regeneration rate is much greater than the PCM melting rate, and the recharge capacity decreases with time.

The higher surrounding temperature can lead to higher cooling capacity and a higher COP, which meets the human's requirements under higher surrounding temperature. With the surrounding temperature of 31°C, the cooling cycle COP increased up to 19%, showing that the PCS could provide the cooling needed efficiently under the high surrounding temperature. On the other hand, the condenser pressure

increased with a higher rate after 3.5 hours, resulting in a faster performance degradation near the end of the cooling cycle. Additionally, the higher compressor speed of 3,100 rpm was recommended, due to the 30% reduced recharge time and 8% decreased overall dual-system COP than the 2,100-rpm case. The cooling time should be set less to than 5 hours to prevent too much reduction in COP.

In summary, the proposed PCS can provide the following benefits: the steady personal cooling, the broad applicability of surrounding conditions, and fast recharge rate. From the PCMHX point of view, this study fills the gaps in the integration of PCM directly with VCC as the only PCM-to-refrigerant condenser rather than the heat exchanger supplementary. Further research will focus on PCMHX optimization to achieve a more uniform PCM melting and a better system performance.

# Chapter 5: Simulation of PCM-to-refrigerant HX in Systems

In this Chapter, PCM-to-refrigerant HX and the coupled PCS were simulated and discussed. The PCS is the same as the system described in Chapter 3 Section 3.1, which used VCC for cooling and thermosiphon for PCM regeneration. In this Chapter, a model of PCM-to-refrigerant HX was developed using Dymola® platform, and models for the compressor, TXV, evaporator and pipes were also carried out in the same platform. Simulation results are validated against the experiment data, including refrigerant and PCM temperature profiles, capacity, and system-level performance. In addition, this Chapter also presents and analyzes the evolutions of the uneven PCM melting in the refrigerant flow direction and its effects on the condensing temperature.

The schematic diagram and experimental test setup are illustrated in Figure 3-1. The PCMHX was designed with multiple parallel tubes with the refrigerant flowing inside tubes and PCM filled in the annular space between PCM container and tubes as illustrated in Figure 3-3(e) and Figure 5-1(a).

## *5.1 PCM-to-Refrigerant HX Model*

A segment-by-segment condenser model was developed for the PCM-to-refrigerant HX. Assumptions of the PCMHX model used were: (1) radiation heat transfer to the surrounding was neglected; (2) the specific heat of PCM was chosen as the average value of the specific heat of liquid and solid phases; (3) refrigerant flows to eight tubes are uniform, and a unit of a single tube and PCM cylinder can represent the other tube units heat transfer performance of original design (Fleming et al., 2013).

Figure 5-1(b) is the single tube unit. To keep the same mass of PCM per tube, the cross-section of the single-tube unit was 1/8 of the original cross-section area. To maintain the same heat transfer area per tube, the tube length of the single unit (L) was the same as the original design.

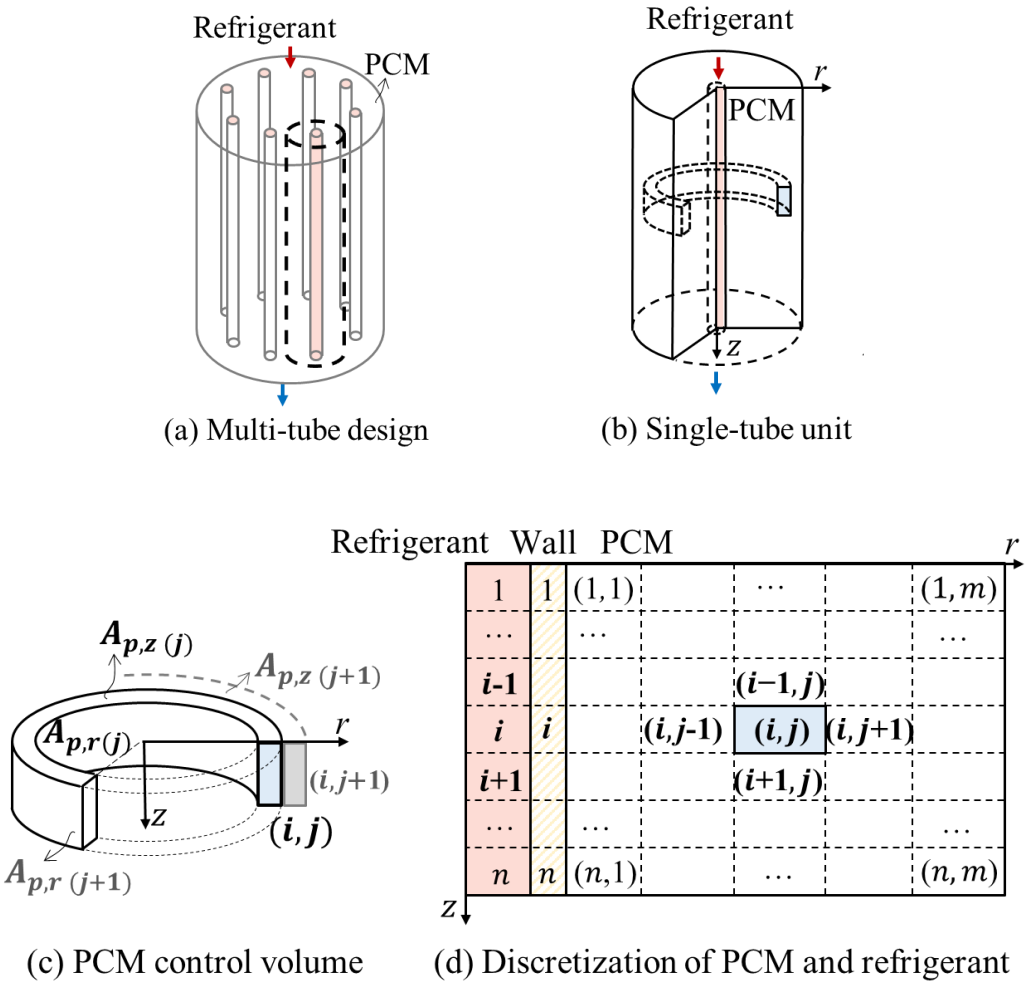


**Figure 5-1. Development of the PCM-to-refrigerant HX discretization.**

### 5.1.1 PCM-side Modeling

Under the cylindrical coordinate system, there is a symmetric heat transfer to PCM in angular direction with respect to the longitudinal axis (see Figure 5-1 (b)). Therefore,

a transient 2-D numerical model was used to simulate the heat transfer and PCM melting process in the PCM condenser. The enthalpy method was adopted for the 2-D PCM modeling. The energy equation is given by Eq. (5-1). $T_p$ and $h_p$ are PCM temperature and enthalpy, respectively. $h_p$ is a function of PCM temperature. $k_{p,r}$ and $k_{p,z}$ are PCM effective thermal conductivity in the radial direction and axial direction, respectively. PCM enthalpy and effective thermal conductivity are two crucial parameters that need to be determined to solve this energy equation.

$$\rho_p \frac{\partial h_p}{\partial t} = k_{p,r} \frac{1}{r} \frac{\partial}{\partial r}\left(r \frac{\partial T_p}{\partial r}\right) + k_{p,z} \frac{\partial^2 T_p}{\partial z^2} \tag{5-1}$$

PCM enthalpy curve with a function of temperature is proposed as Eq. (5-2), in which the first term presents the latent heat of PCM. $C_{p,s}$ and $C_{p,l}$ are the specific heat for solid and liquid PCM, respectively. $T_{ini}$ is the initial PCM temperature. $T_m$ is the melting point of 37°C.

$$h(T_p) = L_p \left(\frac{1.3\ atan(T_p - T_m)}{\pi} + 0.5\right) + (T - T_{ini}) \frac{C_{p,l} + C_{p,s}}{2} \tag{5-2}$$

PCM liquid fraction is given to evaluate the PCM melting process by Eq. (5-3). $T_s$ and $T_l$ are PCM temperatures at the beginning and the end of the phase change process, respectively.

$$\lambda(T_p) = \begin{cases} 0 & h \le h_s \\ \dfrac{T_p - T_s}{T_l - T_s} & h(T_s) < h < h(T_l) \\ 1 & h \ge h_l \end{cases} \quad (5\text{-}3)$$

The PCM effective thermal conductivity of radial direction, $k_{p,r}$, and that of the axial direction, $k_{p,z}$ are significant parameters to address this numerical problem as in Eq. (5-4) and (5-5). $k_{p,r}$ and $k_{p,z}$ are different due to the manufacturing process of PCM/CENG composite (Merlin et al., 2016). During the manufacture process, the thermal conductivity of the CENG matrix in the compression force direction is less than in the direction perpendicular to compression force. In this study, the axial direction is parallel to this compression force direction, and therefore, $k_{p,z} < k_{p,r}$. The correlations used for effective conductivities $k_{p,r}$ and $k_{p,z}$ are proposed by Py et al. (Py et al., 2001), as given in Eq. (5-4) and (5-5). The bulk density, $\rho_{CENG}$, is the mass of CENG matrix divided by the total volume of PCM/CENG composite.

$$k_{p,z} = 3.0 \left(\frac{\rho_{CENG}}{46}\right)^{\frac{2}{3}} \left[2 - \left(\frac{\rho_{CENG}}{46}\right)^{0.17}\right] \quad (5\text{-}4)$$

$$k_{p,r} = 3.0 \left(\frac{\rho_{CENG}}{46}\right)^{\frac{4}{3}+0.17} \quad (5\text{-}5)$$

Boundary conditions for PCM temperature are given in Eqs.(5-6) - (5-9). $R_i$ is the inner radius of the PCM cylinder, which is the same as the tube outer radius. $R_o$ and $L$ are the outer radius of the single-tube unit and the cylinder length, respectively. $A_i$ and

$A_{top}$ is the heat transfer area contacted tube walls and the top area of the PCM cylinder, respectively. $A_o$ is the equivalent outer heat transfer area for the single-tube unit to the surrounding. $A_o = A_o'/8$, in which $A_o'$ is the PCM container outer surface area of the original multi-tube design. $\alpha_1$, $\alpha_2$ and $\alpha_3$ are the natural convection heat transfer coefficients at the outer, top and bottom boundary, which were calculated by the correlation proposed by (Churchill and Chu, 1975). $T_a$ and $T_w$ are the surrounding and wall temperatures, respectively.

$$k_{p,r}\frac{\partial T_p(r,z,t)}{\partial r} = A_i\frac{2k_w}{\delta}\left(T_w(z,t) - T_p(r,z,t)\right) \quad r = R_i \tag{5-6}$$

$$k_{p,r}\frac{\partial T_p(r,z,t)}{\partial r} = \alpha_1 A_o\left(T_p(r,z,t) - T_a\right) \quad r = R_o \tag{5-7}$$

$$k_{p,z}\frac{\partial T_p(r,z,t)}{\partial r} = \alpha_2 A_{top}\left(T_p(r,z,t) - T_a\right) \quad z = 0 \tag{5-8}$$

$$k_{p,z}\frac{\partial T_p(r,z,t)}{\partial r} = \alpha_3 A_{top}\left(T_p(r,z,t) - T_a\right) \quad z = L \tag{5-9}$$

Initial conditions for PCM is shown in Eq. (5-10), in which $T_{ini}$ is initial PCM temperature and equal to the surrounding temperature.

$$T_p(r,z,t) = T_{ini} \ \ (t = 0) \tag{5-10}$$

A finite-volume method was adopted to solve the governing equations for PCM. As illustrated in Figure 5-1(c) and (d), uniform segments were applied for the

discretization along with axial and radial directions in the PCM domain. Each PCM control volume is an annular space designated by *i* and *j* in the axial and radial directions, respectively. The discretized energy equation for PCM heat transfer using the enthalpy method is given in Eq. (5-11). $A_{p,r}$ is the inner heat transfer area of the annular control volume, while $A_{p,z}$ is the upper heat transfer area of each control volume as indicated in Figure 5-1 (c). $A_{p,r}$ and $A_{p,z}$ of each control volume remain constant in the axial direction and only change in the radial direction.

$$\begin{aligned} m_{p_{(i,j)}} \frac{\partial h_{p_{(i,j)}}}{\partial t} = & \frac{k_{p,r}}{dr} A_{p,r_{(j)}} \left( T_{p_{(i,j-1)}} - T_{p_{(i,j)}} \right) \\ & - \frac{k_{p,r}}{dr} A_{p,r_{(j+1)}} \left( T_{p_{(i,j)}} - T_{p_{(i,j+1)}} \right) \\ & + \frac{k_{p,z}}{dz} A_{p,z_{(j)}} \left( T_{p_{(i-1,j)}} - T_{p_{(i,j)}} \right) \\ & - \frac{k_{p,z}}{dz} A_{p,z_{(j)}} \left( T_{p_{(i,j)}} - T_{p_{(i+1,j)}} \right) \end{aligned} \tag{5-11}$$

### 5.1.2 Refrigerant-side Modeling

The refrigerant flow was one-dimensional, and the conductive heat transfer was neglected. The energy equation and continuity equation of the refrigerant flow are given in Eqs. (5-12) and (5-13), respectively. Pressure (*P*) and specific enthalpy (*h*) were selected as state variables (Laughman and Qiao, 2017; Qiao et al., 2015). Refrigerant properties including density, $\rho$, the partial derivative of density with respect to enthalpy, $(d\rho/dh)|_p$, and that with respect to pressure, $(d\rho/dP)|_h$, were

obtained by refrigerant property functions as proposed in (Aute and Radermacher, 2014).

$$\frac{dU}{dt} = V\left[\left(h\frac{d\rho}{dP}\Big|_h - 1\right)\frac{dP}{dt} + \left(h\frac{d\rho}{dh}\Big|_p + \rho\right)\frac{dh}{dt}\right] \tag{5-12}$$

$$\frac{dm}{dt} = V\left(\frac{d\rho}{dP}\Big|_h \frac{dP}{dt} + \frac{d\rho}{dh}\Big|_p \frac{dh}{dt}\right) \tag{5-13}$$

As shown in Figure 5-1 (d), spatial discretization along the axial direction was adopted for the refrigerant flow as well. The discretized energy equation and the continuity equation for refrigerant are given in Eqs. (5-14) and (5-15), respectively. $\alpha_{ref}$ is the convective heat transfer coefficient. For single-phase flow, $\alpha_{ref}$ is calculated from correlations proposed by Gnielinski (2013). For two-phase flow, $\alpha_{ref}$ calculation was based on the correlation by Shah (2009).

$$V_{(i)}\left(\frac{d\rho}{dP}\Big|_{h_{(i)}} \frac{dP}{dt}_{(i)} + \frac{d\rho}{dh}\Big|_{p_{(i)}} \frac{dh}{dt}_{(i)}\right) = \dot{m}_{(i)} - \dot{m}_{(i+1)} \tag{5-14}$$

$$\begin{aligned} V_{(i)}\left[\left(h_{(i)}\ \frac{d\rho}{dP}\Big|_{h_{(i)}} - 1\right)\frac{dP}{dt}_{(i)} + \left(h_{(i)}\frac{d\rho}{dh}\Big|_{p_{(i)}} + \rho_{(i)}\right)\frac{dh}{dt}_{(i)}\right] \\ = \dot{m}_{(i)}h_{(i)} - \dot{m}_{(i+1)}h_{(i+1)} + \alpha_{ref\,(i)}\,A_{p,r(1)}(T_{ref_{(i)}} - T_{w(i)}) \end{aligned} \tag{5-15}$$

### 5.1.3 Tube Wall Model

The discretized one-dimensional energy equation for the tube wall is given in Eq. (5-16), in which, $M_w$, $C_{p,w}$, $k_w$ and $\delta$ are the mass, specific heat, thermal conductivity and thickness of the copper tube wall, respectively. $A_{p,r}$ (1) is PCM inner heat transfer area, as well as the copper tube outer heat transfer area.

$$M_{w(i)} C_{p,w(i)} \left(\frac{dT_w}{dt}\right)_{(i)} = \alpha_{ref(i)} A_{p,r(1)} (T_{ref(i)} - T_{w(i)}) - A_i \frac{2k_w}{\delta} (T_{w(i)} - T_{p(i,1)}) \tag{5-16}$$

## *5.2 Other Component Models*

Different from most of the previous studies on PCM-to-water heat exchangers with the constant inlet water temperature, in this Chapter, PCM-to-refrigerant heat exchanger is not insulated from the system, and the refrigerant flowing inside PCM tubes is the condensing refrigerant. PCM melting process can affect PCM-to-refrigerant heat transfer as well as the system performance, such as the refrigerant condensing temperature. This variation can also be reflected by Eq. (5-6), showing that the PCM boundary condition at $R_i$ is neither the constant heat flux nor the constant wall temperature. Therefore, to simulate the PCM condenser performance, the refrigeration system should be modeled. Component models include the evaporator, expansion valve, compressor, receiver, and pipes are developed in this section.

### 5.2.1 Evaporator Model

A fin-and-tube heat exchanger was selected as the evaporator design with the specification as illustrated in

Table 5-1. Discretized governing equations of refrigerant in evaporator are the same as those in the PCM condenser, as described in Eqs. (5-14) and (5-15). The heat transfer coefficient of refrigerant, $\alpha_{ref}$, was calculated using correlations propose by (Jung and Radermacher, 1989) for two-phase flow and by (Gnielinski, 2013) for single-phase flow. For tube wall and fins, the energy equation is given by Eq. (5-17).

$$\left(M_w C_{p,w} + M_{fin} C_{p,fin}\right)\frac{dT_w}{dt} = \alpha_{HTF} A_{ref}\left(T_w - T_{ref}\right) + \dot{m}_a C_{p,a}\left(T_{a,in} - T_{a,out}\right) + \dot{m}_a H_a(\omega_{a,in} - \omega_{a,out}) \quad (5\text{-}17)$$

In Eq. (5-17), the first term at the right-hand side is the heat transfer between tube walls and refrigerant, the second term means sensible heat released from air to tube walls, and the third term is the latent heat from the air. $\dot{m}_a$, $C_{p,a}$ and $H_a$ are air mass flow rate, air specific heat, and water vaporization heat, respectively. $T_{a,in}$ , $T_{a,out}$, $\omega_{a,in}$ and $\omega_{a,out}$ are air inlet temperature, outlet temperature, inlet humidity ratio and outlet humidity ratio, respectively. $T_{a,in}$ and $\omega_{a,in}$ are known. $T_{a,out}$ and $\omega_{a,out}$ can be solved by Eqs. (5-18) and (5-19), yielding air-side governing equations as described by (Qiao et al., 2015). $A_t$ and $A_{fin}$ are heat transfer area of tube-side and fin-side, respectively. Fin efficiency, $\eta_{fin}$ was calculated using the correlation proposed by Hong and Webb (1996). Airside heat transfer is enhanced by plate wavy-herringbone fins with a staggered tube layout. Thus, the air-side heat transfer coefficient, $\alpha_a$, was obtained

from the correlations proposed by Kim et al. (1997), in which *Le* is the Lewis number yielding $Le^{2/3}$=0.9 (Kuehn et al., 1998).

$$T_{a,out} = T_{a,in} + (T_w - T_{a,in})\left\{1 - exp\left[-\frac{\alpha_a\left(A_t + \eta_{fin}A_{fin}\right)}{\dot{m}_a C_{p,a}}\right]\right\} \quad (5\text{-}18)$$

$$\omega_{a,out} = \omega_{a,in} + \left\{1 - exp\left[-\frac{\alpha_a\left(A_t + \eta_{fin}A_{fin}\right)}{\dot{m}_a C_{p,a} Le^{2/3}}\right]\right\} min\left(0, \omega_{a,sat} - \omega_{a,in}\right) \quad (5\text{-}19)$$

**Table 5-1: Dimension of the evaporator**

| Parameter | Unit | Value |
|---|---|---|
| Number of tubes | -- | 12 |
| Number of circuits | -- | 1 |
| Number of tube banks | -- | 2 |
| Tube length | m | 0.13 |
| Tube ID | mm | 7.899 |
| Tube OD | mm | 9.525 |
| Fin type | -- | Wavy herringbone |
| Fin per inch | -- | 17.5 |

### 5.2.2 TXV Model

TXV was assumed to be adiabatic, and the expansion of the refrigerant was assumed to be isenthalpic. The refrigerant mass flow rate controlled by the TXV is given by Eq. (5-20), in which $C_v$ is the flow coefficient, $A_t$ is the flow area of the throttle, $\Delta p$ is the pressure drop across the valve.

$$\dot{m} = C_v A_t (\rho_{in} \Delta p)^{1/2} \tag{5-20}$$

The refrigerant flow area was controlled by a needle movement, which reflects the superheat degree at the evaporator outlet. The force balance on the diaphragm is given in Eq. (5-21). The sensor provides a force on the one side of the diaphragm, $P_b A_{dia}$, which is the same with the total forces on the other side supplied by evaporator pressure and the spring. $K_{sp}$, $y_{sp}$ and $F_{sp,ini}$ are the spring constant, deflection and the initial force, respectively. The function to obtain $P_b$ are presented by Qiao et al. (2015).

$$K_{sp} y_{sp} + F_{sp,ini} + P_{evap} A_{dia} = P_b A_{dia} \tag{5-21}$$

### 5.2.3 Compressor Model

The efficiency-based compressor model was applied in this study. Volumetric efficiency, $\eta_{vol}$, isentropic efficiency, $\eta_{isen}$, and motor efficiency, $\eta_m$, were used to calculate the compressor power consumption, $W_{comp}$, as given in Eqs. (5-22) to (5-24). $\dot{m}$ and $N$ are the mass flow rate and compressor speed, respectively. $\rho_{in}$ is the refrigerant density at the inlet of the compressor. The correlation of volumetric

efficiency, $\eta_{vol}$, with a function of suction pressure and discharge pressure is based on experimental results.

$$h_{out} = h_{in} + \frac{h_{out,s} - h_{in}}{\eta_{isen}} \tag{5-22}$$

$$\dot{m} = \frac{\eta_{vol}\rho_{in}V_{comp}N}{60} \tag{5-23}$$

$$W_{comp} = \dot{m}\frac{h_{out} - h_{in}}{\eta_m} \tag{5-24}$$

### 5.2.4 Receiver and Pipe Models

The receiver model and connecting pipe model are essentially the same as the evaporator model. The refrigerant-side governing equations can be solved by the discretized equations as in Eq. (5-14) and (5-15), and the energy equation of tube walls is given by Eq. (5-16). No fin efficiency is taken into consideration, and the air-side heat transfer is based on free convection.

## *5.3 Numerical Procedure*

Sensitivities to grid size and aspect ratio were investigated. The model was simulated under different grid sizes and aspect ratios as follows: 40x20, 30x10, 20x10, 10x5, and 5x5 as illustrated in Figure 5-2. The deviation of both pressure and capacity between grids 40x20 and 30x10 is less than 1.0%. Therefore, the grid of 30x10 was good enough to be adopted in the simulation.

The system model was developed in Dymola®, as illustrated in Figure 5-3. The algorithm of Lsodar was adopted, which is an implicit multi-step method. The backward differentiation formula was applied in the algorithm to solve differential equations. Time step size was determined on every step with a tolerance of 1e-6.

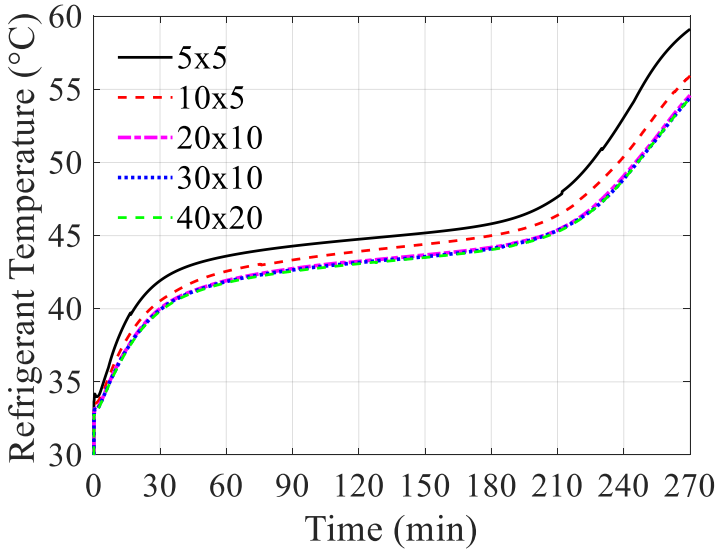


(a) Condenser pressure

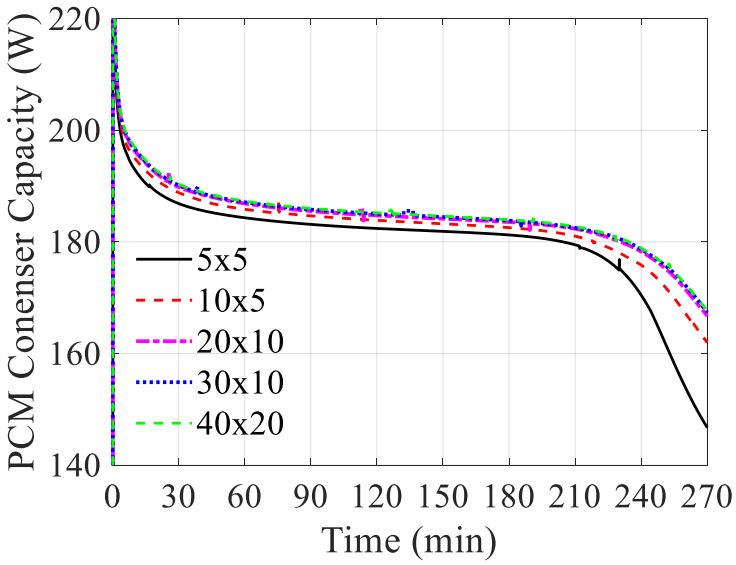


(b) PCM condenser capacity

**Figure 5-2: Grid independency of the numerical solution.**

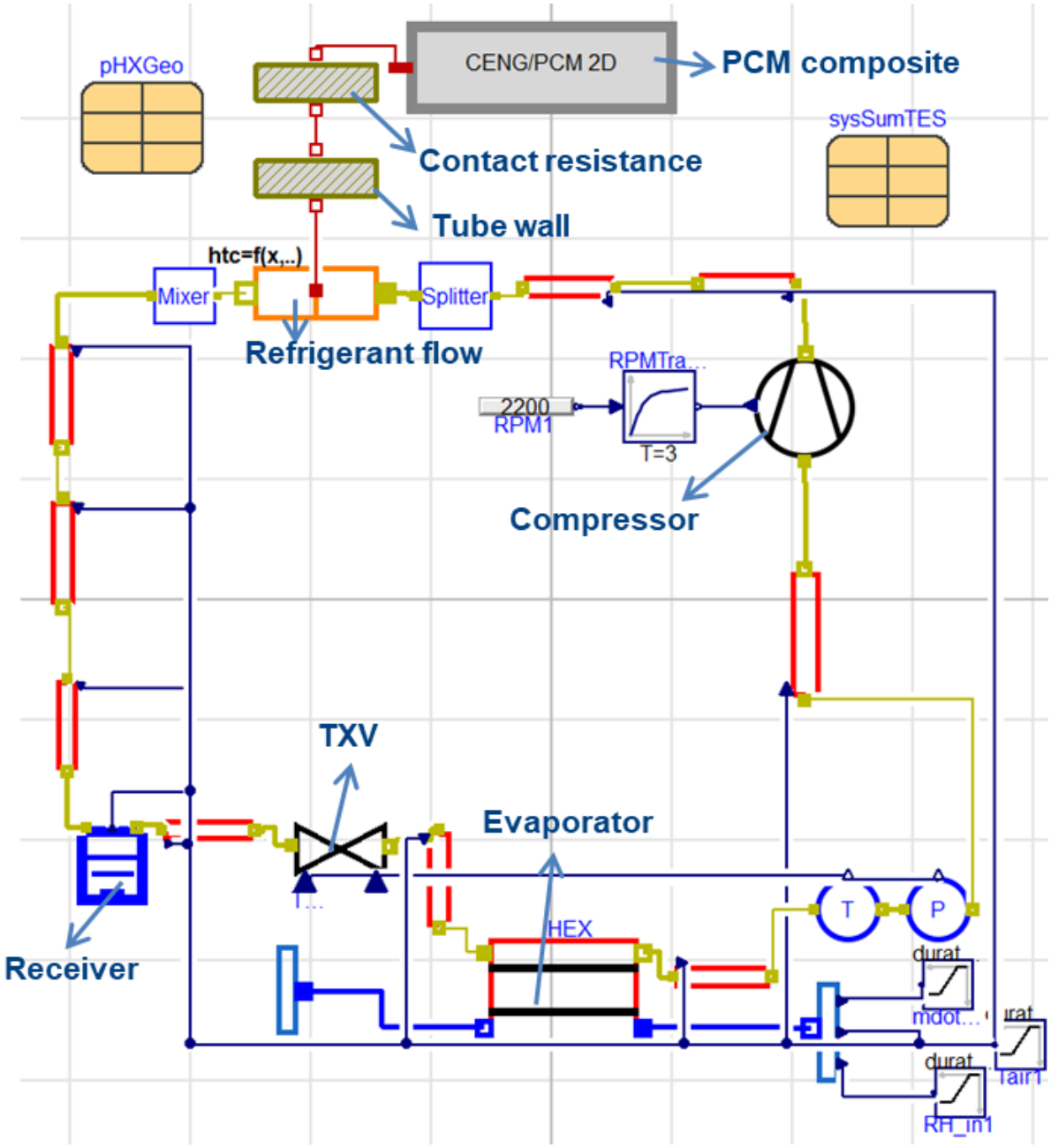


**Figure 5-3: Model diagram for PCMHX coupled system.**

## *5.4 Results and Discussion*

### 5.4.1 Comparison of Experiment and Simulation Results

Figure 5-4 (a)-(e) show the comparison of the experimental and simulation results on refrigerant condensing temperature, operating pressures, subcooling and superheat, mass flow rate and heat exchanger capacity, respectively. The deviations between experiments and simulation results were less than 7%. This good agreement illustrates that the numerical model is acceptable for simulation.

Since PCM-to-refrigerant works as the condenser, PCM absorbs the heat released from the refrigerant, and most PCM changes from solid to two-phase and then to the liquid. Figure 5-4 (a) shows the condensing temperature and PCM temperature increased during the PCM melting process. The top PCM became liquid, while the bottom PCM was still in the phase changing process. Moreover, Figure 5-4 (b) indicates that the evaporator pressure was nearly constant due to the steady evaporating condition, and Figure 5-4 (c) shows that TXV can maintain a constant degree of superheat at the evaporator outlet. As a result, the refrigerant condenser subcooling increased with the increase of the condensing temperature as illustrated by Figure 5-4 (c). The subcooling calculated location is after the condenser outlet. From Figure 5-4 (d), the decrease of the refrigerant mass flow rate before 30 minutes or after 210 minutes is due to the decrease of the compressor volumetric efficiency, which is because of the increase of the condenser pressure. In addition, Figure 5-4 (e) indicates PCM condenser capacity decreased slightly during the thermal storage process, which is due to the decrease of the mass flow rate and the increase of the condensing

temperature. In summary, the performance of PCM melting and the coupled system present three stages process:

(1) Stage I (from 0 to 30 minutes): Most PCM was in solid, and PCM absorbed heat by sensible heat transfer. Condensing temperature, condenser pressure and subcooling at the condenser outlet increased with time (Figure 5-4 (a), (b) and (c)). Mass flow rate and capacity decreased slightly within 10% (Figure 5-4 (d) and (e)).

(2) Stage II (from 30 to 210 minutes): Most PCM was in the two-phase, and PCM performed phase change in latent heat transfer. Condensing temperature, pressure and subcooling increased slightly (Figure 5-4 (a), (b) and (c)). Mass flow rate and capacity were constant (Figure 5-4 (d) and (e)). System performance was stable in Stage II.

(3) Stage III (from 210 to 270 minutes): A part of PCM melt completely to liquid phase, and absorbed heat by sensible heat transfer. The condensing temperature, pressure and subcooling increased significantly (Figure 5-4 (a), (b) and (c)). Mass flow rate and capacity decreased slightly (Figure 5-4 (d) and (e)).

In previous researches, PCM capacity decreases with time gradually, since the inlet HTF temperature is constant (Martinelli et al., 2016; Rahimi et al., 2019; Seddegh et al., 2017). However, in this study, the PCM-to-refrigerant HX capacity in Stage II was maintained at constant, which reflects the significant advantage of using PCM-to-refrigerant HX. More importantly, it implies that the change from Stage II to Stage III occurs when the top part of PCM melts completely. If the top PCM has the same melting rate as the bottom, Stage II can be extended to a longer period.

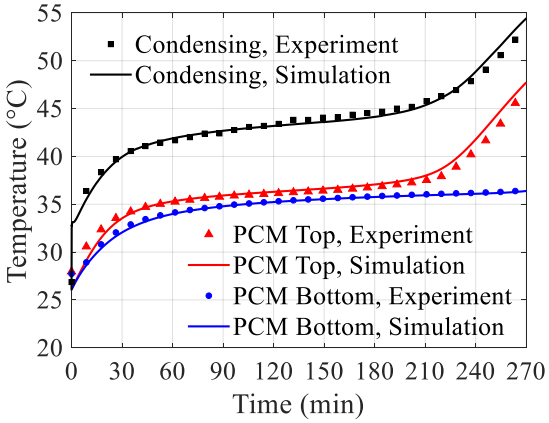


(a) Refrigerant and PCM temperatures

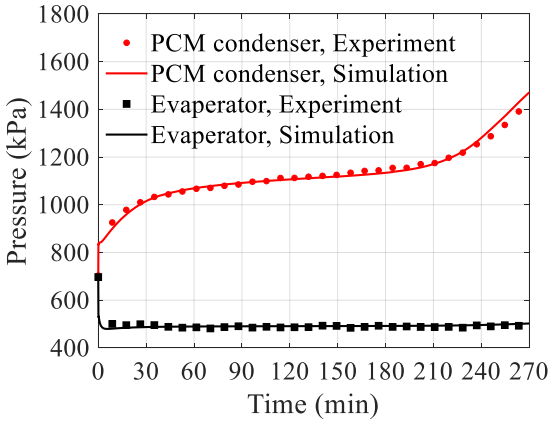


(b) Evaporating and condensing pressure

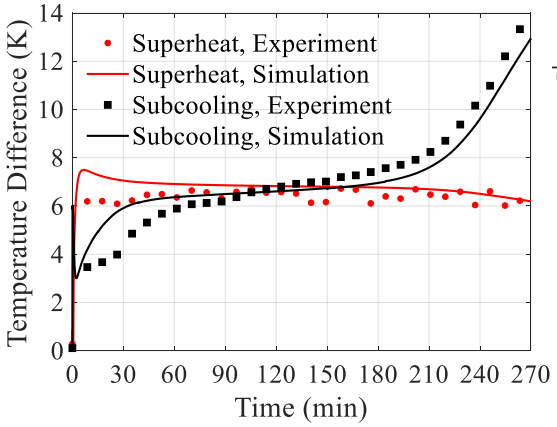


(c) Subcooling and superheat

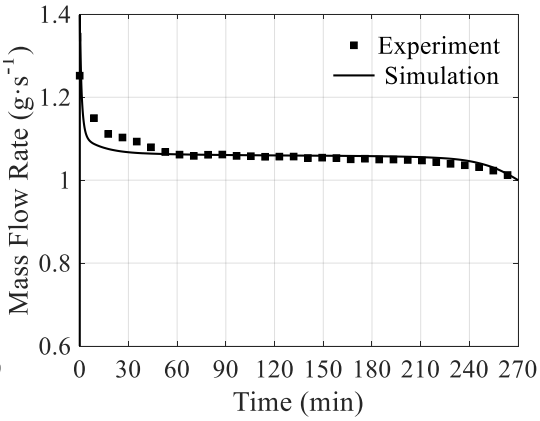


(d) Mass flow rate

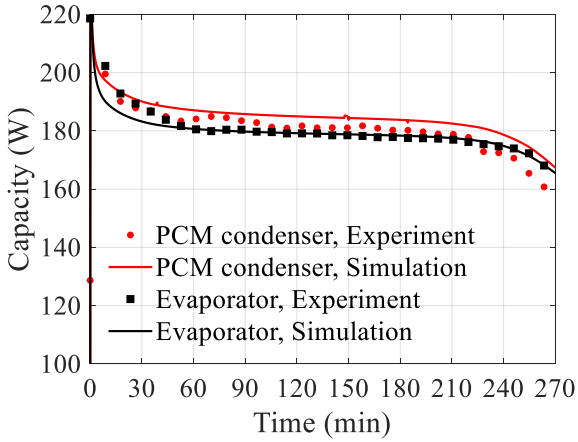


(e) Condenser and evaporator capacity

**Figure 5-4: Numerical results compared with experimental results.**

### 5.4.2 PCM Melting Characteristics

In addition to system-level performance, more detailed PCM melting performance is discussed in this section. Figure 5-5 shows the numerical solution of the PCM and refrigerant temperature profiles, and Figure 5-6 indicates the PCM liquid fraction in the single-tube unit during the charging process. The vertical direction means the condenser tube length direction, and the horizontal direction represents the radial direction. Refrigerant flowed downward from the top to the bottom. It can be found that the PCM temperature gradient in the radial direction was smaller than the axial direction, which is due to the great heat transfer enhancement provided by the CENG matrix.

However, at 210 minutes as illustrated in Figure 5-5 and Figure 5-6, although PCM temperatures in vertical direction were uniform, liquid fractions at the top 1/3 were higher than 0.9, while at the bottom 1/3 PCM liquid fractions were less than 0.4, meaning that the PCM melting rate decreased along the condenser tube length direction. This led to the increase of the condensing temperature in Stage III (Figure 5-4 (a)). In Stage III from 210 to 270 minutes, the bottom PCM temperature was lower than those at the top and middle sections, which can also be verified by Figure 5-4 (a). It can be concluded that the PCM melting along the condenser tube length direction is not uniform, and the utilization ratio of the PCM latent heat needs to be improved to make the Stage II longer.

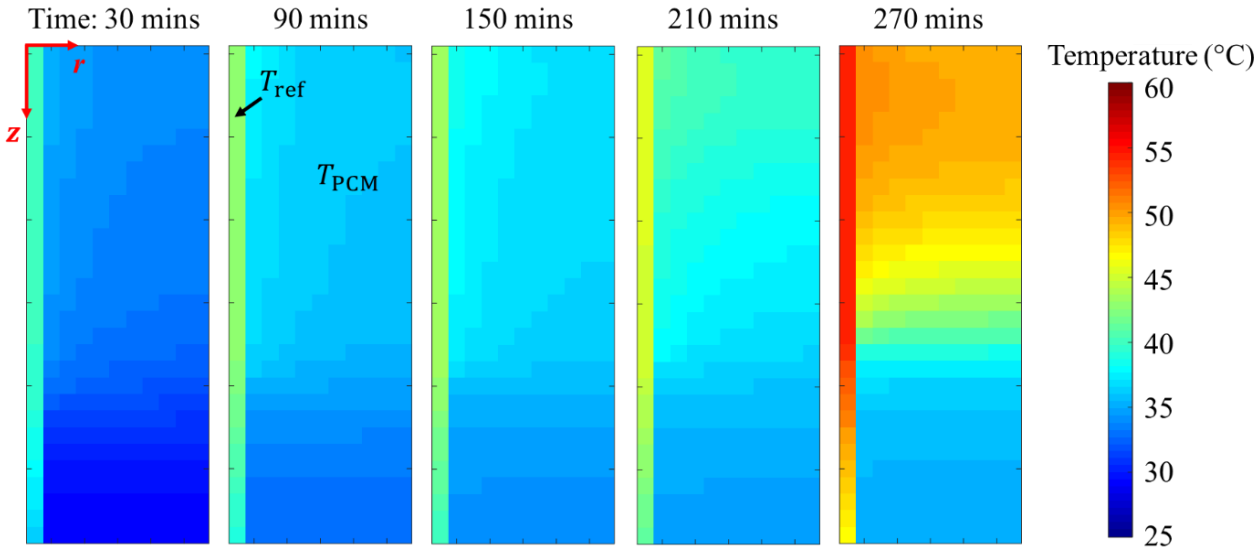


**Figure 5-5: PCM and refrigerant temperatures**

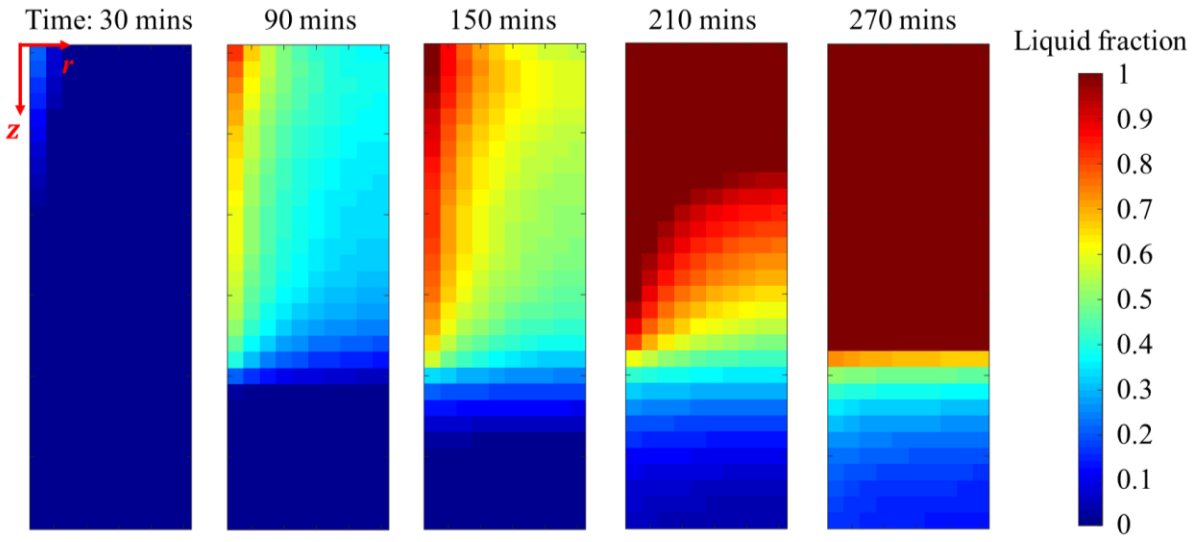


**Figure 5-6: PCM liquid fractions**

### 5.4.3 Effect of Compressor Speed

System simulation with different refrigerant flow rates is conducted. The compressor speed, N, is selected at of 2,300 rpm, 3,450 rpm, 4,600 rpm and 5,750 rpm

to generate different refrigerant mass flow rates, and the system refrigerant charge is the same for the system simulation.

As illustrated in Figure 5-7 (a), the accumulated heat stored in the PCM for the four cases increased with the time. The higher mass flow rate can lead to a greater slope ratio due to the increased PCMHX capacity. In addition, the condensing temperature rises due to the increased compressor speed, so that the approach temperature difference and the condenser capacity increase. In order to analyze the effect of compressor speed on the PCM melting and system performance, the comparison of four cases is based on the same heat storage of $3.4 \times 10^5$ J. The terminal time to accumulate this same amount of heat in PCM is 100, 110, 132 and 183 minutes, as shown by marks of "Δ" in Figure 5-7 (a). The normalized time, *Time**, is set as the ratio of real-time over the terminal time for each case. Therefore, *Time** is in a range of 0 to 1 in this comparison.

Figure 5-7 (b) illustrates the melting fraction at 1/3 from the top and bottom locations, showing that the melting fraction difference at these two locations for Case 1 (N=2,300 rpm) is smaller than the other three cases. This means the compressor speed can not only affect the condenser capacity, but also impact the PCM melting distribution. The slower compressor speed can lead to smaller PCMHX capacity, as well as the smaller condenser subcooling, leading to more uniform PCM melting.

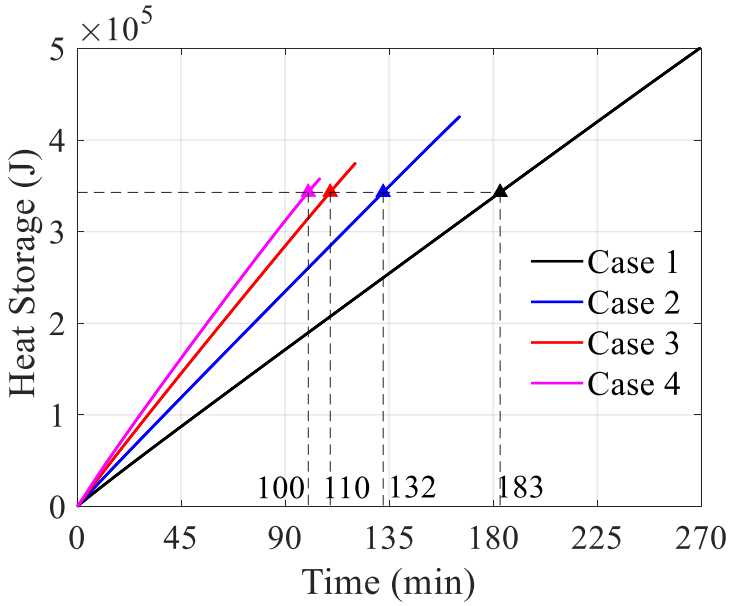


(a) PCM accumulated heat

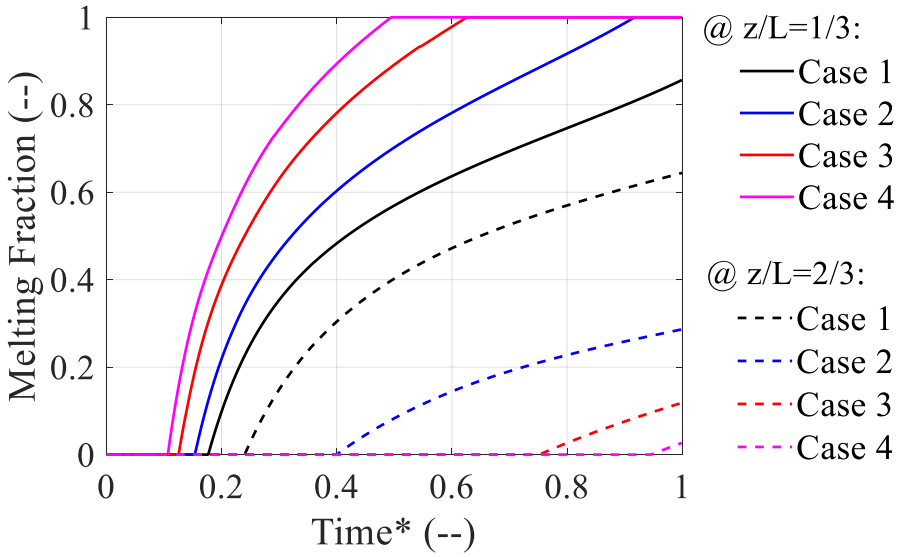


(b) Melting fraction

(Case 1: 2,300 rpm; Case 2: 3,450 rpm; Case 3: 4,600 rpm; Case 4: 5,750 rpm)

**Figure 5-7: PCM accumulated heat and melting fraction changed with compressor speeds**

## 5.5 *Analysis of the Uneven PCM Melting*

Since the refrigerant condensing temperature increased with the PCM temperature, more uniform PCM melting can extend the duration of Stage II and lead to a slower increasing rate of the refrigerant condensing temperature. This is preferred as applied to the PCM-to-refrigerant HX in the system. This section analyzes the reasons for the uneven PCM melting. Essentially, the uneven PCM melting is due to the uneven heat transfer rate in the refrigerant flow direction, as shown in Figure 5-8. The inlet is at z/L = 0, while the outlet is at z/L = 1. The heat flux at the bottom around z/L greater than 0.7 is only 8~15% of the main tube length section. The reason could be explained from two aspects: (1) the heat transfer coefficient (see Figure 5-9); and (2) the temperature difference between refrigerant and PCM (see Figure 5-10) as discussed as follows:

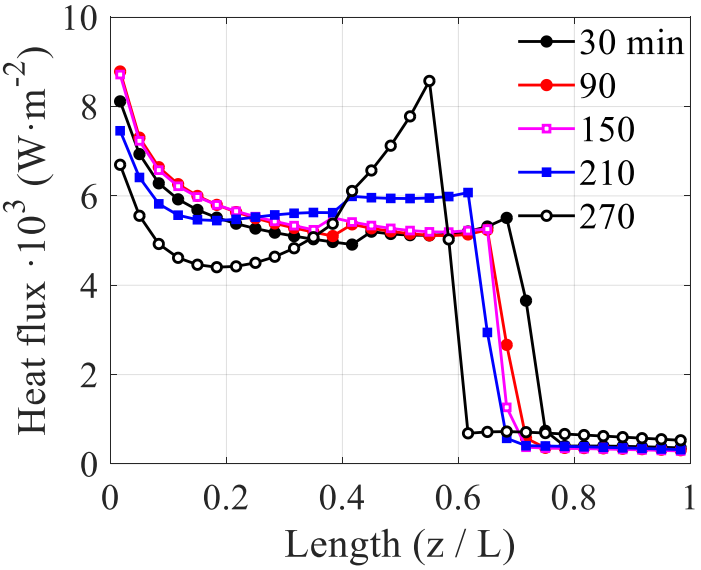


**Figure 5-8: Heat flux at the PCM inner heat transfer area.**

Figure 5-9 shows the refrigerant side heat transfer coefficient, $\alpha_{ref}$, changed in the refrigerant flow direction. The $\alpha_{ref}$ of the two-phase refrigerant decreases from more

than 4,000 W $m^{-1}$ $K^{-1}$ to about 1,500 W $m^{-1}$ $K^{-1}$ in the condenser tube length direction, while it becomes less than 100 W $m^{-1}$ $K^{-1}$ in the subcooled region at around z/L=0.7. Therefore, it can be concluded that the uneven refrigerant-side heat transfer coefficient between the two-phase region and liquid phase region can result in the uneven heat transfer flux as well as uneven PCM melting in the length direction. It can be seen that two-phase $\alpha_{ref}$ also changes slightly in the vertical direction.

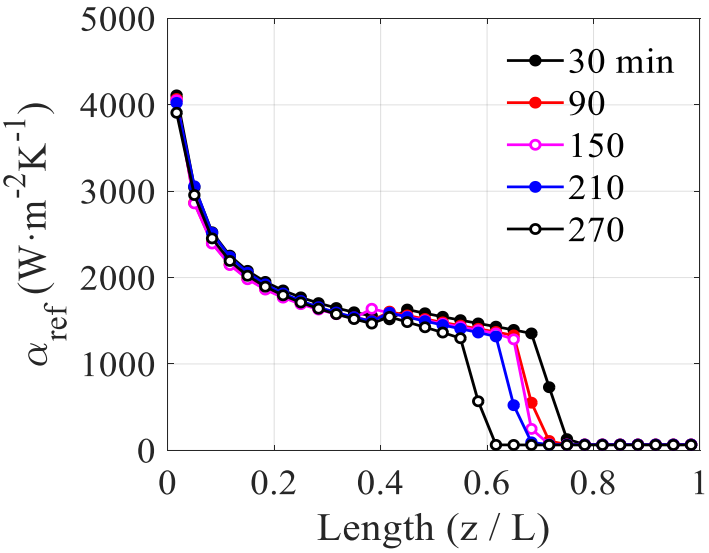


**Figure 5-9: Refrigerant side heat transfer coefficient.**

In Figure 5-10 (a), the refrigerant temperature is constant during the condensation, while the temperature begins to decrease until it becomes the liquid phase near the outlet of the PCM condenser. It also shows that the length of the refrigerant liquid zone increases with time.

Figure 5-10 (b) illustrates the revolution of PCM temperatures attached to the tube wall, which decreases with the condenser tube length direction. Comparing the revolution of the PCM temperature and refrigerant temperature, it can be seen that

refrigerant condensing temperature rises with the increase of the temperature of PCM at the refrigerant two-phase region (z/L <0.7).

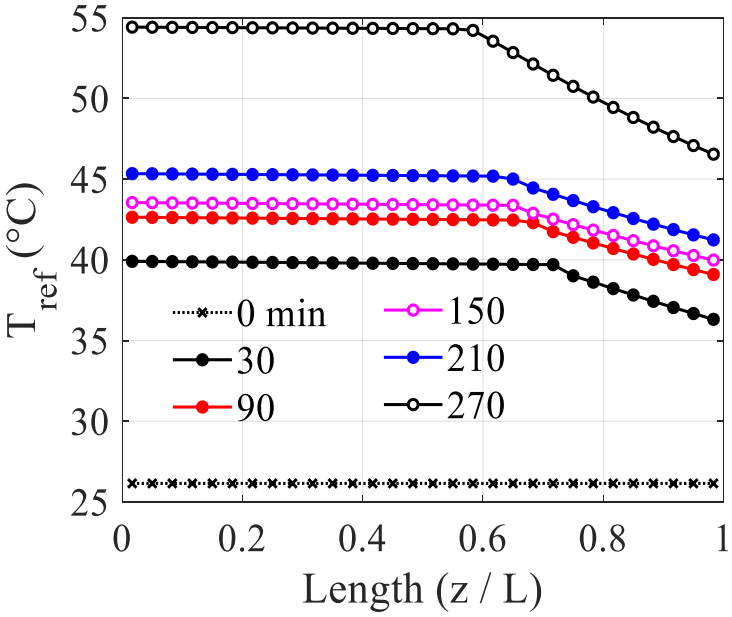


(a) Temperature of the refrigerant

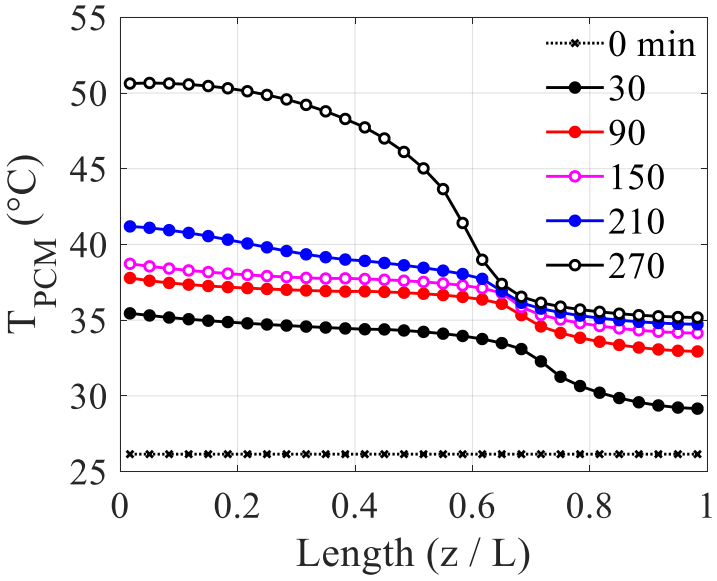


(b) Temperature of the PCM attached tube walls

**Figure 5-10: Refrigerant and PCM temperature.**

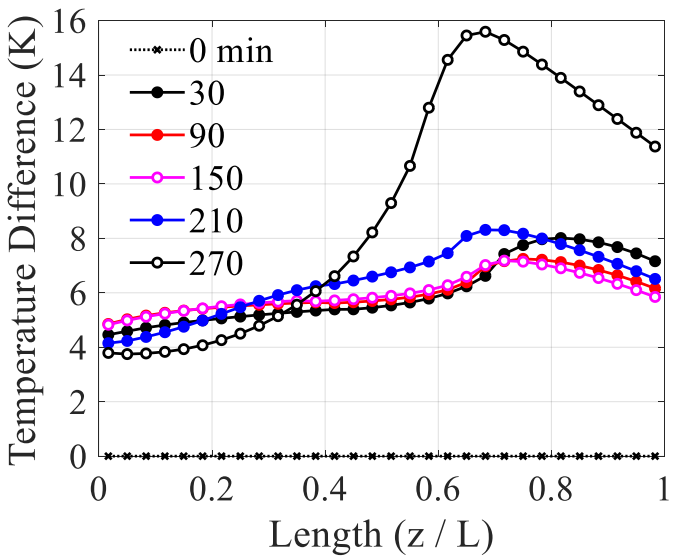


**Figure 5-11 Temperature difference between the PCM attached walls and the refrigerant**

Figure 5-11 presents its temperature difference along the refrigerant flow direction. The temperature difference near the inlet increases slightly and then decreases with the time, while near the outlet at z/L > 0.7, the temperature difference decreases and then increases with the thermal storage process. Especially at 270 minutes, its temperature difference is greater than 10 K. Therefore, the small heat flux near the PCM condenser outlet is due to the small refrigerant heat transfer coefficient of the liquid refrigerant region, rather than the decrease of the local temperature difference, and reversely, the local temperature difference increases indeed.

### *5.6 System Analysis with Less Refrigerant Charge*

As analyzed in Section 5.5, the uneven PCM is due to uneven heat transfer rate along the condenser tube length direction, especially the subcooled-liquid refrigerant region near the condenser outlet. In order to achieve more uniform PCM melting and

extend Stage II, one potential method is to reduce the length of the liquid-refrigerant region in the PCMHX. Moreover, more refrigerant charge can lead to an increase of both the subcooling at the condenser outlet and condensing temperature in refrigeration systems (Corberán et al., 2008). Therefore, system simulations of four cases with different lengths of the liquid-refrigerant region were conducted.

The length of the liquid-refrigerant region is related to the subcooling at the outlet of the PCM-coupled tube (z = L). The subcooling at the outlet of the PCM-coupled tube, z = L, is the subcooling before the condenser collection header, which is different from the subcooling at the condenser outlet as in Figure 5-4 (c). The subcooling at the condenser outlet is 1~2 K greater than that at z = L, due to the heat loss from the refrigerant to the surroundings in the condenser bottom heat and the connection tubes after the condenser outlet. Significantly, the subcooling at the outlet of the PCM-coupled tube, z = L, can reflect the length for the heat transfer from the liquid refrigerant to PCM, and therefore, this section focuses on subcooling at z = L instead of subcooling at the condenser outlet.

In this numerical study, the Case 1 has no refrigerant subcooling at z = L, while the Case 2, Case 3, and Case 4 have greater subcooling as well as greater condensing temperature caused by more refrigerant charge in the system. Figure 5-12 shows the heat accumulated in PCM for four cases. The slope of the heat storage equals the PCM condenser capacity. Case 4 has the smallest condenser capacity because of the smallest enthalpy difference between the condenser inlet and outlet. In order to analyze the effect of the uneven melting on the PCM and system performance, the comparison of four cases is based on the same heat storage of $2.04\times10^6$ J. As illustrated in Figure 5-12,

the normalized time to accumulate this amount of heat in the PCM are similar, which are 186.4, 181.7, 181.3, 181.5 minutes, respectively, for the Case 1, Case 2 and Case 3 as represented by the Δ marks.

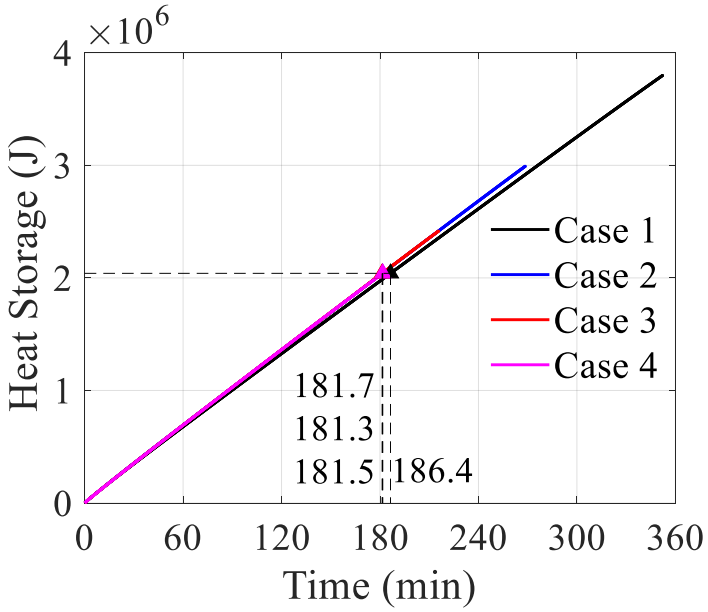


(Δ represents the normalized time for four cases with the same amount of heat stored in the PCM, which is 186.4, 181.7, 181.3 and 181.5 minutes for Case 1, 2, 3, and 4, respectively)

**Figure 5-12: Revolution of the accumulated heat stored in PCM**

The revolutions of the refrigerant subcooling at z = L and the condensing temperatures for four cases are presented in Figure 5-13. As analyzed in Figure 5-4 (c), both the condensing temperature and subcooling increase during the PCM melting process. Moreover, marks presented by Δ indicate the occasion with the same amount of heat stored in the PCM condensers.

Figure 5-13 (b) shows that for Case 1 with no subcooling, the normalized time is near the middle of Stage II, and Stage II ends at 300 minutes. For Case 2, the normalized

time is at 77% in the duration before Stage III, and Stage II terminates at 235 minutes. For Case 3, the normalized time is similar to the end of Stage II. For Case 4, the normalized time is beyond Stage II for 23 minutes. For the system in Case 1, the duration of Stage II plus Stage I can increase by 28%, 65%, 89%, respectively, compared with Case 2, Case 3 and Case 4. Therefore, Case 1 is recommended due to its longest Stage II period as well as the lowest condensing temperature.

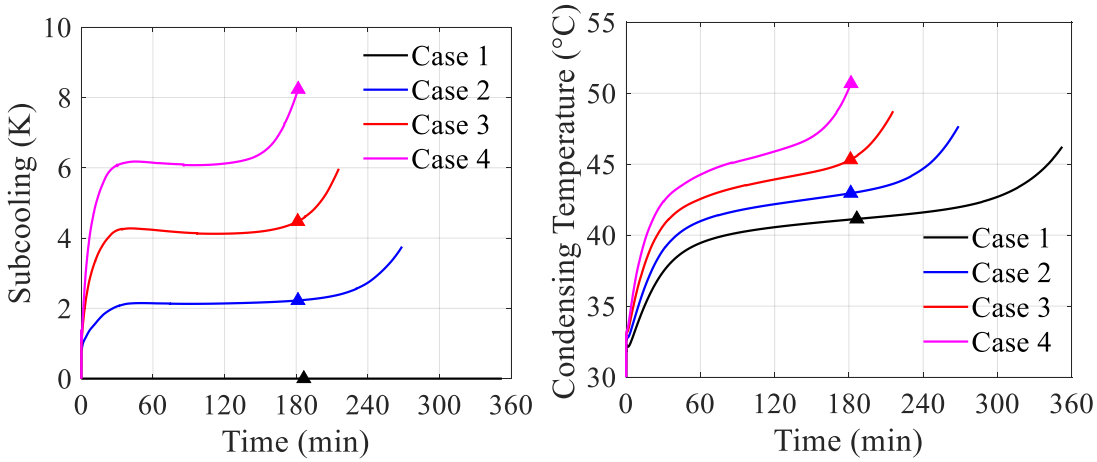


(a) Subcooling at z = L (b) Refrigerant condensing temperature

(Δ represents the normalized time with the same amount of heat stored in the PCM).

**Figure 5-13: Revolution of the condensing temperature and the subcooling in different cases.**

Figure 5-14 shows the PCM melting fractions for four cases at the normalized time, in which the refrigerant inlet is at the top, and the copper tube is at the left. The amount of heat in these four cases are the same. It is noticed that for Case 1 with no subcooling at z = L, the PCM melting rate along the condenser tube length direction is much more uniform than the other cases, and there is even no region with a liquid fraction less than 0.4. As the subcooling increases from Case 1 to Case 4, the area of liquid fraction

smaller than 0.1 becomes larger, and the region with liquid fraction greater than 1 also increases. For Case 4, about the top 40% PCM melts to liquid completely, while about 1/3 of the bottom is still solid. Since the part of PCM melts completely and absorbs heat by sensible heat, this excessive uneven melting makes the system 23 minutes over the Stage II. The PCM liquid fraction distribution in four cases in Figure 5-14 indicates that reducing the subcooled-liquid refrigerant region can lead to a more evenly PCM melting, a slower increase of condensing temperature and a longer period of stable Stage II for the system performance. Considering the application of the PCM-to-refrigerant heat exchanger, to maintain a certain value of the subcooling at the condenser outlet, a smaller subcooling is preferred.

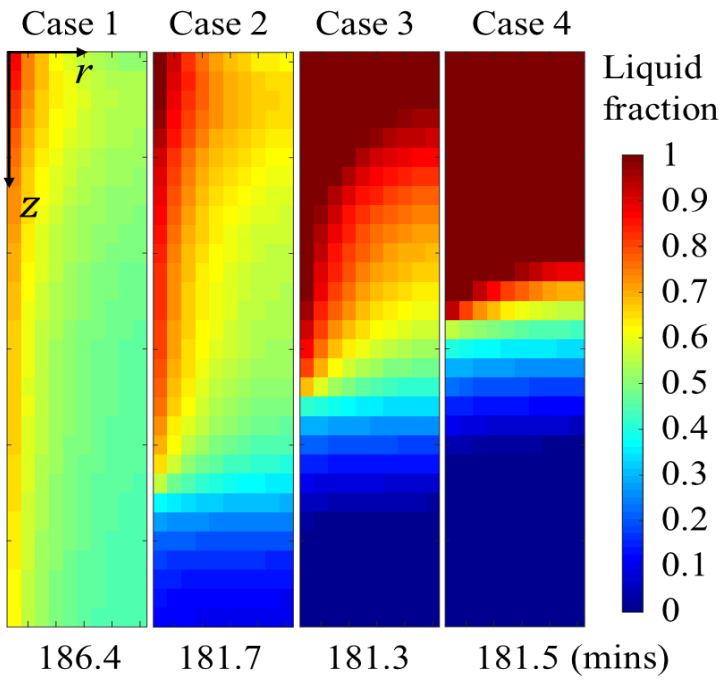


**Figure 5-14: PCM melting fraction at the normalized time with the same amount of heat stored in the PCM.**

## *5.7 Chapter Summary and Conclusions*

This Chapter develops models of the PCM-to-refrigerant HX and the coupled system. It shows a great agreement between simulation results and experimental results in both system-level and component-level performance comparison. The performance of PCM melting and the coupled system presents three stage processes. In Stage I, PCM absorbs heat by sensible heat transfer, and condensing temperature increases obviously. In Stage II, PCM performs phase change leading to a stable capacity and condensing temperature. In Stage III, part of PCM melts to liquid, and system performance begins degrading. PCM melting characteristics including PCM temperature and liquid fraction profile during Stage I, II, and III are discussed showing that the top PCM melts much faster than the bottom, which brings the system into Stage III. To extend the period of Stage II, the reason for the uneven melting is analyzed. The uneven PCM melting is due to the uneven refrigerant-side heat transfer coefficient, rather than the uneven refrigerant temperature along the condenser tube length direction. In the current system, due to the small refrigerant mass flux, the heat transfer coefficient of the single-phase refrigerant is very small.

In addition, the effect of the compressor speeds on the PCM melting rate is also analyzed based on the same accumulated heat store in the PCM. It shows that the refrigerant mass flow rate can affect not only the condenser capacity and operating time, but also the PCM melting distribution. The PCMHX with the greater capacity caused by a greater mass flow rate has more ununiform PCM melting.

The simulation of the system with different subcooling degree shows that reducing the liquid refrigerant region can lead to a more uniform PCM melting, a slower increase of condensing temperature and a longer period of stable Stage II for the system performance. For the system in Case 1 with no subcooling at the condenser outlet, the duration of Stage II plus Stage I can increase by 28%, 65%, 89%, respectively, compared with Case 2, Case 3 and Case 4. Considering the application of the PCM-to-refrigerant heat exchanger, to maintain a certain value of the subcooling at the condenser outlet, a smaller subcooling is preferred.

In summary, this Chapter reveals the reason for uneven PCM melting, and provides insights for further PCMHX heat transfer performance improvement. The effects of compressor speed and subcooling at the condenser outlet are simulated. A further experimental study in the system with different refrigerant charge is needed, which is discussed in Chapter 6.

# Chapter 6: Effects of Condenser Subcooling on PCM-VCC Systems

This chapter investigates the effect of subcooling on the PCM condenser and system performance with a different selection of operation duration. Only the cooling cycle is investigated based on the same experimental setup as illustrated in Chapter 4.

## *6.1 Background of Subcooling Effect on Condenser Characteristics*

The effect of subcooling on general VCC systems under steady-state can be explained as followings. More refrigerant charged in the system could lead to a higher condenser pressure as well as a greater subcooling degree at the condenser outlet. As investigated in Corberán et al. (2008), Figure 6-1 illustrates the condenser outlet characteristics with different subcooling and test conditions. When subcooling is increased from 0 K, condenser pressure increased slightly as presented in the blue circle. During this process, higher subcooling can lead to a noticeably greater condenser and evaporator capacity, while the compressor power increases slightly. Therefore, COP increased with the increase of the subcooling. However, after subcooling reached a certain value, condenser pressure increased significantly as illustrated in the red circle. The increasing rate of compressor power was greater than that of HX capacities. Thus, COP could degrade with the increase of subcooling. As a result, the optimal COP exists in a general VCC system.

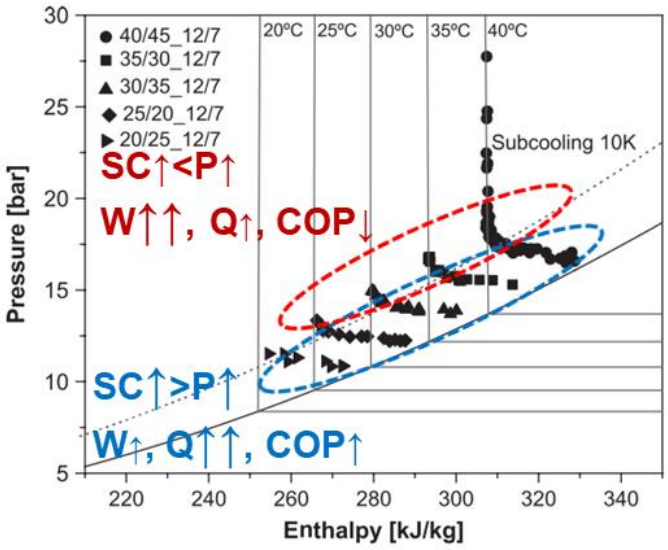


**Figure 6-1. Condenser outlet pressure and enthalpy with different subcooling and test conditions (Corberán et al., 2008).**

Figure 6-2 illustrates the refrigerant temperature along the condenser tube length direction in a water-to-refrigerant HX with the same capacity. The heat transfer area is equivalent to the HX length in this figure. The two-phase heat transfer area, subcooling and approach temperature are illustrated in the figure as well. It is noted that with higher subcooling, shown as a red line, the two-phase heat transfer area is smaller, and the approach temperature is greater. The reason is that since the heat transfer coefficient of the two-phase refrigerant is much greater than the single-phase, the condenser with a smaller two-phase heat transfer area needs a greater approach temperature to maintain the same condenser capacity.

Since the heat transfer flux of the two-phase refrigerant is much greater than that of liquid-phase or vapor-phase refrigerant, a greater subcooling can lead to more uneven heat transfer flux along the condenser tube length direction as shown in Figure 6-2. If we extend this observation to the PCM condenser, the PCM melting rate could

be more non-uniform with a higher subcooling degree. Thus, the PCM temperature profile and melting process change with different subcooling in the system.

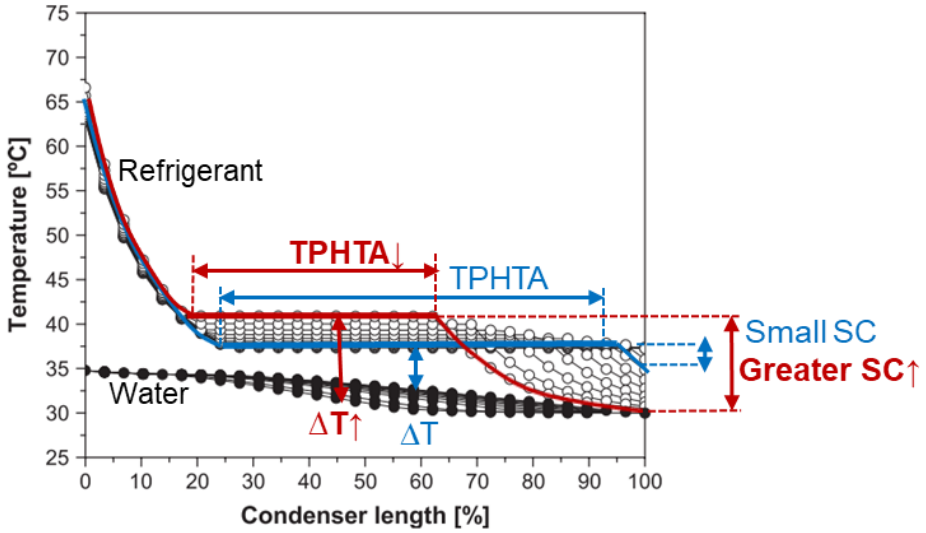


**Figure 6-2. Refrigerant temperature in the condenser tube length direction with different subcooling (Corberán et al., 2008). (SC: subcooling. TPHTA: two-phase heat transfer area. ΔT: approach temperature difference.)**

In this chapter, the effect of the subcooling on the VCC-based system as PCM melting is investigated to ensure the similar result as shown in Figure 6-1 and Figure 6-2. In addition, the PCM melting and system performance over the entire cooling cycle with different subcooling is discussed to see the accumulated effect of the uneven heat flux.

## *6.2 Procedure*

The experimental setup for subcooling effect analysis is the same as the system illustrated in Chapter 4, and the system schematic is illustrated as in Figure 4-1 (b). In Chapter 4, the system performance with both normal cycle and PCM recharge cycle is

discussed. In this Chapter, I will only focus on the effects of subcooling of the PCM condenser in the normal cycle. The experimental study is performed in the environment chamber with a constant ambient temperature of 26 C. All the connecting pipes were insulated with flexible rubber foam to reduce the heat loss to the ambient. Before the test, the whole setup was installed in the chamber for more than 24 hours to ensure that the PCM initial temperature is uniform at 26°C.

Measurement devices used for the experimental study are listed in Table 3-1. More details can be found in Section 4.1. Compared with the study in Chapter 4, the significant different experimental procedure in this Chapter is that the air-side evaporator and refrigerant-side evaporator capacity were compared. Results show a deviation within 5% ensuring the accuracy of the evaporator capacity measurement. Moreover, for the cycle without subcooling, refrigerant-side evaporator capacity cannot be obtained. Therefore, in such cases, only air-side evaporator capacity was used.

The uncertainties of parameters can be obtained from Eq. (3-11). The uncertainties of COP, superheat, subcooling, capacity, temperatures, and compressor power consumption are illustrated by error bars in figures. The uncertainty of COP was less than 4%. The uncertainty of the subcooling was 0.5 K, and that of heat exchanger capacity was less than 2.5%. The normalized accumulated heat uncertainty was less than 1%.

*6.3 Definition of the Normalized Subcooling*

During the PCM melting process, the PCM temperature change is very limited due to a large amount of the latent heat, so that the system performance variation is minimal. Therefore, the system can be regarded as in the 'steady-state'. Therefore, I use the normalized subcooling degree (NSD), to represent the subcooling during the PCM melting process. Essentially, NSD can reflect the refrigerant charge in the system, as discussed in the literature (Kim et al., 2014; Poggi et al., 2008). The relationship between NSD and refrigerant charge in this study is illustrated in Figure 6-3.

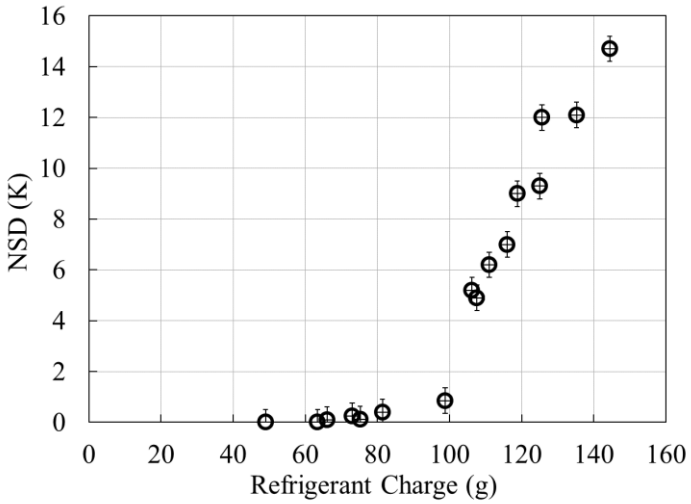


**Figure 6-3. Relationship between NSD and refrigerant charge**

Moreover, during the entire operation, PCM temperature increases from an initial temperature of 26 °C to the melting temperature of 37 °C in terms of sensible heat, then performs phase change within a narrow temperature changing range, and eventually some parts of PCM melt to liquid and increase temperature again in terms of sensible heat. Therefore, the entire operation is a dynamic process with the various PCM and system performance, including variable subcooling. As the various NSD related to the

according refrigerant charge, the different NSD can lead to the different evolution of the PCM heat storage behaviors and system performance during the entire operation. Thus, in Section 6.4.1, this study focuses on the effects of the NSD during the 'steady' PCM melting process, while in Section 6.4.2, the effects of NSD during the entire operating duration are analyzed.

## *6.4 Results and discussion*

### 6.4.1 Performance in the Duration of PCM Melting

PCM melting process can be regarded as a steady state process, the NSD is the real condenser subcooling in this duration. Figure 6-4 shows the impacts of NSD on the condensing temperature, evaporating temperature, and system COP. It is noted that the evaporating temperature, condensing temperature, and COP increased extremely fast with NSD in a range of 0 to 0.5 K because of the influence of the refrigerant charge. With an increased refrigerant charge from a small amount, the pressure in each system component increases, however, most of the refrigerant charge occupies the space in the condenser side due to higher two-phase pressure and refrigerant density there. As the refrigerant charge reaches a certain amount, the liquid begins to form near the condenser outlet that collects most of the charge in the condenser. The higher refrigerant charge amount can contribute to the higher fraction of the liquid region in the condenser as well as the greater subcooling at the condenser outlet. Therefore, during NSD changed from 0 to 0.5 K, the increase of the system temperatures reflects how the system reacts with the charge increasing from a small amount to a certain amount to form the liquid in the condenser. As NSD higher than 0.5 K, the condensing

temperature increased with the NSD, while the evaporating temperature was not affected obviously. It is because, to increase the subcooling at the condenser outlet, greater heat transfer should be conducted in PCM condenser, leading to a greater approach temperature between PCM and refrigerant. Hence, the condensing temperature increased.

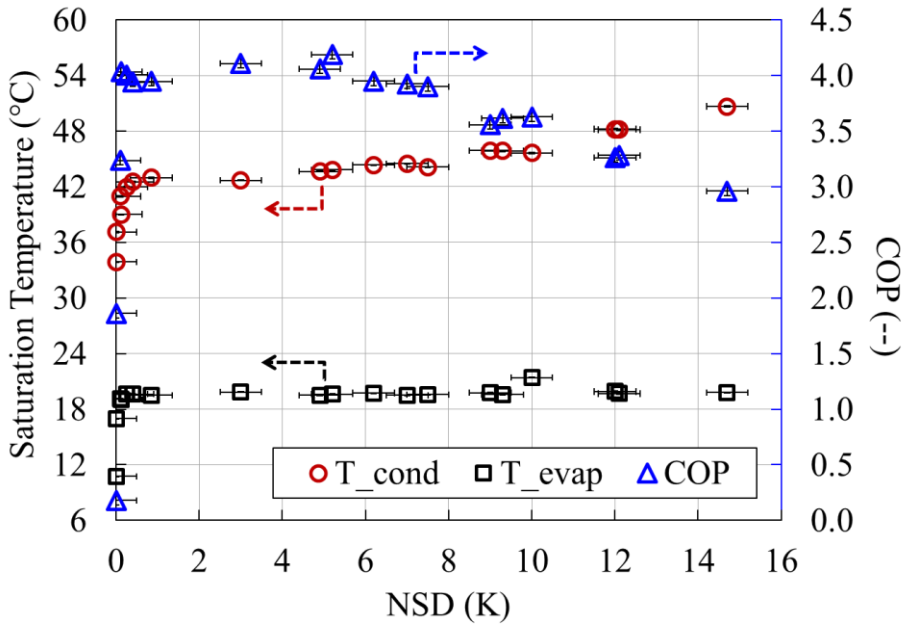


**Figure 6-4. Effect of NSD on the condensing temperature, evaporating temperature, and COP in the PCM-melting duration.**

The superheat at the evaporator outlet, and the mass flow rate can also vary with the NSD, as indicated in Figure 6-5. As NSD raised but smaller than 0.5 K meaning refrigerant charge increased from a minimal amount, the evaporator inlet refrigerant quality decreased, and thus, the evaporator outlet superheat increased sharply. This could lead to the increase of the refrigerant density at the compressor inlet, so that more refrigerant mass flow rate is provided to the compressor. Therefore, the increasing

slope of the mass flow rate is evidently high at a small NSD. After that, as NSD increased, the superheat did not change obviously. At the same time, the mass flow rate dropped gradually due to the decrease of the compressor volumetric efficiency that becomes smaller with a higher-pressure lift.

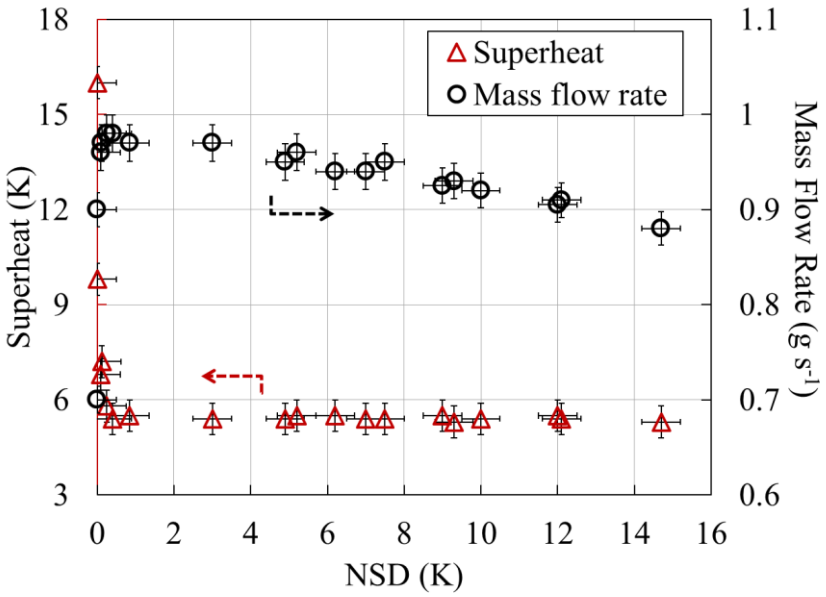


**Figure 6-5. Effect of NSD on superheat and mass flow rate in the PCM-melting duration.**

From Figure 6-4, it is notable that condensing temperature increased slowly with NSD from 1 K to 8 K, while after that, the slope ratio became greater, leading to the tradeoff of the system performance significantly regarding evaporator capacity and compressor power consumption. As the NSD increased but smaller than 8 K, since condensing temperature increment was small, the increase of both the evaporator specific enthalpy difference and the evaporator capacity was greater than that of the power consumption (see Figure 6-6). However, as NSD greater than 8 K, since

condensing temperature increment was great, the increase of the evaporator specific enthalpy difference was smaller than that of the power consumption. Affected by the decrease of the mass flow rate, the evaporator capacity would start to decrease (see Figure 6-6). This tradeoff can result in a maximum value of the system COP, which was 4.2. Similar to the literature (Corberán et al., 2008; Kim et al., 2014), the optimum NSD was about 5 K as illustrated in Figure 6-4.

Figure 6-7 shows the system pressure-enthalpy diagram for the steady-state with five different NSDs. For the five cycles, evaporator pressures were almost the same, and the condenser pressure increases with the NSD. For the NSD of 0 K, the evaporator inlet enthalpy properties were obtained by the air-side heat transfer calculation. As NSD increased, condenser pressure increased slightly, while after NSD reached a certain value, i.e. aforementioned 8 K, the condenser pressure increased rapidly.

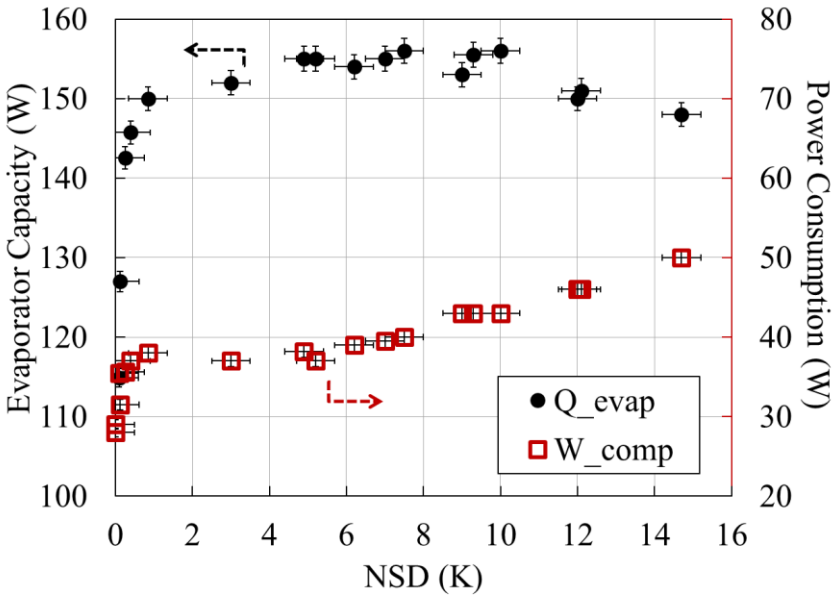


**Figure 6-6. Effect of NSD on the evaporator capacity and compressor power consumption in the PCM-melting duration.**

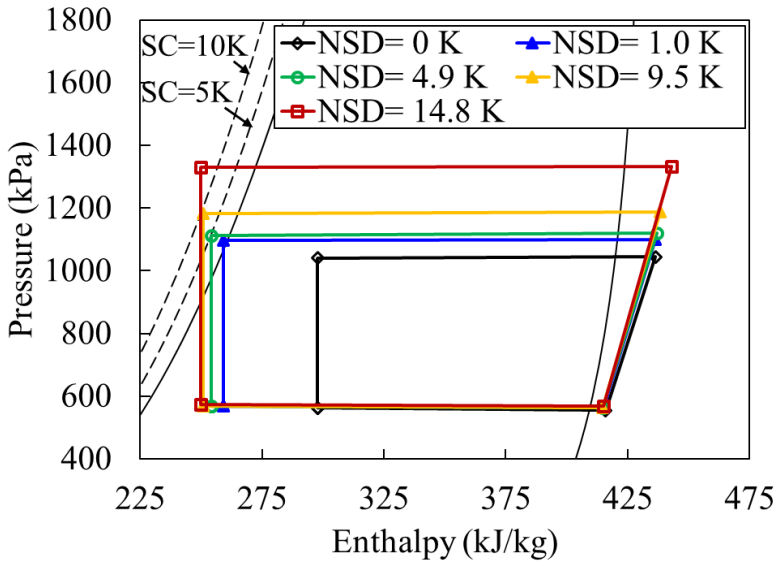


**Figure 6-7. P-h diagram of the system cycle for different NSDs.**

6.4.2 Performance in the Entire Duration

For a system with a specific NSD, which is 7 K, indicating a certain refrigerant charge, its pressure-enthalpy diagram changed with operating time is illustrated in Figure 6-8. The PCM initial temperature is 26 °C, and the PCM melting temperature is 37 °C. As time increased, PCM absorbs heat in terms of sensible heat with the temperature changed from 26 °C to the melting temperature, then latent heat during the melting process, and then sensible heat again with the form of the liquid phase. Therefore, as illustrated in Figure 6-8, the condensing temperature, subcooling, and compressor power consumption increased with the operating time, as well as PCM average temperature, to maintain the approach temperature in the PCM condenser and the cycle operation. Nevertheless, due to the stable evaporating condition and the appropriate operation of the expansion valve, superheat and evaporator pressure did not change obviously.

From Figure 6-8, the system performance is dynamic during the normal operation. Essentially, the dynamic subcooling reflects the system reaction on the PCM performance variation. Since the specific NSD indicates the refrigerant charge in a certain system, systems with different NSD have different dynamic performance. In this section, the effects of the NSD on the system performance and PCM melting characteristics are discussed over the PCM absorbing heat process.

The dynamic performance of subcooling, condensing temperature, evaporator capacity, and COP was analyzed regarding the five NSD of 0.8 K, 2.6 K, 5.3 K, 7.5 K, and 10.5 K meaning five different amounts of the refrigerant charged in systems. Other system operation conditions, such as compressor speed and ambient temperature, were the same for the performance comparison. The operation duration was set from 0 to 5.5 hours, except the case with NSD of 10.5 K terminated at 4.5 hours due to its excessively high condensing temperature.

Before the analysis of the NSD effects, we need to deal with other potential factors that can also influence the dynamic system performance, such as the amount of heat stored in the PCM. If one system with a specific NSD has a greater condenser capacity than other systems, the heat storage in the PCM would be greater, and the condensing temperature could be higher than others. Then, I cannot indicate whether the difference between this system and the others is due to its specific NSD or its greater PCM heat storage because both factors can lead to the change of system performance, for example, condensing temperature. Figure 6-9 indicates the normalized accumulated heat stored in the PCM with the baseline of NSD equal to 0.8 K, showing that the difference between different NSD is within 4% at each period. This comparison makes

the system analysis reasonable so that the performance difference at each duration is because of the different NSD rather than the different amount of heat stored in the PCM.

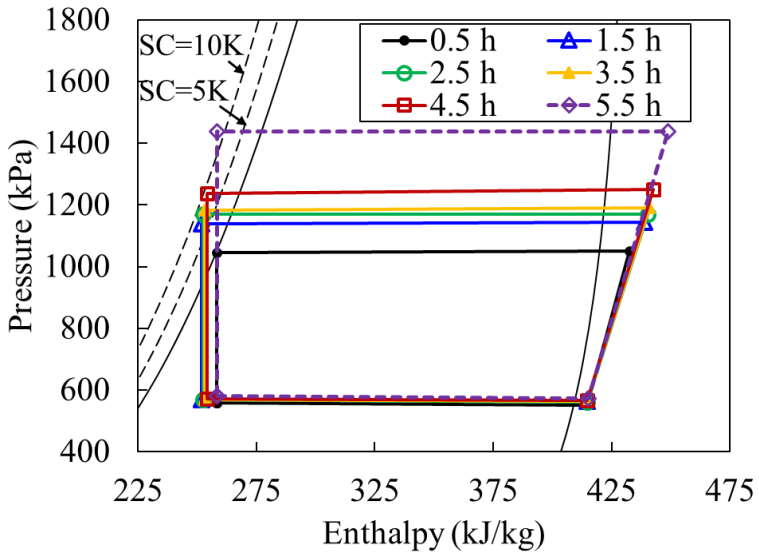


**Figure 6-8. P-h diagram of the system cycle during the entire duration.**

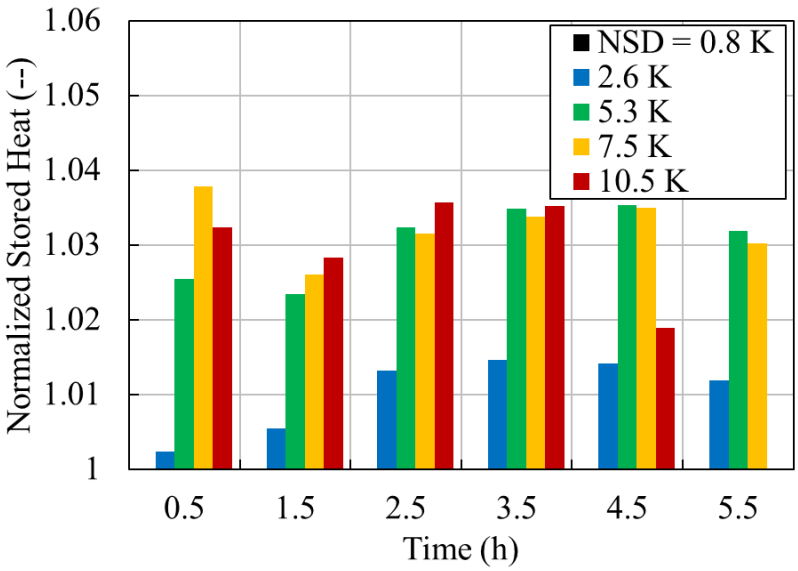


**Figure 6-9. The normalized accumulated heat stored in PCM for different NSD with a baseline of NSD of 0.8 K during the entire duration.**

Figure 6-10 and Figure 6-11 show the evolution of the subcooling and condensing temperature changsed with the NSD at each operation period. In the beginning, such as 0.25 hours and 0.5 hours in Figure 6-10, PCM was in the solid phase with a temperature lower than the melting temperature, and thus, the subcooling was lower than the NSD shown by the dashed line. As time increased, since PCM average temperature increased resulting from more heat absorbed inside, the condensing temperature increased gradually to keep a certain approach temperature in the PCM condenser. The system was adjusted by the expansion valve to maintain a proper superheat degree at the evaporator outlet so that the subcooling increased with PCM temperature as well.

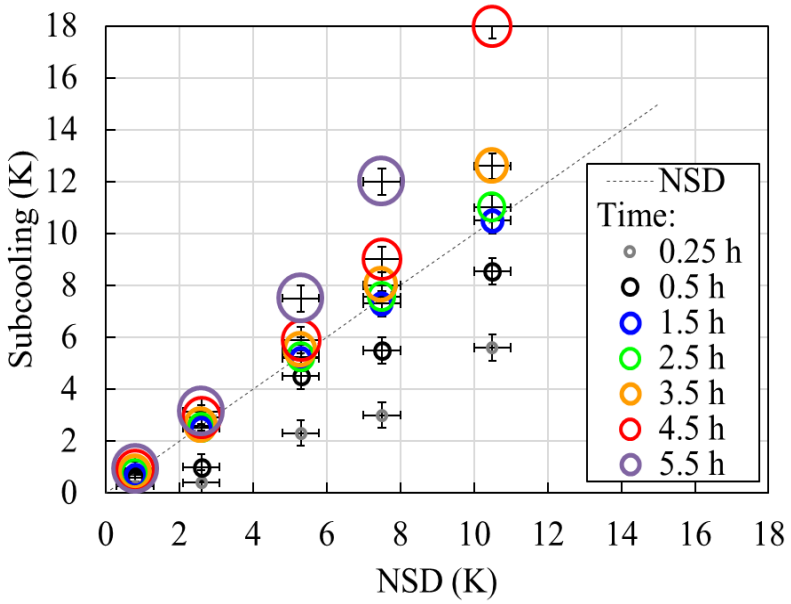


**Figure 6-10. Effect of NSD on subcooling at the condenser outlet during the entire duration.**

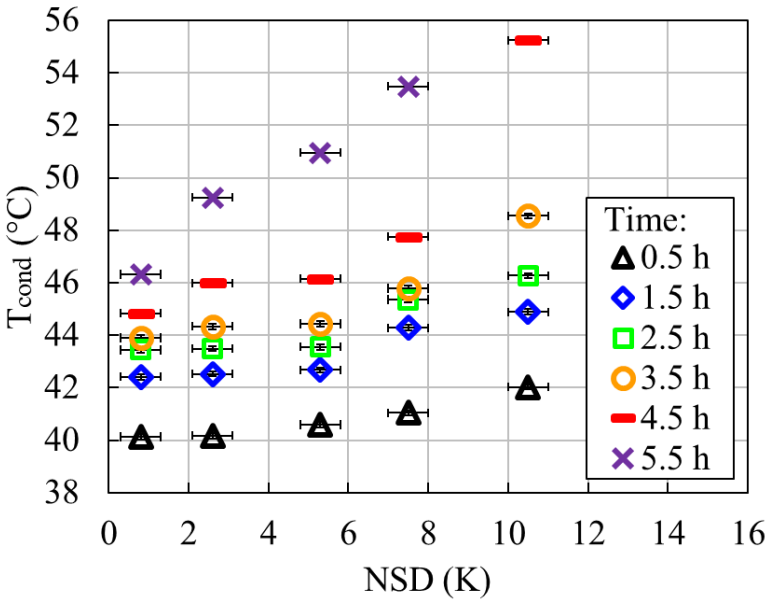


**Figure 6-11. Effect of NSD on condensing temperatures during the entire duration.**

It is noted that with a smaller NSD, the increment of both the subcooling and condensing temperature changed with operation time could be smaller. For example, for the NSD of 0.8 K, the increase of the subcooling from 0.25 hours to 5.5 hours was less than 1 K, while for the NSD of 7.5 K, this increment was greater than 9 K (see Figure 6-10). And it took 5 hours for the system with the NSD of 0.8 K to increase the condensing temperature for 6°C, while for NSD of 10.5 K, during the 4 hours, the condensing temperature increased by 13°C (see Figure 6-11). The reason could be the uneven PCM melting and system reaction impacted by the subcooling variation. In the PCM condenser, most heat transfers from the PCM to the two-phase refrigerant with a greater heat transfer coefficient, and only a small portion of the condenser tube is full of the liquid refrigerant. The liquid refrigerant heat transfer coefficient is much lower than that of the two-phase form, so the heat transfer flux is not uniform along the

condenser tube length direction leading to an uneven PCM melting distribution. As demonstrated in Figure 6-12, the temperature of PCM at the top (dashed lines) is always higher than that at the bottom (solid lines), meaning top PCM melting faster than the bottom. For the system with a smaller subcooling, the liquid refrigerant heat transfer area is smaller. Therefore, the PCM melting is more uniform than the system with a greater subcooling and a greater liquid-refrigerant heat transfer area. As proved in Figure 6-12, for the NSD of 5.3 K, the PCM temperature difference between the top and bottom is much less than that of 10.5 K. In other words, the smaller subcooling can lead to more even PCM heat storage along the condenser tube length direction. Moreover, as both the accumulated heat and the subcooling increased with the time, the uneven distribution of the heat storage can be augmented and make the PCM thermal energy utilization deteriorated. As a result, with a higher NSD, the increment of the condensing temperature and subcooling changed with time are greater.

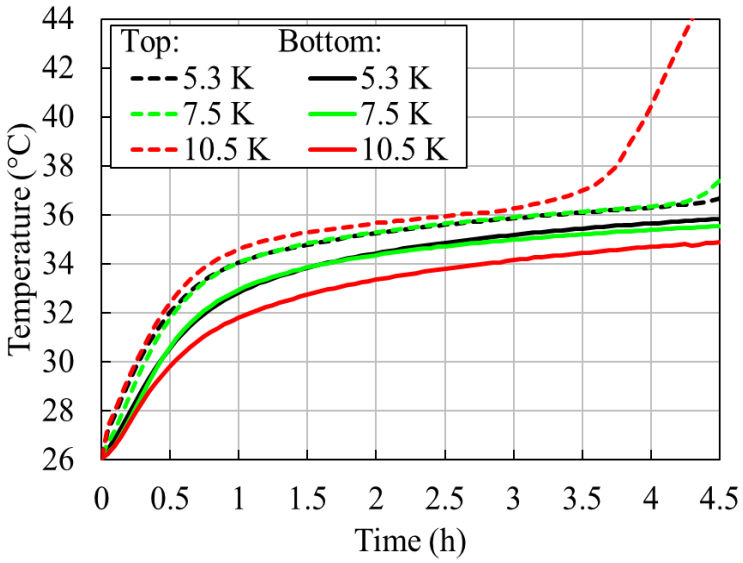


**Figure 6-12. Evolution of the PCM temperature for the system with NSD of 5.3 K, 7.5 K, and 10.5 K, respectively.**

Figure 6-13 shows the evaporator capacity affected by NSD and operating time. For a certain NSD, i.e., 2.6 K, as time increased, the system evaporator capacity decreased all the time, which is due to the decreased specific enthalpy difference (see Figure 6-8) and mass flow rate. Moreover, for a certain period, similar to the analysis in Figure 6-6, the increase of NSD in a certain range means greater evaporator specific capacity. However, the decreased mass flow rate can reduce the evaporator capacity. At 0.5 hours, the condensing temperatures and subcooling for all systems with different NSD were very low, so that the increase of NSD led to a greater evaporator capacity. After 0.5 hours, the evaporator capacity changed with NSD shows the tradeoff between the evaporator specific enthalpy difference and the mass flow rate. That explains why the maximum and minimum evaporator capacity for different NSD changed with operating time.

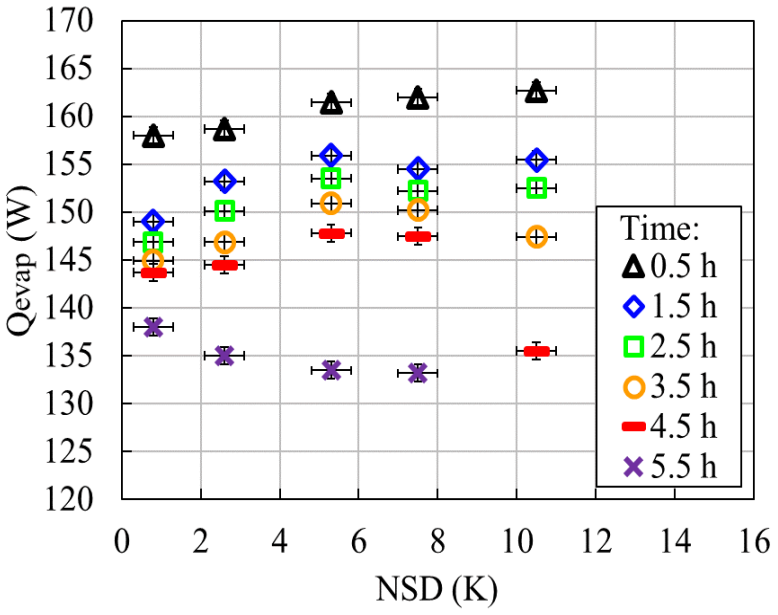


**Figure 6-13. Effect of NSD on evaporator capacity during the entire duration.**

For a certain system, its COP decreased with time caused by the increased condensing temperature and decreased evaporator capacity, as shown in Figure 6-14. Besides, as discussed in the 'steady-state' COP, the optimal NSD is about 5 K for the maximum COP. Similarly, for the dynamic system, the maximum COP is obtained at NSD of 5.3 K before 3.5 hours. However, after that, the maximum COP is achieved at NSD of 0.8 K. Moreover, for the NSD of 0.8 K, COP decreased by 31.3% during the period from 0.5 hours to 5.5 hours, while it dropped by 44.2% for the NSD of 5 K, and for a greater NSD, this COP decrease is even larger. It implies that the subcooling effect on the uneven PCM melting (see Figure 6-12) made the heat storage utilization deteriorated and led to system performance degradation.

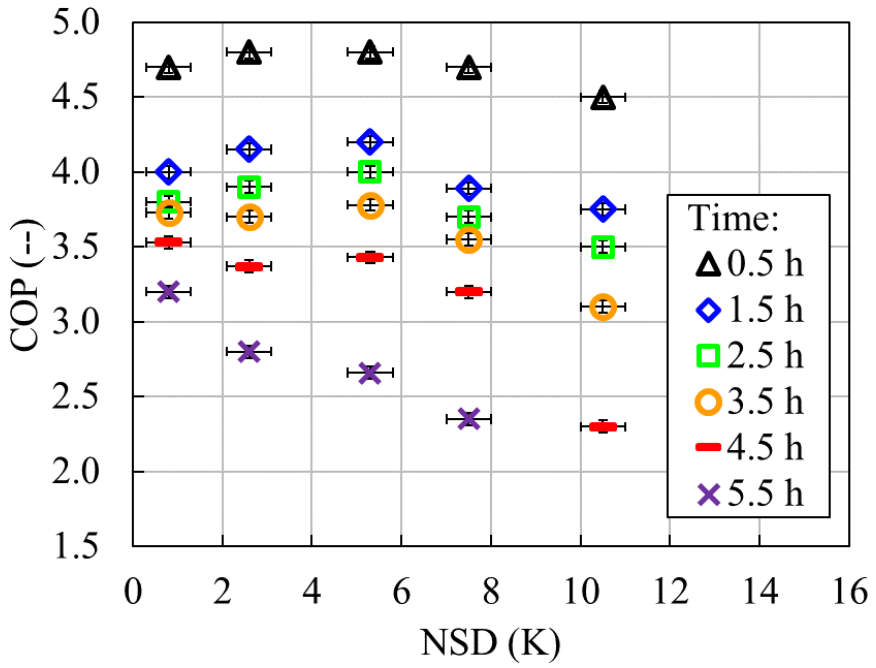


**Figure 6-14. Effect of NSD on system COP during the entire duration.**

### 6.4.3 Suggestion on Further PCM-to-Refrigerant Condenser Application

The systems coupled with PCM-to-refrigerant condensers are more likely to be dynamic, as the PCM initial temperature is not equal to the melting temperature in most cases. To maximize the thermal energy utilization ratio, improve system performance, and extend the operating duration, the most uniform PCM melting is very much preferred. The suggestion to improve the PCM condenser coupled system performance is provided as follows:

(1) NSD selection of the current system. If the operation period is relatively shorter and the PCM initial temperature is closer to the melting temperature, the subcooling could be selected approximately as the optimal NSD of 5 K to maintain the optimal system performance. However, either the operation period needs to be long, or the PCM initial and terminal temperatures are far from the melting temperature range, the smaller NSD is recommended to have more uniform PCM melting and less system performance degradation varied with operating time.

(2) System-level improvement. For other systems applied PCM condensers, adding a sub-cooler after the PCM-to-refrigerant condenser and controlling the temperature at the outlet of the PCM condenser to keep the refrigerant two-phase could help to reduce the impact of the uneven heat transfer flux along the condenser tube length direction, although the heat transfer coefficient still changes with refrigerant quality. Moreover, applying a subcooling regenerator is also a great choice, since it can be beneficial for both reducing the subcooling effect on PCM melting and increasing heat exchanger capacity.

(3) PCM-to-refrigerant condenser improvement. The PCM-to-refrigerant condenser configuration can be optimized further to figure out approaches to obtain the most uniform PCM melting. For example, the tube could be U-shape to ensure the fastest-melting region overlapped or adjacent to the slowest-melting region. Moreover, in the future numerical study, both PCM-side and refrigerant-side phase change processes should be considered, as the refrigerant-side temperature and subcooling are in dynamic process as well.

## *6.5 Chapter Summary and Conclusions*

In this study, the vapor compression system coupled with PCM-to-refrigerant condenser is experimentally studied regarding the subcooling effects. When PCM is in the two-phase state, the system operation could be regarded as steady-state since PCM average temperature variation is small. The impacts of the normalized subcooling at this 'steady-state' on the system COP, condensing temperature, evaporator capacity, and mass flow rates are investigated. The obtained maximum COP shows a trade-off between the evaporator capacity and the compressor power consumption changed with the NSD. The optimal NSD is 5 K, with a COP of 4.2.

Moreover, the effects of the NSD during the entire operation process are comprehensively analyzed. During the system operation, PCM absorbs heat and changes from the solid to the two-phase state, and then the liquid. Therefore, condensing temperature increases to maintain a certain approach temperature difference, which could result in the degradation of both PCM heat transfer characteristics and system performance. Results show that a greater NSD can lead to a

faster increase in the condensing temperature and decrease of the COP. For the NSD of 0.8 K, COP decreased by 31.3% during the period from 0.5 hours to 5.5 hours, while it dropped by 44.2% for the NSD of 5 K, and for a greater NSD, this COP decrease is even larger. This is because the heat transfer coefficient of the liquid refrigerant is much lower than that of the two-phase. Therefore, the heat transfer rate along the condenser tube length direction is not uniform, leading to the uneven PCM melting and thermal storage distribution.

Further, a greater NSD can augment this uneven PCM melting, the condensing temperature increment, and the system performance deterioration. It indicates that for the current system and PCM-to-refrigerant condenser design, the current operating condition setting such as the compressor speed and ambient temperature, and the designed operation time of 5.5 hours, the maximum COP is achieved at NSD of 0.8 K.

This study also provides suggestions on further PCM-to-refrigerant condenser application, including reducing subcooling, adding sub-cooler, and improving PCM condenser configuration as considering the subcooling effects and uneven PCM melting.

# Chapter 7: General-purpose PCMHX Model Development

This Chapter focuses on the development of a general-purpose PCMHX model in order to simulate and optimize the multi-tube PCMHX with any PCM and HTF flow configuration. The preliminary model is proposed based on a novel modeling approach to simulate the multi-tube configuration and the flexible grid of the PCM domain. In addition, a case study is conducted to evaluate if the proposed model is capable of modeling generalized PCMHX designs.

## *7.1 Background and Model Development Objectives*

As mentioned in Section 1.2.5 of Literature Review, most PCM-related simulations have been performed using commercial CFD software, while a few PCM models have been completed through first-principle self-programmed code. Through CFD software, the heat transfer mechanism during the PCM phase change process can be analyzed in detail. Three governing equations including the continuity, thermal energy, and momentum equations constitute the PCM numerical model treated by the finite volume method, so that the natural convection can be observed during the PCM melting process. The model can be applied in complicated PCM configurations. However, this approach has a high computational cost and long engineering time. In addition, the boundary conditions, such as the HTF inlet temperature or wall temperature, should be given before the simulation. As a result, the PCM model is hard to be implemented in the system model with unpredicted PCMHX boundary conditions. For example, in the VCC-based system with a PCM condenser, the inlet refrigerant

temperature and mass flow rate are transient and reflect the system response according to the PCM states and conditions, which cannot be predicted and given before using this approach.

Contrarily, through the self-programmed code, PCM numerical models are based on thermal energy equations. An equivalent heat transfer coefficient term can be added in the thermal energy equation to simulate the free convection effect for the heat transfer enhancement, while the simulation of the liquid PCM movement is not easy to be handled. The advantages of this approach include its lower computational cost and the ability to be coupled with other transient system models with un-predicted HTF boundary condition inputs. For example, the mass flow rate and the HTF inlet temperature could vary with dynamic system performance, and can be inputted in the PCMHX at each time step. Nevertheless, the drawback of this approach is that these models are not easy to be used in multi-tube or comprehensive PCMHX configurations. From the related literature review, most of the research used simple-configured PCMHX, such as cubic PCM (Ghahramani Zarajabad and Ahmadi, 2018; Mandilaras et al., 2015), single shell-and-tube PCMHX (Adine and El Qarnia, 2009; Tao and He, 2011) or the single shell-and-tube configuration simplified from multi-tube PCMHX (Fleming et al., 2013).

The objective of this chapter is to develop a general-purpose PCMHX model for comprehensive single and multi-tube PCMHX configurations. The HTF could be air, liquid/brine or refrigerant regardless of whether the HTF performs phase change. The variations of both the HTF and PCM configurations are taken into consideration. This means that the developed model can predict the thermal performance of PCMHX with

more than one type of HTF. The model should be able to model the PCMHX with any shapes of PCM blocks and structure relations between PCM and HTF tubes.

## *7.2 General PCMHX Model Development*

### 7.2.1 Model Assumptions and Capabilities

To develop the general-purpose PCMHX mathematical model, several assumptions are made including:

- PCMHX is in quasi-steady state operation.
- No heat exchanges in the HTF flow direction meaning the heat transfer occurs only in the radial direction.
- HTF is a one-dimension flow.
- Longitudinal wall conduction is neglected.
- In this preliminary model, the gravity force is not considered, so that the PCM natural convection and buoyancy force effects are not considered. The model is more suitable for the CENG/PCM composite compared with the pure PCM, since the natural convection effect in the CENG/PCM composite can be ignored.
- HTF properties of each segment are based on the HTF segment inlet states, and the inlet is determined by the HTF flow direction.
- PCM properties are uniform across the PCM cell.

In addition, the model is capable to handle the flexibility of the HTF tubes arrangement. Different HTF parameters in different tubes, such as flow directions, heat transfer coefficients, mass flow rates and HTF properties, are considered. The

flexibility of the PCM block configuration is considered meaning the PCM block can be any shapes.

### 7.2.2 PCM Domain Flexible Mesh Generation

In Section 5.1, the uniform PCM-side mesh is applied for the PCM domain in the single-tube unit to address the PCM heat transfer analysis. The uniform mesh can handle a specific simulation for PCM domain with given tube locations and PCM boundaries and shapes. However, in this model, if the PCMHX configuration needs to be changed, the current generated uniform grids should be reformed. To achieve the model flexibility in terms of the tube locations and PCM block shapes, non-uniform grids are applied in the proposed generalized PCMHX model, which is different from conventional self-coding models using uniform PCM-side grids.

In this generalized model, the Voronoi grid as first described in (Dirichlet, 1850), is applied for PCM domain discretization. To better understand the properties and advantages of the Voronoi grid, the grid generation process is illustrated in Figure 7-1 (Angelucci and Mollaioli, 2018). The Voronoi grid consists of convex polygon cells defined by a set of points or seeds. Figure 7-1(a) illustrates seeds distributed in the calculation domain. Each point is then connected to the nearest points as shown in Figure 7-1 (b) to form a set of triangles, which are called Delaunay Triangulation. The perpendicular bisector lines of each segment of the triangle can be made to find the center of each triangle as illustrated in Figure 7-1 (c). As a result, the generated lines are defined as the edges of the Voronoi grids as illustrated in Figure 7-1 (d), and the located centers are vertices of Voronoi cells that defined by the set of seeds.

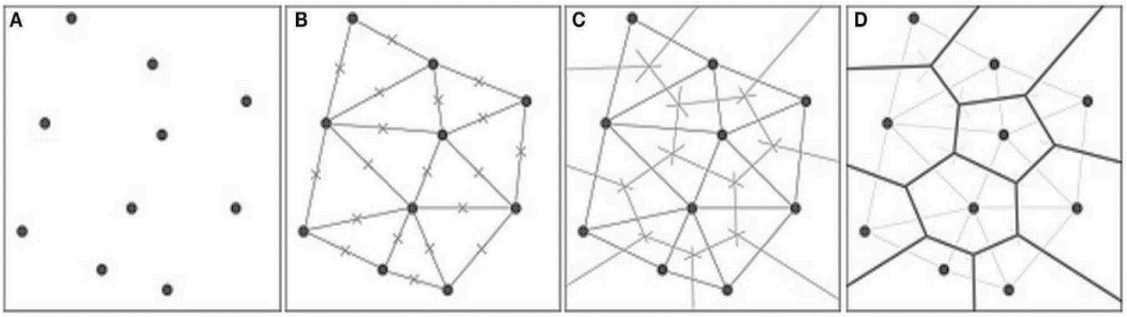


(a) Points (b) Delaunay Triangulation (c) Perpendicular bisectors (d) Voronoi grids

**Figure 7-1: Generation process of the Voronoi grids**

In this model, the seeds in the PCM domain to generate the Voronoi grids consist of two type of points: (1) points representing PCM cells for PCM domain discretization and (2) points representing tube locations. As illustrated in Figure 7-2, the nodes presented by P*x* (*x*=1, 2, 3…) are the points to generate the PCM Voronoi grids. The blue ones represent the PCM cells, while the red nodes show locations of tubes. The blue points can be selected and changed in different cases, so that grids are flexible for most PCMHX configurations with different tube locations, tube numbers and PCM block shapes. One set of codes can generate different Voronoi grids using different selected seeds for different HX cases. For example, Figure 7-2 (a) is the original design with two tubes located at P7 and P8. The red box shows the shape boundary of the PCM domain, in which seven PCM cell points plus two tube location points generate the Voronoi grids (black lines). If the PCMHX configuration changes from (a) to the case with one more tube, and other parameters, such as PCM shape boundary, original two tube locations, and seven PCM cell points remain the same, the same set of grid generation codes can be applied to obtain the new Voronoi grids, as illustrated in Figure 7-2 (b), with one more tube located at P3 compared with the Figure 7-2 (a).

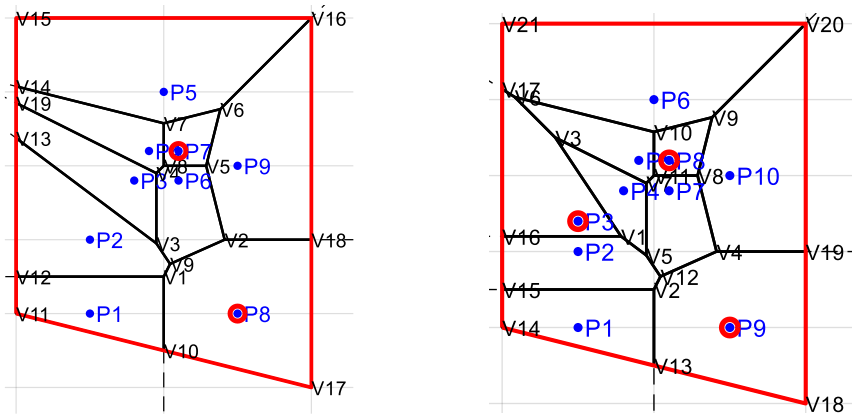


(a) Original design (b) New design with one more tube (P3)

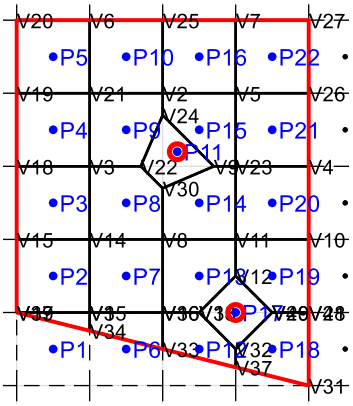


(c) Original design with new Voronoi grid using more seeds of PCM cells

**Figure 7-2: Examples of the PCMHX cross-section area perpendicular to the HTF flow direction with different Voronoi grids.**

Moreover, the Voronoi grid is easy for the grid size sensitivity check. To adjust the grid size, different number and distribution of the seeds that represent PCM cells can be applied. Since more seeds distributed in the domain means the smaller grid size, different seed numbers can be used to check if the simulation results are independent of the grid size. For example, with the same PCMHX configurations, Figure 7-2 (a) and (c) present the different seeds selected for PCM cells. Analyzing the simulation results of these two grids setting, the mesh size sensitivity can be evaluated.

In addition, since each edge is the perpendicular bisector line for the segment line connecting two points of two adjacent cells, the thermal conduction between these two cells is easy to calculate once given the edge length and the distance between the edge to either point of adjacent cells. So that the Voronoi grids have the advantage for heat transfer analysis.

### 7.2.3 Solution Scheme of the Multi-tube PCMHX

Figure 7-3 illustrates the simplified PCMHX schematic that is parallel to the HTF flow direction. The HTF flow direction can be either upward or downward. Although the figure shows a certain number of the tubes evenly distributed in the PCM block, the generalized model can handle different PCMHX cases with different numbers and different distribution patterns of HTF tubes. The PCMHX with M tubes is divided into N slices with a length of *l*. One of the slices is denoted by a blue dash-line box. As mentioned in assumptions, HTF properties at the segment inlet shown by a black node represent the properties in the segment. The wall temperature in each segment is also regarded as the same. For each slice, the PCM domain cross-section area is perpendicular to the HTF flow direction and is divided by the Voronoi grids for the PCM domain discretization. In each slice, the heat exchanges from the PCM domain to the wall segment, and then from the wall segment to the HTF segment. The schematic of the slice(z) can be different from z meaning that the cross-section area along the HTF direction can be different, which is decided by the HX configuration. Examples of the slice schematics can be found in Figure 7-2 (a) and (b). In these examples, the

HTF tube number M = 2 in the PCMHX slice of Figure 7-2 (a), and M = 3 in in the PCMHX slice of Figure 7-2 (b).

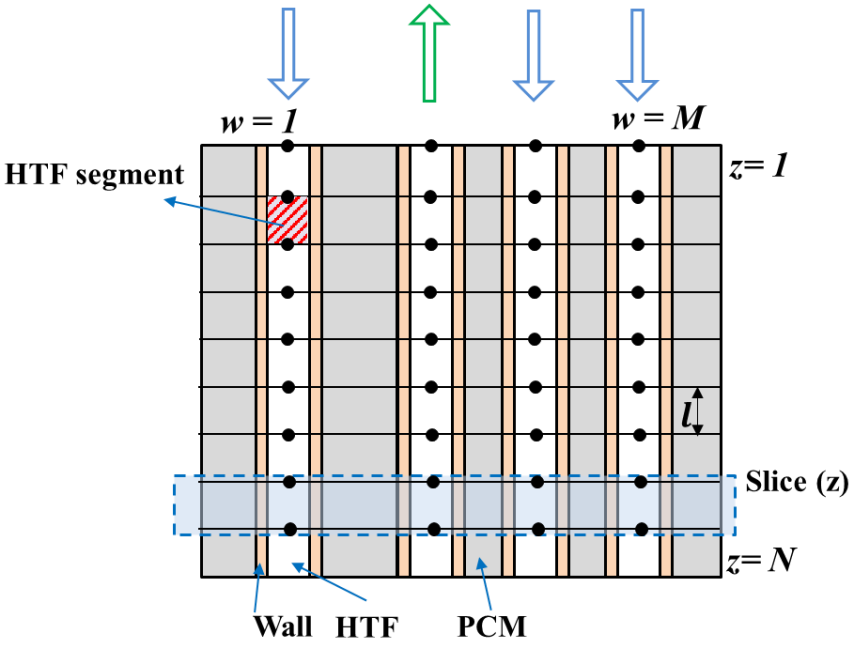


**Figure 7-3: Simplified schematic of PCMHX.**

The solution of the multi-tube PCMHX model can be divided into two levels: the slice solver and the top-level solver. The aim of the slice solver is to calculate the HTF outlet properties, such as pressure and enthalpy, given the inlet HTF states in the same slice. The aim of the top-level solver is to calculate the pressures and enthalpies of all segments in all slices as given the PCMHX inlet HTF states.

7.2.3.1 Slice Solver

Qiao et al. (2013) presented the slice-solver approach in a novel plate heat exchanger model to obtain the wall temperature and the heat transfer capacity of each HTF segment, so that the plate heat exchanger model can predict the performance of the generalized cases. Similarly, in the PCMHX model, to calculate the HTF segment

outlet properties given inlet HTF states in the same slice, wall temperatures and PCM properties need to be obtained. Thus, in the slice solver, mathematical models and calculations are based on the slice schematic as an example of Figure 7-4. The PCM block domain is bounded by red lines, and the HTF tubes are denoted as small red circles. Due to advantages of the Voronoi grid, the PCM domain is divided into nine cells using Voronoi grids denoted by black lines in the slice schematic. Points representing the cell nodes are selected randomly in the given domain. PCM Cell is denoted by P*x* (x=1, 2, …), and the vertices of edges are denoted by *Vx* (x=1, 2, …).

The enthalpy method is applied in this PCM mathematical model. The PCM cell is identified by *i* (*i*=1, 2, …9 in the given example). Edges with adjacent cells are denoted by *j*. Since the PCMHX is in quasi-steady state operation, the PCM thermal energy equation in a small time-step $\Delta t$ for each PCM cell *i* is given in Eq. (7-1). PCM effective thermal conductivity, specific heat, mass and temperature are denoted by $k_p$, $C_p$, $m_p$ and $T_p$, respectively. $L$ is the length of the cell edge, and $x$ is the distance from the cell node to the edge. $\Delta l$ is the length of each slice in the HTF flow direction. $L(j)$ is mutual edges with the neighboring cells. Therefore, the total heat transfer from adjacent cells to Cell *i* is the first term $\sum_j \frac{k_p}{2x(j)} L(j)\Delta l \left(T_p(j)^t - T_p(i)^t\right)$ in the equation.

$$m_p(i)\frac{\int_{T_p(i)^t}^{T_p(i)^{t+\Delta t}} C_p(i)^t dT}{\Delta t} = \sum_j \frac{k_p}{2x(j)} L(j)\Delta l \left(T_p(j)^t - T_p(i)^t\right) + Q_T(i)^t + Q_B(i)^t \qquad (7\text{-}1)$$

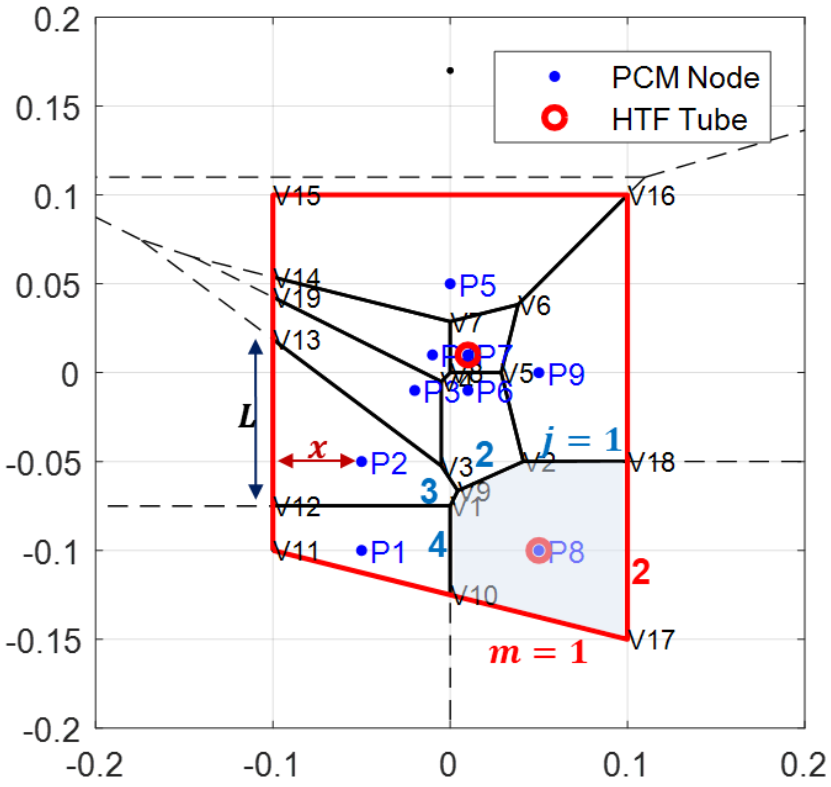


(a) PCM domain with two tubes of HTF

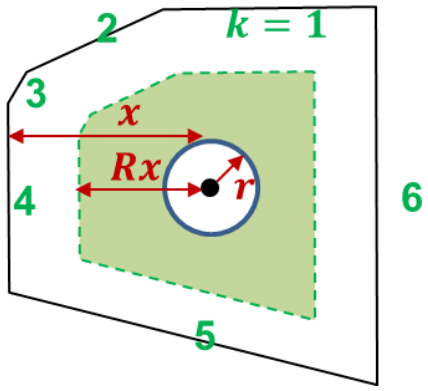


(b) Cell P8 with HTF tube coupled

**Figure 7-4: Example of the PCMHX slice schematic with the Voronoi grid.**

$Q_T$ and $Q_B$ are the heat transfer from the tube to the cell and that from the boundary to the cell, respectively. $Q_T$ calculation can be found in Eq. (7-2). If the Cell $i$ denotes

the PCM cell rather than the tub location meaning no tubes inside the cell, i.e. $i$ = 1, 2…6, 9 in the example as illustrated in Figure 7-4, the heat transfer rate from the tube to the PCM cell $Q_T$ is zero. For the Cell $i$ denotes the tube location, i.e. $i$ = 7 and 8, meaning the tube is coupled in the cell, $Q_T$ (7) and $Q_T$ (8) can be calculated once given the wall temperature $T_w$. $r$ is the tube outer diameter, and $k$ denotes the edge sequence of the cell. $x(k)$ ($k$ = 1, 2, …$K$) represents the distance from the center of the tube to the cell edge $k$. As illustrated in Figure 7-4 (b) for example, Cell P8 is coupled with the HTF tube, and $x(k)$ with $k$=1, 2, …6 represented the distance from the tube surface to six edges. Although the PCM temperatures in Cell P8 are the same everywhere, to calculate the heat transfer $Q_T$ (8) from the tube outer wall to PCM Cell P8, the equivalent 'center' is necessary to be specified for the thermal conduction area and distance calculation. The thermal conduction area is the tube outer surface area, which is $2\pi r\Delta$l. The equivalent 'center' is on the green dashed line that divides the PCM domain into two regions (the green and white) with the equal PCM volume. So that the ratio parameter $R$ with a range from 0 to 1 is proposed to specify the equivalent 'center' line as given in Eq. (7-3). Thus, the thermal conduction distance from the tube center to the edge $k$ is denoted by ( $R \cdot x(k)$ ). Therefore, the average distance is $\frac{1}{K}\sum_{k=1}^{K}\left(R \cdot x(k)\right)$.

$$Q_T(i)^t = \begin{cases} 0\ , & No\ Tube\ in\ Cell\ i \\ \frac{k_p}{\frac{1}{K}\sum_{k=1}^{K}(Rx(k))} 2\pi r\Delta l\ \left(T_W(w)^t - T_p(i)^t\right), & Tube\ in\ Cell\ i \end{cases} \quad (7\text{-}2)$$

$$R = \sqrt{\frac{\pi r^2}{\sum_k (L(k)x(k))} + \frac{1}{2}} \tag{7-3}$$

The heat transfer rate from the boundary to PCM cells, $Q_B$, can be calculated in Eq. (7-4). If the cell is not adjacent to the boundary, $Q_B$ is zero. Otherwise, $Q_B$ is obtained based on the convective heat transfer calculation given the air temperature $T_a$ and convective heat transfer coefficient $h_a$. The sequence of adjacent edges to the boundary is denoted by $m$. Therefore, $Q_B$ is the summation of the heat transfer from each boundary edge denoted by $m$. For example, the Cell P8 has two edges that is adjacent to the boundary, i.e. V10-V17 ($m$ = 1) and V17-V18 ($m$ = 2), and the $Q_B$ is the sum of heat transfer rate from PCM to the ambient through these two boundary edges.

$$Q_B(i)^t = \begin{cases} 0 \ , & Cell\ i\ is\ NOT\ adjacent\ to\ the\ boundary \\ h_{air} \sum_m L(m)\ \Delta l \left(T_a - T_p(i)^t\right), & Cell\ i\ is\ adjacent\ to\ the\ boundary \end{cases} \tag{7-4}$$

In the slice solver, once given the wall temperature, PCM temperature can be obtained by Eq. (7-5).

$$T_p(i)^{t+\Delta t} = \frac{\left(\sum_j \frac{k_p}{2x(j)} L(j)\Delta l \left(T_p(j)^t - T_p(i)^t\right) + Q_T(i)^t + Q_B(i)^t\right)\Delta t}{m_p(i)\ C_p(i)^t} + T_p(i)^t \tag{7-5}$$

HTF properties calculation is based on segment inlet conditions. The heat transder rate between the tube and the HTF is given in Eq. (7-6), in which $\alpha_f$ is the heat transfer coefficient at the HTF side determined by HTF properties and states.

$$Q_f = 2\pi r\, \Delta l\, \alpha_f (T_W - T_f) \tag{7-6}$$

The heat transfer from PCM to the wall should equal that of the wall to the HTF: $Q_T = Q_f$. $Q_T$ and $Q_f$ can be calculated from Eq. (7-2) and (7-6), respectively. Therefore, for each slice, the wall temperature can be obtained by solving the residual equation Eq. (7-7).

$$Q_f - Q_t = 0 \tag{7-7}$$

After obtained the wall temperature $T_w$ and the heat transfer rate from the wall to the HTF segment $Q_f$, the HTF segment outlet states can be determined. Since no heat exchanges in the HTF flow direction as demonstrated in the model assumption, the calculation of wall temperatures and HTF outlet states for a certain slice is independent of other slice. As a result, the slice solver can handle all slices in parallel.

7.2.3.2 Top-level Solver

The goal of the top-level solver is to obtain the HTF states of all slices given the PCMHX inlet states including HTF pressure and enthalpy for each tube. As illustrated in Figure 7-3, the number of the given inlet state variables is 2M, including pressures and enthalpies for M tubes. The unknowns, with the number of 2MN, are the pressures

and enthalpies for all segments. For example with two HTF flows as illustrated in Figure 7-4, if the PCMHX has two HTF tubes and is divided into 30 slices in the HTF flow direction, there are 120 unknowns, which consist of 60 pressures and 60 enthalpies of segments. The given 4 parameters consist of pressures and enthalpies at the PCMHX inlets of two tubes.

Figure 7-5 shows the flow chart of the calculation scheme. In the beginning, the guessed inlet pressures and enthalpies at all segments are set as the pressures and the enthalpies at the corresponding HTF tube inlets, respectively. Then, the heat transfer rate from the tube wall to PCM, $Q_T$, of all tubes at each slice can be obtained from Eq. (7-2), and heat transfer rate from the HTF to the wall, $Q_f$, can be obtained from Eq. (7-6). The wall temperature $T_w$ of all (WxM) segments can be obtained based on the residual equation Eq. (7-7) through the slice solver.

Once obtained heat transfer rate from the HTF $Q_f$, all the HTF states leaving each segment can be calculated based on $Q_f$. After that, the HTF states leaving each segment are selected as the guessed inlet states for the connected segment in the flow direction in the next iteration. Only the first segments at the HX inlet uses the given HX inlet states as the segment inlet states. For the tube with HTF downward flow, since the inlet is at the top meaning z=1, pressures and enthalpies are set as the inlet ($P$(w, z=1) = $P_{in}$(w), $h$(w, z=1) = $h_{in}(w)$). For the tube with upward flow, as the inlet is at the bottom, the pressures and enthalpies at Z = N are set as inlet values ($P$(w, z=N) = $P_{in}$(w), $h$(w, z=N) = $h_{in}(w)$).

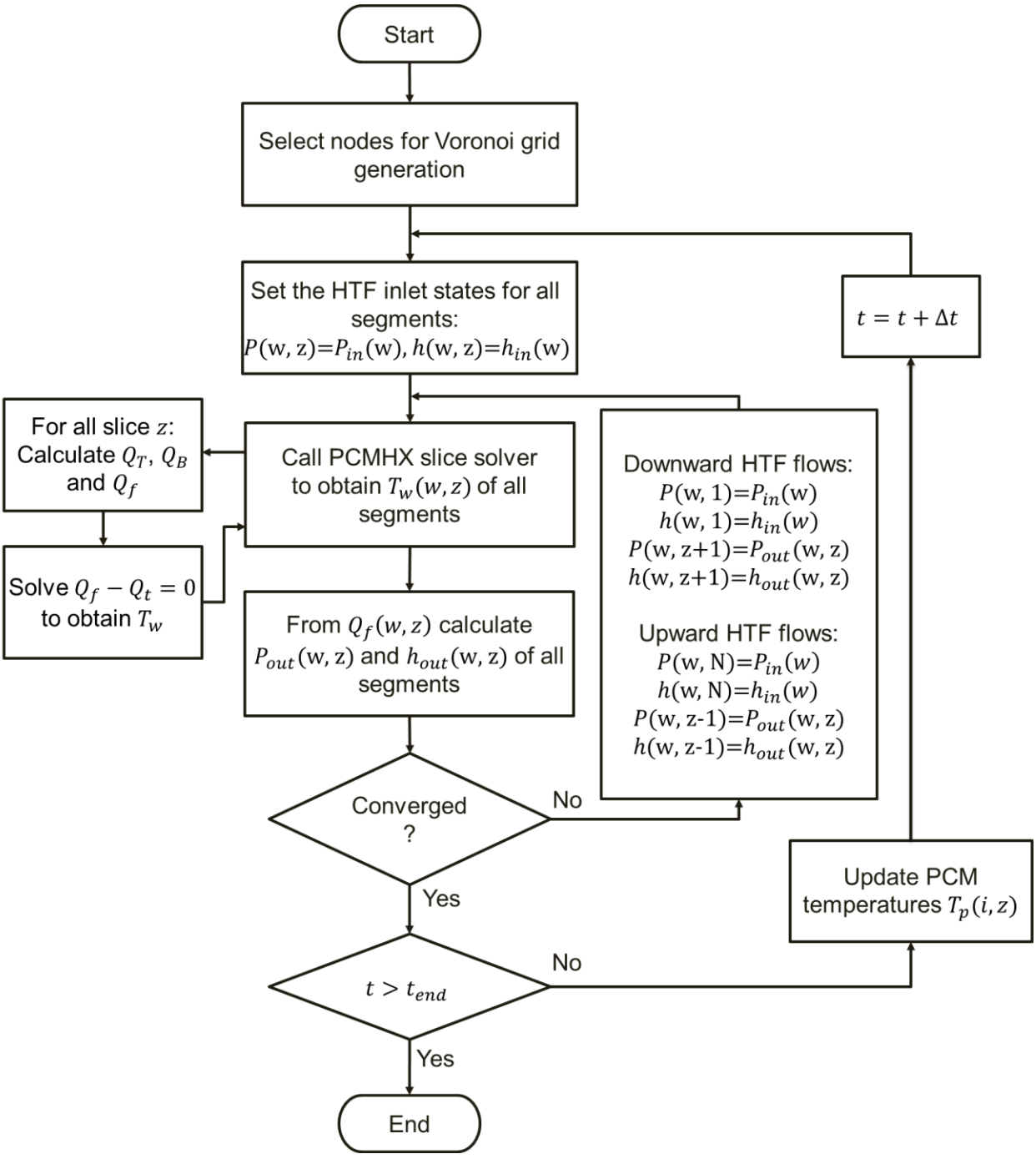


**Figure 7-5: Flow chart of the solution scheme**

This iteration terminates until the difference of the obtained HTF state leaving each segment between two successive iterations is less than the user-specified tolerance. The difference for downward flows can be represented by $|P_{out}(\mathrm{w, z})-P_{in}(w, z+1)|$ $and$ $|h_{out}(\mathrm{w, z}) = h_{in}(w, z+1)|$, and that of the upward flow can be calculated by $|P_{out}(\mathrm{w, z})-P_{in}(w, z-1)|$ and $|h_{out}(\mathrm{w, z}) = h_{in}(w, z-1)|$.

The terminated iteration means that the PCM and HTF states are solved in this time-step. Then the PCM side temperatures of each cell in each slice can be updated based on Eq. (7-5) as the heat transfer from the wall and the boundary are obtained. As long as the time is less than the operation terminal time, the calculation of HTF states for the next time step, $t+\Delta t$, can be continued.

### 7.2.4 Solution for the Example

The PCMHX example is depicted in Figure 7-4 with two HTF flows from the top to the bottom. Figure 7-6 shows the simplified schematic with 30 slices in the flow direction meaning that Z=1 denotes the top, and z=30 denotes the bottom location. The tube in the PCM Cell 7 is denoted by w = 1, and that of Cell 8 is denoted by w = 2. The PCMHX geometric parameters and the inlet states are given in Table 7-1. R-134a works as the HTF. The inlet refrigerant states are set to be constant with the two-phase conditions. HTF inlet properties and mass flow rates for two tubes are the same. The parameters such as tube diameters for two tubes are the same. The CENG/PCM is applied in this example with the horizontal effective thermal conductivity of 22 W $m^{-1}$ $K^{-1}$. Operating time is one hour with a time-step of 3 seconds.

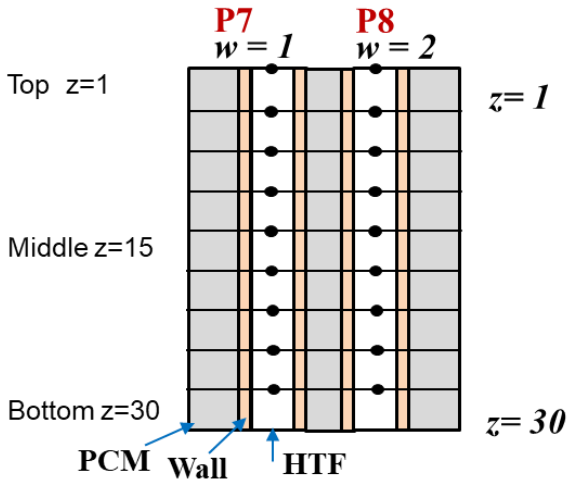


**Figure 7-6: Simplified schematic of the Example in Figure 7-4**

**Table 7-1: Input parameters for the PCMHX example**

| Parameter | | Unit | Value |
|---|---|---|---|
| PCM | Initial temperature | °C | 26 |
| | Thermal conductivity | W $m^{-1}K^{-1}$ | 22 |
| | Melting temperature | °C | 37 |
| | Latent heat | kJ $kg^{-1}$ | 210 |
| | Density | kg $m^{-3}$ | 920 |
| | Mass | kg | 12.4 |
| HTF | Inlet pressure | kPa | 1200 |
| | Inlet enthalpy | J $kg^{-1}$ | 414000 |
| | Mass flow rate | g $s^{-1}$ | 3 |
| Other information | Length | m | 0.3 |
| | Tube radius | m | 0.02 |
| | Ambient temperature | °C | 26 |
| | Operation time | s | 3600 |
| | Length for each slice | m | 0.01 |
| | Number of slices | - | 30 |

Figure 7-7 to Figure 7-9 shows the simulation results of the PCMHX example. HTF temperature is higher than the PCM initial temperature, so PCM absorbs heat and melts. As time increases, since PCM temperature increases, while the inlet HTF states are constant, the approach temperature decreases. This can lead to a decrease of the heat transfer rate of each tube and the PCMHX capacity, as illustrated in Figure 7-7 (a). HTF outlet refrigerant quality for each tube is shown in Figure 7-7 (b), in which $x$ increases due to the decrease of the heat transfer rate.

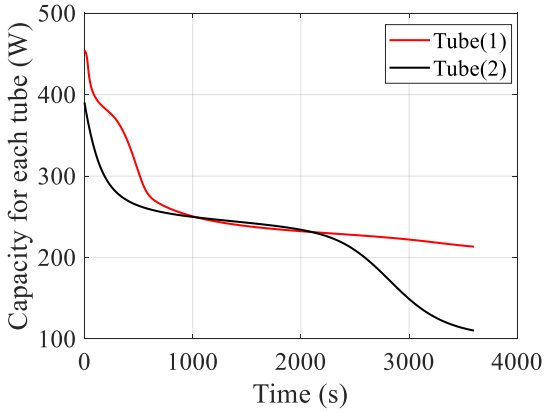


(a) Capacity for each tube

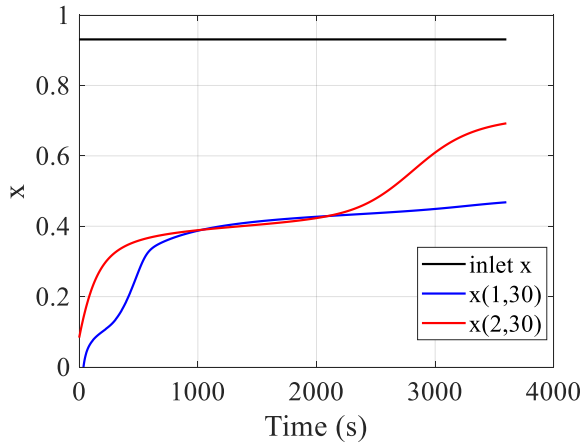


(b) HTF outlet qualities

**Figure 7-7: Capacity and HTF quality of each tube in the PCMHX example.**

Figure 7-8 (a) and (b) show tube temperatures and PCM temperature at Cell 7 and 8 at the top (z=1), middle (z=15) and the bottom (z=30), respectively, in which top tube and PCM temperatures are higher than that of the middle and the bottom. This is because of the higher HTF heat transfer coefficient with a greater quality *x* at the top. The heat transfer rates of Cell 7 before 800 seconds are greater than that of the Cell 8, so PCM temperatures of Cell 7 are greater than the Cell 8. PCM in both Cell 7 and 8 become liquid completely at the end of the operation.

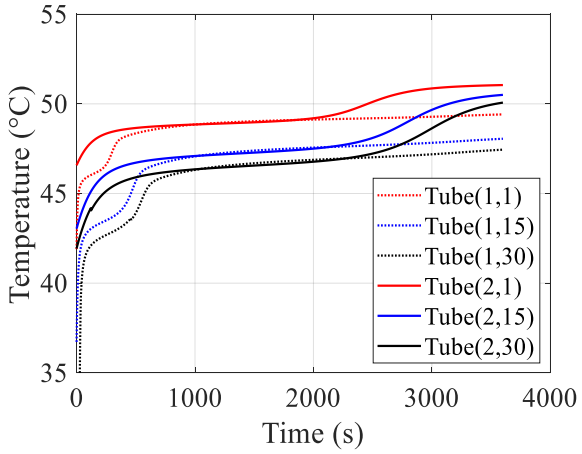


(a) Tube temperatures

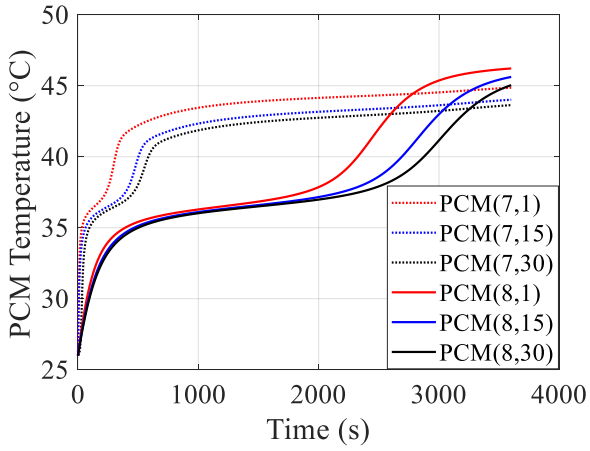


(b) PCM temperatures at the cell with tubes

**Figure 7-8: Temperatures of tubes and the adjacent PCM cells in the example.**

In addition, as shown in Figure 7-9 (a), the heat transfer rate at the top is higher than the other locations. Figure 7-9 (b) indicates that except for the PCM Cell 7 and 8, other PCM cells are still in the two-phase state.

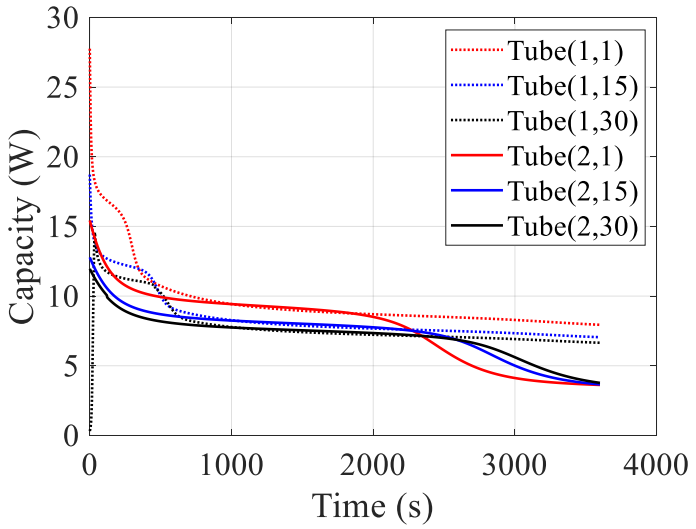


(a) Heat transfer at different segments

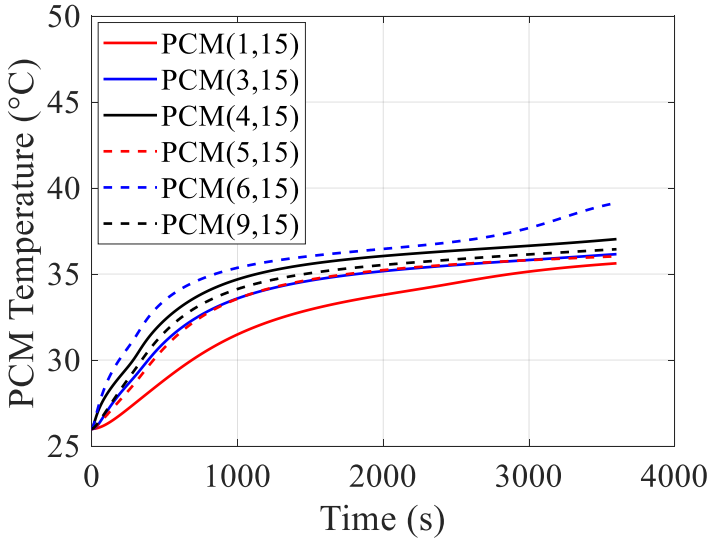


(b) PCM temperatures at cells without tube

**Figure 7-9: Other results in the PCMHX example.**

In some ways, results of the PCMHX example simulation can demonstrate that the proposed scheme can solve the multi-tube PCMHX. However, this simulation needs to be improved, since the pressure drop is not taken into consideration, and the mesh size and time step size independency need to be checked. More different parameters could be considered.

### *7.3 Model verification*

In this section, a multi-tube PCMHX design is proposed to demonstrate the ability of the proposed general-purpose PCMHX model. The multi-tube HX design is illustrated in Figure 7-10. As shown in Figure 7-10 (a), three HTF inlets are at the top of Tube 2, 4 and 5. One inlet is in the middle of Tube 7. As illustrated in Figure 7-10 (b), HTF from the bottom of Tube 2 splits into two flows entering Tube 1 and Tube 3. Through Tube 5 and Tube 4, HTF flow into Tube 8 and Tube 6 from the bottom to the top respectively. In Tube 7, HTF splits into two flows with one upward and one downward. The mass flow rate of the Tube 2 equal the sum of the Tube 1 and Tube 3. The tube diameters of Tube 1 and Tube 6 are greater than the others. In summary, the proposed configuration has 8 tubes, 4 flows, 4 inlets, 5 outlets, 2 different tube diameters and 2 different mass flux. Based on the specification of this multi-tube PCMHX design, the capability of the current model can be explained in detail.

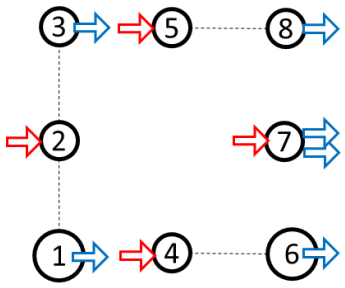


(a) Top view of HTF flows

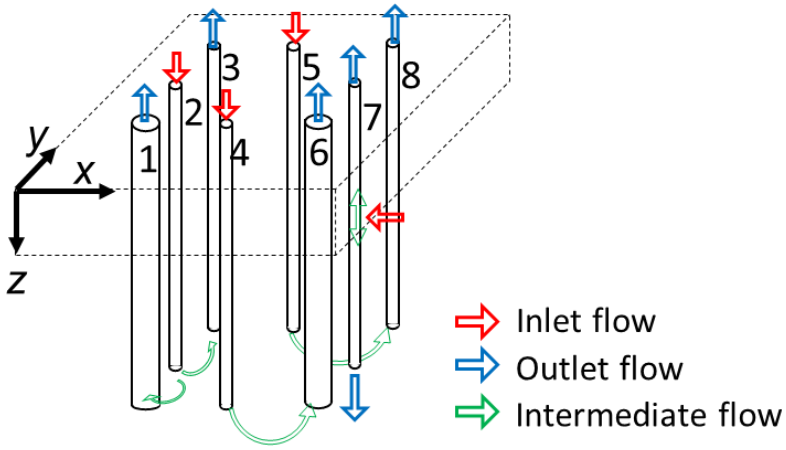


(b) HTF flow directions and tube arrangements

**Figure 7-10: HTF flow configuration of the proposed multi-tube PCMHX**

The Voronoi grids for each slice of this PCMHX configuration are illustrated in Figure 7-11. The total number of the PCM cell is 129. Vertices of each cell are denoted by V*x* (*x* = 1, 2, …). The dimension of the cross-section area of the PCM block is 0.1 m x 0.1 m. Table 7-2 lists the inlet parameters for the simulation. The selected HTF is R-134a, and the inlet states are set as constant. HTF inlet temperature is 60.5 °C at a quality of 0.91. For single-phase HTF flow, the heat transfer coefficient is calculated from correlations proposed in (Gnielinski, 2013). For two-phase flow, the heat transfer coefficient calculation was based on the correlation in (Shah, 2009). In this preliminary

modeling process, the pressure drop is ignored. The heat loss from the PCM boundary to the surrounding is considered. The CENG/PCM is applied with the melting temperature of around 37 °C and the horizontal effective conductivity of 22 $Wm^{-1}$ $K^{-1}$.

Since HTF flow directions for these eight tubes are different, in the iteration process of the top-level solver, enthalpies and pressures of the HTF in Tube 1, 3, 6 and 8, which has the inlet at the bottom, have the different iteration update direction compared with other tubes.

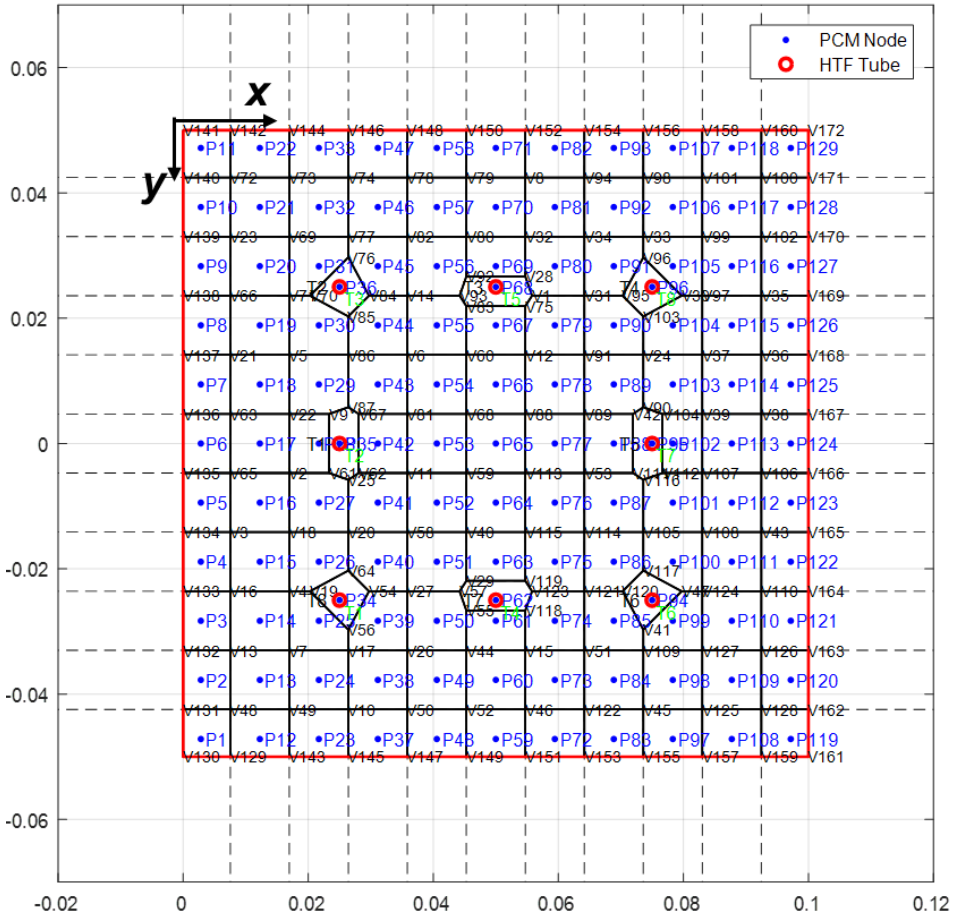


**Figure 7-11: Slice schematic of the proposed multi-tube PCMHX design with the generated Voronoi grid**

**Table 7-2: input parameters for the proposed multi-tube PCMHX**

| Parameter | | Unit | Value |
|---|---|---|---|
| PCM | Initial temperature | °C | 26 |
| | Thermal conductivity | W $m^{-1}K^{-1}$ | 22 |
| | Melting temperature | °C | 37 |
| | Latent heat | kJ $kg^{-1}$ | 210 |
| | Density | kg $m^{-3}$ | 920 |
| | Mass | kg | 5.52 |
| HTF | Inlet pressure | kPa | 1,700 |
| | Inlet enthalpy | kJ $kg^{-1}$ | 414 |
| | Mass flow rate | g $s^{-1}$ | Tube 2: 5<br>Other tubes: 2.5 |
| Other information | Length | m | 0.6 |
| | Tube radius | m | Tube 1 and Tube 6: 0.004<br>Other tubes: 0.003 |
| | Ambient temperature | °C | 26 |
| | Operation time | s | 2,000 |
| | Length for each slice | m | 0.02 |
| | Number of slices | - | 30 |

The simulation results based on the developed model are illustrated in Figure 7-12 and Figure 7-13. Figure 7-12 shows the HTF qualities *x* at the inlet and outlet of each tube. The inlet is at the top of Tube 2, so that *x* (2, z=1) is constant. *x* (2,30) means the outlet quality of Tube 2, and it is also the inlet quality of Tube 1 and Tube 3, which

increases with the time because of the decrease heat transfer rate as discussed in the last section. *x* at Tube 3 outlet (z=1) is greater than that of Tube 1 due to the greater heat transfer rate. This is because the diameter of Tube 1 is greater, while the mass flow rates of Tube 1 and Tube 3 are the same. Figure 7-12 (b) shows the qualities of Tube 4 and Tube 5 with inlets at the top and that of the Tube 6 and Tube 8 with inlets at the bottom. The quality difference between the Tube 6 and 8 is due to the different tube diameter and the heat transfer area.

In addition, Figure 7-12 (c) illustrates the HTF states at different locations along with Tube 7 including the top outlet, ¼ length from the top, the inlet at the middle, ¾ length from the top and the bottom outlet. HTF qualities are symmetric with the middle inlet, since HTF from the inlet at the middle splits into two equal steams towards the top and bottom individually. Since the heat transfer area of one single stream in Tube 7 is less than that of the others, the heat transfer rate along Tube 7 is less, and qualities at Tube 7 outlets are greater compared with other tubes.

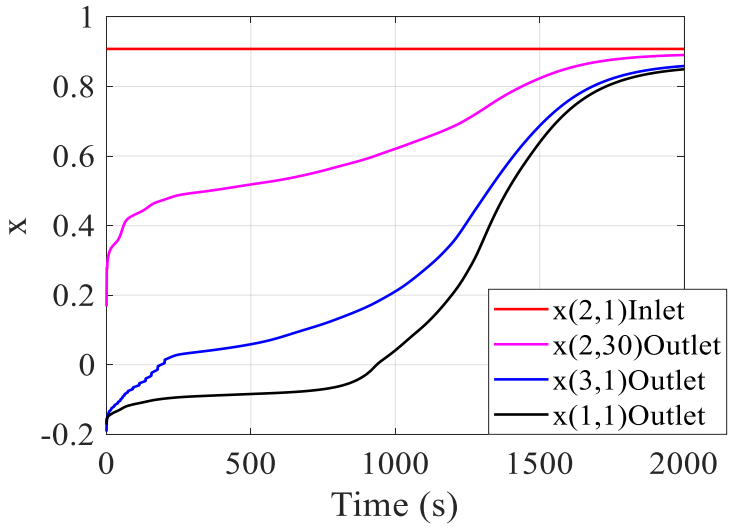


(a) HTF *x* at the inlet and outlet of Tube 1, 2 and 3

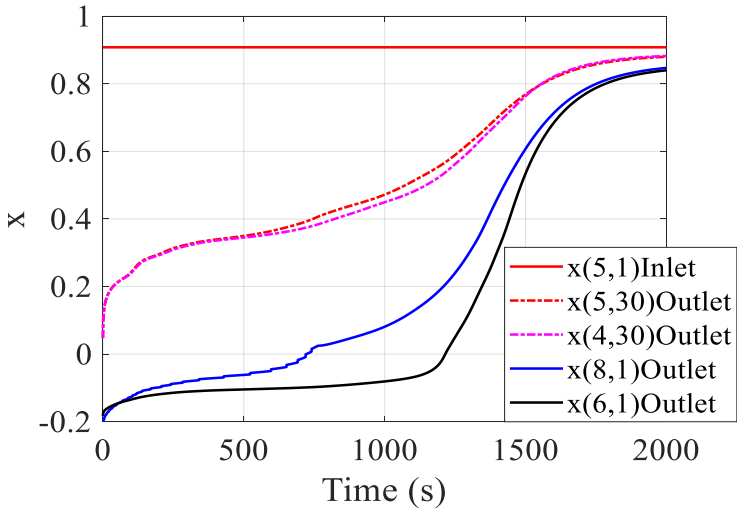


(b) HTF *x* at the inlet and outlet of Tube 4, 5, 6 and 8

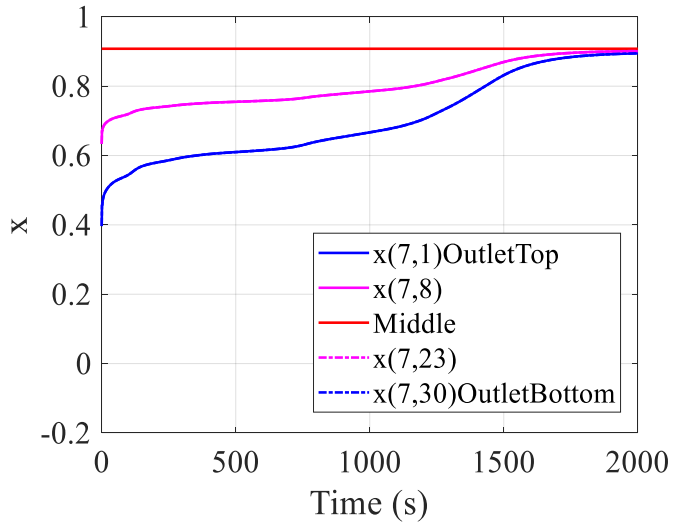


(c) Tube 7 HTF *x* at the inlet (middle), outlet (the top and bottom), and ¼ and ¾ of the length from the top

**Figure 7-12: Evolutions of HTF qualities**

Figure 7-13 illustrates the PCM temperature profiles changed with time in the selected cross-section area A. The cross-section area A is parallel to the HTF flow direction and overlapped with tube axes of Tube 2 and Tube 7 as illustrated in Figure 7-13 (a).

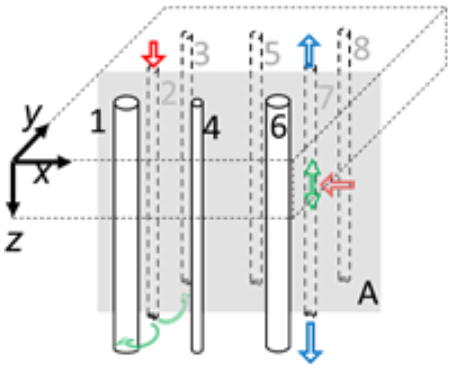


(a) Selected cross-section area A

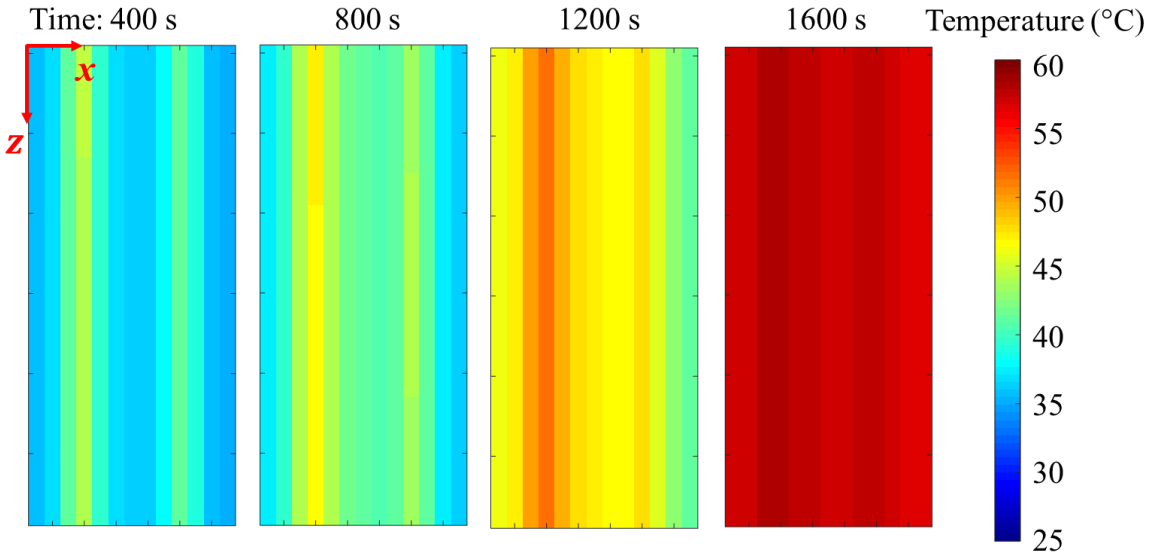


(b) PCM temperature profiles

**Figure 7-13: PCM temperature files in the selected cross-section area**

Two bars with higher temperatures represent temperatures of the PCM close to the walls of Tube 4 and 7 as shown in Figure 7-13 (b), in which the left one denotes the Tube 2 and the right is the Tube 7. It shows that the temperature near Tube 2 is higher than that of Tube 7, which is due to the greater heat transfer rate along with Tube 2. It is noted that PCM melting along the HTF flow direction is very uniform compared with the temperature profile of Figure 5-5 in Chapter 5. At 1600 s, all PCM is melted. This

is because of the more reasonable HTF flow arrangement in this PCMHX design, in which inlets and outlets are set on the same side. The region with a slower PCM melting rate is affected by the region with a higher PCM temperature. Therefore, the PCM temperature distribution is more uniform compared with that of the single-tube PCMHX unit as illustrated in Figure 5-5.

## *7.4 Improvement Aspects in Future Work*

The model verification shows that this preliminary model can handle multi-tube PCMHX with complicated HTF flow arrangement. This preliminary PCMHX model still needs to be improved in the following aspects:

- The pressure-drop correlations need to be implemented.
- The model with different inlet parameters needs to be verified.
- Although the model is designed to handle the PCMHX with different cross-section areas, such as helical tube HX, more cases with different cross-sections should be tested.
- PCM thermal conduction and/or free convection enhancement effects in the HTF flow direction can be considered in the future improved model.
- Computational speed needs to be considered.
- An experimental study for multi-tube PCMHX is required for model validation.

## *7.5 Chapter Summary*

This chapter proposes a new generalized model to predict the thermal performance for comprehensive multi-tube PCMHXs. The model divides PCMHX into slices in the

HTF flow direction. Non-uniform grids, i.e. Voronoi grids, are generated for PCM side domain discretization. In each slice, the heat transfer from the wall to PCM and that from the HTF to the wall are calculated separately once given the guessed wall temperatures. The wall temperature can be obtained in each slice solution. HTF states of all segments in all slices can be solved through the iteration process.

In addition, the preliminary model is verified by a new PCMHX design, which has 8 tubes and a complex flow configuration. The result shows that this preliminary model can solve multi-tube PCMHX with complicated tube configuration.

# Chapter 8: Conclusions and Future work

## *8.1 Conclusions*

This dissertation focuses on the investigation of a VCC-based PCS with PCMHX and the development of the general-purpose PCMHX model. The heat-transfer-enhanced PCM was used for thermal storage in the condenser. Both experimental and numerical studies were carried out for PCS performance analysis and PCM thermal characteristics discussion, in which a challenge of uneven PCM melting was observed. To improve the system performance, the effect of the subcooling was then discussed and several solutions were proposed. In addition, to widen the application of the PCMHX model, a generalized multi-tube PCMHX model was developed to predict the performance of comprehensive PCMHX configurations. The conclusions include the following aspects.

- The PCM enthalpy-temperature correlation based on the DSC curve was proposed for the development of the PCMHX model.
- PCM heat transfer enhancement is necessary to decrease the condenser temperature and increase the system COP for the PCS. Compared with the baseline, which is non-enhanced PCMHX, PCM/CENG composite PCMHX (ET-GM) was found to be the best with the highest COP (49% over baseline), highest UA (2.6 times higher than the baseline), and 18% smaller inner volume. The copper-sponge-enhanced PCMHX (ET-CS) was the second-best with 32% increased COP, 30% higher UA, and two times larger heat transfer area. Coupled with CENG, the overall heat transfer

coefficient reached more than 900 $Wm^{-2} K^{-1}$, and the PCM effective heat transfer coefficient was increased by a factor of 10.

- The PCS integrated CENG/PCMHX experimental study shows that the proposed PCS can provide a stable cooling with a capacity of 160 W for 4.5 hours. The higher ambient temperature can result in higher cooling capacity as well as a higher COP. COP can increase by 19% with the ambient temperature increased from 26°C to 31°C, while the performance degradation happened earlier. In addition, the compressor speed of 3,100 rpm in the recharge cycle is recommended for 30% reduced recharge time and only 8% reduced overall COP, compared with the baseline. The cooling time should be controlled in less than 5 hours to prevent the reduction of system performance.
- Based on the model validation, the developed PCM-coupled VCC system model can predict both system and PCMHX melting performance well within the deviation less than 7%. The effect of the compressor power shows that it cannot only affect the condenser capacity but also the PCM melting distribution. Uneven heat transfer in PCMHX was analyzed. In the current design, the uneven PCM melting was due to the lower refrigerant side heat transfer coefficient instead of the lower approach temperature near the outlet of the condenser. The numerical study shows that with smallest subcooling and refrigerant charge, the duration of Stage II plus Stage I can increase by 28%, 65%, 89%, respectively, compared with other cases.

- The experimental study on the effect of the NSD shows that the optimal subcooling was 5 K with the maximum COP of 4.2 as PCM performed phase change. However, considering the entire cooling cycle, the less subcooling was preferred. For NSD of 0.8 K, COP is decreased by 31.3% for 5.5 hours, while for NSD of 5 K, by 44.2%. Several suggestions to eliminate the subcooling effect were proposed considering the current system design and the other future PCM-to-refrigerant HX application.
- The general-purpose PCMHX model was developed using a novel multi-tube heat exchanger heat transfer algorithm. The slice solver and top-level solver were implemented. For the PCM side, Voronoi grids were applied to achieve the flexibility of the model. The preliminary model can handle multi-tube PCMHX and was verified by a PCMHX example. Some aspects of future work were provided to improve this generalized PCMHX model.

## *8.2 Future work*

Based on the knowledge obtained from the experimental and numerical investigation in the study, future research could focus on the following aspects.

### 8.2.1 PCM Heat Transfer Enhancement

It is needed to investigate more on PCM heat transfer enhancement methods. The heat transfer enhancement methods are listed in Chapter 1. However, most of the studies focused on the simple PCMHX configuration, such as a single tube cylinder heat exchanger. In addition, the HTF-side heat transfer conditions can affect the PCM-side heat transfer enhancement. Although this study shows the different heat transfer

enhancement in multi-tube PCMHX, the configuration is quite simple. Therefore, wider and more complicated PCMHX applications, such as the HX shown in Chapter 7 with four inlets and 5 outlets, need to be considered.

The effect of the CENG fraction needs to be investigated. For the CENG/PCM HX with a specific volume as illustrated in Table 8-1, more CENG matrix can lead to less PCM volume but higher effective conduction. As a result, the condenser pressure can be lower, however, the cooling time is reduced with a certain terminal condensing pressure. Therefore, there is a tradeoff between condensing temperature and the cooling time. Thus, the effect of the CENG fraction needs to be investigated. Similarly, parameters in other PCM heat transfer enhancement methods could also be considered to improve the performance as apply in systems.

The effective thermal conductivity with different heat transfer enhancement methods needs to be investigated. The thermal conductivity used in this study comes from the literature, however, for some heat transfer enhancement methods, there is a research gap of the measurement of the thermal conductivity. For example, Figure 8-1(a) shows the pourable-CENG PCM with different gravel sizes, and (b) shows an example of the PCMHX. The advantage of the pourable-CENG PCMHX is that different gravels can be easier to be filled in the PCM container, and after filled with pure PCM, the gaps between CENG and the tubes can be much smaller to reduce the thermal resistance. However, the effective thermal conductivity has not been investigated. Considering the easier manufacturing process and the potentially better thermal performance, the measurement and investigation of the pourable-CENG matrix are necessary.

**Table 8-1: CENG/PCM HX specification with different CENG volume fractions**

| CENG Volume fraction | -- | 2% | 4% | 6% | 8% | 10% | 12% | 14% | 20% | 26% |
|---|---|---|---|---|---|---|---|---|---|---|
| Mass of CENG | kg | 0.694 | 1.388 | 2.082 | 2.776 | 3.47 | 4.164 | 4.859 | 6.941 | 9.023 |
| Volume of CENG | $10^{-3}$ $m^3$ | 0.31 | 0.61 | 0.92 | 1.23 | 1.53 | 1.84 | 2.15 | 3.07 | 3.99 |
| Mass of PCM | kg | 13.8 | 13.6 | 13.3 | 13.0 | 12.7 | 12.4 | 12.1 | 11.3 | 10.5 |
| Volume of PCM | $m^3$ | 15 | 14.7 | 14.4 | 14.1 | 13.8 | 13.5 | 13.2 | 12.3 | 11.4 |
| Total Mass | kg | 14.5 | 14.9 | 15.4 | 15.8 | 16.2 | 16.6 | 17.0 | 18.2 | 19.5 |
| Total Volume | $m^3$ | | | | | 0.0153 | | | | |
| CENG Mass fraction | -- | 4.8% | 9.3% | 13.6% | 17.6% | 21.4% | 25.1% | 28.6% | 38.1% | 46.3% |
| Porosity | - | 98% | 96% | 94% | 92% | 90% | 88% | 86% | 80% | 74% |
| Bulk density | kg $m^{-3}$ | 45.2 | 90.4 | 135.7 | 180.9 | 226.1 | 271.3 | 316.5 | 452.2 | 587.9 |
| $k_{\parallel}$ | $Wm^{-1}K^{-1}$ | 3 | 4.1 | 4.9 | 5.5 | 6 | 6.3 | 6.6 | 7.2 | 7.5 |
| $k_{\perp}$ | $Wm^{-1}K^{-1}$ | 2.9 | 8.3 | 15.2 | 23.5 | 32.9 | 43.2 | 54.5 | 93.2 | 138.2 |

The effective thermal conductivity with different heat transfer enhancement methods needs to be investigated. The thermal conductivity used in this study comes from the literature. However, for some heat transfer enhancement methods, there is a research gap of the measurement of the thermal conductivity. For example, Figure

8-1(a) shows the pourable-CENG PCM with different gravel sizes, and (b) shows an example of the PCMHX. The advantage of the pourable-CENG PCMHX is that different gravels can be easier to be filled in the PCM container, and after filled with pure PCM, the gaps between CENG and the tubes can be much smaller to reduce the thermal resistance. However, the effective thermal conductivity has not been investigated. Considering the easier manufacturing process and the potentially better thermal performance, the measurement and investigation of the pourable-CENG matrix are necessary.


(a) Different sizes of CENG gravels

(b) Pourable-CENG PCMHX

**Figure 8-1: The example of a Pourable-CENG PCMHX and Pourable-CENG gravels**

### 8.2.2 Personal Cooling

More experimental studies for the PCS as illustrated in Chapter 4 needs to be addressed. The effects of the ambient temperature, compressor speed and cooling are discussed. However, more parameters need to be considered. The system performance in a various ambient temperature or various air flow rate can be further investigated. Since in the realistic application, the room temperature varies in the daytime, and occupants can adjust the air-flow rate or compressor speed depending on their preference. The effective cooling capacity also needs to be evaluated and the current capacity design may be modified. More detailed experiments can improve personal cooling performance.

### 8.2.3 PCM coupled PCS Simulation

The PCMHX and the coupled system models in Chapter 5 need to be improved. More numerical study in terms of CENG porosity, PCMHX geometric parameters and system operation conditions need to be performed, and the according PCM melting performance should be analyzed. For example, with different tube numbers, the PCS system performance could be different as illustrated in Figure 8-2. The system operation parameters are the same as in Chapter 5. The compressor speed is 2200 rpm and leads to a mass flow rate of about 1 $gs^{-1}$. In this example, the mass flux in each case is the same. Other PCMHX parameters are listed in Table 8-2. The example shows that the PCMHX with more tubes could have a greater COP and lower condenser temperature. However, more parametric studies should be addressed to find the optimal design. In addition to PCMHX parameters, better system design can be done based on

the current Dymola model to figure out potential solutions for more even PCM melting and thus longer cooling time.

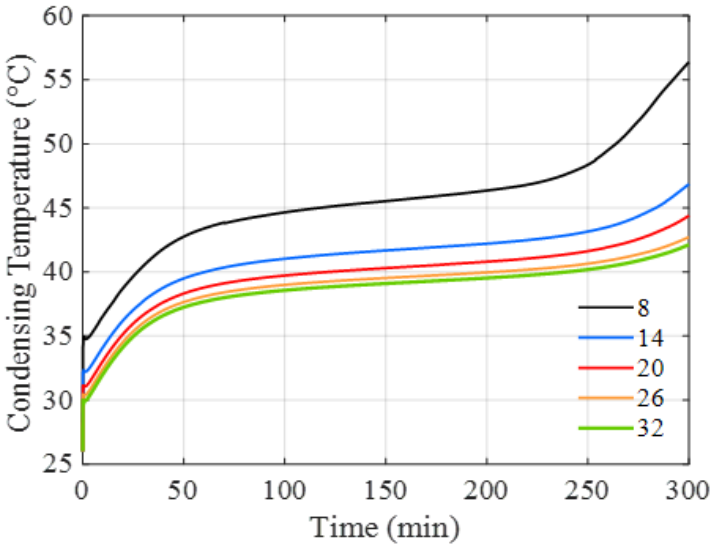


(a) Condensing temperature

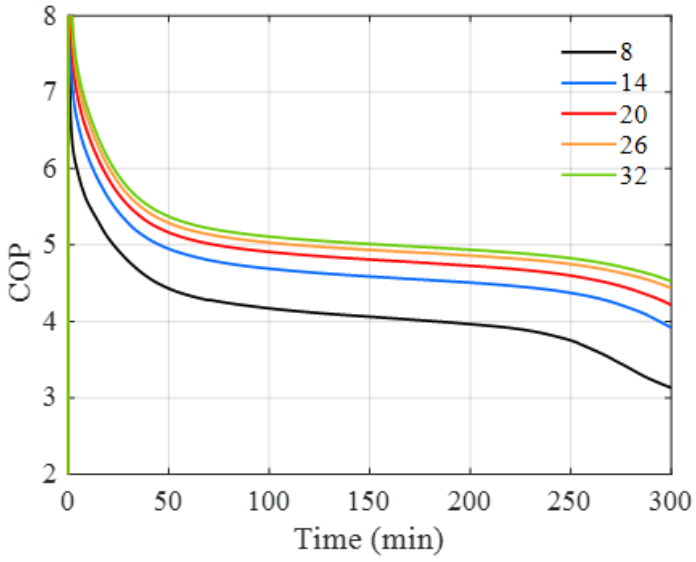


(b) System COP

**Figure 8-2: The example of the parametric study with different tube numbers and the same mass flux in PCMHXs**

**Table 8-2: Parameters in the example of a PCMHX parametric study**

| Parameter | Unit | Value |
|---|---|---|
| Mass flow rate | kg $s^{-1}$ | ~0.001 |
| Mass flux | kg $s^{-1}$ | ~25 |
| $A_{cross,total}$ | $10^{-6}$ $m^{-2}$ | 40 |
| Tube wall thickness | mm | 0.76 |
| Tube length | m | 0.29 |
| Tube number | -- | 8, 14, 20, 26, 32 |

### 8.2.4 PCMHX Design Improvement and Optimization

As for the PCMHX, to take advantage of more latent of the bottom PCM, new PCMHX designs need to be proposed and optimized. The uneven PCM mass distribution could be considered in new PCMHX designs. Figure 8-3 shows an example. The baseline is the same as the eight-tube PCM/CENG HX in Chapter 4, and the PCM model is simplified into a single-tube unit as described in Chapter 4. The length of the tube is L, and the radius is denoted by R. In the new design, the length L keeps the same with the baseline to maintain the same heat transfer area, while PCM is divided into the top and bottom sections with different radius. The top radius is greater than the bottom considering the greater heat transfer flux at the top. The total mass of the PCM for the new design and the baseline are identical for performance comparisons. Figure 8-4 shows the system pressures for both designs, and terminal pressures are the same. It shows that the new design (green line) can achieve a cooling time of 320 minutes, which increases by 18%. Since the heat transfer area and the PCM composite thermal

properties for both designs are the same, the pressures of these two PCMHXs are almost the same before 160 min.

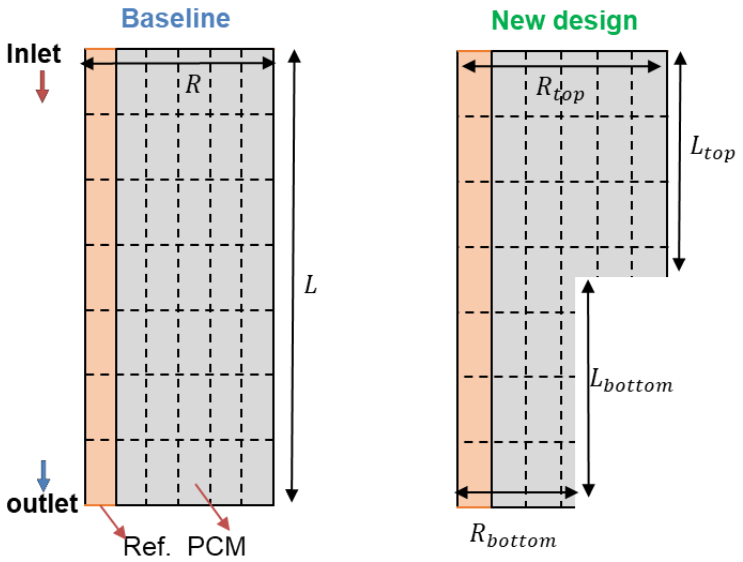


**Figure 8-3: The example of the new PCMHX design and the baseline with single-tube unit**

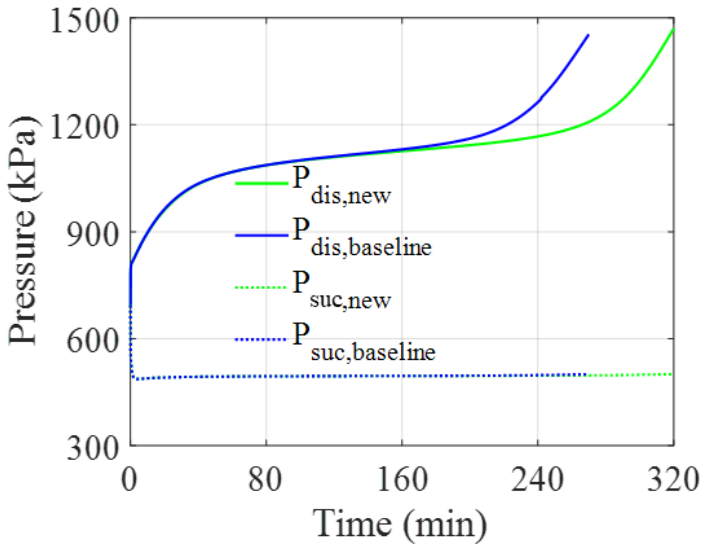


**Figure 8-4: Pressure comparison between two PCMHX designs**

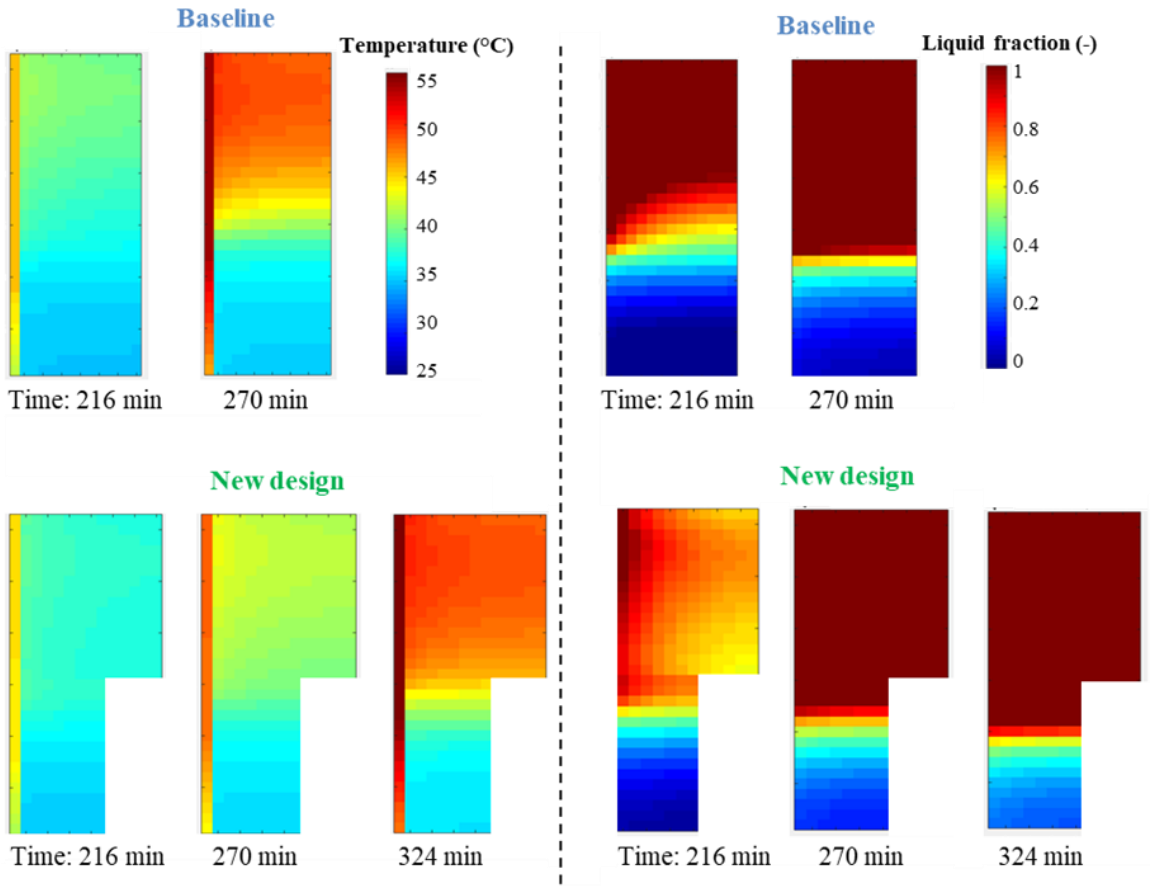


(a) Temperature (b) PCM liquid fraction

**Figure 8-5: PCM and refrigerant temperature profiles and PCM liquid fractions during the cooling cycle for both PCMHX designs**

Figure 8-5 shows the PCM and refrigerant temperature profiles and the liquid PCM fractions of both PCMHX designs changed with the cooling time. At 216 minutes, although PCM temperatures of both designs are similar, the liquid fraction of the baseline is much greater than that of the new design. At the end of the cooling time, PCM melting rates in the new design are more uniform than the baseline, which explains the reason for the longer cooling time of the new design. Based on this

example, it is noted that new PCMHX designs are needed to improve PCMHX thermal performance considering the effect of uneven PCM melting.

### 8.2.5 PCM-coupled System Improvement

As discussed in Section 6.4.3, system-level improvement is needed. For other systems applied PCM condensers, adding a sub-cooler after the PCM-to-refrigerant condenser and controlling the temperature at the outlet of the PCM condenser to keep the refrigerant two-phase could help to reduce the impact of the uneven heat transfer flux along the condenser tube length direction, although the heat transfer coefficient still changes slightly with refrigerant quality. In addition, applying a subcooling regenerator is also a great choice, since it can be beneficial for both reducing the subcooling effect on PCM melting and increasing condensers and evaporators capacity.

### 8.2.6 General-purpose PCMHX Model Development

The preliminary general-purpose PCMHX model, as presented in Chapter 7, needs to be improved in several aspects: (1) In the current model, to save computational time, the pressure drop is ignored. In future work, pressure-drop correlations need to be implemented. (2) The model with different inlet parameters needs to be verified to demonstrate the robustness of the model. (3) Although the model is designed to handle the PCMHX with different cross-section areas, such as helical tube HX, more PCMHX cases with different cross-sections should be tested. (4) Equivalent heat transfer coefficients evaluating the PCM natural convection need to be implemented in the model to widen the selection of the PCM. (5) PCM thermal conduction and/or free convection enhancement effects in the HTF flow direction can be considered in the

further improved model. (6) Computational speed needs to be considered. (7) More experimental investigation for multi-tube PCMHX are required for model validation.

# Chapter 9: Contributions

## *9.1 Summary of Contributions*

This dissertation presents the investigation on PCM heat transfer enhancement methods, PCS and PCMHX, and the development of the general-purpose PCMHX model. The major contributions are summarized as follows:

**1. PCM Heat Transfer Enhancement Methods (Chapter 3)**

- Ranked different PCM heat transfer enhancement methods with new complicated boundary conditions
    - In Chapter 3, the thermal performance of the PCM was improved by applying different heat transfer enhancement methods. It was demonstrated that the graphite matrix has the best heat transfer enhancement compared with the copper sponge. Moreover, the refrigerant temperature variation at the PCMHX inlet cannot be predicted and obtained in advance, so the boundary conditions in this study are more complicated than that in the literature. The dissertation presented different enhanced-PCMHX performance comparisons with new complicated boundary conditions.
- Extended the system-level PCM heat transfer enhancement application
    - Most previous research on PCM heat transfer enhancement usually applied water-loop systems with constant inlet temperatures or constant wall temperatures, so that the PCMHX capacity decreased with time, which limits the application of the PCMHX. Reversely,

Chapter 3 demonstrated the steady PCMHX capacity with various inlet HTF conditions. This HTF condition essentially reflected systems' response to the PCM thermal performance. The research results can be further used in other complicated systems, in which PCM works as a condenser.

- Analyzed the uneven PCM melting in the horizontal direction and its effects on the condenser temperature
    - In Chapter 3, it was also highlighted the influence of the uneven PCM melting in the horizontal direction caused by the maldistribution of the HTF, which was not found in any previous study. It was demonstrated that the uneven HTF flow in the PCMHX can lead to performance degradation, which needs to be prevented in further PCMHX applications.

**2. PCS Experimental Investigation (Chapter 4)**

- Analyzed the VCC-based PCS with cooling and regeneration cycles
    - Chapter 4 investigated the PCS system with PCMHX. It established the system operation of the proposed PCS. The personal cooling performance is better than other PCS technologies due to its longer cooling time, shorter recharge time, higher movability, more steady cooling capacity and higher coefficient.
- Evaluated the PCS performance considering the effects of thermostat setpoint, recharge rates and cooling time

- The experimental parametric study presented the performance variation with changed operating conditions, i.e. thermostat setpoint, recharge rates and cooling time, which can provide the significant information of this PCS for further real application.

**3. PCM-coupled PCS Model Development and Simulation (Chapter 2 and Chapter 5)**

- Proposed a correlation of PCM temperature and enthalpy
  - In Chapter 2, the developed the temperature-enthalpy correlation of PureTemp37 can be used for PCM model development and melting process analysis.
- Developed a 2-D PCM-to-refrigerant condenser model and the coupled system model
  - Chapter 5 developed and validated a 2-D PCM-to-refrigerant model and coupled PCS model. Since in previous research, the common HTF was in a single phase. The detailed PCMHX model considered the refrigerant-side state variation and fulfilled the literature research gap.
- Evaluated the uneven melting considering refrigerant-side condition variation
  - Chapter 5 also revealed the reason for the uneven PCM melting in the HTF flow direction, which is the uneven heat transfer coefficient instead of the uneven approaching temperature. The analysis of the effects of the uneven PCM melting showed that to

obtain a better system performance and longer cooling time, more uniform PCM was suggested. It highlighted the drawback of using phase-change HTF and provided insights on PCM-to-refrigerant HX application.

**4. Investigation on Refrigerant Subcooling Effects on PCM-coupled Systems (Chapter 6)**

- Filled the research gap of the effect of refrigerant subcooling on uneven PCM melting and system performance
    - Based on the experimental study, Chapter 6 presented the subcooling effect analysis on PCM-coupled VCC systems and filled the research gaps on the PCMHX. The research on subcooling influence on regular VCC systems can be found. However, there was a research gap about the subcooling effect on PCM-coupled VCC systems. In these systems, subcooling can affect not only the VCC but also the PCM melting performance and the liquid PCM distribution, which was necessary to be investigated.
- Proposed guidelines to reduce the negative influence of the uneven PCM melting for future studies
    - Chapter 6 proposed guidelines to reduce the negative effect of uneven PCM melting in three aspects: subcooling selection of the current system, PCMHX component improvement and system-level modification. These insights can improve PCMHX-coupled system performance in further investigation and application.

**5. Development of the General-purpose PCMHX Model (Chapter 7)**

- Achieved the PCMHX model flexibility by developing a new algorithm, and filled the research gap of 3-D general-purpose multi-tube PCMHX model
    - Chapter 6 developed a new algorithm for PCMHX modeling to achieve model flexibility. The generalized model considered variable tubes and PCM arrangement. Tube numbers, HTF types, HTF flow numbers, PCM shapes, and other parameters can be selected by users. Since no such general-purpose multi-tube PCMHX models have been found, the proposed model filled the research gap.
- Provided PCMHX design and optimization approach
    - The flexible model can be used as a PCMHX design tool in further study. In addition, the model can be used for PCMHX parameters optimization.

## *9.2 List of Related Publications*

Based on this work, four journal papers and two conference papers were published, and three more papers are under development. The publication outcomes are listed as follows:

### 9.2.1 Peer-reviewed Journal Papers

**Y. Qiao**, T. Cao, J. Muehlbauer, Y. Hwang, R. Radermacher, Experimental study of a personal cooling system integrated with phase change material, Appl. Therm. Eng. 170 (2020).

**Y. Qiao**, Y. Du, J. Muehlbauer, Y. Hwang, R. Radermacher, Experimental study of enhanced PCM heat exchangers applied in a thermal energy storage system for personal cooling, Int. J. Refrig. 102 (2019) 22–34.

R. Dhumane, **Y. Qiao**, J. Ling, J. Muehlbauer, V. Aute, Y. Hwang, R. Radermacher, Improving system performance of a personal conditioning system integrated with thermal storage, Appl. Therm. Eng. 147 (2019) 40–51.

R. Dhumane, A. Mallow, **Y. Qiao**, K.R. Gluesenkamp, S. Graham, J. Ling, R. Radermacher, Enhancing the thermosiphon-driven discharge of a latent heat thermal storage system used in a personal cooling device, Int. J. Refrig. 88 (2018) 599–613.

### 9.2.2 First-authored conferences papers

**Y. Qiao**, T. Cao, Y. Hwang, J. Ling, V. Aute, Numerical investigation on PCM-to-refrigerant heat exchangers for thermal energy storage, in: 13th IEA Heat Pump Conf., 2020

**Y. Qiao**, A. Mallow, J. Muehlbauer, Y. Hwang, J. Ling, V. Aute, R. Radermacher, K.R. Gluesenkamp, Experimental Study on Portable Air-Conditioning System with Enhanced PCM Condenser, 17th International Refrigeration and Air Conditioning Conference, 2018 Purdue University.

### 9.2.3 Publications under development

**Y. Qiao**, T. Cao, Y. Hwang, R. Radermacher, Experimental investigation on subcooling effects of phase change material (PCM)-to-refrigerant condenser, manuscripts completed.

**Y. Qiao**, Y. Hwang, R. Radermacher, Numerical study on phase change material (PCM)-to-refrigerant heat exchanger coupled thermal energy storage system, manuscripts completed.

**Y. Qiao**, Y. Hwang, R. Radermacher, Numerical study for multi-tube PCM heat exchanger.

# References

Adine, H.A., El Qarnia, H., 2009. Numerical analysis of the thermal behaviour of a shell-and-tube heat storage unit using phase change materials. Appl. Math. Model. 33, 2132–2144. https://doi.org/10.1016/j.apm.2008.05.016

Ahmadi, R., Hosseini, M.J., Ranjbar, A.A., Bahrampoury, R., 2018. Phase change in spiral coil heat storage systems. Sustain. Cities Soc. 38, 145–157. https://doi.org/10.1016/j.scs.2017.12.026

Al-Abidi, A.A., Bin Mat, S., Sopian, K., Sulaiman, M.Y., Mohammed, A.T., 2013. CFD applications for latent heat thermal energy storage: a review. Renew. Sustain. Energy Rev. 20, 353–363. https://doi.org/10.1016/j.rser.2012.11.079

Al-Abidi, A.A., Mat, S., Sopian, K., Sulaiman, M.Y., Mohammad, A.T., 2014. Experimental study of melting and solidification of PCM in a triplex tube heat exchanger with fins. Energy Build. 68, 33–41. https://doi.org/10.1016/j.enbuild.2013.09.007

Al Assaad, D., Habchi, C., Ghali, K., Ghaddar, N., 2018. Simplified model for thermal comfort, IAQ and energy savings in rooms conditioned by displacement ventilation aided with transient personalized ventilation. Energy Convers. Manag. 162, 203–217. https://doi.org/10.1016/j.enconman.2018.02.033

Alam, T.E., Dhau, J.S., Goswami, D.Y., Stefanakos, E., 2015. Macroencapsulation and characterization of phase change materials for latent heat thermal energy storage systems. Appl. Energy 154, 92–101. https://doi.org/10.1016/j.apenergy.2015.04.086

Angelucci, G., Mollaioli, F., 2018. Voronoi-like grid systems for tall buildings. Front. Built Environ. 4, 1–20. https://doi.org/10.3389/fbuil.2018.00078

Antoun, S., Ghaddar, N., Ghali, K., 2016. Coaxial personalized ventilation system and window performance for human thermal comfort in asymmetrical environment. Energy Build. 111, 253–266. https://doi.org/10.1016/j.enbuild.2015.11.030

Arasu, A.V., Mujumdar, A.S., 2012. Numerical study on melting of paraffin wax with Al 2O 3 in a square enclosure. Int. Commun. Heat Mass Transf. 39, 8–16. https://doi.org/10.1016/j.icheatmasstransfer.2011.09.013

Arıcı, M., Tütüncü, E., Kan, M., Karabay, H., 2017. Melting of nanoparticle-enhanced paraffin wax in a rectangular enclosure with partially active walls. Int. J. Heat Mass Transf. 104, 7–17. https://doi.org/10.1016/j.ijheatmasstransfer.2016.08.017

Aute, V., Radermacher, R., 2014. Standardized Polynomials for Fast Evaluation of Refrigerant Thermophysical Properties, in: International Compressor Engineering, Refrigeration and Air Conditioning, and High Performance Buildings Conferences. pp. 1–10.

Azzouz, K., Leducq, D., Gobin, D., 2008. Performance enhancement of a household refrigerator by addition of latent heat storage. Int. J. Refrig. 31, 892–901. https://doi.org/10.1016/j.ijrefrig.2007.09.007

Azzouzi, D., Kelkouli, M., Amaryoucef, F., 2017. Parametric study of the wire-on-tube condenser subcooling effect on the performance of vapor compression refrigeration system. Appl. Therm. Eng. 122, 528–534. https://doi.org/10.1016/j.applthermaleng.2017.05.003

Bakhshipour, S., Valipour, M.S., Pahamli, Y., 2017. Parametric analysis of domestic

refrigerators using PCM heat exchanger. Int. J. Refrig. 83, 1–13. https://doi.org/10.1016/j.ijrefrig.2017.07.014

Berardi, U., Soudian, S., 2019. Experimental investigation of latent heat thermal energy storage using PCMs with different melting temperatures for building retrofit. Energy Build. 185, 180–195. https://doi.org/10.1016/j.enbuild.2018.12.016

Bonnissel, M., Luo, L., Tondeur, D., 2001. Compacted exfoliated natural graphite as heat conduction medium, Carbon. https://doi.org/10.1016/S0008-6223(01)00032-X

Bouhal, T., El Rhafiki, T., Kousksou, T., Jamil, A., Zeraouli, Y., 2018. PCM addition inside solar water heaters: Numerical comparative approach. J. Energy Storage 19, 232–246. https://doi.org/10.1016/j.est.2018.08.005

Caron-Soupart, A., Fourmigué, J.F., Marty, P., Couturier, R., 2016. Performance analysis of thermal energy storage systems using phase change material. Appl. Therm. Eng. 98, 1286–1296. https://doi.org/10.1016/j.applthermaleng.2016.01.016

Chakroun, W., Ghaddar, N., Ghali, K., 2011. Chilled ceiling and displacement ventilation aided with personalized evaporative cooler. Energy Build. 43, 3250–3257. https://doi.org/10.1016/j.enbuild.2011.08.026

Chen, C., Zhang, H., Gao, X., Xu, T., Fang, Y., Zhang, Z., 2016. Numerical and experimental investigation on latent thermal energy storage system with spiral coil tube and paraffin / expanded graphite composite PCM. Energy Convers. Manag. 126, 889–897. https://doi.org/10.1016/j.enconman.2016.08.068

Cheng, W.-L., Yuan, X.-D., 2013. Numerical analysis of a novel household refrigerator

with shape-stabilized PCM (phase change material) heat storage condensers. Energy 59, 265–276. https://doi.org/10.1016/J.ENERGY.2013.06.045

Choi, H.S., Yun, S., Whang, K. i., 2007. Development of a temperature-controlled car-seat system utilizing thermoelectric device. Appl. Therm. Eng. 27, 2841–2849. https://doi.org/10.1016/j.applthermaleng.2006.09.004

Churchill, S.W., Chu, H.H.S., 1975. Correlating equations for laminar and turbulent free convection from a vertical plate. Int. J. Heat Mass Transf. 18, 1323–1329. https://doi.org/10.1016/0017-9310(75)90243-4

Corberán, J.M., Martínez, I.O., Gonzálvez, J., 2008. Charge optimisation study of a reversible water-to-water propane heat pump. Int. J. Refrig. 31, 716–726. https://doi.org/10.1016/j.ijrefrig.2007.12.011

Dannemand, M., Johansen, J.B., Furbo, S., 2016. Solidification behavior and thermal conductivity of bulk sodium acetate trihydrate composites with thickening agents and graphite. Sol. Energy Mater. Sol. Cells 145, 287–295. https://doi.org/10.1016/j.solmat.2015.10.038

Dardir, M., Panchabikesan, K., Haghighat, F., El Mankibi, M., Yuan, Y., 2019. Opportunities and challenges of PCM-to-air heat exchangers (PAHXs) for building free cooling applications—A comprehensive review. J. Energy Storage. https://doi.org/10.1016/j.est.2019.02.011

de Gracia, A., 2019. Dynamic building envelope with PCM for cooling purposes – Proof of concept. Appl. Energy 235, 1245–1253. https://doi.org/10.1016/j.apenergy.2018.11.061

Dhumane, R., Ling, J., Aute, V., Radermacher, R., 2017. Portable personal

conditioning systems: Transient modeling and system analysis. Appl. Energy 208, 390–401. https://doi.org/10.1016/j.apenergy.2017.10.023

Dhumane, R., Qiao, Y., Ling, J., Muehlbauer, J., Aute, V., Hwang, Y., Radermacher, R., 2019. Improving system performance of a personal conditioning system integrated with thermal storage. Appl. Therm. Eng. 147, 40–51. https://doi.org/10.1016/j.applthermaleng.2018.10.004

Dirichlet, G.L., 1850. Über die Reduction der positiven quadratischen Formen mit drei unbestimmten ganzen Zahlen. J. für die reine und Angew. Math. 1850, 209–227. https://doi.org/10.1515/crll.1850.40.209

Dutil, Y., Rousse, D.R., Salah, N. Ben, Lassue, S., Zalewski, L., 2011. A review on phase-change materials: Mathematical modeling and simulations. Renew. Sustain. Energy Rev. 15, 112–130. https://doi.org/10.1016/j.rser.2010.06.011

Eyres, N.R., Hartree, D.R., Ingham, J., Jackson, R., Sarjant, R.J., Wagstaff, J.B., 1946. The Calculation of Variable Heat Flow in Solids. Philos. Trans. R. Soc. A Math. Phys. Eng. Sci. 240, 1–57. https://doi.org/10.1098/rsta.1946.0002

Fang, Y., Niu, J., Deng, S., 2018. Numerical analysis for maximizing effective energy storage capacity of thermal energy storage systems by enhancing heat transfer in PCM. Energy Build. 160, 10–18. https://doi.org/10.1016/j.enbuild.2017.12.006

Fleming, E., Wen, S., Shi, L., Da Silva, A.K., 2013. Thermodynamic model of a thermal storage air conditioning system with dynamic behavior. Appl. Energy 112, 160–169. https://doi.org/10.1016/j.apenergy.2013.05.058

Gasia, J., de Gracia, A., Peiró, G., Arena, S., Cau, G., Cabeza, L.F., 2018. Use of partial load operating conditions for latent thermal energy storage management. Appl.

Energy 216, 234–242. https://doi.org/10.1016/j.apenergy.2018.02.061

Ghahramani Zarajabad, O., Ahmadi, R., 2018. Numerical investigation of different PCM volume on cold thermal energy storage system. J. Energy Storage 17, 515–524. https://doi.org/10.1016/j.est.2018.04.013

Ghani, S., ElBialy, E.M.A.A., Bakochristou, F., Gamaledin, S.M.A., Rashwan, M.M., 2016. The effect of forced convection and PCM on helmets' thermal performance in hot and arid environments. Appl. Therm. Eng. 111, 624–637. https://doi.org/10.1016/j.applthermaleng.2016.09.142

Gnielinski, V., 2013. On heat transfer in tubes. Int. J. Heat Mass Transf. 63, 134–140. https://doi.org/10.1016/j.ijheatmasstransfer.2013.04.015

Gu, Z., Liu, H., Li, Y., 2004. Thermal energy recovery of air conditioning system - Heat recovery system calculation and phase change materials development. Appl. Therm. Eng. 24, 2511–2526. https://doi.org/10.1016/j.applthermaleng.2004.03.017

Haillot, D., Goetz, V., Py, X., Benabdelkarim, M., 2011. High performance storage composite for the enhancement of solar domestic hot water systems. Part 1: Storage material investigation. Sol. Energy 85, 1021–1027. https://doi.org/10.1016/j.solener.2011.02.016

He, D., Li, N., He, Y., He, M., Song, C., Chen, H., 2017. Experimental Study on Thermal Sensation of Radiant Cooling Workstation and Desktop Fan in Hot-humid Environment, in: Procedia Engineering. pp. 757–764. https://doi.org/10.1016/j.proeng.2017.10.007

He, Y., Li, N., He, M., He, D., 2017. Using radiant cooling desk for maintaining

comfort in hot environment. Energy Build. 145, 144–154. https://doi.org/10.1016/j.enbuild.2017.04.013

Heidarinejad, M., Dalgo, D.A., Mattise, N.W., Srebric, J., 2018. Personalized cooling as an energy efficiency technology for city energy footprint reduction. J. Clean. Prod. 171, 491–505. https://doi.org/10.1016/j.jclepro.2017.10.008

Hong, K.T., Webb, R.L., 1996. Calculation of Fin Efficiency for Wet and Dry Fins. HVAC&R Res. 2, 27–41.

Hosseini, M.J., Rahimi, M., Bahrampoury, R., 2014. Experimental and computational evolution of a shell and tube heat exchanger as a PCM thermal storage system. Int. Commun. Heat Mass Transf. 50, 128–136. https://doi.org/10.1016/j.icheatmasstransfer.2013.11.008

Hou, J., Yang, Z., Xu, P., 2019. Design and performance evaluation of novel personal cooling garment. Appl. Therm. Eng. https://doi.org/10.1016/j.applthermaleng.2019.02.013

Hoyt, T., Arens, E., Zhang, H., 2014. Extending air temperature setpoints: Simulated energy savings and design considerations for new and retrofit buildings. Build. Environ. 88, 89–96. https://doi.org/10.1016/j.buildenv.2014.09.010

Huang, J., Gurney, K.R., 2016. The variation of climate change impact on building energy consumption to building type and spatiotemporal scale. Energy 111, 137–153. https://doi.org/10.1016/j.energy.2016.05.118

Hunter, L.W., Kuttler, J.R., 1989. The enthalpy method for heat conduction problems with moving boundaries. J. Heat Transfer 111, 239–242. https://doi.org/10.1115/1.3250668

Jian-you, L., 2008. Numerical and experimental investigation for heat transfer in triplex concentric tube with phase change material for thermal energy storage. Sol. Energy 82, 977–985. https://doi.org/10.1016/j.solener.2008.05.006

Jin, X., Hu, H., Shi, X., Zhou, X., Zhang, X., 2018. Comparison of two numerical heat transfer models for phase change material board. Appl. Therm. Eng. 128, 1331–1339. https://doi.org/10.1016/j.applthermaleng.2017.09.015

Jmal, I., Baccar, M., 2018. Numerical investigation of PCM solidification in a finned rectangular heat exchanger including natural convection. Int. J. Heat Mass Transf. 127, 714–727. https://doi.org/10.1016/j.ijheatmasstransfer.2018.08.058

Joybari, M.M., Haghighat, F., Seddegh, S., Al-Abidi, A.A., 2017. Heat transfer enhancement of phase change materials by fins under simultaneous charging and discharging. Energy Convers. Manag. 152, 136–156. https://doi.org/10.1016/J.ENCONMAN.2017.09.018

Jung, D.S., Radermacher, R., 1989. Prediction of pressure drop during horizontal annular flow boiling of pure and mixed refrigerants. Int. J. Heat Mass Transf. 32, 2435–2446. https://doi.org/10.1016/0017-9310(89)90203-2

Kang, Z., Udayraj, Wan, X., Wang, F., 2018. A new hybrid personal cooling system (HPCS) incorporating insulation pads for thermal comfort management: Experimental validation and parametric study. Build. Environ. 145, 276–289. https://doi.org/10.1016/j.buildenv.2018.09.033

Khalifa, H.E., Koz, M., 2016. Numerical investigation of the freezing of a phase change material in a thermal storage device with an embedded evaporator, in: ASME 2016 Heat Transfer Summer Conference, HT 2016.

Kim, D.H., Park, H.S., Kim, M.S., 2014. The effect of the refrigerant charge amount on single and cascade cycle heat pump systems. Int. J. Refrig. 40, 254–268. https://doi.org/10.1016/j.ijrefrig.2013.10.002

Kim, N.-H., Yun, J.-H., Webb, R.L., 1997. Heat Transfer and Friction Correlations for Wavy Plate Fin-and-Tube Heat Exchangers. J. Heat Transfer 119, 560–567. https://doi.org/10.1115/1.2824141

Kuehn, T.H., Ramsey, J.W., Threlkeld, J.L., 1998. Thermal Environmental Engineering, Prentice Hall.

Lamberg, P., Lehtiniemi, R., Henell, A.M., 2004. Numerical and experimental investigation of melting and freezing processes in phase change material storage. Int. J. Therm. Sci. 43, 277–287. https://doi.org/10.1016/j.ijthermalsci.2003.07.001

Lamberg, Piia, Sirén, K., 2003. Approximate analytical model for solidification in a finite PCM storage with internal fins. Appl. Math. Model. 27, 491–513. https://doi.org/10.1016/S0307-904X(03)00080-5

Lamberg, P., Sirén, K., 2003. Analytical model for melting in a semi-infinite PCM storage with an internal fin. Heat Mass Transf. 39, 167–176. https://doi.org/10.1007/s00231-002-0291-1

Laughman, C.R., Qiao, H., 2017. On the influence of state selection on mass conservation in dynamic vapour compression cycle models. Math. Comput. Model. Dyn. Syst. 23, 262–283. https://doi.org/10.1080/13873954.2017.1298625

Li, M.-J., Jin, B., Ma, Z., Yuan, F., 2018. Experimental and numerical study on the performance of a new high-temperature packed-bed thermal energy storage

system with macroencapsulation of molten salt phase change material. Appl. Energy 221, 1–15. https://doi.org/10.1016/J.APENERGY.2018.03.156

Liu, C., Groulx, D., 2014. Experimental study of the phase change heat transfer inside a horizontal cylindrical latent heat energy storage system. Int. J. Therm. Sci. 82, 100–110. https://doi.org/10.1016/j.ijthermalsci.2014.03.014

Lizana, J., de-Borja-Torrejon, M., Barrios-Padura, A., Auer, T., Chacartegui, R., 2019. Passive cooling through phase change materials in buildings. A critical study of implementation alternatives. Appl. Energy 254, 113658. https://doi.org/10.1016/j.apenergy.2019.113658

Longeon, M., Soupart, A., Fourmigué, J.-F., Bruch, A., Marty, P., 2013. Experimental and numerical study of annular PCM storage in the presence of natural convection. Appl. Energy 112, 175–184. https://doi.org/10.1016/J.APENERGY.2013.06.007

Lorente, S., Bejan, A., Niu, J.L., 2014. Phase change heat storage in an enclosure with vertical pipe in the center. Int. J. Heat Mass Transf. 72, 329–335. https://doi.org/10.1016/j.ijheatmasstransfer.2014.01.021

Lou, L., Wu, Y.S., Fan, J., Zhao, D., Wang, Q., Fan, T., Yang, R., Lu, X., 2018. Personal thermal management using portable thermoelectrics for potential building energy saving. Appl. Energy 218, 282–291. https://doi.org/10.1016/j.apenergy.2018.02.158

Mahdi, J.M., Nsofor, E.C., 2017. Solidification enhancement in a triplex-tube latent heat energy storage system using nanoparticles-metal foam combination. Energy 126, 501–512. https://doi.org/10.1016/j.energy.2017.03.060

Makhoul, A., Ghali, K., Ghaddar, N., 2013. Thermal comfort and energy performance

of a low-mixing ceiling-mounted personalized ventilator system. Build. Environ. 60, 126–136. https://doi.org/10.1016/j.buildenv.2012.11.016

Mallow, A., Abdelaziz, O., Graham, S., 2018. Thermal charging performance of enhanced phase change material composites for thermal battery design. Int. J. Therm. Sci. 127, 19–28. https://doi.org/10.1016/j.ijthermalsci.2017.12.027

Mandilaras, I.D., Kontogeorgos, D.A., Founti, M.A., 2015. A hybrid methodology for the determination of the effective heat capacity of PCM enhanced building components. Renew. Energy 76, 790–804. https://doi.org/10.1016/j.renene.2014.11.078

Martinelli, M., Bentivoglio, F., Caron-Soupart, A., Couturier, R., Fourmigue, J.F., Marty, P., 2016. Experimental study of a phase change thermal energy storage with copper foam. Appl. Therm. Eng. 101, 247–261. https://doi.org/10.1016/j.applthermaleng.2016.02.095

Mat, S., Al-Abidi, A.A., Sopian, K., Sulaiman, M.Y., Mohammad, A.T., 2013. Enhance heat transfer for PCM melting in triplex tube with internal-external fins. Energy Convers. Manag. 74, 223–236. https://doi.org/10.1016/j.enconman.2013.05.003

Medrano, M., Yilmaz, M.O., Nogués, M., Martorell, I., Roca, J., Cabeza, L.F., 2009. Experimental evaluation of commercial heat exchangers for use as PCM thermal storage systems. Appl. Energy 86, 2047–2055. https://doi.org/10.1016/j.apenergy.2009.01.014

Merlin, K., Delaunay, D., Soto, J., Traonvouez, L., 2016. Heat transfer enhancement in latent heat thermal storage systems: Comparative study of different solutions and

thermal contact investigation between the exchanger and the PCM. Appl. Energy 166, 107–116. https://doi.org/10.1016/j.apenergy.2016.01.012

Mills, A., Farid, M., Selman, J.R., Al-Hallaj, S., 2006. Thermal conductivity enhancement of phase change materials using a graphite matrix. Appl. Therm. Eng. 26, 1652–1661. https://doi.org/10.1016/j.applthermaleng.2005.11.022

Mondal, S., 2008. Phase change materials for smart textiles - An overview. Appl. Therm. Eng. 28, 1536–1550. https://doi.org/10.1016/j.applthermaleng.2007.08.009

Murray, R.E., Groulx, D., 2014. Experimental study of the phase change and energy characteristics inside a cylindrical latent heat energy storage system: Part 2 simultaneos charging and discharging. Renew. Energy 62, 571–581. https://doi.org/10.1016/j.renene.2013.10.004

Oró, E., De Gracia, A., Cabeza, L.F., 2013. Active phase change material package for thermal protection of ice cream containers. Int. J. Refrig. 36, 102–109. https://doi.org/10.1016/j.ijrefrig.2012.09.011

Pasut, W., Zhang, H., Arens, E., Zhai, Y., 2015. Energy-efficient comfort with a heated/cooled chair: Results from human subject tests. Build. Environ. 84, 10–21. https://doi.org/10.1016/j.buildenv.2014.10.026

Pitarch, M., Hervas-Blasco, E., Navarro-Peris, E., Gonzálvez-Maciá, J., Corberán, J.M., 2017. Evaluation of optimal subcooling in subcritical heat pump systems. Int. J. Refrig. 78, 18–31. https://doi.org/10.1016/j.ijrefrig.2017.03.015

Poggi, F., Macchi-Tejeda, H., Leducq, D., Bontemps, A., 2008. Refrigerant charge in refrigerating systems and strategies of charge reduction. Int. J. Refrig. 31, 353–

370. https://doi.org/10.1016/j.ijrefrig.2007.05.014

Pottker, G., Hrnjak, P., 2015. Effect of the condenser subcooling on the performance of vapor compression systems. Int. J. Refrig. 50, 156–164. https://doi.org/10.1016/j.ijrefrig.2014.11.003

PureTemp, n.d. PureTemp -37 technical data sheet [WWW Document]. URL http://www.puretemp.com/stories/puretemp-37-tds (accessed 8.9.18).

Py, X., Olives, R., Mauran, S., 2001. paraffin/porous-graphite-matrix composite as high and constant power thermal storage material. Int. J. Heat Mass Transf. 44, 2727–2737.

Qiao, H., Aute, V., Lee, H., Saleh, K., Radermacher, R., 2013. A new model for plate heat exchangers with generalized flow configurations and phase change. Int. J. Refrig. 36, 622–632. https://doi.org/10.1016/j.ijrefrig.2012.11.020

Qiao, H., Aute, V., Radermacher, R., 2015. Transient modeling of a flash tank vapor injection heat pump system - Part I: Model development. Int. J. Refrig. 49, 169–182. https://doi.org/10.1016/j.ijrefrig.2014.06.019

Qiao, Y., Du, Y., Muehlbauer, J., Hwang, Y., Radermacher, R., 2019. Experimental study of enhanced PCM exchangers applied in a thermal energy storage system for personal cooling. Int. J. Refrig. 102, 22–34. https://doi.org/10.1016/J.IJREFRIG.2019.03.006

Rahimi, M., Hosseini, M.J., Gorzin, M., 2019. Effect of helical diameter on the performance of shell and helical tube heat exchanger: An experimental approach. Sustain. Cities Soc. 44, 691–701. https://doi.org/10.1016/j.scs.2018.11.002

Seddegh, S., Wang, X., Joybari, M.M., Haghighat, F., 2017. Investigation of the effect

of geometric and operating parameters on thermal behavior of vertical shell-and-tube latent heat energy storage systems. Energy 137, 69–82. https://doi.org/10.1016/j.energy.2017.07.014

Shah, M.M., 2009. An improved and extended general correlation for heat transfer during condensation in plain tubes. HVAC&R Res. Sept. 15.

Stritih, U., Tyagi, V. V., Stropnik, R., Paksoy, H., Haghighat, F., Joybari, M.M., 2018. Integration of passive PCM technologies for net-zero energy buildings. Sustain. Cities Soc. 41, 286–295. https://doi.org/10.1016/j.scs.2018.04.036

Tan, F.L., Fok, S.C., 2006. Cooling of helmet with phase change material. Appl. Therm. Eng. 26, 2067–2072. https://doi.org/10.1016/j.applthermaleng.2006.04.022

Tao, Y.B., He, Y.L., 2011. Numerical study on thermal energy storage performance of phase change material under non-steady-state inlet boundary. Appl. Energy 88, 4172–4179. https://doi.org/10.1016/j.apenergy.2011.04.039

Tay, N.H.S., Belusko, M., Bruno, F., 2012. An effectiveness-NTU technique for characterising tube-in-tank phase change thermal energy storage systems. Appl. Energy 91, 309–319. https://doi.org/10.1016/j.apenergy.2011.09.039

Tian, Y., Zhao, C.Y., 2011. A numerical investigation of heat transfer in phase change materials (PCMs) embedded in porous metals. Energy 36, 5539–5546. https://doi.org/10.1016/j.energy.2011.07.019

Trp, A., 2005. An experimental and numerical investigation of heat transfer during technical grade paraffin melting and solidification in a shell-and-tube latent thermal energy storage unit. Sol. Energy 79, 648–660.

https://doi.org/10.1016/j.solener.2005.03.006

Wang, F., Maidment, G., Missenden, J., Tozer, R., 2007a. The novel use of phase change materials in refrigeration plant. Part 1: Experimental investigation. Appl. Therm. Eng. 27, 2893–2901. https://doi.org/10.1016/J.APPLTHERMALENG.2005.06.011

Wang, F., Maidment, G., Missenden, J., Tozer, R., 2007b. The novel use of phase change materials in refrigeration plant. Part 2: Dynamic simulation model for the combined system. Appl. Therm. Eng. 27, 2902–2910. https://doi.org/10.1016/j.applthermaleng.2005.06.009

Wang, W., Li, Y., Cao, F., 2019. Extremum seeking control for efficient operation of an air-source heat pump water heater with internal heat exchanger cycle vapor injection. Int. J. Refrig. 99, 153–165. https://doi.org/10.1016/j.ijrefrig.2019.01.002

Wang, X., Guo, Q., Zhong, Y., Wei, X., Liu, L., 2013. Heat transfer enhancement of neopentyl glycol using compressed expanded natural graphite for thermal energy storage. Renew. Energy 51, 241–246. https://doi.org/10.1016/j.renene.2012.09.029

Weinlader, H., Klinker, F., Yasin, M., 2016. PCM cooling ceilings in the Energy Efficiency Center - Passive cooling potential of two different system designs. Energy Build. 119, 93–100. https://doi.org/10.1016/j.enbuild.2016.03.031

Wu, J., Gagnière, E., Couenne, F., Hamroun, B., Latour, T., Jallut, C., 2015. A hybrid transient model for simulation of air-cooled refrigeration systems: Description and experimental validation. Int. J. Refrig. 53, 142–154.

https://doi.org/10.1016/j.ijrefrig.2014.10.008

Wu, M., Xu, C., He, Y., 2016. Cyclic behaviors of the molten-salt packed-bed thermal storage system filled with cascaded phase change material capsules. Appl. Therm. Eng. 93, 1061–1073. https://doi.org/10.1016/J.APPLTHERMALENG.2015.10.014

Yang, X.H., Bai, J.X., Yan, H. Bin, Kuang, J.J., Lu, T.J., Kim, T., 2014. An Analytical Unit Cell Model for the Effective Thermal Conductivity of High Porosity Open-Cell Metal Foams. Transp. Porous Media 102, 403–426. https://doi.org/10.1007/s11242-014-0281-z

Yang, Y., Stapleton, J., Diagne, B.T., Kenny, G.P., Lan, C.Q., 2012. Man-portable personal cooling garment based on vacuum desiccant cooling. Appl. Therm. Eng. 47, 18–24. https://doi.org/10.1016/j.applthermaleng.2012.04.012

Yao, Y., Wu, H., Liu, Z., 2015. A new prediction model for the effective thermal conductivity of high porosity open-cell metal foams. Int. J. Therm. Sci. 97, 56–67. https://doi.org/10.1016/j.ijthermalsci.2015.06.008

Yi, W., Zhao, Y., Chan, A.P.C., 2017. Evaluation of the ventilation unit for personal cooling system (PCS). Int. J. Ind. Ergon. 58, 62–68. https://doi.org/10.1016/J.ERGON.2017.02.009

Youssef, W., Ge, Y.T., Tassou, S.A., 2018. CFD modelling development and experimental validation of a phase change material (PCM) heat exchanger with spiral-wired tubes. Energy Convers. Manag. 157, 498–510. https://doi.org/10.1016/J.ENCONMAN.2017.12.036

Yuan, F., Li, M.-J., Ma, Z., Jin, B., Liu, Z., 2018. Experimental study on thermal

performance of high-temperature molten salt cascaded latent heat thermal energy storage system. Int. J. Heat Mass Transf. 118, 997–1011. https://doi.org/10.1016/J.IJHEATMASSTRANSFER.2017.11.024

Zhai, Y., Zhang, H., Zhang, Y., Pasut, W., Arens, E., Meng, Q., 2013. Comfort under personally controlled air movement in warm and humid environments. Build. Environ. 65, 109–117. https://doi.org/10.1016/J.BUILDENV.2013.03.022

Zhao, C.Y., Lu, W., Tian, Y., 2010. Heat transfer enhancement for thermal energy storage using metal foams embedded within phase change materials (PCMs). Sol. Energy 84, 1402–1412. https://doi.org/10.1016/j.solener.2010.04.022

Zhao, M., Gao, C., Wang, F., Kuklane, K., Holmér, I., Li, J., 2013. A study on local cooling of garments with ventilation fans and openings placed at different torso sites. Int. J. Ind. Ergon. 43, 232–237. https://doi.org/10.1016/j.ergon.2013.01.001

Zheng, H., Wang, C., Liu, Q., Tian, Z., Fan, X., 2018. Thermal performance of copper foam/paraffin composite phase change material. Energy Convers. Manag. 157, 372–381. https://doi.org/10.1016/j.enconman.2017.12.023

Zhu, S., Dalgo, D., Srebric, J., Kato, S., 2017. Cooling efficiency of a spot-type personalized air-conditioner. Build. Environ. 121, 35–48. https://doi.org/10.1016/j.buildenv.2017.05.007

Zukowski, M., 2007. Mathematical modeling and numerical simulation of a short term thermal energy storage system using phase change material for heating applications. Energy Convers. Manag. 48, 155–165. https://doi.org/10.1016/j.enconman.2006.04.017